Dissertation
submitted to the
Combined Faculties for the Natural Sciences and for Mathematics
of the
Ruperto-Carola-University of Heidelberg
for the degree of
Doctor of Natural Sciences

Put forward by

Aleksandr Chatrchyan

born in: *Dubna*

Oral examination: *July 21, 2020*

Nonperturbative dynamics in the early universe: from axion-like particles to dark matter and condensates

Referees:

Prof. Dr. Jürgen Berges
Prof. Dr. Björn Malte Schäfer

Abstract

Scalar fields play an important role in cosmology. They can be responsible for cosmic inflation in the very early universe, as well as are among well-motivated dark matter (DM) candidates. The aim of this dissertation is to contribute to a better understanding of the dynamics of such fields in the nonperturbative regime.

Motivated by cosmological scenarios, we consider coherent oscillations of a scalar field in potentials that are summed from periodic and monomial terms, which have recently attracted much attention in the context of axion-like particles (ALP). We investigate the resonant amplification of quantum fluctuations, as well as the subsequent nonlinear dynamics after the fragmentation of the field.

Our studies are extended to the nonthermal production of ALP DM. It is found that the process of fragmentation imprints strong overdensities of DM on small scales, as well as can produce a stochastic gravitational wave background, potentially within reach of future detectors.

Finally, we investigate the role of experiments with ultracold atoms for the quantum simulation of nonperturbative dynamics and describe how, by means of a modulation of the interatomic interaction strength, such Bose gases can go through the characteristic stages of the dynamics of relativistic systems in the early universe.

Zusammenfassung

Skalare Felder spielen eine wichtige Rolle in der Kosmologie. Sie können für die kosmische Inflation in der Frühzeit des Universums verantwortlich sein und stellen ein wohlbegründetes Modell zur Erklärung Dunkler Materie zur Verfügung. Ziel dieser Arbeit ist ein Beitrag zum besseren Verständnis der Dynamik solcher Felder im nicht-perturbativen Regime.

Motiviert durch kosmologische Szenarien betrachten wir kohärente Oszillationen eines Skalarfeldes in Potentialen, die durch eine Summe periodischer und monomischer Terme gegeben sind und die unlängst viel Aufmerksamkeit im Kontext von Axionen-ähnlichen Teilchen generiert haben. Wir untersuchen die resonante Verstärkung von Quantenfluktuationen sowie die anschließende Fragmentierung des Feldes.

Weiterhin studieren wir die nicht-thermische Produktion von Dunkler Materie aufgebaut aus Axionen-ähnlichen Teilchen. Zentrales Ergebnis ist, dass der Prozess der Fragmentierung übermäßige Dichten Dunkler Materie auf kleinen Skalen hervorruft und einen stochastischen Gravitationswellen-Hintergrund erzeugen kann möglicherweise messbar durch künftige Detektoren.

Zum Schluss untersuchen wir die Rolle von Experimenten mit ultrakalten Atomen zur Quantensimulation der nicht-perturbativen Dynamik und beschreiben, wie durch Modulation der interatomaren Wechselwirkungsstärke solch Bose-Gase die charakteristischen Regime der Dynamik relativistischer Systeme im frühen Universum durchlaufen können.

Declaration of Authorship

I, Aleksandr Chatrchyan, declare that this thesis titled, "Nonperturbative dynamics in the early universe: from axion-like particles to dark matter and condensates" and the work presented in it are my own. I confirm that:

- Where any part of this thesis has previously been submitted for a degree or any other qualification at this University or any other institution, this has been clearly stated.

- Where I have consulted the published work of others, this is always clearly attributed.

- Where I have quoted from the work of others, the source is always given. With the exception of such quotations, this thesis is entirely my own work.

- Parts of this dissertation have been published in the following articles [1–3]:
  - J. Berges, K. Boguslavski, A. Chatrchyan and J. Jaeckel,
    Attractive versus repulsive interactions in the Bose-Einstein condensation dynamics of relativistic field theories,
    Phys. Rev. D 96 (7), 076020 (2017).
  - J. Berges, A. Chatrchyan and J. Jaeckel,
    Foamy Dark Matter from Monodromies,
    JCAP, 2019 (08), 020.
  - A. Chatrchyan and J. Jaeckel,
    Gravitational waves from the fragmentation of axion-like particle dark matter,
    Preprint: 2004.07844 [hep-ph], prepared for the submission to JCAP.

- In addition, large parts of chapter 6 are based on work in preparation [4], in collaboration with Jürgen Berges, Kevin Geier, Philipp Hauke and Markus Oberthaler as well as the members of the "BECK" experiment in the Oberthaler group.

"The dark side of the Force is a pathway to many abilities some consider to be unnatural."

Emperor Palpatine

Contents

Abstract iii

Zusammenfassung v

Declaration of Authorship vii

1 Introduction 1

2 Preliminaries 7
- 2.1 Axion-like particles 7
  - 2.1.1 The QCD axion 8
  - 2.1.2 Axions from string theory compactifications 9
  - 2.1.3 ALPs with quasiperiodic potentials: monodromy 10
- 2.2 Scalar fields in inflationary cosmology 11
  - 2.2.1 ALPs driving inflation 12
  - 2.2.2 ALPs as dark matter fields 13
- 2.3 Nonequilibrium quantum dynamics of scalar fields 14
  - 2.3.1 Nonequilibrium generating functional 14
  - 2.3.2 Correlation functions 15
  - 2.3.3 The 2PI formalism and quantum equations of motion 16
  - 2.3.4 Kinetic description 18
  - 2.3.5 Classical-statistical approximation 20
  - 2.3.6 Summary 23

3 Scalar field dynamics in quasiperiodic potentials 25
- 3.1 The model 26
- 3.2 Background oscillations and instabilities 27
  - 3.2.1 Outline of the dynamics and power counting 27
  - 3.2.2 Linear regime: parametric resonance 29
  - 3.2.3 Nonlinear regime: secondary instabilities 31
  - 3.2.4 Classical-statistical simulations 34
  - 3.2.5 The decay of background oscillations 34
- 3.3 Universal dynamics near nonthermal fixed points 35
  - 3.3.1 Dynamics at low momenta 36
  - 3.3.2 Dynamics at high momenta 39
  - 3.3.3 $1/N$ resummation and kinetic description 40
- 3.4 Finding the lowest minimum 44
  - 3.4.1 Resonance-enhanced transitions 45
  - 3.4.2 Explosive bubble nucleation 47
  - 3.4.3 Getting trapped 49
- 3.5 Summary 50

4 Nonperturbative production of axion-like particle dark matter 53
- 4.1 ALPs as dark matter and monodromy 54
- 4.2 The dynamics of vacuum realignment 55
  - 4.2.1 Initial conditions 55
  - 4.2.2 Amplification of fluctuations: linear regime 56
  - 4.2.3 Amplification of fluctuations: beyond the linear regime 59
- 4.3 Structure formation, the equation of state and today's energy density 60
  - 4.3.1 Viability as DM 61
  - 4.3.2 Equation of state 62
  - 4.3.3 Energy density today 64
- 4.4 Strong fluctuations on small scales and their evolution 66
  - 4.4.1 Power spectrum of density fluctuations 67
  - 4.4.2 The fate of the overdensities 68
- 4.5 Summary 71

5 Gravitational wave signatures of nonperturbative dynamics 73
- 5.1 GW backgrounds 74
  - 5.1.1 Linearized theory of gravity 74
  - 5.1.2 Detection of GWs 75
- 5.2 GW production from ALP DM fragmentation 76
  - 5.2.1 Outline of the dynamics 76
  - 5.2.2 Analytical estimates 78
  - 5.2.3 GW production from lattice simulations 81
- 5.3 Enhanced GW signal from an extended ultrarelativistic dynamics . . 83
  - 5.3.1 The small mass and repulsive self-interactions 85
  - 5.3.2 The dynamics and GW production 85
  - 5.3.3 Simplified kinetic description of the late-time dynamics . . . 88
  - 5.3.4 Enlarged parameter space for the GW signal 89
  - 5.3.5 Constraints from structure formation 91
- 5.4 Summary 93

6 Simulating cosmological dynamics with ultracold quantum gases 95
- 6.1 Field-theoretical methods for ultracold atoms 96
  - 6.1.1 Microscopic description 96
  - 6.1.2 Nonequilibrium dynamics 97
- 6.2 Expanding spacetime 98
- 6.3 Connection to relativistic dynamics 101
- 6.4 Preheating in an atomic BEC 103
  - 6.4.1 Linearized equations of motion 103
  - 6.4.2 Linear amplification of fluctuations 105
  - 6.4.3 Secondary instabilities 106
- 6.5 Turbulent thermalization of Bose gases 109
  - 6.5.1 Kinetic description 109
  - 6.5.2 Scaling exponents from kinetic theory 110
  - 6.5.3 Comparison with classical-statistical simulations 112
  - 6.5.4 Thermalization versus expansion 113
- 6.6 Summary 115

7 Conclusion and outlook 117

Acknowledgements 121

A The calculation of the source term for secondary instabilities 123

B The modified spherical collapse model 127

C Simplified kinetic description 129
C.1 Deviations from the self-similar evolution 130
C.2 Kinetic description and the freeze-out 131
C.3 Energy conservation for the direct cascade 132

Bibliography 135

List of Abbreviations

nPI	**n**-**p**article **i**rreducible
ALP	**A**xion-**L**ike **P**articles
BBN	**B**ig **B**ang **N**ucleosynthesis
BBO	**B**ig **B**ang **O**bserver
BEC	**B**ose-**E**instein **C**ondensate
CMB	**C**osmic **M**icrowave **B**ackground
CDM	**C**old **D**ark **M**atter
CP	**C**harge-**P**arity
DM	**D**ark **M**atter
FRW	**F**riedmann-**R**obertson-**W**alker
GPE	**G**ross-**P**itaevskii **E**quation
GW	**G**ravitational **W**ave
KK	**K**aluza-**K**lein
LISA	**L**aser **I**nterferometer **S**pace **A**ntenna
LO	**L**eading **O**rder
MOT	**M**agneto-**O**ptical **T**rap
NLO	**N**ext-to-**L**eading **O**rder
NTFP	**N**on-**T**hermal **F**ixed **P**oint
pNGB	**p**seudo **N**ambu-**G**oldstone **B**osons
PQ	**P**eccei-**Q**uinn
QCD	**Q**uantum **C**hromo**D**ynamics
QFT	**Q**uantum **F**ield **T**heory
SKA	**S**quare **K**ilometre **A**rray
SM	**S**tandard **M**odel
SSB	**S**pontaneous **S**ymmetry **B**reaking
UV	**U**ltra**V**iolet

Chapter 1

Introduction

The discovery of the Higgs boson at the Large Hadron Collider (LHC) [5, 6] completed the Standard Model (SM) of particle physics. In contrast to its predecessors, the SM seems to provide a satisfactory theoretical description for natural phenomena occurring on earth and remains self-consistent all the way up to the Planck scale of quantum gravity. It also reaffirms the role of quantum field theory (QFT) as the proper theoretical framework for the description of quantum many-body systems. Nevertheless, SM is not free of shortcomings, especially when combined with general relativity on cosmological scales. Already the evidence, coming from cosmological and astrophysical observations [7–10], that there is about five times more matter in the universe than explained by SM, indicates the existence of new degrees of freedom yet to be discovered.

It is widely believed that scalar fields played an important role in the early universe. In particular, typical models of cosmic inflation, which corresponds to a phase of an accelerated expansion of the very early universe, involve a scalar field, whose potential energy dominated over the kinetic energy. Such an inflationary phase provides a dynamical solution to the puzzles of the homogeneity, isotropy and flatness of the universe [11–13]. It also explains the generation of the density perturbations for structure formation from the quantum fluctuations during inflation [14]. A phase of reheating of the universe necessarily follows inflation, during which the inflaton decays, e.g. into the lighter SM degrees of freedom [15]. While in principle the Higgs field can play the role of the inflaton, its quartic self-coupling $\lambda \sim 0.1$ significantly exceeds the value $\lambda \sim 10^{-13}$ required for the measured spectrum of density perturbations [16].

Inflation leaves the energy budget of the universe stored predominantly in a homogeneous inflaton field, thereby setting seemingly simple initial conditions for the post-inflationary dynamics. However, in a large class of models of inflation, where the amplitude of the inflaton oscillations is very large, $\phi \sim 1/\sqrt{\lambda}$, particle production occurs in a nonperturbative way [17]. The standard methods of perturbative QFT, which describe well the scattering experiments at the LHC, fail to properly describe the particle production in the presence of such strong fields. The solution to this issue involves a proper resummation of the perturbative expansion and a fully dynamical treatment of the problem. A convenient framework, which can describe the evolution in this regime, is provided by the two-particle irreducible (2PI) effective action [18] in conjunction with the Schwinger-Keldysh closed-time contour [19] (see [20] for an overview).

The theoretical understanding of particle production from a coherently oscillating background field and of the subsequent nonequilibrium dynamics has substantially improved within the last decades. Sufficiently strong oscillations trigger the resonant production of particles with certain momenta [17, 21]. This process, which in the inflationary context is called preheating, results in large occupation numbers, however the produced particles are distributed nonthermally and, thus, the system is still far from equilibrium. The dynamics in the subsequent regime of strong fluctuations usually involves the approach of the system towards nonequilibrium attractors with self-similar scaling behavior of the correlation functions and the particle momentum distribution function, known as nonthermal fixed points (NTFPs) [22–25]. Such scaling dynamics describes the transport of conserved quantities, such as energy or particle number, in momentum space, until the system eventually reaches thermal equilibrium.

The dynamics in the presence of "nonperturbatively" large fields is not restricted to the inflationary setting. As it will be demonstrated in this work, the nonthermal production of scalar dark matter (DM) can involve similar dynamics in the early universe. This dynamics would leave its signatures in today's spatial structure of DM on small scales inside galaxies and can produce a strong gravitational wave (GW) background. We will also describe how the characteristic stages of the dynamics can be simulated in tabletop experiments with ultracold bosonic atoms.

Axion-like particles and dark matter

Very light scalars are also among well-motivated candidates for the DM in the universe [26]. The small mass assures the stability of such fields on cosmological scales, as well as allows them to be naturally produced in the post-inflationary, radiation-dominated universe, in the form of a coherently oscillating field, via the so-called misalignment mechanism [26–29]. The masses of such particles can be as small as 10^{-22}eV, which would lead to an unusually large de Broglie wavelength $\lambda_{DB} \sim 10^{16}$km inside galaxies. The nonthermal production via the misalignment mechanism allows such scalar fields to behave as standard cold dark matter (CDM) on scales large compared to λ_{DB}, whereas on smaller scales the quantum uncertainty prevents the formation of structures [30, 31], providing a possible solution to the small-scale crises of CDM [32].

One may wonder how realistic such small masses are in QFT. As it is known, the square of the mass of a scalar field is subject to quadratically divergent quantum corrections. Given that the theory has an intrinsic cut-off at e.g. the Planck scale, a mass of that order is more favorable.[1] A small mass would instead be natural if it is protected by some approximate symmetry. This is the case for pseudo Nambu-Goldstone bosons (pNGBs) of continuous global symmetries. An important representative of this class is the well-motivated axion [33–35], a pNGB of a hypothetical chiral $U(1)$ symmetry, proposed as a dynamical solution to the problem of the absence of CP violation in quantum chromodynamics (QCD) [33]. Axion-like particles (ALPs) also arise from the compactification of extra-dimensional theories, including string theory, where their mass is protected by the higher-dimensional gauge symmetry (see e.g. [36, 37]). In particular, a plentitude of $10 - 100$ axions is a generic prediction of string theory [38–41]. The approximate shift symmetry of ALPs also makes them appealing candidates for the role of the inflaton, protecting the potential from quantum gravity corrections for super-Planckian field values.

An important feature of pNGBs, as well as standard ALPs, is their periodic potential, which is conventionally parametrized as $U(\phi) \propto \cos(\phi/f)$ [42]. The field can thus oscillate only within a finite range and, in the presence of expansion, the

---

[1] The unnaturalness of the Higgs mass is known as the electroweak hierarchy problem.

resonant particle production through the self-interactions is known to be negligible [27, 28] unless the initial misalignment field value is tuned with very high precision to the top of the potential [43, 44]. The field thus remains essentially homogeneous until the formation of galactic structures in the matter-dominated universe.

ALP potentials can also have more complicated shapes and, in particular, they can be summed from a periodic term and a term breaking the periodicity e.g. a monomial. Such quasiperiodic potentials can arise from the mixing of multiple ALPs [45–48], or from the spontaneous breaking of the higher-dimensional symmetry [49]. In the second case the ALP is said to exhibit a monodromy which, for string axions, can be realized by adding branes or fluxes [50–52]. Importantly, both types of potentials allow large field excursions over multiple "fundamental" periods of the potential. This property was employed in inflationary model building [50, 52], as well as in some dynamical mechanisms addressing the fine-tuning problems of the electroweak scale [53] and the cosmological constant [54, 55].

For ALP DM the possibility of large field displacements implies that the resonant decay channel can become efficient, as it was noted in [56]. It is therefore very important to obtain an understanding of the nonperturbative dynamics in such systems and to investigate its cosmological implications as well as possible observational signatures, which has not been done so far and is a central topic of this thesis.

Ultracold atomic gases as simulators of many-body dynamics

The dynamics of scalar fields, driven far from equilibrium, plays an important role in the early universe cosmology. Its theoretical description in terms of QFT naturally leads to the question of existence of analog systems where this regime of many-body dynamics can be explored experimentally. An appealing platform for this purpose is provided by ultracold atomic gases [57], trapped with magnetic and optical fields, which are readily available in many laboratories. Due to their high degree of controllability and isolation from the surrounding environment such systems can serve as quantum simulators of many-body dynamics.

With the help of modern cooling techniques the temperatures of atomic gases can be lowered down to $T \sim \mu$K, which allows the formation of a Bose-Einstein condensate (BEC). Such a coherent state of atoms is reminiscent of the coherent field present e.g. after inflation. The conservation of the atomic number, however, prevents the resonant conversion of condensate atoms which, as such, is a relativistic effect. As we demonstrate in this thesis, a time-dependent modulation of the interaction strength, which can experimentally be achieved via magnetic Feshbach resonances [58], would lead to the resonant of amplification of sound waves on top of the condensate [59–61], in analogy to post-inflationary preheating. Remarkably, this can drive the system through the characteristic stages of the dynamics that are also observed in the relativistic case.

The three systems that are considered in this thesis, which despite having vastly different mass scales are capable of exhibiting very similar dynamics, are illustrated in Fig. 1.1. The mass scale of the inflaton $m \sim 10^{-5} M_{Pl}$ is based on constraints from cosmic microwave background (CMB) observations for quadratic inflation [62, 63]. Constraints for the mass of ALP DM $10^{-22}\text{eV} \lesssim m \lesssim 10^{3}\text{eV}$ arise from structure formation surveys and relic photon detection [26, 31].

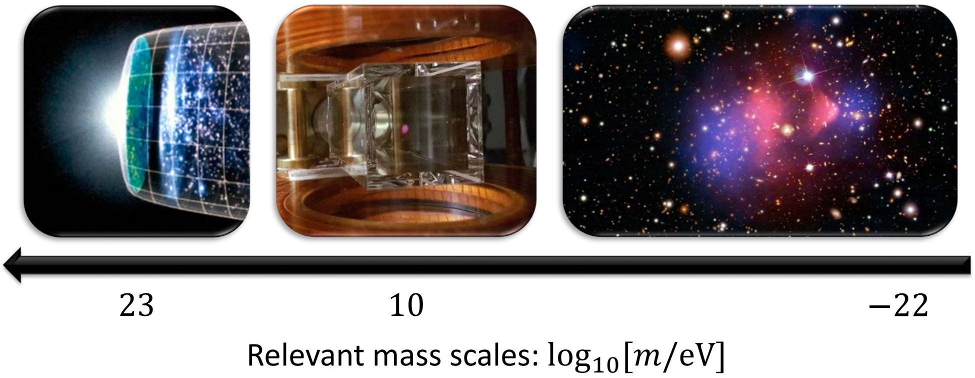

FIGURE 1.1: The three different systems, considered in this work, with the associated typical mass scales indicated on the horizontal axis. **Left:** The inflaton (the illustration of cosmic inflation taken from NASA/WMAP Science Team). **Center:** Cold atom gas (the cloud of atoms in the center of a magneto-optical trap (MOT), scattering the light from the MOT beams, image taken from the "BECK" experiment in the Oberthaler group). **Right:** Dark matter (the composite image of the Bullet cluster [9], with the mass distribution as determined by gravitational lensing shown in blue and the X-ray image shown in pink, image taken from [64]).

Outline of this work

We now present the outline of this thesis. The aim of chapter 2 is to provide some theoretical background for our studies. We start by reviewing the main properties of ALPs, as well as describing the phenomenon of monodromy. We then discuss the significance of scalar fields in cosmology, in the context of cosmic inflation as well as DM, emphasizing the role played by ALPs. In the final section of the chapter we describe the theoretical framework of nonequilibrium QFT that is used in this work [20]. We revisit the construction of the path integral and the derivation of equations of motion for the correlation functions from the 2PI effective action, applying the formalism to the case of the ALPs. We also demonstrate the emergence of effective classical-statistical field theory [65, 66], as well as kinetic descriptions [67], which are extensively used in the next chapters. The first description allows numerical lattice simulations of the field dynamics and becomes applicable in the regime of large occupation numbers at the characteristic momenta.

While there were many studies of the resonant decay of coherent oscillations in monotonic potentials, such as the φ^4 [17, 21, 22, 68, 69], the case of quasiperiodic potentials is much less explored. The latter is the main focus of chapter 3. There we consider Minkowski spacetime to separate the effects due to expansion. It is found that instabilities lead to the process of complete fragmentation of the background field. The approach to NTFPs is strongly affected by the repulsive versus the attractive nature of the self-interactions. Our numerical studies based on the classical-statistical approximation are complemented with a derivation of a vertex-resummed kinetic theory, similar to [25, 70, 71]. In the case of sufficiently strong "wiggles" the potential can have several local minima separated by potential barriers. We discuss how the amplification of fluctuations impacts the field's ability to overcome such barriers and demonstrate how it can induce dynamical transitions between the local minima.

In chapter 4 we study the role of the dynamics for ALP DM. As we demonstrate with the help of numerical simulations, for sufficiently strong "wiggles" and field displacements the initially homogeneous field is completely converted into strong fluctuations on relatively small length scales, soon after the onset of oscillations. We also consider constraints for successful structure formation and find that for a wide range of masses the ALPs still remain viable as CDM. By deriving a modified version of the Press-Schechter spherical collapse model [72, 73] we study the impact of gravity on the over-densities imprinted from fragmentation. It is found that the internal pressure of such over-densities prevents them from forming gravitationally bound objects, such as miniclusters [72, 74]. Based on this, we estimated the typical size of the over-densities today.

The process of fragmentation produces a stochastic GW background [75–77], which is studied in chapter 5. We estimate the spectrum of this background analytically, as well as calculate it numerically, by evolving linear metric perturbations. We find that a particularly strong background from ALP DM is produced if the final mass near the bottom of the potential is very small. This leads to an extended intermediate phase of ultra-relativistic dynamics after fragmentation. The dynamics is governed by NTFPs which allows us to study it by means of a simplified kinetic description. Such GW background can possibly be explored with future experiments, including pulsar timing arrays [78] as well as high-sensitivity space-based detectors [79], offering a new probe of the properties of DM.

In chapter 6 we study the dynamics of nonrelativistic Bose gases with a tunable interaction strength, applying the methods of nonequilibrium QFT from previous chapters in the nonrelativistic limit. After an appropriate transformation of the variables, the spatial expansion is encoded into the time-dependence of the interaction strength, $g \propto a^{2-d}$, where d is the number of spatial dimensions of the trap and a is the scale factor. A preheating stage is simulated by applying a periodic modulation of the scattering length. This induces an amplification of the sound waves on top of the condensate, mimicking particle production, as well as subsequent nonlinear effects, such as secondary instabilities and self-similar energy transport to higher momenta. The final stages of the dynamics, when the system relaxes to thermal equilibrium, are not captured by semiclassical approximation methods, which motivates an experimental study of this process.

The thesis concludes with chapter 7, where the main results are summarized and an outlook for future studies is given. The appendices contain details of some calculations. Unless stated explicitly otherwise, we set $\hbar = c = 1$ and use the signature $(+,-,-,-)$ for the spacetime metric.

Chapter 2

Preliminaries

The goal of this chapter is to provide a theoretical background for this work. The chapter is divided into three sections. In the first section we introduce the class of ALPs and review the motivation for such particles both from a bottom-up point of view, in QCD, and from a top-down consideration, in string theory compactifications. The phenomenon of axion monodromy is also discussed. In the next section we describe the importance of scalar fields, and particularly ALPs, in inflationary cosmology. Having emphasized the role of dynamical phenomena, in the final section we describe the framework of nonequilibrium QFT that is used for studying quantum many-body dynamics.

Most of the material presented in this chapter is by no means original. Section 2.1.1 about the QCD axion follows [2, 80], section 2.2.1 on cosmic inflation is based on [69, 80, 81]. The discussion of the methods of nonequilibrium QFT in section 2.3 follows along the lines of [20], at the same time the formalism being applied to the considered massive sine-Gordon model. The remaining parts of this chapter contain explicit references to various sources as well as my own arguments in some cases.

2.1 Axion-like particles

ALPs appear in QFT as pNGBs of spontaneously broken global symmetries. Exact Goldstone bosons are massless and enjoy a continuous shift symmetry. The term pseudo refers to the fact that the underlying symmetry is only approximate, explicitly broken e.g. due to nonperturbative effects, which generates a small mass for the ALP. An important representative of this class is the QCD axion [33–35], which acquires its mass through an anomalous coupling to the gluons and provides a solution to the "strong CP" problem of the SM. ALPs also arise from the compactification of theories with extra-dimensions, including string theory [38–41], as the Kaluza-Klein (KK) zero modes of high-dimensional gauge fields.

Nonperturbative effects reduce the continuous shift symmetry of ALPs down to a discrete one. Denoting the ALP field by φ, the ALP potential remains invariant under

$$\varphi \to \varphi + 2\pi f. \tag{2.1}$$

Here the decay constant f is the scale of the spontaneous symmetry breaking (SSB), or the string scale for string axions. In the so-called dilute instanton gas approximation, the potential can typically be parametrized as [42]

$$U(\varphi) = \Lambda^4 \Big[1 - \cos\Big(\frac{\varphi}{f}\Big)\Big], \tag{2.2}$$

where Λ denotes the scale of the explicit symmetry breaking effects.

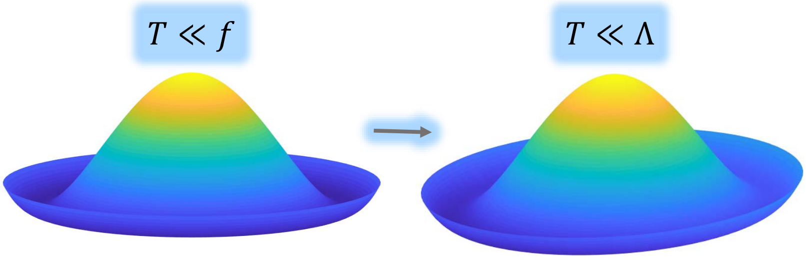

FIGURE 2.1: Schematic illustration of a pNGB. SSB occurs at temperatures below the decay constant f, while the nonperturbative effects leading to explicit breaking become important at $T < \Lambda$.

The ALP mass near the bottom of the above potential is given by

$$m_a = \frac{\Lambda^2}{f}. \tag{2.3}$$

The small mass of ALPs is therefore linked to a high scale of fundamental physics i.e. the decay constant f. Similarly, all couplings of ALPs are suppressed by powers of the decay constant, as a consequence of the shift symmetry. The potential of a pNGB is illustrated in Fig. 2.1.

2.1.1 The QCD axion

The QCD axion is the pNGB of an additional global chiral $U(1)$ symmetry of the SM of particle physics. Such symmetry suffers from chiral anomaly and is explicitly broken due to quantum effects [82]. Because of this anomaly, the axion is linearly coupled to the gluon fields $F_a^{\mu\nu}$ via the Chern-Simons coupling,

$$\mathcal{L} = -\frac{\varphi}{f}\frac{g_s^2}{32\pi^2} F_{a\mu\nu}\widetilde{F}_a^{\mu\nu}. \tag{2.4}$$

Here $\tilde{F}_a^{\mu\nu} = \frac{1}{2}\epsilon^{\mu\nu\alpha\beta}F_{a\alpha\beta}$ is the dual of the field strength tensor and g_s is the gauge coupling. The axion is a prediction of the Peccei-Quinn (PQ) mechanism [33], proposed in 1977 and providing the most elegant solution to the so-called "strong CP" problem of the SM, which is described below.

As confirmed by many experiments, the combined transformation of charge conjugation (C) and spatial reflection (P), also known as CP, is not a fundamental symmetry of nature and is violated by weak interactions. Nevertheless, strong interactions seem to conserve CP, as no experimental indication for its violation has been found so far. This is puzzling from the point of view of the SM and the current understanding of the theory of strong interactions. Concretely, a topological (total derivative) term

$$\mathcal{L}_{\bar{\Theta}} = -\bar{\Theta}\frac{g_s^2}{32\pi^2} F_{a\mu\nu}\widetilde{F}_a^{\mu\nu}, \tag{2.5}$$

is allowed in the QCD Lagrangian [83]. $\bar{\Theta}$ is a parameter of the theory, summed from two independent contributions,

$$\bar{\Theta} = \Theta + \arg \det\mathcal{M}. \tag{2.6}$$

Θ is a result of the topologically nontrivial vacuum structure in nonabelian gauge theories [84]. More precisely, the correct vacuum states of QCD are always characterized by some value of Θ (the so-called Θ-vacua) and the choice of a particular vacuum effectively induces the corresponding nonperturbative contribution of the form of (2.5) in the Lagrangian. The second term in (2.6) involves the complex phase of the determinant of the quark mass matrix $\mathcal{M}$. The observed CP violation in the weak sector suggests a $\mathcal{O}(1)$ value for it.

The parameter $\bar{\Theta}$ characterizes the amount of CP violation in QCD. Unless $\bar{\Theta} = 0 \text{ mod } 2\pi$, the topological term causes CP violation. Experiments with neutron electric dipole moment [85] severely constraint its value to $\bar{\Theta} < 10^{-10}$ [86]. This value is considered unnatural, since it requires two quantities of unrelated origin to cancel each other to very high precision. The corresponding fine-tuning problem is referred to as the "Strong CP" problem. Even though the CP-conserving ($\Theta = 0$) vacuum is the one with the lowest energy [87], as in Eq. (2.2), Θ has no way to relax to that state, since it is a constant.

The PQ mechanism provides an elegant and intriguing solution to the strong CP problem. The additional chiral $U(1)$ symmetry, postulated in this mechanism and referred to as the PQ symmetry, is broken both spontaneously and explicitly, giving birth to the QCD axion with the term (2.4) in the Lagrangian. The CP-violating angle is then effectively

$$\bar{\Theta} \to \bar{\Theta} + \frac{\varphi}{f}, \tag{2.7}$$

allowing the axion to dynamically relax to the CP-conserving lowest-energy Θ-vacuum.

2.1.2 Axions from string theory compactifications

The interest towards ALPs is further increased by the fact that a large number (10-100) of such particles is contained in the low-energy spectrum of string theory [38, 39, 41]. It is often referred to as the string axiverse [39]. String axions can arise as the KK zero modes of higher-dimensional gauge fields. Their discrete shift symmetry is inherited from the higher gauge symmetry. The interaction terms of the Chern-Simons form (2.4) are generated on the nonperturbative level, as a result of anomaly cancelation conditions, and can generate masses in a range spanning many orders of magnitude.

Instead of going into the details of string theory, it is instructive to demonstrate the emergence of ALPs in a simpler toy model. To this end, we consider a five-dimensional $U(1)$ gauge theory [36], where the fifth dimension is a circle of radius r, i.e. the spacetime is taken to be $\mathbb{M} = \mathbb{R}^{1,3} \times S_1$. This is schematically illustrated in Fig. 2.2. The 5d action has the form

$$S = \int \mathrm{d}^4x \int_0^{2\pi r} \mathrm{d}y \Big[-\frac{1}{4g^2_{(5D)}} F_{MN}F^{MN} + \bar{\Psi} i \not{D} \Psi \Big], \tag{2.8}$$

where $F_{MN} = \partial_M A_N - \partial_N A_M$, (M, N) denote 5d spacetime indices and $x^4 = y$ corresponds to the compact dimension. Only in this section we use a different normalization of the gauge field, $A \to gA$, which shifts the gauge coupling dependence on from the interaction terms to the kinetic term. Periodicity along that dimension imposes boundary conditions for all fields, e.g. $\Psi(x_\mu, y + 2\pi r) = \Psi(x_\mu, y)$.

The action (2.8) is invariant under local gauge transformations of the form,

$$\Psi \to e^{i\chi}\Psi, \quad A^M \to A^M + \partial^M \chi. \tag{2.9}$$

The boundary conditions for the fields restrict the class of possible functions $\chi(x)$ to those that satisfy $\chi(x_\mu, y + 2\pi r) = \chi(x_\mu, y) + 2\pi k$, where $k \in \mathbb{Z}$.

In order to see how the five-dimensional theory looks like at low-energies from the four-dimensional perspective, one performs the so-called KK reduction [88–90]. By expanding

$$A^M(x_\mu, y) = \sum_{n=-\infty}^{\infty} A^M_{(n)}(x_\mu) e^{i(n/r)y},$$

the first term in the action (2.8) can be re-written as

$$S = \int \mathrm{d}^4x \Big[-\frac{1}{4g^2_{(4D)}} F_{(0)\mu\nu} F^{\mu\nu}_{(0)} + \frac{1}{g^2_{(4D)}} \frac{1}{2} \partial_\mu \varphi_{(0)} \partial^\mu \varphi_{(0)} + \text{KK tower} + ... \Big], \tag{2.10}$$

where $g_{(4D)} = g_{(5D)}/\sqrt{2\pi r}$ and $\varphi = A^4$. The spectrum, thus, consists of a $U(1)$, 4-dimensional gauge field, a massless scalar and the KK tower of heavy fields which can be ignored at low-energies (see [91] for a detailed calculation of the KK spectrum of a 5D gauge field).

Under an arbitrary (allowed) gauge transformation the canonically normalized field $\varphi_{(0)}$ transforms as

$$\varphi_{(0)} \to \varphi_{(0)} - \frac{\int_0^{2\pi r} \mathrm{d}y \partial_y \chi}{2\pi r g_{(4D)}} = \varphi_{(0)} - \frac{\chi(y + 2\pi r) - \chi(y)}{2\pi r g_{(4D)}} = \varphi_{(0)} + \frac{k}{r g_{(4D)}}. \tag{2.11}$$

In other words, the local higher-dimensional gauge symmetry in the presence of a charged field implies a discrete shift symmetry for the scalar field.

Similarly, in string theory ALPs arise from integrating a gauge field p-form over nontrivial cycles in the compactification manifold. At the tree level ALPs are still massless, as is the case in (2.10). The small masses are generated through nonperturbative effects (see [37, 92–94] for the case of the 5d model where the small mass is generated via a Coleman-Weinberg mechanism).

2.1.3 ALPs with quasiperiodic potentials: monodromy

Recently much attention has been drawn towards the possibility of breaking the periodicity of the ALP potential and, thus, lifting the degeneracy of its local minima. Such ALPs are said to exhibit a monodromy [50, 51]. From the point of view of

FIGURE 2.2: A schematic illustration of the spacetime of the form $\mathbb{R}^{1,3} \times S_1$.

pseudo-Goldstone bosons, this idea may seem unfeasible, as the field range of such bosons is intrinsically compact i.e. the values φ and $\varphi + 2\pi f$ correspond to the same physical state. String axions provide more freedom for having such quasiperiodic potentials, as we discuss below.

In the simple toy model from the previous subsection, the 5d $U(1)$ gauge symmetry can be broken spontaneously e.g. through the coupling to a "Higgs" field obtaining a vacuum expectation value (VEV). This VEV generates a mass for the gauge field (and, thus, the ALP), which "eats" the Goldstone boson from the symmetry breaking (see [95], as well as [96]),

$$S_{SSB} \supset \int \mathrm{d}^4x \int_0^{2\pi r} \mathrm{d}y \, \mu^3 A_M A^M \xrightarrow{\text{KK reduction}} \int d^4x \frac{1}{2} m^2 \varphi_{(0)}^2 + \ldots \tag{2.12}$$

In other words, in the presence of a nonvanishing VEV, winding an additional period costs extra-energy. If the breaking effect is relatively weak, the underlying periodic structure of the potential can be partially preserved, leading to an interesting "wiggly" structure of the potential. For sufficiently strong wiggles the potential generally contains a series of local minima.[1]

The monodromy potential is thus a sum of a periodic term and a symmetry-breaking term, a quadratic monomial in the above example,

$$U(\varphi) = \frac{1}{2} m^2 \varphi^2 + \Lambda^4 \Big[1 - \cos\Big(\frac{\varphi}{f}\Big) \Big]. \tag{2.13}$$

This corresponds to the so-called massive sine-Gordon model, which will be mostly considered throughout this work.

Returning to string theory, the monodromy effect can be realized for string axions [50, 52]. There the periodicity of the axion can be lifted by the coupling to background fluxes [52, 97–99] or branes [50, 51] wrapping the p-cycle of the axion.

Similar "wiggly" potentials, possibly featuring many local minima, can also arise in models involving two axions, such as the so-called "aligned" axions [45] or the "hierarchical" axions [46], and multiple axions [47, 48, 100]. In [101] the combination of two axions with a monodromy was considered.

2.2 Scalar fields in inflationary cosmology

Having reviewed the main properties of ALPs, we now discuss their importance in the early universe cosmology.

A crucial ingredient in cosmology is the expansion of the universe, which can be well described by means of the Friedmann-Robertson-Walker (FRW) metric. The latter corresponds to a homogeneous and isotropic spacetime, which is Minkowski at each time slice, such as the universe appears to be on large scales. The flat FRW metric is characterized by a scale factor $a(t)$, which relates the spatial comoving coordinates to physical distances at a given time,

$$ds^2 = dt^2 - a^2(t) d\mathbf{x}^2. \tag{2.14}$$

---

[1] The appearance of potentials with many local minima is a common feature of the compactification of extra-dimensions i.e. the string theory landscape.

The scale factor grows with time in an expanding universe and its time-dependence is determined by the content of the universe via Einstein's equations (see [80] for an overview).

2.2.1 ALPs driving inflation

Cosmic inflation is a well-established paradigm, that solves the puzzles of flatness, homogeneity and isotropy of the universe [11–13] and explains the generation of the density perturbations for structure formation [14]. According to this paradigm, the very early universe underwent a stage of accelerated expansion, $\ddot{a} > 0$, which, in the simplest case, is driven by a scalar field, whose potential energy dominates over the kinetic energy.

During inflation the energy budget of the universe is stored predominantly in the homogeneous inflaton field $\phi(t)$. Other kinds of matter and radiation are diluted away, whereas any inhomogeneities of the inflaton field, even if present initially, are stretched out in the course of the accelerated expansion. The equations of motion of such a field in an FRW universe have the form

$$\ddot{\phi} + 3H\dot{\phi} + U'(\phi) = 0, \tag{2.15}$$

where the prime denotes $d/d\phi$. $H(t) = \dot{a}/a$ is the Hubble parameter which is in turn determined by the energy density of the inflaton,

$$H^2 = \frac{8\pi}{3M_{Pl}^2}\Big(\frac{1}{2}\dot{\phi}^2 + U(\phi)\Big). \tag{2.16}$$

The universe inflates enough if the so-called "slow-roll" conditions [81, 102],

$$\frac{M_{Pl}^2}{2}\Big(\frac{U'(\phi)}{U(\phi)}\Big)^2 \ll 1, \qquad M_{Pl}^2\frac{U''(\phi)}{U(\phi)} \ll 1, \tag{2.17}$$

are satisfied. As can be seen, they require either a very flat region of the potential or, for generic monomial potentials, super-Planckian field displacement, $\phi \gtrsim M_{Pl}$. The second case, referred to as large-field inflation, requires less tuning of the potential and of the initial field value. As it is known (see e.g. [81]), due to the super-Planckian field values, higher-dimensional operators in the Lagrangian, suppressed by the powers of M_{Pl}, are expected to become important and can dramatically alter the shape of the potential and the slow-roll conditions.

ALPs are considered as particularly attractive candidates for large-field inflation, as their approximate shift symmetry protects the potential in a natural way from uncontrolled ultraviolet (UV) corrections. This version of inflation is called natural inflation [103]. However, from the point of view of string theory $f < M_{Pl}$ is required for controlled compactification. For periodic ALPs [104] this clearly contradicts super-Planckian field displacements. Instead, monodromic ALPs allow to combine the small decay constant with $\phi \gtrsim M_{Pl}$ and have been used extensively in constructing models of large field inflation [50, 51]. The enhancement of the field range in the presence of a monodromy is illustrated in Fig. 2.3.

Inflation is necessarily followed by a reheating phase [15, 69], during which the inflaton decays e.g. into SM degrees of freedom and the latter eventually come to thermal equilibrium at the reheating temperature. Reheating thus connects the inflationary paradigm to the standard big-bang cosmology. The consistency between big bang nucleosynthesis (BBN) calculations and the measured abundances of light

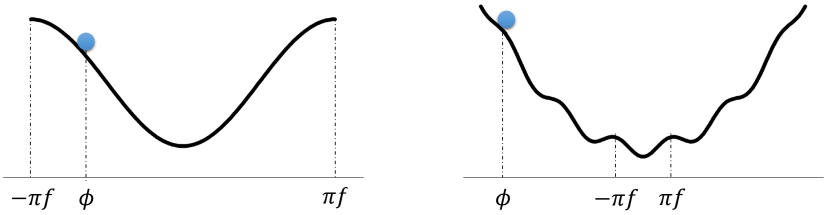

FIGURE 2.3: The scalar field ϕ rolling down the potential in the absence (left) and in the presence (right) of a monodromy, with the second case allowing displacements over several fundamental periods of the potential, $\phi > \pi f$.

elements requires the universe to be in thermal equilibrium already by the time of BBN [105], $T \sim 10\text{MeV}$.

Reheating starts after the inflaton has rolled down into the sub-Planckian region, $\phi < M_{Pl}$, where the conditions (2.17) are no longer satisfied. The field then starts to oscillate around the bottom of its potential. The presence of "wiggles" and, possibly, local minima in the potential can play an important role at this stage [106], especially for the early phase of preheating when the quantum fluctuations of the inflaton are rapidly amplified due to its oscillations.

2.2.2 ALPs as dark matter fields

While there is no lack of evidence for the existence of DM in galaxies and galaxy clusters, its nature remains one of the biggest mysteries. ALPs with very small masses, and similar light bosons, are natural DM candidates, because they can be produced in the early universe via the so-called vacuum misalignment mechanism [26–29], in the form of a coherent field oscillating around the minimum of its potential. Such ALPs are weakly interacting and extremely long-lived due to their small mass, and the coherent oscillations mimic the behavior of pressureless matter.

In the simplest case of this mechanism [26], the ALP field is present during inflation as a subdominant spectator field. Its dynamics is governed by (2.15), however the influence on the expansion rate of the spacetime is negligible. Due to the small mass, (2.15) describes a strongly overdamped system during inflation $H \gg m_a$, such that the ALP field is essentially frozen. Inflation homogenizes the field across the observable universe to some misalignment field value ϕ_1.

In the post-inflationary universe the Hubble parameter decreases with time. Once it drops below m_a, the system (2.15) enters the underdamped regime[2]. The ALP field then starts to coherently oscillate around the minimum of the potential with an amplitude decreasing as the universe expands. For standard ALPs, due to the periodic shape of the potential, very soon the oscillations take place in the approximately quadratic region near the minimum of the potential. In this way the field behaves as nonrelativistic matter and can successfully participate in the formation of galactic structures. The presence of a monodromy, as in the case of inflation, allows for large misalignment "angles", $\phi_1/f \gg 1$, which has two important implications. Firstly, assuming that the ALP field accounts for all DM in the universe, the value of ϕ_1 is then fixed, for a given ALP mass, from today's abundance of DM.

---

[2] Here for simplicity we treat the potential as quadratic.

Therefore, a monodromy allows smaller values of the decay constant f [56]. At the same time, it may lead to an amplification of fluctuations and nontrivial dynamics after the onset of oscillations.

2.3 Nonequilibrium quantum dynamics of scalar fields

The nontrivial shape of the potential can lead to the amplification of quantum fluctuations of the field. In this section we describe the formalism used for studying such quantum field dynamics. The (exact) equations of motion for one- and two-point field correlation functions can be obtained from the 2PI effective action [18], formulated on the Schwinger-Keldysh closed real-time contour [19]. We review this framework as well as how different effective descriptions, that will be employed in the next chapters, emerge from it.

A great overview of nonequilibrium QFT can be found in [20], which we mostly follow in this section, at the same time applying the formalism to the considered massive sine-Gordon model. In particular, in section 2.3.5 we derive the validity conditions for the classical-statistical approximation for that model.

2.3.1 Nonequilibrium generating functional

A typical task in nonequilibrium QFT is to follow the time evolution of expectation values of physical variables for a given initial state. The state is usually described with a density operator/matrix $\hat{\rho}$. In the Schroedinger picture the evolution of the density operator is governed by the von Neumann equation,

$$i\partial_t \hat{\rho}(t) = [\hat{H}(t), \hat{\rho}(t)], \qquad \hat{\rho}(t_0) = \hat{\rho}_0, \tag{2.18}$$

where $\hat{H}$ is the possibly time-dependent Hamiltonian. The above equation is solved by $\hat{\rho}(t) = \hat{U}(t,t_0)\hat{\rho}_0\hat{U}(t_0,t)$, where $\hat{U}(t,t') = \mathcal{T}\exp(-i\int_t^{t'} \hat{H}(\tau)d\tau)$ is the unitary evolution operator, involving a time-ordered exponent. The expectation value of any operator $\hat{O}$ at time t is then given by

$$\langle \hat{O}(t) \rangle = \frac{\mathrm{Tr}\{\hat{O}\hat{\rho}(t)\}}{\mathrm{Tr}\{\hat{\rho}(t)\}} = \frac{\mathrm{Tr}\{\hat{O}\hat{U}(t,t_0)\hat{\rho}_0\hat{U}(t_0,t)\}}{\mathrm{Tr}\{\hat{\rho}_0\}}. \tag{2.19}$$

Inserting a unity operator in the above equation, $\hat{1} = \hat{U}(t,\infty)\hat{U}(\infty,t)$, leads to an evolution along the closed-time Schwinger-Keldysh contour C [19], which starts at the initial time t_0, runs forwards along the real-time axis and then returns back to t_0.

$$\langle \hat{O}(t) \rangle = \frac{\mathrm{Tr}\{U(t_0,\infty)U(\infty,t)\hat{O}\hat{U}(t,t_0)\hat{\rho}_0\}}{\mathrm{Tr}\{\hat{\rho}_0\}}. \tag{2.20}$$

Using standard techniques, the above expression can be brought into a form involving a path integral,

$$\hat{O} = \int d\varphi_0^+ d\varphi_0^- \langle \varphi_0^+ | \hat{\rho}_0 | \varphi_0^- \rangle \int_{\varphi_0^+}^{\varphi_0^-} \mathcal{D}'\varphi \mathcal{O} e^{iS_C[\varphi]}. \tag{2.21}$$

Here $\varphi_0^\pm$ are the eigenstates of the field operator at time t_0 for both branches of the Schwinger-Keldysh contour, $\hat{\varphi}^\pm(0)|\varphi_0^\pm\rangle = \varphi_0^\pm|\varphi_0^\pm\rangle$. In the argument of the exponent in the path integral is the (classical) action,

$$S_C[\varphi] = \int_{t,C} \Big[\pi \partial_t \varphi - H\Big]. \tag{2.22}$$

integrated over the Schwinger-Keldysh contour. The prime on the path integral measure indicates that the field values are fixed at $t = t_0$. The denominator of (2.20) has been included in the measure of the path integral. Adding a label $\varphi \to \varphi(\mathbf{x})$ generalizes[3] the above expression to QFT.

In QFT the central objects of interest are the field correlation functions. It is convenient to introduce a functional, which generates all such correlation functions. Using a path integral representation, the generating functional can be written as[4]

$$\begin{aligned} Z[J,R] = e^{iW[J,R]} = \int [d\varphi_0^+][d\varphi_0^-]\langle\varphi_0^+|\hat{\rho}_0|\varphi_0^-\rangle \\ \times \int_{\varphi_0^+}^{\varphi_0^-} \mathcal{D}'\varphi \exp\Big[i\Big(S_C[\varphi] + \int_{x,C} J(x)\varphi(x) + \frac{1}{2}\int_{xy,C}\varphi(x)R(x,y)\varphi(y)\Big)\Big]. \end{aligned} \tag{2.23}$$

Here J and R are linear and bilinear external source terms, respectively. As can be seen, the calculation of the expectation value involves both quantum fluctuations from the dynamics, and statistical fluctuations from averaging over the mixed state $\hat{\rho}_0$.

2.3.2 Correlation functions

All time-ordered (along the Schwinger-Keldysh contour) correlation functions can be obtained by taking functional derivatives of the generating function with respect to the source terms and setting the sources to zero afterwards. In particular, the one-point function, which will also be referred to as the background field, can be expressed as

$$\phi_a(x) = \langle\hat{\varphi}_a(x)\rangle = \frac{\delta W[J,R]}{\delta J_a(x)}\Big|_{J,R=0}. \tag{2.24}$$

The connected two-point function i.e. the full propagator, can be written as

$$G_{ab}(x,y) = \langle\mathcal{T}_C\hat{\varphi}_a(x)\hat{\varphi}_b(y)\rangle - \phi_a(x)\phi_b(y) = 2\frac{\delta W[J,R]}{\delta R_{ab}(x,y)}\Big|_{J,R=0} - \phi_a(x)\phi_b(y). \tag{2.25}$$

The full propagator (2.25) is a complex-valued function and it is convenient to separate its real and imaginary parts [107]. They can be associated with the expectation values of the commutator and anti-commutator of the field operators. The decomposition is given by

$$G(x,y) = F(x,y) - \frac{i}{2}\rho(x,y)\mathrm{sgn}_C(x^0 - y^0),$$

where

$$\begin{aligned} F(x,y) &= \frac{1}{2}\langle\{\hat{\varphi}(x),\hat{\varphi}(y)\}\rangle - \phi(x)\phi(y), \\ \rho(x,y) &= i\langle[\hat{\varphi}(x),\hat{\varphi}(y)]\rangle, \end{aligned} \tag{2.26}$$

---

[3] The integration measure the becomes $\int[d\varphi_0^{\pm}] = \int \Pi_{\mathbf{x}} d\varphi_0^{\pm}(\mathbf{x})$.

[4] We denote $\int_{x,C} = \int_C dt \int d^3\mathbf{x}$.

and $\mathrm{sgn}_C(x^0 - y^0)$ is ± 1 depending on whether x^0 is after or before y^0 along the Schwinger-Keldysh contour. $\rho(x,y)$ is the spectral function and $F(x,y)$ denotes the statistical propagator. Both are real functions with different symmetry properties, $F(x,y) = F(y,x)$ and $\rho(x,y) = -\rho(y,x)$. Importantly, these correlation functions do not distinguish between the two branches of the Schwinger-Keldysh contour. The spectral function provides information about the spectrum of the theory and, in particular, encodes the equal-time commutation relations,

$$\rho(x,y)|_{x^0=y^0} = \partial_{x^0}\partial_{y^0}\rho(x,y)|_{x^0=y^0} = 0, \qquad \partial_{x^0}\rho(x,y)|_{x^0=y^0} = \delta(\mathbf{x}-\mathbf{y}). \tag{2.27}$$

The statistical propagator provides information about how the states are occupied. We will be interested in spatially homogeneous systems, for which the two-point functions depend on the relative spatial coordinate, e.g. $F(x,y) = F(x^0, y^0, \mathbf{x}-\mathbf{y}) = \int \frac{d^3\mathbf{p}}{(2\pi)^3} F(x^0, y^0, \mathbf{p}) e^{-i\mathbf{p}(\mathbf{x}-\mathbf{y})}$. For such systems time-dependent "occupation numbers" can be defined as [20, 23]

$$n(t,\mathbf{p}) + 1/2 = \sqrt{F(t,t',\mathbf{p})\partial_t\partial_{t'}F(t,t',\mathbf{p})}|_{t'=t}, \tag{2.28}$$

in analogy to the free theory. Although the notion of particles is not uniquely defined in an interacting relativistic field theory, this definition turns out to provide a useful quasi-particle interpretation for scalar systems.

2.3.3 The 2PI formalism and quantum equations of motion

The 2PI effective action $\Gamma[\phi, G]$ is defined as the double Legendre transform of the connected generating functional $W[J,R]$ with respect to the sources,

$$\Gamma[\phi, G] = W - \int_{x,C} J(x)\frac{\delta W}{\delta J(x)} - \int_{xy,C} R(x,y)\frac{\delta W}{\delta R(x,y)}.$$

The equations of motion for one- and two-point functions can be then obtained by varying the action for vanishing sources,

$$\frac{\delta \Gamma}{\delta \phi(x)} = 0, \qquad \frac{\delta \Gamma}{\delta G(x,y)} = 0. \tag{2.29}$$

For Gaussian initial states the 2PI effective action can be written as [18]

$$\Gamma[\phi, G] = S_C[\phi] + \frac{i}{2}\mathrm{Tr}_C \ln G^{-1} + \frac{i}{2}\mathrm{Tr}_C\{G_0^{-1}(\phi)G\} + \Gamma_2[\phi, G] + \mathrm{const.} \tag{2.30}$$

Here the traces denote spacetime integration $\int_{x,C}$ and G_0^{-1} is the inverse classical propagator, defined as

$$iG_0^{-1}(x,y;\phi) = \frac{\delta^2 S_C[\phi]}{\delta\phi(x)\delta\phi(y)}.$$

$\Gamma_2[\phi, G]$ is the sum of all 2PI vacuum graphs with full propagator lines and interaction vertices from the classical action $S_C[\phi + \varphi]$, expanded around the background field $\phi(x)$, which we denote by $S_{\text{int}}[\varphi;\phi]$. 2PI graphs are those, that do not become disconnected after removing two inner propagator lines. Note that the dependence on the density matrix $\hat{\rho}_0$ in (2.30) is re-absorbed into the initial conditions of ϕ and G, which is possible for Gaussian initial states only [20].

In the (massive) sine-Gordon model, the interaction part of the action $S_{\text{int}}[\varphi;\phi]$ is given by

$$
\begin{aligned}
S_{\text{int}}[\varphi;\phi] &= \quad -\int_{x,C}\sum_{n=2}^{\infty}(-1)^{n+1}\frac{\Lambda^4}{f^{2n}}\frac{[\phi(x)+\varphi(x)]^{2n}}{(2n)!} \\
&= -\int_{x,C}\sum_{l=3}^{\infty}\Big(-\frac{\Lambda^4}{f^l}\Big)\cos\Big(\frac{\phi(x)}{f}+\frac{\pi l}{2}\Big)\frac{\varphi^l(x)}{l!},
\end{aligned}
\tag{2.31}
$$

where the cosine-term is Taylor expanded. As can be seen, the presence of the background field generates interaction vertices with arbitrary number of legs, starting from cubic. For $\phi = 0$ vertices with only even number of legs remain.

Evolution of the propagator: Using the decomposition of the full propagator into the statistical and spectral components (2.26), the equation for the full propagator in (2.29) can be replaced by a pair of coupled evolution equations, known as Kadanoff-Baym equations [20],

$$
[\Box_x + M^2(x)]F(x,y) = -\int_0^{x_0} dz\Sigma^\rho(x,z)F(z,y) + \int_0^{y_0} dz\Sigma^F(x,z)\rho(z,y), \tag{2.32}
$$

$$
[\Box_x + M^2(x)]\rho(x,y) = -\int_{y_0}^{x_0} dz\Sigma^\rho(x,z)\rho(z,y). \tag{2.33}
$$

where $\int_{t_1}^{t_2} dz = \int_{t_1}^{t_2} dz^0 \int d^3\mathbf{z}$. The effective mass term $M^2(x)$ in the above equations for the considered massive sine-Gordon model is given by

$$
M^2(x) = m^2 + \frac{\Lambda^4}{f^2}\cos\frac{\phi(x)}{f} + \Sigma^{(0)}(x). \tag{2.34}
$$

The self-energies $\Sigma^{(0)}$, Σ^F and Σ^ρ are defined as

$$
2i\frac{\delta\Gamma_2[\phi,G]}{\delta G(x,y)} = -i\Sigma^{(0)}(x)\delta(x-y) + \Sigma^F(x,y) - \frac{i}{2}\Sigma^\rho(x,y)\text{sgn}_C(x^0-y^0), \tag{2.35}
$$

and sum all 1PI graphs, obtained by opening a propagator line in the vacuum graphs of Γ_2.

To solve (2.32) and (2.33), initial conditions for the statistical propagator have to be prescribed. Gaussian initial conditions with quasi-particle occupation numbers $n_0(\mathbf{p})$, that are considered in this chapter, correspond to [107]

$$
F(t,t',\mathbf{p})|_{t=t'=t_0} = \frac{n_0(\mathbf{p})+1/2}{\omega_{\mathbf{p}}}, \tag{2.36}
$$

$$
\partial_t F(t,t',\mathbf{p})|_{t=t'=t_0} = 0, \tag{2.37}
$$

$$
\partial_t\partial_{t'} F(t,t',\mathbf{p})|_{t=t'=t_0} = \Big(n_0(\mathbf{p})+1/2\Big)\omega_{\mathbf{p}}, \tag{2.38}
$$

where $\omega_{\mathbf{p}} = \sqrt{\mathbf{p}^2+M^2}$ is the dispresion relation. In contrast, the initial conditions for the spectral function are fixed by (2.27).

Evolution of the background field: Using the decomposition of Eq. (2.30), the first equation in (2.29) for the background field ϕ can be written as [20]

$$\frac{\delta S}{\delta\phi(x)}+\frac{i}{2}\frac{\delta\{\mathrm{Tr}G_0^{-1}(\phi)G\}}{\delta\phi(x)}+\frac{\delta\Gamma_2}{\delta\phi(x)}=0. \tag{2.39}$$

Taking into account the details of our mode, the above equation takes the form

$$\Big(\Box+m^2\Big)\phi(x)+\frac{\Lambda^4}{f}\Big(1-\frac{F(x,x)}{2f^2}\Big)\sin\frac{\phi(x)}{f}=\frac{\delta\Gamma_2}{\delta\phi(x)}. \tag{2.40}$$

As initial conditions $\phi|_{t=t_0}=\phi_0$ and $\dot{\phi}|_{t=t_0}=0$ will be chosen in the simplest cases in this work.

Truncation methods for the effective action: The expression (2.30) provides a starting point for further approximations of the effective action. Once an appropriate approximation has been made, the 2PI evolution equations can be solved numerically.

An important truncation scheme is based on a "perturbative" loop expansion of Γ_2 [18]. Already at the three-loop approximation the 2PI equations are capable of describing thermalization [108]. In the 2PI formalism such a perturbative expansion is parameterized in terms of full propagator G and not the bare one. This resummation allows avoiding the emergence of secular terms. However, even in the presence of weak couplings, the dynamics of G can alter the power counting with time hindering the control over the expansion.

Another powerful approximation scheme is provided by the 2PI $1/N$ expansion [70, 71]. It is applicable to N-component scalar field theories with an $\mathcal{O}(N)$ symmetry and is based on classification of the contributions to the 2PI effective action according to their scaling with N. Particularly, the leading order (LO) contribution usually scales proportionally to N, next-to-leading order (NLO) contributions are $\mathcal{O}(N^0)$, and so on. Importantly, this provides a controlled expansion parameter and does not restrict to systems with small couplings or to small occupation numbers. It is a nonperturbative method in the sense that a given order sums an infinite subset of Feynman diagrams. Applications of the 2PI $1/N$ expansion can be found in [70, 71, 109, 110]

2.3.4 Kinetic description

Kinetic theory is a powerful framework for the description of nonequilibrium many-body dynamics [22, 24, 111]. The relevant degrees of freedom in this framework are the occupation numbers of single-particle states, and their evolution is governed by the Boltzmann equation. For homogeneous systems it has the form

$$\frac{\partial n(t,\mathbf{p})}{\partial t}=C[n](t,\mathbf{p}), \tag{2.41}$$

where the collision integral $C[n]$ represents a sum over all possible "scattering" processes with in- or outgoing momentum $\mathbf{p}$.

It is possible to recast the 2PI equations of motion into a form reminiscent of a kinetic Boltzmann equation. This can be done under several assumptions about the dynamics of the system [20, 67].

One of the assumptions for the kinetic limit is the effective memory loss about the initial conditions, which allows taking $t_0 \to \infty$. Furthermore, a gradient expansion to the lowest order is employed, which means that only the lowest order terms in the number of derivatives with respect to the center coordinates X^μ and powers of the relative coordinates s^μ, defined as

$$X^\mu = \frac{x^\mu + y^\mu}{2}, \quad s^\mu = x^\mu - y^\mu, \tag{2.42}$$

are kept. Such a description is expected to be suitable for comparably smooth time evolution, with the occupation numbers changing much slower compared to the oscillations of the momentum modes.

It is convenient to Fourier transform the two-point functions with respect to the relative coordinates

$$F(X,p) = \int_s e^{ips} F(X + \frac{s}{2}, X - \frac{s}{2}), \tag{2.43}$$

$$\widetilde{\rho}(X,p) = -i \int_s e^{ips} \rho(X + \frac{s}{2}, X - \frac{s}{2}), \tag{2.44}$$

where the factor $-i$ is included in the definition of $\widetilde{\rho}$ to make it real-valued. Similar transformations are done for the self-energies. Taking into account all abovementioned approximations, the 2PI equations of motion can be recast into the following form [20]

$$2p^\mu \frac{\partial F(X,p)}{\partial X^\mu} = \widetilde{\Sigma}_\rho(X,p) F(X,p) - \Sigma_F(X,p) \widetilde{\rho}(X,p), \tag{2.45}$$

$$2p^\mu \frac{\partial \widetilde{\rho}(X,p)}{\partial X^\mu} = 0, \tag{2.46}$$

For spatially homogeneous systems the dependence on X reduces to the dependence on the central time t and (2.46) implies constant $\widetilde{\rho}(p)$ that does not depend on time. In other words, in this approximation the particle spectrum does not change with time.

The time evolution of the particle occupation numbers is obtained from (2.45). The effective occupation number distribution can be defined as

$$n(t,\mathbf{p}) = \int_0^\infty \frac{dp^0}{2\pi} 2p^0 \widetilde{\rho}(p) n(t,p), \tag{2.47}$$

where

$$F(t,p) = \Big(n(t,p) + 1/2\Big) \widetilde{\rho}(p). \tag{2.48}$$

For the free-field form of the spectral function, this definition gives the on-shell particle number, coinciding with (2.28). Plugging this into (2.45) leads to

$$\frac{\partial n(t,\mathbf{p})}{\partial t} = \frac{\partial n(t, p^0 = \omega_\mathbf{p}, \mathbf{p})}{\partial t} = \int_0^\infty \frac{dp^0}{2\pi} \left[\widetilde{\Sigma}_\rho(t,p) F(t,p) - \Sigma_F(t,p) \widetilde{\rho}(p) \right] \tag{2.49}$$

which, after inserting the approximate expressions for the self-energies and reexpressing the propagators, takes the form of a Boltzmann equation.

2.3.5 Classical-statistical approximation

An approximate description of quantum field dynamics in terms of the classical-statistical evolution is applicable in the regime of large occupation numbers at low momenta, for small enough couplings such that quantum fluctuations are suppressed compared to the statistical ones [112].

The idea of classical-statistical field theory consists in sampling over initial conditions and evolving each realization in real-time according to the classical field equation of motion. Observables are obtained by averaging over classical trajectories. In particular, the background field and the statistical propagator are given by

$$\phi(x) = \int [d\varphi_0][d\pi_0] W[\varphi_0, \pi_0] \int_{t>t_0} \mathcal{D}'\varphi \varphi(x) \delta\Big[\frac{\delta S[\varphi]}{\delta\varphi}\Big], \tag{2.50}$$

$$F(x,y) + \phi(x)\phi(y) = \int [d\varphi_0][d\pi_0] W[\varphi_0, \pi_0] \int_{t>t_0} \mathcal{D}'\varphi \varphi(x)\varphi(y) \delta\Big[\frac{\delta S[\varphi]}{\delta\varphi}\Big], \tag{2.51}$$

where the prime on the functional integral measure indicates that the field is fixed to $\varphi(x)|_{t=t_0} = \varphi_0(\mathbf{x})$ and $\partial_t\varphi(x)|_{t=t_0} = \pi_0(\mathbf{x})$, and $W[\varphi_0, \pi_0]$ is the normalized probability functional at $t = t_0$.

Initial conditions, described in the previous sections, can be sampled as [20]

$$\varphi_0(\mathbf{x}) = \phi_0 + \int_{\mathbf{p}} \sqrt{\frac{n_0(\mathbf{p}) + 1/2}{\omega_{\mathbf{p}}}} c_{\mathbf{p}} e^{i\mathbf{p}\mathbf{x}}, \tag{2.52}$$

$$\pi_0(\mathbf{x}) = \pi_0 + \int_{\mathbf{p}} \sqrt{\omega_{\mathbf{p}}(n_0(\mathbf{p}) + 1/2)} \widetilde{c}_{\mathbf{p}} e^{i\mathbf{p}\mathbf{x}}, \tag{2.53}$$

where $c_{\mathbf{p}}$ and $\widetilde{c}_{\mathbf{p}}$ are random Gaussian numbers multiplied by random complex phase factors, satisfying $\langle c_{\mathbf{p}} c_{\mathbf{p}'}\rangle = \langle \widetilde{c}_{\mathbf{p}} \widetilde{c}_{\mathbf{p}'}\rangle = (2\pi)^3\delta(\mathbf{p} - \mathbf{p}')$, while all other correlators vanish.

The classical-statistical approximation is a powerful tool for studying the dynamics of highly occupied fields [65, 66]. It can be implemented numerically with the help of lattice calculations. Below we first derive the generating function for classical-statistical field theory and then describe the above-mentioned condition for the validity of the approximation

Mapping to classical-statistical field theory: The starting point for the mapping is the path integral representation of the generating functional (2.23). The first step is to separate forward and backward time integration in (2.23) and re-express it in terms of two fields $\varphi^+(x)$ and $\varphi^-(x)$ taken on C^+ and C^- branches respectively [113]. A further replacement of φ^+ and φ^- by their linear combinations $\varphi = (\varphi^+ + \varphi^-)/2$ and $\widetilde{\varphi} = \varphi^+ - \varphi^-$ is performed. In terms of these new degrees of freedom, the classical action in the exponent of the path integral reads,

$$\begin{aligned} S_C[\varphi] = S_{\mathrm{q}}[\varphi, \widetilde{\varphi}] &= \int_{t>t_0} \Big[\partial_\mu\widetilde{\varphi}\partial^\mu\varphi - \Big(U(\varphi + \widetilde{\varphi}/2) - U(\varphi - \widetilde{\varphi}/2)\Big)\Big] \\ &= \int_{t>t_0} \Big[\partial_\mu\widetilde{\varphi}\partial^\mu\varphi - m^2\widetilde{\varphi}\varphi - 2\Lambda^4 \sin\Big(\widetilde{\varphi}/(2f)\Big) \sin\Big(\varphi/f\Big)\Big], \end{aligned} \tag{2.54}$$

where in the second line the form of the classical potential for our model, given by (3.1), was inserted and Taylor expanded. The generating functional now has the form

$$Z_{\mathrm{q}} = \int [d\varphi_0][d\widetilde{\varphi}_0]\langle\varphi_0 + \widetilde{\varphi}_0/2|\hat{\rho}_0|\varphi_0 - \widetilde{\varphi}_0/2\rangle \int \mathcal{D}'\varphi\mathcal{D}'\widetilde{\varphi}\exp\Big[i\Big(S_{\mathrm{q}}[\varphi,\widetilde{\varphi}] + \text{sources}\Big)\Big]. \tag{2.55}$$

where the sources are also expressed in terms of the new degrees of freedom. One can show that the one- and two-point correlation functions are given by

$$\begin{aligned} \phi(x) &= \int [d\varphi_0][d\widetilde{\varphi}_0]\rho[\varphi_0,\widetilde{\varphi}_0] \int \mathcal{D}'\varphi\mathcal{D}'\widetilde{\varphi}\varphi(x)e^{iS_{\mathrm{q}}[\varphi,\widetilde{\varphi}]}, \\ F(x,y) + \phi(x)\phi(y) &= \int [d\varphi_0][d\widetilde{\varphi}_0]\rho[\varphi_0,\widetilde{\varphi}_0] \int \mathcal{D}'\varphi\mathcal{D}'\widetilde{\varphi}\varphi(x)\varphi(y)e^{iS_{\mathrm{q}}[\varphi,\widetilde{\varphi}]}, \\ \rho(x,y) &= i\int [d\varphi_0][d\widetilde{\varphi}_0]\rho[\varphi_0,\widetilde{\varphi}_0] \int \mathcal{D}'\varphi\mathcal{D}'\widetilde{\varphi}\Big(\varphi(x)\widetilde{\varphi}(y) - \widetilde{\varphi}(x)\varphi(y)\Big)e^{iS_{\mathrm{q}}[\varphi,\widetilde{\varphi}]}. \end{aligned} \tag{2.56}$$

A similar generating functional can be constructed for the correlation functions in classical-statistical field theory [113], such as (2.50) and (2.51), and is given by

$$\begin{aligned} Z_{\mathrm{cl}} &= \int [d\varphi_0][d\pi_0]W[\varphi_0,\pi_0] \int \mathcal{D}'\varphi\,\delta\left[\frac{\delta S[\varphi]}{\delta\varphi}\right]e^{i\,\text{sources}} \\ &= \int [d\varphi_0][d\pi_0]W[\varphi_0,\pi_0] \int \mathcal{D}'\varphi\mathcal{D}\widetilde{\varphi}\exp\Big[i\Big(\int_{t>t_0}\widetilde{\varphi}(x)\frac{\delta S[\varphi]}{\delta\varphi(x)} + \text{sources}\Big)\Big]. \end{aligned} \tag{2.57}$$

The initial classical density matrix $\rho[\varphi_0,\widetilde{\varphi}_0]$ is then defined as the Fourier transform of the probability distribution functional at the initial time,

$$\rho[\varphi_0,\widetilde{\varphi}_0] = \int [d\pi_0]W[\varphi_0,\pi_0]e^{i\int d^3\pi(t_0,\mathbf{x})\widetilde{\varphi}(t_0,\mathbf{x})}. \tag{2.58}$$

Performing an integration by parts in the exponent of the path integral, one can re-write the generating functional as

$$Z_{\mathrm{cl}} = \int [d\varphi_0][d\widetilde{\varphi}_0]\rho[\varphi_0,\widetilde{\varphi}_0] \int \mathcal{D}'\varphi\mathcal{D}'\widetilde{\varphi}\exp\Big[i\Big(S_{\mathrm{cl}}[\varphi,\widetilde{\varphi}] + \text{sources}\Big)\Big], \tag{2.59}$$

where $S_{\mathrm{cl}}[\varphi,\widetilde{\varphi}]$ is the part of $S_{\mathrm{q}}[\varphi,\widetilde{\varphi}]$ linear with respect to $\widetilde{\varphi}$. For our model it is given by,

$$S_{\mathrm{cl}}[\varphi,\widetilde{\varphi}] = \int_{t>t_0}\Big[\partial_\mu\widetilde{\varphi}\partial^\mu\varphi - m^2\widetilde{\varphi}\varphi - \widetilde{\varphi}(\Lambda^4/f)\sin\Big(\varphi/f\Big)\Big]. \tag{2.60}$$

Therefore, if the initial density matrices are chosen to be the same, the only difference between the quantum dynamics and the classical-statistical dynamics is the absence of the interaction vertices, which are nonlinear in $\widetilde{\varphi}$ in the second case.

The validity of the classical-statistical approximation: We now discuss the conditions under which the additional quantum vertices can be neglected in the path integral and, thus, the classical-statistical approximation is justified.

First we make all dimensionful quantities dimensionless by rescaling them with appropriate powers of the characteristic mass scale $m_\Lambda^2 = \Lambda^4/f^2$.[5] Denoting the

---

[5] Note that in the massive sine-Gordon model there are two mass scales, m^2 and Λ^4/f^2. We assume that these two scales are parametrically of similar order.

rescaled quantities with a label "r", the two actions read

$$S_{\mathrm{cl},r}[\varphi_r,\widetilde{\varphi}_r]=\int_{t>t_0}\Big[\partial_\mu\widetilde{\varphi}_r\partial^\mu\varphi_r-m_r^2\widetilde{\varphi}_r\varphi_r-\widetilde{\varphi}_r f_r\sin\left(\varphi_r/f_r\right)\Big],$$
$$S_{\mathrm{q},r}[\varphi_r,\widetilde{\varphi}_r]=\int_{t>t_0}\Big[\partial_\mu\widetilde{\varphi}_r\partial^\mu\varphi_r-m_r^2\widetilde{\varphi}_r\varphi_r-2f_r^2\sin\Big(\widetilde{\varphi}_r/(2f_r)\Big)\sin\left(\varphi_r/f_r\right)\Big],$$

A necessary condition for the vertices, nonlinear in $\widetilde{\varphi}$, to be negligible in the path integral is that $f_r\gg 1$. In that case, using the small angle approximation, one can replace

$$2f_r\sin(\widetilde{\varphi}_r/(2f_r))\approx\widetilde{\varphi}_r,$$

in the above expression for $S_{\mathrm{q},r}$. In terms of the original dimensionful quantities $f_r=f/m_\Lambda=1/\sqrt{\lambda}$, where $\lambda=\Lambda^4/f^4$ is the dimensionless quartic coupling from (2.31). Therefore, the condition $f_r\gg 1$ implies the requirement of weak couplings, i.e. $\lambda\ll 1$, for the validity of the classical-statistical approximation

Obviously, this requirement alone is not sufficient since it can similarly eliminate also the interactions nonlinear in φ from the other sine term. An important additional requirement is that the typical values of φ are larger than those of $\widetilde{\varphi}$. In terms of field correlation functions this condition can be expressed as $|\langle...\varphi\rangle|\gg|\langle...\widetilde{\varphi}\rangle|$ which, according to (2.56), for the two-point functions reduces to

$$F(x,y)\gg\rho(x,y). \tag{2.61}$$

In other words, the typical values of the statistical propagator are larger compared to those of the spectral function. Since, according to (2.48), the ratio of these two is proportional to the occupation number the requirement is equivalent to having large characteristic occupation numbers, $n_{\mathrm{p}}\gg 1$.

Sending the momentum cut-off to infinity: Because of the classical Rayleigh-Jeans divergence, a UV momentum cutoff Λ_{UV} has to be imposed in classical-statistical field theory [112]. In the relevant regime of weak couplings and large occupation numbers at low momenta, the dynamics is insensitive to variations of the cut-off within the range of accessible values from the point of view of lattice simulations. Quantum corrections from the UV modes are suppressed by weak couplings, in contrast to unsuppressed corrections from the highly occupied low-momentum modes. Cut-off dependence is expected to become important once Λ_{UV} is comparable to f, which is also the scale at which the effective description in terms of (2.13) breaks down.

In terms of the rescaled fields,

$$\varphi\to\varphi'=\sqrt{\lambda}\varphi,\quad \widetilde{\varphi}\to\widetilde{\varphi}'=\varphi/\sqrt{\lambda},$$

all λ-dependence (or f_r-dependence) of the classical-statistical evolution is in the initial conditions, as can be seen from the above expression for $S_{cl,r}$. More specifically, the "quantum half" in the nonrescaled statistical propagator is replaced by $\lambda/2$ in the rescaled one. It is possible to perform the $\lambda\to 0$ limit, by keeping the rescaled variables fixed (this means that $F\to\infty$). Note that the system does not become noninteracting, since the vertices in S_{cl} in terms of the rescaled fields do not depend on λ. Importantly, this limit eliminates the vacuum fluctuations from the initial conditions and allows us to send the momentum cut-off to infinity.

2.3.6 Summary

To summarize, in this subsection we have described how the nonequilibrium dynamics of quantum fields can be studied with the help of the 2PI formalism. We have also demonstrated how the effective kinetic and classical-statistical field theory descriptions of the dynamics, which will be frequently employed in the next chapters, emerge in this framework.

There is yet another important emergent description of the quantum field dynamics. At low energies, when the typical oscillation frequencies of the momentum modes are dominated by the bare mass of the scalar field, $\omega_{\mathrm{p}} \approx m$, an approximate description in terms of nonrelativistic QFT is applicable [20, 114, 115]. This will be discussed in greater detail in chapter 6. Note that, in contrast to the classical-statistical and kinetic descriptions, the nonrelativistic limit does not lead to a new type of degrees of freedom. Instead, it is characterized in terms of slowly-varying fields with a conserved total particle number.

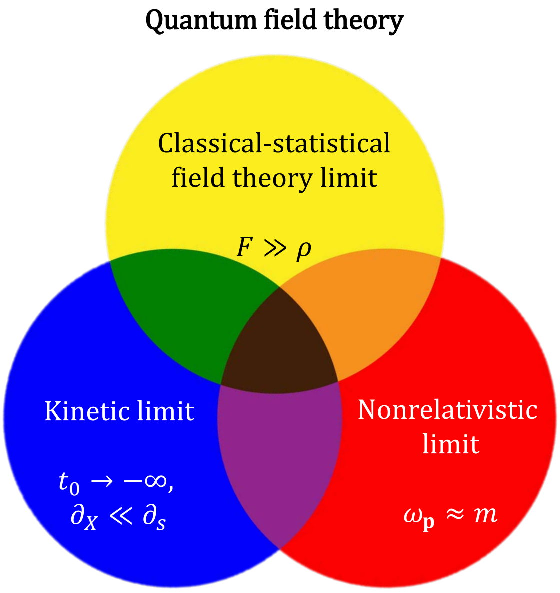

FIGURE 2.4: Effective descriptions of quantum field dynamics indicated by the three circles.

We illustrate the three approximate descriptions in Fig. 2.3 as the three circles. The overlap regions of the circles denote the regimes in which more than one description is valid. For example, the green region corresponds to the kinetic description with large occupation numbers i.e. the so-called wave kinetic theory [111].

Chapter 3

Scalar field dynamics in quasiperiodic potentials

The dynamics of scalar fields with quasiperiodic potentials can be very rich. The shape of the potential typically leads to instabilities and the amplification of quantum fluctuations. This process heavily impacts the oscillations of the initially homogeneous field. Moreover, the field can get trapped in a false minimum. The subsequent transition to a lower minimum, in an attempt to minimize the energy, is then induced by fluctuations. This chapter is devoted to the investigation of the dynamics in such systems.

In section 3.1, we briefly summarize the main properties of the model that is used for our analysis, the $3+1$-dimensional massive sine-Gordon model. We make the simple choice of an oscillating homogeneous background field present initially, with this situation being particularly relevant both to the post-inflationary preheating [15], as well as to the DM production via the vacuum misalignment mechanism [26]. Static Minkowski spacetime is considered throughout this chapter, although we also discuss how things change in an expanding universe.

Section 3.2 focuses on the instabilities that trigger the growth of quantum fluctuations. We explain how fluctuations with ultrarelativistic momenta can be produced in this process in our model. Both the linear regime of parametric resonance instabilities in the presence of an oscillating background field, as well as the onset of nonlinear effects, such as the secondary amplification of fluctuations, are discussed [21]. We also demonstrate how instabilities eventually lead to the complete fragmentation of the background field. Some details of the calculations are delegated to Appendix A.

In section 3.3 we discuss the nonperturbative regime of the dynamics after fragmentation, when the field settles in the (usually global) minimum of the potential. This stage of the dynamics involves turbulent cascades in momentum space with universal self-similar evolution of the correlation functions, as the system approaches to a nonthermal fixed point (NTFP) [22, 116]. The universal behavior and the scaling exponents are investigated both numerically by means of classical-statistical simulations, as well as by deriving the effective kinetic description based on an $1/N$ resummation of the 2PI effective action to NLO for the massive sine-Gordon model, with both methods leading to consistent predictions for the exponents. We discuss the two qualitatively different regimes of the dynamics depending on the attractive versus repulsive nature of the self-interactions.

In section 3.4 we study the important role of nonlinear dynamics and of the energy transfer from the background field into the fluctuations on the field's ability to overcome the barriers of the potential. We observe resonance-enhanced transitions between local minima as well as an effective smearing out of the wiggles by the fluctuations.

Finally, we summarize in section 3.5.

The content presented in section 3.3 of this chapter is partially based on the work in collaboration with Jürgen Berges, Kirill Boguslavski and Joerg Jaeckel, that has been published in [2]. In that work I did the main computations and writing of the script. The figures and some parts of the text in sections 3.3.1 and 3.3.3 are taken from that reference. The 2PI $1/N$ expansion for polynomial self-interactions as well as the numerical studies of the dynamics near NTFPs in scalar field theory with quartic and sextic self-interactions were part of my Master's thesis. These results are briefly reviewed in sections 3.3.1 and 3.3.3 for the sake of completeness of the presentation and because they are used afterwards.

3.1 The model

We consider a real scalar field theory in 3+1 dimensions, with a classical potential being a sum of a quadratic term and a periodic term,

$$S[\varphi] = \int d^4x \Big[\partial_\mu\varphi\partial^\mu\varphi - U(\varphi)\Big], \qquad U(\varphi) = \frac{1}{2}m^2\varphi^2 + \Lambda^4\Big(1-\cos\frac{\varphi}{f}\Big). \tag{3.1}$$

This is referred to as massive sine-Gordon model. In principle, an arbitrary phase parameter can be included in the argument of the cosine. We set it to zero for simplicity, so that the potential is $\mathbb{Z}_2$-symmetric and has a global minimum at $\varphi = 0$. The mass term breaks the discrete shift symmetry $\varphi \to \varphi + 2\pi f$, present in the standard sine-Gordon model.

The shape of the potential, namely the relative strength of the "wiggles", is determined by the value of the dimensionless parameter κ, defined as

$$\kappa^2 = \frac{\Lambda^4}{m^2 f^2}. \tag{3.2}$$

In terms of the rescaled field $\theta = \varphi/f$, the potential has the form

$$U = m^2 f^2 U_\mathrm{r} = m^2 f^2 \Big[\frac{1}{2}\theta^2 + \kappa^2(1-\cos\theta)\Big]. \tag{3.3}$$

The rescaled potential is shown in Fig. 3.1 for the values $\kappa = 3$ and $\kappa = 10$. Note that in addition to the global minimum, the potential develops an increasing number of local minima in the range $-\kappa^2 \le \theta \le \kappa^2$ as κ grows beyond $\kappa \sim 1$. The approximate number of these minima is $[\kappa^2/\pi]$.

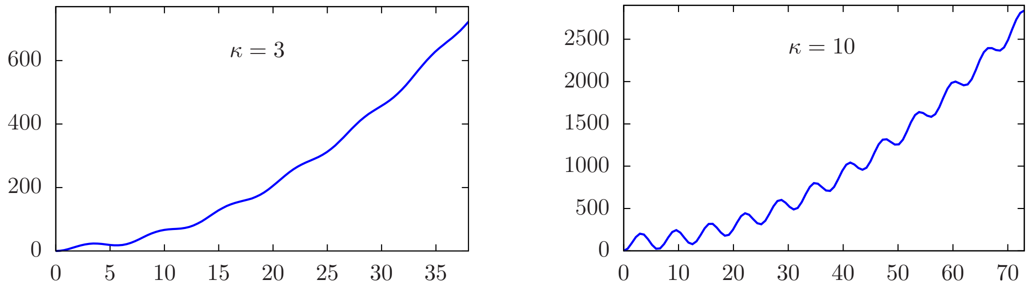

FIGURE 3.1: The shape of the rescaled potential $\theta^2/2 + \kappa^2(1-\cos\theta)$ for $\kappa = 3$ and $\kappa = 10$.

Due to the cosine potential the field features a whole sequence of self-interactions. All self-couplings of the potential in (3.1) are suppressed by powers of f. Alternatively, the strength of the couplings can be characterized by the dimensionless parameter λ, defined as

$$\lambda = \frac{\Lambda^4}{f^4} = \frac{(\kappa m)^2}{f^2}, \tag{3.4}$$

coinciding with the quartic coupling from the expansion of the potential in (3.1) around $\varphi = 0$,

$$U(\varphi) = \frac{1}{2}m^2(1+\kappa^2)\varphi^2 - \frac{\lambda}{4!}\varphi^4 + ... \tag{3.5}$$

In this chapter we consider very weak couplings, $\lambda \ll 1$, as motivated by the cosmological models of interest.

3.2 Background oscillations and instabilities

In this section the instabilities and the amplification of quantum fluctuations in our model, in the presence of an oscillating background field $\phi(t)$, are discussed. For simplicity we assume vacuum (quantum) fluctuations at the initial time t_0 and denote the initial homogeneous value of the background field by ϕ_0. Our analysis is based on the 2PI equations of motion with a loop expansion of the self-energies, as well as on classical-statistical simulations.

The evolution of the background field is governed by (2.40). Quantum fluctuations are negligible for the dynamics of the background field at early times and the equations of motion simplify to

$$\ddot{\phi}(t) + m^2\phi(t) + \frac{\Lambda^4}{f}\sin\frac{\phi(t)}{f} = 0. \tag{3.6}$$

It is worth noting at this point that, depending on the initial value, the background field oscillates either around the true minimum, or around a false minimum, inside a "potential well". In the first case ϕ_0 coincides with the oscillation amplitude and the oscillation frequency ω_0 is approximately m for sufficiently large amplitudes. The latter is a consequence of the periodic term in (3.6) being "averaged out". In the second case the frequency of background oscillations is usually larger.

3.2.1 Outline of the dynamics and power counting

Loop corrections, which are contained in the self-energies in equations (2.32) and (2.33), are suppressed at early times by powers of the coupling λ. Indeed, as can be seen from the expression for the interaction part of the action (2.31), each interaction vertex with l legs in a Feynman graph carries a factor of

$$\frac{\Lambda^4}{f^l} = \frac{\lambda^{l/2-1}}{(\kappa m)^{l-4}}. \tag{3.7}$$

In contrast, the ϕ-dependent correction to the effective mass in (2.34) is proportional to $(\kappa m)^2$ and does not depend on λ. The cosine-terms, present both in (2.31) and in (2.34), do not affect this power counting since, due to the oscillations of ϕ with an amplitude $\phi_0 \gtrsim f$, they vary in the range $[-1; 1]$. The assumption $\lambda \ll 1$, together with κ being not too large, justifies neglecting the self-energies in the equations of motion at early times, which makes the dynamics approximately linear. In other

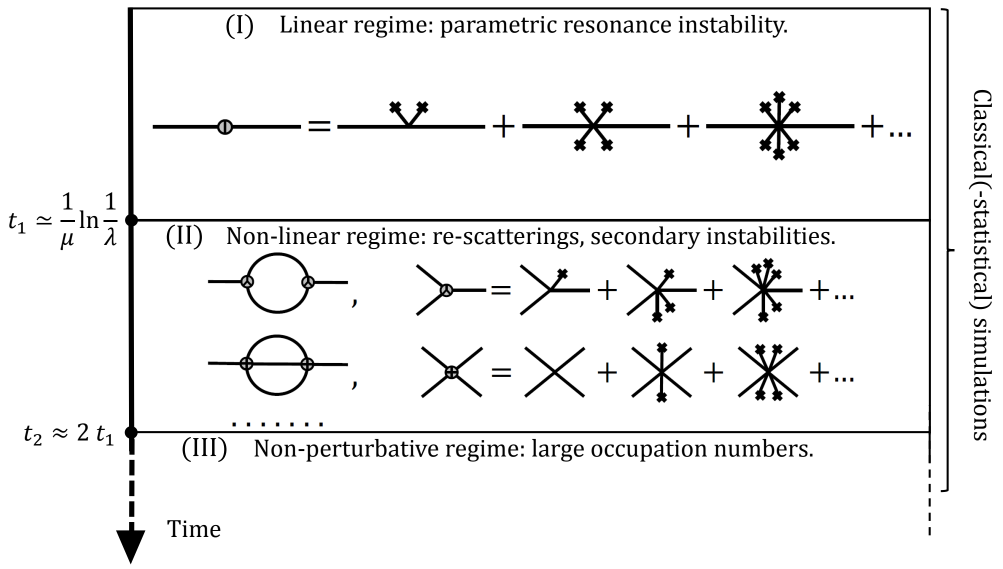

FIGURE 3.2: Schematic illustration of different stages of the dynamics, together with the diagrammatic representation of those corrections to the 2PI equations of motion for the propagator, which are important in that regime.

words, at early times different momentum modes of the propagator can be viewed as not interacting with each other. This stage of the dynamics involves exponential growth of fluctuations with certain momenta due to the parametric resonance instability [15, 21] and will be discussed in section 3.2.2. The term in the equations of motion, which dominates the dynamics in this stage (the ϕ-dependent correction to the effective mass), is diagrammatically illustrated in the upper section of Fig. 3.2.

As the fluctuations grow, the right-hand side in the evolution equations becomes important making the dynamics nonlinear. Moreover, standard power counting, discussed above, breaks down. The first term in Γ_2 that becomes relevant is a two-loop vacuum graph, given by

$$\Gamma_2[\phi, G] = \frac{i}{3!2}\int_{xy,C} \frac{\Lambda^4}{f^3}\sin\left(\frac{\phi(x)}{f}\right) G^3(x,y) \frac{\Lambda^4}{f^3}\sin\left(\frac{\phi(y)}{f}\right). \tag{3.8}$$

The corresponding one-loop self-energy, obtained by opening one of the propagator lines, is shown in the middle section of Fig. 3.2. Using Eq. (2.35) one finds the following expression for the components of the self-energy,

$$\Sigma^F(x,y) = -\frac{1}{2}\frac{\Lambda^4}{f^3}\sin\left(\frac{\phi(x)}{f}\right)\left[F^2(x,y) - \frac{1}{4}\rho^2(x,y)\right]\frac{\Lambda^4}{f^3}\sin\left(\frac{\phi(y)}{f}\right), \tag{3.9}$$

$$\Sigma^\rho(x,y) = -\frac{\Lambda^4}{f^3}\sin\left(\frac{\phi(x)}{f}\right)\left[F(x,y)\rho(x,y)\right]\frac{\Lambda^4}{f^3}\sin\left(\frac{\phi(y)}{f}\right). \tag{3.10}$$

Each cubic vertex contributes in the above expression with a factor $\Lambda^4/f^3 = m\kappa\sqrt{\lambda}$, therefore this term becomes parametrically $\mathcal{O}(\lambda^0)$, when $F \sim \mathcal{O}(\lambda^{-1/2})$. In contrast, the other one-loop contribution to the self-energy i.e. the tadpole term with a quartic vertex, carries a factor of λ, and becomes $\mathcal{O}(\lambda^0)$ only when $F \sim \mathcal{O}(\lambda^{-1})$. The next relevant term is also shown in the middle section of Fig. 3.2. It is the two-loop "sunset" diagram, which becomes important when $F \sim \mathcal{O}(\lambda^{-2/3})$.

When the statistical propagator becomes $\mathcal{O}(\lambda^{-1})$, the above described perturbative expansion breaks down, since diagrams with more loops are no longer suppressed. This stage of the dynamics, shown in the lower section of Fig. 3.2, requires nonperturbative approximation schemes, such as the classical-statistical approximation.

The conditions for the validity of classical-statistical approximation, described in the previous chapter, are not satisfied during the early stages of the dynamics. On the other hand, during the linear regime all loop corrections are suppressed and the dynamics is dominated by the large background field, which is also treated in classical-statistical field theory. Classical-statistical approximation is thus applicable also in the linear regime[1], which allows to start the simulations from $t = t_0$.

3.2.2 Linear regime: parametric resonance

The linearized version of the evolution equation (2.32) for the momentum modes of the statistical propagator is[2]

$$\left[\partial_t^2 + \mathbf{p}^2 + m^2\left(1 + \kappa^2 \cos\frac{\phi(t)}{f}\right)\right] F(t, t', \mathbf{p}) = 0. \tag{3.11}$$

The most important mechanism contributing to the growth of quantum fluctuations is the parametric resonance instability [15, 21, 56], arising due to the periodically varying effective mass. The situation is similar to a pendulum with a periodically changing length. Parametric resonance leads to an exponential growth of fluctuations with resonant momenta, $F(t, t', \mathbf{p}) \sim \exp\left(\mu(\mathrm{p})t\right)$, where $\mu(\mathrm{p}) \geq 0$. The symmetry property of the statistical propagator implies

$$F(t, t', \mathbf{p}) \sim \exp\left\{\mu(\mathrm{p})(t + t')\right\}. \tag{3.12}$$

The occupation numbers, given by (2.28), thus grow as $\sim e^{2\mu(\mathrm{p})t}$, implying the physical interpretation of an explosive particle production. The linearized equation (2.32) for the spectral function has exactly the same form as (3.11) and leads to an exponential growth, however for equal times $\rho(t, t, \mathbf{p}) = 0$, which follows from the commutation relations.

If all dimensionful quantities are expressed in units of m, the exponent $\mu(\mathrm{p})$ depends only on the values of ϕ_0/f and κ, since these are the only parameters entering Eq. (3.11). $\mu(\mathrm{p}/m)$ is shown in Fig. 3.3 for several values of κ, where the dark regions correspond to stable modes with $\mu = 0$. The plots were obtained by solving (3.11), together with (3.6) numerically, averaging over the oscillation periods and fitting an exponential growth. The extracted exponents coincide with the ones found in [56].

One observes a complicated pattern with many instability bands in Fig. 3.3. The strength and the width of the bands grow with κ, which is a consequence of the periodically varying term in (3.11) being proportional to κ^2. The instabilities also get weaker on average, when the field amplitude is increased. This is an important difference compared to models with monomial self-interactions, i.e. of the form φ^{2n}. There the periodically varying term in the effective mass is $\sim \phi^{2n-2}(t)$, thus the resonance is stronger for larger amplitudes of oscillations.

---

[1] However, the limit $\lambda \to 0$, followed by $\Lambda_{UV} \to \infty$, explained in the previous chapter, cannot be performed in this case, since this would eliminate the vacuum fluctuations and there would be no instabilities.

[2] The same equation is satisfied by the Heisenberg mode functions of the field.

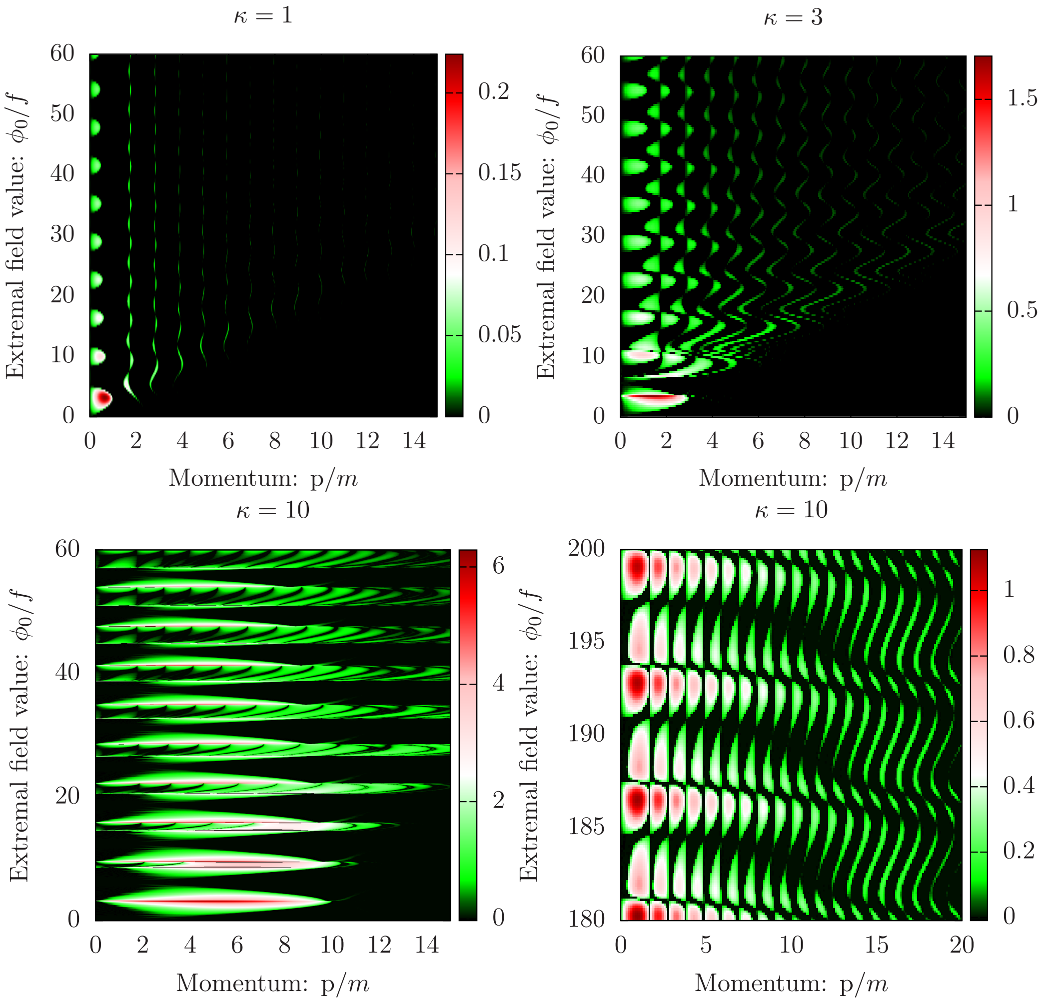

FIGURE 3.3: The growth exponent μ/m, characterizing the parametric resonance instability, for $\kappa = 1$, $\kappa = 3$ and $\kappa = 10$. On the vertical axis is the initial/extremal value of the background field ϕ_0/f. On the horizontal axis is the momentum p/m. The dark regions correspond to stable modes.

We first consider values of ϕ_0/f, for which the background oscillations occur around $\phi = 0$. The instability bands in this regime extend from nonrelativistic momenta up to some $\mathrm{p} = \mathrm{p}_{max}$, which depends on ϕ_0/f. One observes in Fig. 3.3, that $\mathrm{p}_{max}/m \approx (\phi_0/f)/2$ for not too small field values. The momentum extent of the instability bands is, thus, significantly larger compared to the case of monomial self-interactions and can involve ultra-relativistic modes for large field amplitudes. This is a feature of the considered model or similar models with "wiggly"potentials and can be understood as follows. During one oscillation of the background field, the cosine term in (3.11) performs "oscillations" with a "changing" frequency, whose instantaneous value is given by $\omega(t) = \partial_t\phi(t)/f$. Since $\partial_t\phi(t)$ is maximal when the field is near the bottom of the potential, the cosine term oscillates fastest there and one can write for the maximal resonant momenta

$$\mathrm{p}_{max} \approx \omega_{max} \sim \frac{\partial_t\phi(\phi = 0)}{f} \approx \frac{m\phi_0}{f}. \tag{3.13}$$

We observe in Fig. 3.3 that, for a given value of ϕ_0/f, the centers of adjacent instability bands are typically separated by intervals $\Delta\omega_{\mathbf{p}} \approx m$. Their width and strength decrease on average with p, however are not entirely monotonic, as can be seen from the lower right panel of Fig. 3.3. For small κ-s the bands become narrow and their locations are approximately given by $\mathrm{p} = \sqrt{n^2-1}m$. In other words, the resonant frequencies in that case are multiples of the background field oscillation frequency, $\omega_{\mathbf{p}} \approx nm$, where $n \in \mathbb{N}$ (see also [56]).

The pattern of the instability bands strongly depends on ϕ_0/f, but well bellow p_{max} it is approximately periodic under $\phi_0 \to \phi_0 + 2\pi f$, although the strength and the width of the bands slowly decrease with ϕ_0. The quasiperiodicity at low momenta hints that most of the important dynamics for these modes occurs when the field is within a couple of cosine-periods from its extremal value, while otherwise the fast oscillations of the cosine term "average out". If $\kappa > 1$, depending on the initial field value the exponential growth of the low-momentum modes can get a strong contribution from the tachyonic instability [117]. Indeed, the effective mass in (3.11) can take negative values in that case, which leads to exponential growth. Tachyonic instability can occur only for modes with $\mathrm{p}^2 \geq (\kappa^2-1)m^2$.

Differences from the above-described pattern of the instability bands occur if the background field oscillates within a single potential well. This includes the case when the field is trapped in a false minimum and oscillates around $\phi \neq 0$. In the latter case ϕ_0 does not coincide with the actual oscillation amplitude. Parametric resonance in this regime has similarities with the one in the standard sine-Gordon model [43]. In particular, there is one wide dominant instability band with momenta not exceeding κm, as can be seen from Fig. 3.3. The strength and width of the band increase with the amplitude of oscillations. The strongest resonance occurs when $\phi_0/f \approx \pi$.

Finally, in the presence of expansion the amplitude of the oscillations decreases with time, and the momenta of fluctuations are red-shifted. As a result, each comoving momentum mode flows through different instability bands of Fig. 3.3.

3.2.3 Nonlinear regime: secondary instabilities

Parametric resonance leads to an exponential growth of fluctuations with certain momenta. Eventually, the loop corrections in (2.32) and (2.33) become important. In this section we study the leading correction i.e. the one-loop self-energy, depicted in Fig. 3.2, and demonstrate how it leads to secondary instabilities i.e. exponential amplification of modes outside the primary resonance band with a twice larger rate. Our analysis follows the same lines as in [21]. Analogous higher-order corrections are also discussed.

Approximate evolution equations: Inserting (3.9) and (3.10) into the evolution equations for the statistical propagator $F(t,t',\mathbf{p})$ and neglecting the $\mathcal{O}(\rho^3)$ term one obtains

$$\begin{aligned}\left[\partial_t^2 + \mathbf{p}^2 + m^2 + \frac{\Lambda^4}{f^2}\cos\frac{\phi(t)}{f}\right] & F(t,t',\mathbf{p}) \\ = \left(\frac{\Lambda^4}{f^3}\right)^2 \sin\frac{\phi(t)}{f}\int_{\mathbf{q}}\Bigg[& \int_0^t d\tau \sin\frac{\phi(\tau)}{f} F(t,\tau,\mathbf{p}-\mathbf{q})\rho(t,\tau,\mathbf{q})F(\tau,t',\mathbf{p}) \\ & - \frac{1}{2}\int_0^{t'} d\tau \sin\frac{\phi(\tau)}{f} F(t,\tau,\mathbf{p}-\mathbf{q})F(t,\tau,\mathbf{q})\rho(\tau,t',\mathbf{p})\Bigg]. \end{aligned} \tag{3.14}$$

The $\mathcal{O}(\rho^3)$ term accounts for genuine quantum corrections [21]. It is expected to become sub-dominant as F grows exponentially.

In order to obtain a qualitative picture, several approximations are performed to make the right-hand side of the above equation local in time, as in [21, 70]. Firstly, because of the exponential growth of the fluctuations, the memory integrals in Eq. (3.14) are dominated by late times. For simplicity we replace the full time integrals by integrals over time of the order of the last oscillation period,

$$\int_0^t \to \int_{t-\alpha/\omega_0}^t, \qquad \int_0^{t'} \to \int_{t'-\alpha/\omega_0}^{t'},$$

where $\alpha = \mathcal{O}(1)$. Furthermore, the terms inside the intregrals are expanded in Taylor series around the upper-time limits up to the leading nonvanishing order, e.g. in the first integral,

$$\sin\frac{\phi(\tau)}{f} \approx \sin\frac{\phi(t)}{f}, \qquad F(t,\tau,\mathbf{p}) \approx F(t,t,\mathbf{p}),$$

and, for the spectral function, using (2.27),

$$\rho(t,\tau,\mathbf{p}) \approx 0 + (\tau - t)\partial_\tau \rho(t,\tau,\mathbf{p})|_{\tau=t} \approx t - \tau. \tag{3.15}$$

We emphasize that these approximations are sufficient only for qualitative analysis. Using the above assumptions, Eq. (3.14) can be written as,

$$\begin{aligned}&\Big[\partial_t^2 + \mathbf{p}^2 + m^2\Big(1 + \kappa^2 \cos\frac{\phi(t)}{f}\Big)\Big]F(t,t',\mathbf{p}) \\ &= \lambda\kappa^2 m^2 \frac{\alpha^2}{2m^2}\Bigg[\sin^2\frac{\phi(t)}{f}\Big(\int_{\mathbf{q}} F(t,t,\mathbf{q})\Big)F(t,t',\mathbf{p}) \\ &+ \frac{1}{2}\sin\frac{\phi(t)}{f}\sin\frac{\phi(t')}{f}\int_{\mathbf{q}} F(t,t',\mathbf{p}-\mathbf{q})F(t,t',\mathbf{q})\Bigg].\end{aligned} \tag{3.16}$$

Discussion: Let us now discuss the two terms on the right-hand side of (3.16). The first term has the form of a mass shift (within our approximations). Like the standard one-loop tadpole correction, it becomes important once the typical occupancies and, consequently, the term $\int_{\mathbf{q}} F(t,t,\mathbf{q})$ become $\mathcal{O}(\lambda^{-1})$. This timescale t_{nonpert} is also when the dynamics becomes fully nonperturbative (see also [21]) and can be parametrically estimated as

$$t_{\mathrm{nonpert}} \simeq \ln(\lambda^{-1})/(2\mu_0), \tag{3.17}$$

with μ_0 characterizing the growth exponent of the strongest peak.

The second term in (3.16) becomes important earlier, at $t_{\mathrm{source}} \simeq t_{\mathrm{nonpert}}/2$, and acts as a source inducing secondary instabilities. It is proportional to the momentum integral,

$$I(t,t',\mathrm{p}) = \int_{\mathbf{q}} F(t,t',\mathbf{p}-\mathbf{q})F(t,t',\mathbf{q}). \tag{3.18}$$

The source term and its impact on the evolution equations are analyzed in Appendix A. In particular, we show that, if the dominant peak from parametric resonance is centered at some momentum p_0 and exhibits an exponential growth

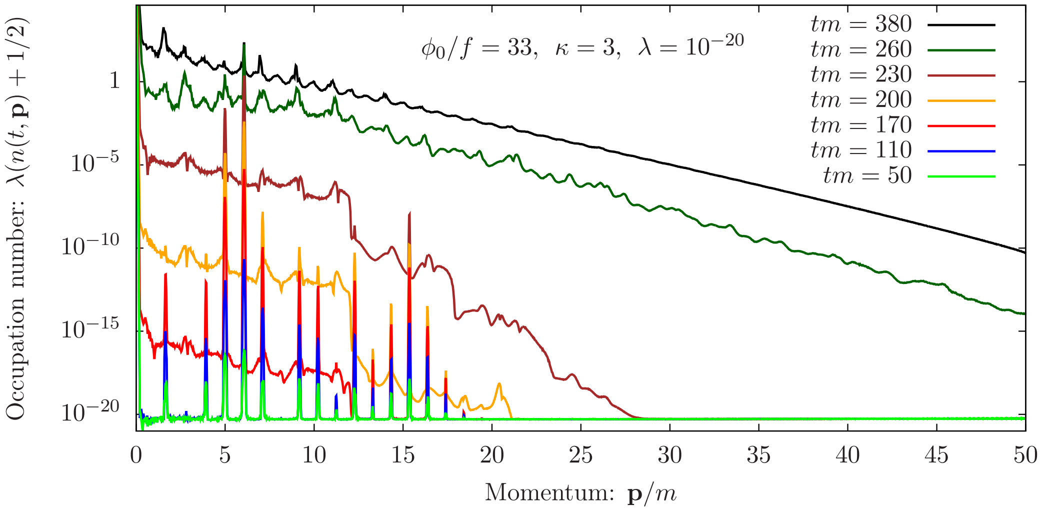

FIGURE 3.4: The time evolution of the mode occupation numbers for the values of parameters $\phi_0/f = 33$, $\kappa = 3$ and $\lambda = 10^{-20}$. On the vertical axis is the occupation number (2.28), multiplied by the coupling λ. On the horizontal axis is the rescaled momentum. The narrow peaks at early times are due to parametric resonance. The broad bands as well as the new peaks at later times are due to nonlinear effects.

$F(t, t', \mathbf{p}_0) \sim e^{\mu_0(t+t')}$, fluctuations with momenta in the range $0 \leq |\mathbf{p}| \lesssim 2\mathrm{p}_0$ exhibit secondary amplification and grow "twice faster", $F(t, t', \mathbf{p}) \sim e^{2\mu_0(t+t')}$, after the source term dominates their dynamics.

Secondary instabilities can be interpreted as the re-scattering of the produced excitations via three-body interactions involving two quanta with resonant and one with nonresonant momenta. Cubic interactions in our model, illustrated in Fig. 3.2 and given by (2.31), arise in the presence of the background field.

Similar arguments can be made for higher-order instabilities. For instance, tertiary instabilities, arising from the two-loop graph in Fig. 3.2, set in at $t \gtrsim 2t_{\text{nonpert}}/3$, involve momenta up to $0 \leq \mathrm{p} \lesssim 3\mathrm{p}_0$ and lead to a growth $F(t, t', \mathbf{p}) \sim e^{3\mu_0(t+t')}$.

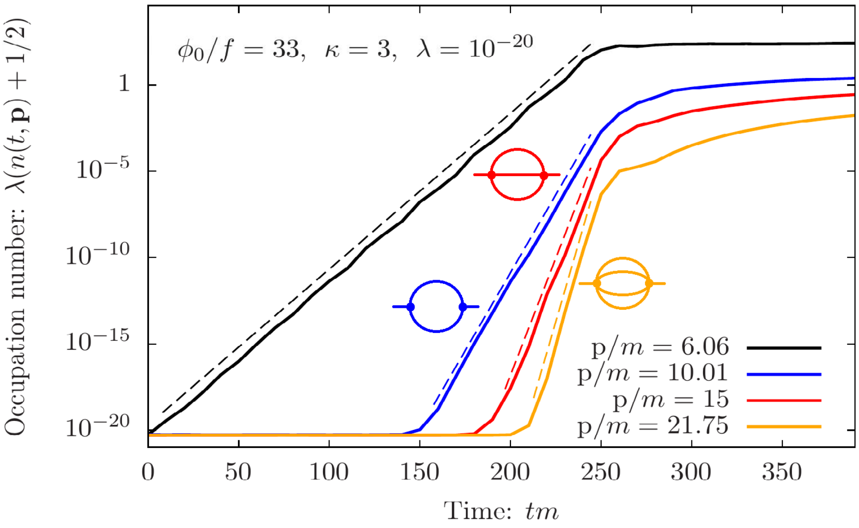

FIGURE 3.5: The time evolution of individual mode occupation numbers (2.28) for the values of parameters $\phi_0/f = 33$, $\kappa = 3$ and $\lambda = 10^{-20}$.

3.2.4 Classical-statistical simulations

Above-described features of the dynamics are observed in our classical-statistical field theory simulations. The simulations are performed on cubic lattices with up to 1024^3 points and periodic boundary conditions. The computations are done using a C++ program and parallelized using "Message Passing Interface", by dividing the grid along the third direction. In each classical simulation, the discretized field equations are solved using the leap-frog algorithm. We sample the Gaussian initial conditions, as explained in section 2.3.5, with $n_0(\mathrm{p}) = 0$. The "quantum $1/2$" is seeded, as in (2.52), in all momentum modes bellow a certain cut-off Λ_{UV}. We checked that shown results are insensitive to variations of the momentum cut-offs. The time-dependent occupation numbers are extracted using (2.28). The Fourier transform of the field is computed using the "Fastest Fourier Transform in the West" library. In most cases ergodicity of the system allows replacing the statistical averages by volume averages [112].

In Fig. 3.4 several snapshots of occupation numbers $\lambda(n(t, \mathbf{p}) + 1/2)$, obtained from simulations with $\phi_0/f = 33$, $\kappa = 3$ and $\lambda = 10^{-20}$, are shown. At early times, $tm \lesssim 140$, several peaks with exponentially growing occupation numbers are observed, corresponding to parametric resonance. The strongest peak is located at $|\mathbf{p}_0| \approx 6m$. The broad low-momentum band at $tm = 170$ is generated from secondary instabilities. Note that the band cuts off at $|\mathbf{p}| \approx 12m \approx 2|\mathbf{p}_0|$, consistent with the above discussion. Similarly, at $tm = 230$ one observes the cut-off for tertiary instabilities at $|\mathbf{p}| \approx 18m \approx 3|\mathbf{p}_0|$. As explained in Appendix A, low-momentum modes are enhanced more compared to the high-momentum ones, which tends to make the spectrum monotonic at late times.

The broad spectrum usually has a "peaky"structure, as in Fig. 3.4. These peaks are different from the ones from parametric resonance, although some of them have very close locations. They are also typically wider and extend beyond $\mathrm{p} \approx \phi_{\mathrm{r},0}/2$. As explained in Appendix A, these peaks are expected to correspond to resonant frequencies of the source term. Certain momentum modes within the band satisfy resonance conditions, as in the case of parametric resonance, and get singled out on top of the exponential growth.

In Fig. 3.5 the time-evolution of individual mode occupation numbers is plotted for the same values of the parameters. The black line corresponds to $|\mathbf{p}_0| \approx 6m$, from the strongest peak of parametric resonance. This mode exhibits an exponential growth $n(t, \mathbf{p}_0) \sim e^{2\mu_0 t}$ with $\mu_0 \approx 0.1$, as indicated by the dashed black line. The remaining three modes are chosen within the secondary (blue), tertiary (red) and quaternary (orange) instability bands. Their evolution coincides well with the expected exponential growth $e^{4\mu_0 t}$, $e^{6\mu_0 t}$ and $e^{8\mu_0 t}$, respectively. The exponential growth is indicated by dashed lines of corresponding colors. Moreover, the diagrams that account for each of the instability bands are also depicted in the figure.

3.2.5 The decay of background oscillations

When the typical occupation numbers become parametrically $\mathcal{O}(\lambda^{-1})$, the dynamics becomes nonperturbative. In Fig. 3.4 this happens at $tm \approx 250$. During this stage the energy continues to be transferred from the background field ϕ to the fluctuations and the back-reaction on ϕ becomes non-negligible. This leads to the decay of the background oscillations, described in this subsection.

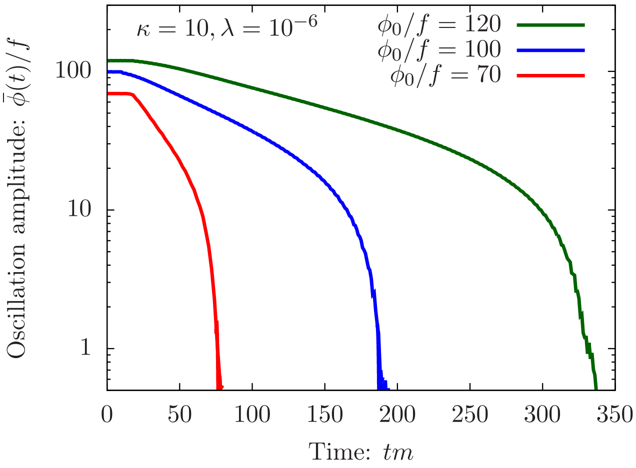

FIGURE 3.6: The decreasing amplitude of the oscillations of the background field $\phi(t)$, denoted by $\bar{\phi}(t)$, as a function of time, for $\kappa = 10$, $\lambda = 10^{-10}$ and several initial field values. After the stage of rapid decrease, the background field is fragmented.

In the case of large initial amplitudes $\phi_0/f \gg 1$, the background field performs oscillations around the minimum with a gradually decreasing amplitude[3]. Th classical-statistical simulations show that the amplitude decreases slower for smaller values of κ, as well as for larger initial amplitudes ϕ_0/f. A similar tendency was described in the discussion of linear instabilities in Section 3.2. Interestingly, for most of the time the decay of the amplitude by its form is close to exponential i.e. $\bar{\phi}(t) \sim \exp(-\Gamma_{\text{decay}} t)$, with decay rate Γ_{decay} a slowly increasing in time. This is demonstrated in Fig. 3.6, where the amplitude of the background oscillations $\bar{\phi}(t)/f$, extracted from classical-statistical simulations, is plotted versus time for $\kappa = 10$, $\lambda = 10^{-10}$ and several values of the initial amplitude.

The energy, transferred from the background field during its decay in the nonperturbative regime, is mostly spent on broadening the fluctuation spectrum towards higher momenta. The low momentum occupation numbers do not grow much in this stage. For some time one observes peaks at low momenta, such as in Fig. 3.4 at $tm = 380$. These peaks correspond to the influx of the energy from the background field. Re-scattering of the fluctuations leads to the gradual smoothening of the spectrum with time.

In the cases, depicted in Fig. 3.6, the field finds itself in the lowest minimum after the background oscillations die out. It is also possible, although less likely, that the field settles in one of the false minima. This possibility is discussed in Section 3.4.

3.3 Universal dynamics near nonthermal fixed points

In this section we investigate the dynamics after the oscillating background field has been converted into strong fluctuations. At this stage the field features large occupation numbers $\sim 1/\lambda$ at low momenta and, thus, is still far from thermal equilibrium.

---

[3] In an expanding spacetime this decrease is combined with overall dilution.

Many characteristic properties of the dynamics in such "highly occupied" regime turn out to be insensitive to the details of the underlying model and to the initial conditions. The emergence of such universality is based on the existence of NTFPs [23, 25, 118, 119] that are nonequilibrium attractor solutions with self-similar scaling behavior of correlation functions. More specifically, the self-similar evolution of the particle momentum distribution in the vicinity of a NTFP has the form

$$n(t, \mathrm{p}) = \left(\frac{t}{t_S}\right)^{\alpha} n\left(t_S, \left(\frac{t}{t_S}\right)^{\beta} \mathrm{p}\right) = \left(\frac{t}{t_S}\right)^{\alpha} n_S\left(\left(\frac{t}{t_S}\right)^{\beta} \mathrm{p}\right), \tag{3.19}$$

Here α and β are real scaling exponents and n_S is the fixed point distribution at t_S.

Self-similar evolution is associated with the transport of some conserved quantity in momentum space [22, 111]. The scaling regions can represent transport of energy towards high momenta, or particle number transport towards the zero-mode. While the first case drives the thermalization process by pushing the typical energy scale to larger momenta [22], the second one may lead to the macroscopic occupation of the zero-momentum mode i.e. the formation of a condensate out-of-equilibrium [68]. Both cascades have been observed in different regions of the same momentum distribution function in scalar models with positive quartic self-coupling [25, 120].

In the following two subsections we study the dynamics in the two momentum ranges separately, by using classical-statistical simulations. Our numerical studies are complemented with an analytical investigation in the last subsection, based on an effective kinetic description of the dynamics. The kinetic equations are derived from a 2PI $1/N$ expansion to NLO, that we perform for the considered model.

3.3.1 Dynamics at low momenta

The amplitude of background oscillations drops rapidly after becoming of the order of a "wiggle period", $\phi/f \sim \mathcal{O}(\pi)$, as can be seen in Fig. 3.6. This is when the attractive nature of the leading self-interactions becomes important.

In general, for self-interactions of the form $\lambda_{2n}(\varphi^2)^n$, the positive or negative sign of a coupling determines whether the corresponding self-interaction is repulsive or attractive. While repulsive interactions have the tendency to dilute concentrations of energy density over position space, attractive interactions encourage such local concentrations. This can be understood by noting that, depending on the sign of the coupling, the potential gets steeper or shallower near $\phi = 0$.

The coupling of the leading quartic self-interactions in (3.5) has a negative sign. The self-interactions in the (massive) sine-Gordon model are thus attractive and, as a consequence, tend to fragment the background field and lead to the destruction of long-range coherence (for more details see [1, 76, 121]). This is indeed observed in Fig. 3.6. In individual runs of the classical-statistical simulations, relatively short-lived compact field configurations, such as oscillons, emerge in this stage of the dynamics [76].

In contrast, a homogeneously oscillating field is an energetically preferred configuration if the leading self-interactions are repulsive [1, 121]. Such interactions lead to the build-up of a homogeneous and long-lived condensate after the fragmentation. Condensation occurs as a consequence of a universal inverse particle cascade to the zero-momentum mode with a self-similar scaling behavior [1]. In our numerical simulations we find scaling exponents for the inverse cascade close to

$$\beta = 1/2, \qquad \alpha = 3\beta \qquad \text{(inverse cascade, repulsive self-interactions).} \tag{3.20}$$

For reasons that will become clear in Chapter 5, it is instructive to consider this scenario in more detail and delineate the differences to the attractive case. For this we first consider a simpler model with only quartic and sextic self-interactions, consider both signs in front of the quartic coupling, and afterwards return to our original model.

Repulsive versus attractive interactions: In order to observe the condensation, it is convenient to start directly with a vanishing background field and large initial occupation numbers of the following form

$$n(t_0, \mathrm{p}) = \frac{A_0}{\lambda}(\mathrm{p}_0 - \mathrm{p}), \qquad \phi(t_0) = \dot{\phi}(t_0) = 0. \tag{3.21}$$

These initial conditions correspond to a 'box' in momentum space up to the momentum scale p_0, with the amplitude $A_0 \gtrsim 1$. We set the sextic self-coupling to $\lambda_6 = 2\lambda^2/m^2$, which ensures that the potential is convex even for $\lambda < 0$.

We first consider the repulsive scenario, with a "plus" sign in front of the quartic coupling and $A_0 = 100$. In the upper left panel of Fig. 3.7 we show the rescaled distribution function $t^{-\alpha} n(t, |\mathbf{p}|)$ as a function of the rescaled momentum $t^{\beta}|\mathbf{p}|$ at different times for the values $\alpha = 3/2$ and $\beta = 1/2$ while the inset gives the same distributions without rescaling. Since the rescaled curves lie on top of each other, the system follows a self-similar evolution with the given values for the exponents α and β. The fixed point distribution n_S exhibits an approximate power-law behavior $\sim |\mathbf{p}|^{-\kappa}$, with $\kappa \approx 4.5$. The same values for these three exponents have been observed also for the φ^4 model [25].

The occupancy of the zero-momentum mode grows during the self-similar evolution approximately as a power-law $\sim t^{\alpha}$. This can be directly understood from Eq. (3.19), by setting $\mathbf{p} = 0$. For a finite volume this growth continues until $F(t, t, \mathbf{p} = 0)$ becomes proportional to the volume V, which signals the emergence of the condensate according to [68] with the replacement $(2\pi)^3\delta(\mathbf{0}) \to V$. This is demonstrated in the upper right panel of Fig. 3.7, where the quantity $F(t, t, \mathbf{p} = 0)/V$ is shown as a function of time for several volumes. All of this has also been observed in the φ^4 model [25]. There it was also shown that this dynamics implies that the time required for creating a condensate scales with volume.

While the initial background field and the later condensate are very similar, it is worth emphasizing their difference from the point of view of classical-statistical field theory. The first one corresponds to a nonvanishing field one-point function, $\phi(t)$. After the collapse, however, this expectation value vanishes and the build-up of the condensate corresponds to the growth of the zero-momentum mode of the two-point function $F(t, t, \mathrm{p} = 0)$ instead. While in each simulation of the classical-statistical ensemble a homogeneous field component emerges as a result of condensation, leading to a nonvanishing volume average of the field, their phases become uncorrelated after the collapse, resulting in a vanishing one-point function. This loss of ergodicity is due to the emergence of long-range order in the system.

The dynamics in the "attractive" scenario is significantly different and the inverse particle cascade is absent. This is demonstrated in the bottom left panel of Fig. 3.7, which contains several snapshots of the distribution function. Here we

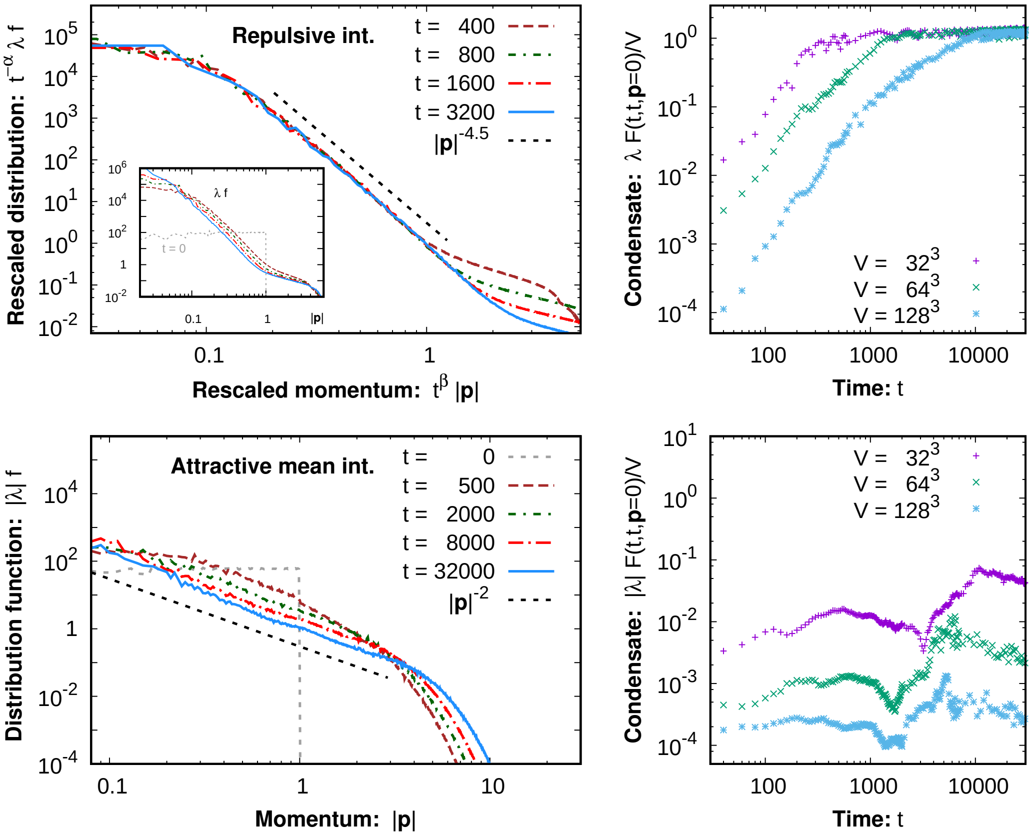

FIGURE 3.7: Snapshots of the distribution function as a function of the momentum (left column) and the zero-momentum correlation function divided by the volume for several volumes (right column). **Upper row:** Repulsive theory; distribution function and momentum in the left panel are rescaled with powers of time, with the inset showing the original distribution without any rescaling; right panel demonstrates formation of a condensate. **Lower row:** Attractive theory. Note that the momentum is not rescaled.

start with a not too large amplitude, $A_0 = 60$, to make sure that the dynamics is dominated by the attractive quartic self-interaction. While a transient growth of the low momentum occupancies is observed at early times, it does not lead to an enhancement of infrared modes as strong as in the repulsive models, $\sim |\mathbf{p}|^{-4.5}$, that were discussed above. For comparison, a power law $\sim |\mathbf{p}|^{-2}$ is additionally shown in the plot.

Due to the absence of an inverse particle cascade, the zero-momentum mode does not develop a condensate part. This is demonstrated in the bottom right panel of Fig. 3.7, where the time evolution of the correlation function $F(t, t, \mathbf{p} = 0)$ divided by the volume V is shown for several volumes. As was mentioned in the previous section, for a finite volume, the presence of a condensate would lead to a contribution in $F(t, t, \mathbf{p} = 0)$, which scales proportionally to V. Such a contribution is clearly absent in the attractive case, which becomes more stringent when compared to the repulsive system depicted in the upper right panel of Fig. 3.7. In other words, no long-range order is being established.

The same qualitative behavior and scaling exponents are observed in the massive sine-Gordon model. Repulsive self-interactions at the bottom of the potential can be achieved by substituting $\Lambda^4 \to -\Lambda^4$ in the potential (3.1), which flips the signs of all couplings (see also section 3.3.3). The classical potential remains convex around its minimum if $\kappa < 1$. We have performed numerical simulations for this case, which have shown that the decay of the background field oscillations is practically unaffected by the above modification. At later times the background field indeed transforms into a homogeneous condensate.

3.3.2 Dynamics at high momenta

Even after the decay of background oscillations, energy continues to be transferred to higher, previously unoccupied momenta, resulting in gradual decrease of low-momentum occupancies. This reflects the tendency of the system to thermalize. In the absence of expansion, the dominant contribution to the energy budget after some time comes from ultra-relativistic modes, with $\omega_{\mathbf{p}} \approx \mathrm{p}$. The transfer of energy, often referred to as free turbulence, occurs via a direct cascade that the mode occupancies exhibit at high momenta [22]. The dynamics of this cascade is also characterized by universal self-similar evolution of the distribution function according to (3.19) [22, 116].

Classical-statistical simulations reveal that the scaling exponents are insensitive to the form of the potential and to whether the self-interactions are attractive or repulsive. We find exponents close to

$$\beta = -1/5, \qquad \alpha = 4\beta \qquad \text{(direct cascade).} \tag{3.22}$$

Due to the energy cascade the characteristic comoving momentum, which we denote by $\bar{\mathrm{p}}$, grows as

$$\bar{\mathrm{p}}(t) \propto t^{-\beta},$$

with time (t is the conformal time). This follows from the form of the self-similar evolution, noting that the characteristic momentum maximizes the energy per mode,

$$\mathrm{p}^3 n(t,\mathrm{p}) = \left(\frac{t}{t_S}\right)^{\alpha-3\beta}\left[\left(\left(\frac{t}{t_S}\right)^{\beta}\mathrm{p}\right)^3 n_S\left(\left(\frac{t}{t_S}\right)^{\beta}\mathrm{p}\right)\right] \qquad \rightarrow \qquad \left(\frac{t}{t_S}\right)^{\beta}\bar{\mathrm{p}}(t) = \text{const.}$$

Also the occupation number at that characteristic momentum $\bar{n}$ decreases with time,

$$\bar{n}(t) = n(t,\bar{\mathrm{p}}(t)) = \left(\frac{t}{t_S}\right)^{\alpha}\left[n_S\left(\left(\frac{t}{t_S}\right)^{\beta}\bar{\mathrm{p}}(t)\right)\right] \propto t^{\alpha}.$$

Extracting the scaling exponents: We have extracted the exponents α and β by performing likelihood fits, similar to [116]. More specifically, for different times t' we have compared the distribution function, multiplied by the momentum cubed, which in the ultra-relativistic regime gives the energy density per momentum, at $t = t'$ and $t = 2t'$. Assuming the self-similar behavior of (3.19), we tested different values of the exponents and for each pair defined the (normalized) likelihood,

$$W(\alpha,\beta) \propto \exp\Big[-\chi(\alpha,\beta)/(2\bar{\chi})\Big], \tag{3.23}$$

where

$$\chi(\alpha,\beta) = \frac{\int[(n(t',\mathrm{p}) - 2^{-\alpha}n(2t',2^{-\beta}\mathrm{p}))\mathrm{p}^3]^2 d\mathrm{p}}{\int[n(t',\mathrm{p})\mathrm{p}^3]^2 d\mathrm{p}}. \tag{3.24}$$

Here $\bar{\chi}$ is the minimal observed value of $\chi(\alpha,\beta)$, which corresponds to the best fit. The integrals are performed over large momenta, $\mathrm{p} \gg M$, for which $n(\mathrm{p}) \gg 1$.

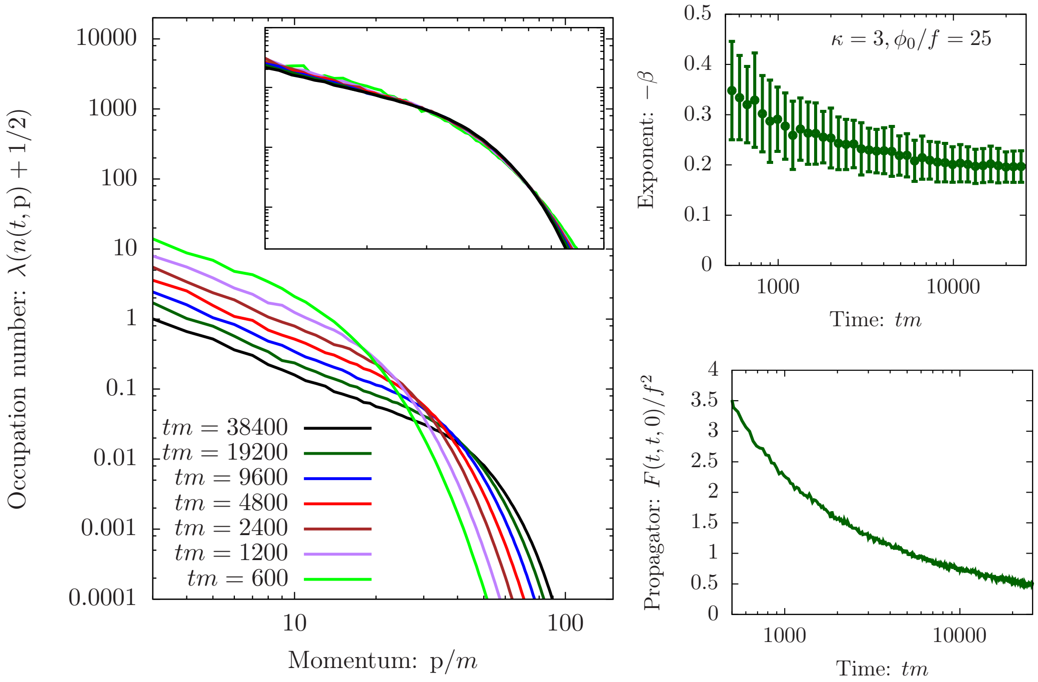

FIGURE 3.8: The direct energy cascade for $\phi_0/f = 25$ and $\kappa = 3$. **Left**: Several snapshots of the distribution function with (inset) and without (main plot) rescaling. **Right**: The time-evolution of the numerically extracted scaling exponent β, describing the direct cascade (upper), and the equal-time statistical propagator $F(t,t,\mathbf{x}-\mathbf{y} = 0)$ (lower). The cascade gradually slows down, with β approaching -1/5.

We found the values of the exponents, for which the fit was the best and identified the fitting errors with the gaussian widths of the marginal likelihoods $\int W d\beta$ and $\int W d\alpha$.

Extracted in this way exponents turn out to be time-dependent, but tend to fixed values. The ratio of the exponents quickly approaches $\alpha/\beta \approx 4$. The value of the exponent β comparably slower (especially for large initial field values) decreases to $\beta \approx -1/5$. Therefore, the cascade is faster in the beginning, but gradually slows down. This is illustrated in Fig. 3.8 for the case of $\kappa = 3$ and $\phi_0/f = 25$. In the left panel several snapshots of the cascading distribution function are shown on a log-log plot. In the inset the same after an appropriate rescaling is displayed. As can be seen, the functions overlap quite well, although a slow change of their shape with time is observed. The upper right panel shows the exponent $\beta(t)$, extracted numerically, as described above, as a function of time together with its errors. The value $\beta = -1/5$ was also reported in other scalar models [1, 22].

3.3.3 $1/N$ resummation and kinetic description

The observation that the scaling exponents governing the dynamics near NTFPs are unaffected by the presence of additional self-interactions in the sine-Gordon model, compared to the φ^4 theory, requires a better analytical understanding.

The slow dynamics in the vicinity of a NTFP can be studied by means of the kinetic description. This corresponds to the green region in Fig. 2.4. The scaling exponents for the cascades in φ^4 theory have been calculated in [25] by applying kinetic theory based on the 2PI $1/N$ expansion to NLO [70, 71]. In this section we generalize that expansion for the sine-Gordon model and derive the corresponding

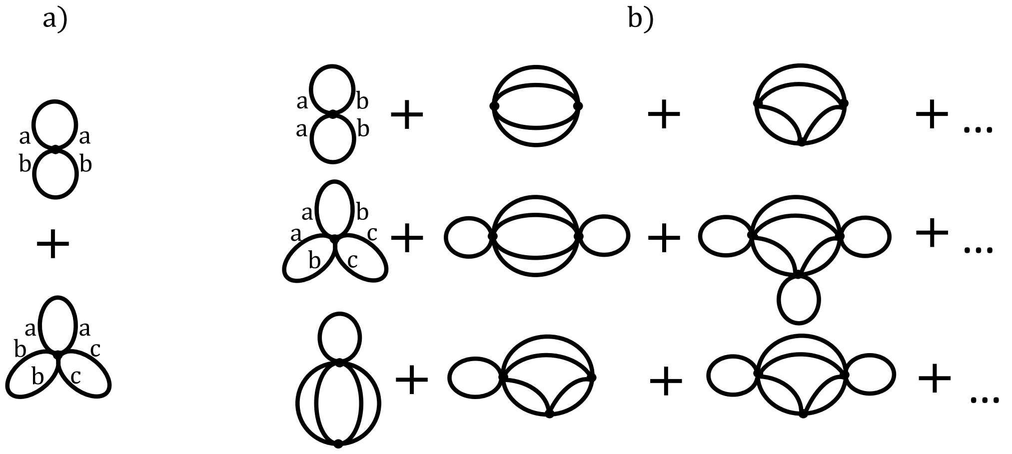

FIGURE 3.9: The LO (a) and NLO (b) diagrams of the 2PI $1/N$ expansion for scalar field theories with quartic and sextic self-interactions.

transport equations, which allow understanding of the observed universality of the exponents.

In order to perform the above-described classification our single-component model should be first embedded into an $\mathcal{O}(N)$-symmetric model,

$$U(\varphi)=\frac{1}{2}m^2\varphi^2+N\Lambda^4\Big[1-\cos\Big(\frac{\varphi}{f\sqrt{N}}\Big)\Big], \tag{3.25}$$

where $\varphi=\sqrt{\varphi_a\varphi_a}$ and the cosine-term can be understood in terms of its Taylor expansion. Note that the factors of N in (3.25) are chosen such that the classical action $S[\varphi]=\int_x[\frac{1}{2}\partial^\mu\varphi_a\partial_\mu\varphi_a-U(\varphi)]$ scales proportional to N. For $N=1$ one recovers (3.1). Although the convergence of the expansion relies on a large value of N, it has been successfully applied to models with a moderate number of field components and was able to describe observed phenomena [20, 70, 71].

We consider the stage of the dynamics after the background oscillations have decayed away i.e. assume that $\phi=0$. The $1/N$ expansion can be performed by classifying the contributions to $\Gamma_2[\phi=0,G]$ based on their scaling with the number of field components N.

Leading order: At the LO each of the polynomial self-interactions $\sim\lambda_{2n}(\varphi^2)^n$, that are present in (3.25), contributes with a single "bubble" diagram [122, 123], resulting in

$$\Gamma_2^{\mathrm{LO}}[G]=-\sum_{n=2}^{\infty}\frac{\lambda_{2n}}{(2n)!N^{n-1}}\int_{x,C}\Big(G_{aa}(x,x)\Big)^n. \tag{3.26}$$

These correspond to diagrams with one vertex where propagators $G_{aa}(x,x)$ connect legs with the same indices forming closed bubbles. The first two such diagrams are shown in panel (a) of Fig. 3.9. Because of the implicit summation over the index a, each bubble, and consequently each of the two shown diagrams, scales proportional to N.

Inserting the expression for the couplings in the sine-Gordon model, $\lambda_{2n}=(-1)^{n+1}\Lambda^4/f^{2n}$ (see also Eq. (2.31)), and summing the series inside the integral gives[4]

$$\Gamma_2^{\mathrm{LO}}[G] = N\Lambda^4 \int_{x,C} \left[\cos\left(\sqrt{\frac{F(x,x)}{f^2}}\right) - 1 + \frac{F(x,x)}{2f^2}\right]. \tag{3.27}$$

As can be seen from (3.26), this order contributes to the local self-energy $\Sigma^{(0)}$ and, thus, the corrections manifest themselves as a coordinate-dependent shift to the effective mass. In other words, no scattering processes are included at LO.

Next-to-leading order: First interactions between different momentum modes appear only at NLO. This contribution consists of an infinite series of diagrams [123]. Those that involve only quartic and sextic vertices are shown in panel (b) of Fig. 3.9. The first row contains all diagrams without sextic vertices. It is the complete NLO contribution in the φ^4 theory and has been resummed in [70]. In the two lower rows, diagrams include at least one sextic vertex. The latter, whenever encountered, necessarily contains one closed bubble $G_{aa}(x,x)$ to compensate its additional factor of $1/N$, while the rest of its legs form the same propagator chains as in the first row. Note that the two diagrams appearing at LO are also encountered at NLO, however, with a different index structure, as explicitly shown in Fig. 3.9. The same analogy holds for the higher-order self-interactions.

To combine the diagrams of the first row with those containing higher-order vertices, it is convenient to introduce a coordinate-dependent "modified" coupling,

$$\widetilde{\lambda}(x;F) = \sum_{n=2}^{\infty} \frac{6(n-1)\lambda_{2n}}{(2n-1)!} \Big(F(x,x)\Big)^{n-2}. \tag{3.28}$$

which plays the role of the quartic coupling at NLO in presence of additional self-interaction. With this, the resummation of the NLO diagrams proceeds in the same way as for the φ^4 theory and yields [123]

$$\Gamma_2^{\mathrm{NLO}}[G] = \frac{i}{2}\,\mathrm{Tr}_C \ln[\widetilde{B}(G)], \tag{3.29}$$

where we have defined $\widetilde{B}(x,y;G) = \delta(x-y) + i\frac{\widetilde{\lambda}(x)}{6N}G^2(x,y)$, with $G^2(x,y) = G_{ab}(x,y)G_{ab}(x,y)$, and the logarithm sums the infinite series

$$\begin{aligned} \mathrm{Tr}_C \ln[\widetilde{B}(G)] = &\int_{x,C} i\,\frac{\widetilde{\lambda}(x)}{6N}\,G^2(x,x) \\ -\frac{1}{2}\int_{xy,C} &\Big(i\,\frac{\widetilde{\lambda}(x)}{6N}\,G^2(x,y)\Big)\cdot\Big(i\,\frac{\widetilde{\lambda}(y)}{6N}\,G^2(y,x)\Big) + \ldots\,. \end{aligned} \tag{3.30}$$

Remarkably, the NLO contribution to the effective action has the same structure as in φ^4 theory, with the only difference being that the quartic coupling λ is replaced by a modified coupling $\widetilde{\lambda}$. The modified quartic coupling $\widetilde{\lambda}$ is the only place where the details of the self-interactions enter. Inserting the expression for the couplings $\lambda_{2n} = (-1)^{n+1}\Lambda^4/f^{2n}$ in the sine-Gordon model and summing the series gives

$$\widetilde{\lambda}(x;F) = 3\frac{\Lambda^4}{f^4}\left[\frac{\cos\left(\sqrt{\frac{F(x,x)}{f^2}}\right)}{\frac{F(x,x)}{f^2}} - \frac{\sin\left(\sqrt{\frac{F(x,x)}{f^2}}\right)}{\left(\frac{F(x,x)}{f^2}\right)^{3/2}}\right]. \tag{3.31}$$

---

[4] In Eq. (3.27) we have used the fact that $\rho_{aa}(x,x) = 0$ and we have defined $F(x,x) = F_{aa}(x,x)/N$.

Resummed kinetic theory: With the expressions (3.27) and (3.29) at hand, the corresponding self-energies can be calculated using (2.35) and, thus, the 2PI equations of motion at that order can be derived. This derivation is presented in [1]. The 2PI equations can be further recast into the form a kinetic Boltzmann equation, as it was explained in section 2.3.4. Inserting the expressions for the self-energies into (2.49), the corresponding kinetic transport equations can be obtained. Again, referring to [1] and the references therein for the details of the calculation, here we present the final expressions.

The collision integral $C[n]$ coincides with the analogous expression for $2 \leftrightarrow 2$ scatterings in φ^4 theory and is given by [20]

$$C[n](t,\mathbf{p}) = \int d\Omega^{2\leftrightarrow 2}[n](t,\mathbf{p},\mathbf{q},\mathbf{r},\mathbf{l})[(n_\mathbf{p}+1)(n_\mathbf{l}+1)n_\mathbf{q}n_\mathbf{r} - n_\mathbf{p}n_\mathbf{l}(n_\mathbf{q}+1)(n_\mathbf{r}+1)], \tag{3.32}$$

with the shortcut notation $n_\mathbf{p} = n(t,\mathbf{p})$. Note that, being derived from 2PI equations, it automatically contains the Bose enhancement factors $n_\mathbf{p}+1$. The integration measure of the Boltzmann equation,

$$\int d\Omega^{2\leftrightarrow 2}[f](t,\mathbf{p},\mathbf{q},\mathbf{r},\mathbf{l}) = \int_{\mathbf{lqr}} \frac{\widetilde{\lambda}^2_{\text{eff}}(t,\mathbf{p},\mathbf{q},\mathbf{r},\mathbf{l})}{6N}(2\pi)^4\delta(\mathbf{p}+\mathbf{l}-\mathbf{q}-\mathbf{r})\frac{\delta(\omega_\mathbf{p}+\omega_\mathbf{l}-\omega_\mathbf{q}-\omega_\mathbf{r})}{2\omega_\mathbf{p}2\omega_\mathbf{l}2\omega_\mathbf{q}2\omega_\mathbf{r}}. \tag{3.33}$$

writing $\int_\mathbf{q} = \int d^3\mathbf{q}/(2\pi)^3$, involves δ-functions reflecting energy and momentum conservation, as well as the time- and momentum-dependent effective four-vertex,

$$\widetilde{\lambda}^2_{\text{eff}}(t,\mathbf{p},\mathbf{q},\mathbf{r},\mathbf{l}) = \frac{\widetilde{\lambda}^2(t;F)}{3}\left[\frac{1}{|1+\Pi_R(t,\omega_\mathbf{p}+\omega_\mathbf{l},\mathbf{p}+\mathbf{l})|^2} + \frac{1}{|1+\Pi_R(t,\omega_\mathbf{p}-\omega_\mathbf{q},\mathbf{p}-\mathbf{q})|^2} + \frac{1}{|1+\Pi_R(t,\omega_\mathbf{p}-\omega_\mathbf{r},\mathbf{p}-\mathbf{r})|^2}\right], \tag{3.34}$$

that is a consequence of the infinite series of 2PI diagrams at NLO (3.30)[5]. The "one-loop" retarded self-energy Π_R in (3.34) corresponds to two propagator lines and one modified coupling in this picture, i.e. a "chain link". It can be expressed as [25]

$$\Pi_R(t,\omega,\mathbf{p}) = \lim_{\epsilon\to 0}\frac{\widetilde{\lambda}(t;F)}{12}\int_\mathbf{q}\frac{n(t,\mathbf{p}-\mathbf{q})}{\omega_\mathbf{q}\omega_{\mathbf{p}-\mathbf{q}}}\left[\frac{1}{\omega_\mathbf{q}+\omega_{\mathbf{p}-\mathbf{q}}-\omega-i\epsilon} + \frac{1}{\omega_\mathbf{q}-\omega_{\mathbf{p}-\mathbf{q}}-\omega-i\epsilon} + \frac{1}{\omega_\mathbf{q}+\omega_{\mathbf{p}-\mathbf{q}}+\omega+i\epsilon} + \frac{1}{\omega_\mathbf{q}-\omega_{\mathbf{p}-\mathbf{q}}+\omega+i\epsilon}\right]. \tag{3.35}$$

Having found the corresponding Boltzmann equation, we now discuss its properties and implications for the scaling exponents of NTFPs. First we note that the form of the NLO collision term coincides with the one for the φ^4 theory, except for the replacement of the quartic coupling $\lambda \mapsto \widetilde{\lambda}(t;F)$. This is an important result, which explains the observed universality of the scaling exponents from the point of view of the resummed kinetic theory.

---

[5] Eq. (3.33) differs from the perturbative expression in φ^4 theory by the replacement $\widetilde{\lambda}^2_{\text{eff}} \to \lambda^2(N+2)/N$. The perturbative approach is however not expected to provide an accurate description of the time evolution of the highly occupied infrared modes.

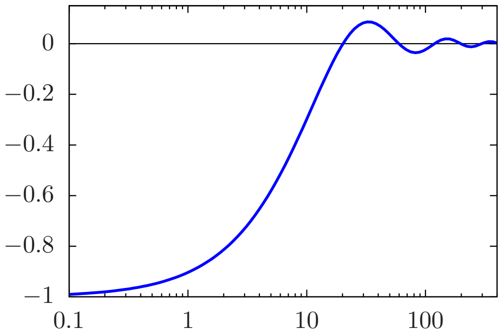

FIGURE 3.10: The shape of the modified quartic coupling $\widetilde{\lambda}$ from (3.31), divided by $\lambda = \Lambda^4/f^4$, as a function of the rescaled statistical propagator $F(x,x)/f^2$, and given by $3[\cos(\sqrt{x})/x - \sin(\sqrt{x})/x^{3/2}]$. Due to the negative sign of the quartic coupling in (3.5), the ratio $\widetilde{\lambda}/\lambda$ approaches minus one for $F \to 0$.

At high momenta, where the typical occupation numbers are not too large, $n \ll |\lambda|^{-1}$, such that $|\Pi_R| \ll 1$, the effective vertex is approximately $\widetilde{\lambda}^2_{\text{eff}} \approx \widetilde{\lambda}^2$. In this regime there is no dependence on the sign of the coupling in the kinetic equation, which is consistent with the observation that the dynamics of the direct cascade does not depend on that sign.

The situation is different at low momenta where, due to the large occupation numbers $n \sim |\lambda|^{-1}$, the retarded self-energy Π_R cannot be neglected anymore in the expression for $\widetilde{\lambda}^2_{\text{eff}}$. Since $\Pi_R \propto \widetilde{\lambda}(t;F)$ this also induces a dependence on the attractive or repulsive nature of the self-interactions into the kinetic equation, consistent with the observations from classical-statistical simulations.

The modified coupling for the sine-Gordon model (3.31) as a function of the statistical propagator is plotted in Fig. 3.10 and its shape has a simple interpretation. For weak fluctuations the modified coupling agrees with the coupling of the leading quartic self-interaction, which is negative in our model. In other words, the dominant interactions in this case are attractive. For large fluctuations, different interaction terms in the cosine potential "cancel each other", leading to weaker mean interactions, averaging to zero in the limit of $F \to \infty$.

3.4 Finding the lowest minimum

A common feature of field theories with quasiperiodic potentials is that the potential can contain several local minima. This allows scenarios in which the field is trapped in one of the false minima. In our considered model (3.1) the number of these minima increases with κ (see Fig. 3.1), while for small values of κ ($\kappa \lesssim 2.14554$) the only minimum is at $\varphi = 0$.

Having investigated the amplification and the subsequent dynamics of fluctuations in the previous sections, we now turn to the important question of how these processes impact the field's ability to overcome the barriers of the potential and to perform transitions between local minima. The following effects are expected:

- The energy transfer to fluctuations decreases the amplitude of the background field oscillations. This hinders the ability of the field to overcome potential barriers and can lead to trapping.

- The amplification of fluctuations modifies the effective potential exhibited by the background field ϕ. This can be demonstrated by taking the expectation value of the classical field equations of motion in the presence of statistical fluctuations,

$$\ddot{\phi} + m^2\phi + \frac{\Lambda^4}{f}\langle \sin\frac{\varphi}{f}\rangle = 0. \tag{3.36}$$

For the simple case when the fluctuations have a Gaussian distribution one arrives at

$$\langle \sin\Big(\frac{\varphi(t,\mathbf{x})}{f}\Big)\rangle = \sin\frac{\phi(t)}{f}\langle \cos\Big(\frac{\varphi(t,\mathbf{x})-\phi(t)}{f}\Big)\rangle = \sin\frac{\phi(t)}{f}\exp -\frac{F(t,t,\mathbf{x}-\mathbf{x})}{2f^2}, \tag{3.37}$$

where F is the equal-time statistical propagator, i.e.

$$\langle\varphi^2(t,\mathbf{x})\rangle - \phi^2(t) = F(t,t,\mathbf{x}-\mathbf{x}) = \int_{\mathbf{p}} F(t,t,\mathbf{p}), \tag{3.38}$$

This implies that the wiggles are smeared out by a factor of $e^{-F/2f^2}$ in the effective potential compared to the bare potential, which makes trapping more difficult. Note that the resulting equations of motion,

$$\ddot{\phi} + m^2\phi + \frac{\Lambda^4}{f}e^{-\frac{F}{2f^2}}\sin\frac{\phi}{f} = 0, \tag{3.39}$$

coincide with (2.40) in the linear regime.

The aim of this section is to understand the combined impact of the energy transfer from the background field to the fluctuations on getting trapped in a false minimum as well as on finding the way out of such a minimum. In the first two subsections we consider the situation when the background field is trapped in a local minimum from the beginning. The case of the field getting trapped in the course of its dynamics is discussed in the third subsection.

3.4.1 Resonance-enhanced transitions

In order to understand how the energy transfer to the fluctuations affects the ability of the field to overcome potential barriers, we consider the situation in which the background field oscillates around a false minimum from the beginning. In other words we choose the initial field value ϕ_0 to lie inside one of the potential wells. Our analysis of the dynamics is based on the classical-statistical description, which is applicable due to the large field values/occupation numbers.

It is worth mentioning that, if expansion of the spacetime is taken into account, a similar scenario of getting trapped in the linear regime can occur even if the initial field value is outside of any of the potential wells. Indeed, due to the "Hubble friction", the amplitude of oscillations decreases with time. This can lead to the field getting trapped at relatively early times and performing further oscillations around the corresponding local minimum.

In the presence of background oscillations, fluctuations are subject to an exponential amplification via the parametric resonance instability. In the case when the oscillations are around a false minimum there is typically one strong instability band at low momenta, $|\mathbf{p}|/m < \kappa$, as it was explained in section 3.2. We have performed simulations for different values of κ and ϕ_0/f, for which the field initially oscillates around one of the false minima. Remarkably, depending on the values of these parameters, in some of the simulations a transition to a lower minimum indeed took place, once the unstable fluctuations became sufficiently large.

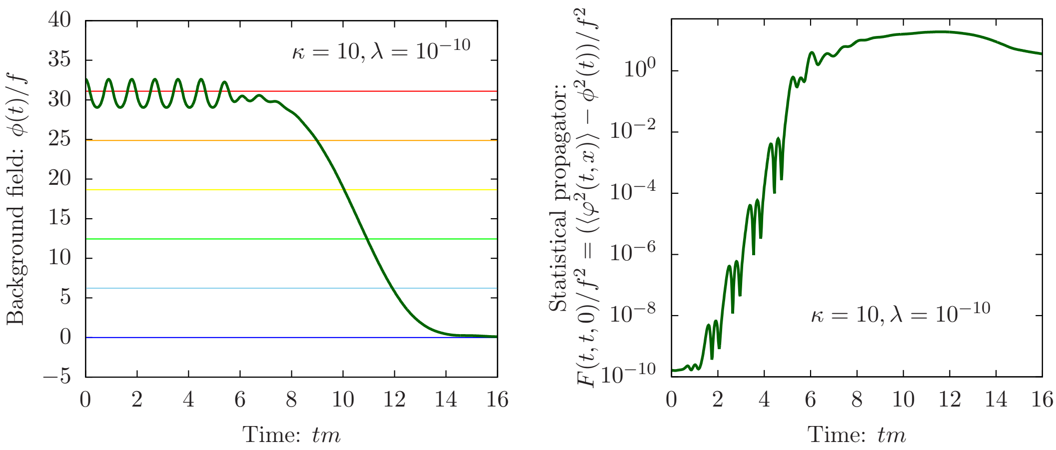

FIGURE 3.11: The evolution of the background field $\phi(t)/f$ (left plot) and the equal-time statistical propagator $F(t,t,0)/f^2 = (\langle\varphi^2(t,\mathbf{x})\rangle - \phi^2(t))/f^2$ (right plot). Different colors indicate the locations of different minima of the classical potential. Before the transition the background field oscillates around a false minimum and the fluctuations exhibit an exponential amplification. Bubbles are nucleated after $tm \approx 6$ and lead to a transition to the lowest minimum. We employ $\kappa = 10, \lambda = 10^{-10}$ and $\phi_0/f = 32.6$.

One such "resonance-enhanced" transition is illustrated in Fig. 3.11, where we used $\phi_0/f = 32.6$, $\kappa = 10$ and $\lambda = 10^{-10}$. In the left panel of that figure the time evolution of the background field $\phi(t)/f$ is shown. Different local minima of the classical potential are indicated by different colors. Initially the background field performs oscillations around the false minimum, indicated by the red line. In the right panel of Fig. 3.11 the equal-time statistical propagator from (3.38), integrated over all momentum-modes and divided by f^2 is shown. As one would expect, it exhibits an exponential growth due to the parametric resonance. At around $tm \approx 6$, when the fluctuations become nonperturbatively large, the background field starts to roll down from the local minimum all the way to $\phi = 0$.

In the example of Fig. 3.11, the background field settles in the lowest minimum after the transition, which is not always the case. Also, the background oscillations are absent after the transition in that example. Remarkably, if the potential energy of the local minimum, around which the field oscillates initially, is large enough, background oscillations around $\phi = 0$ can emerge after the transition. This is illustrated in Fig. 3.12, where the evolution of $\phi(t)/f$, starting from different local minima, is shown. It was observed, that the amplitude of these oscillations decays exponentially, in analogy to what was described in section 3.2.5. Also, the distribution function $n(t,\mathbf{p})$ enters the regime of the direct cascade after the transition, as it was described in section 3.3.2.

In the above-mentioned examples the initial amplitude of oscillations was chosen sufficiently large such that the background field started to roll down from the false minimum very soon. Decreasing the amplitude, the transition time increases and for small field values it is not observed at all in the simulations. Nevertheless, our analysis demonstrates a remarkable, far-from-obvious result: the net effect of the amplification of fluctuations is such that it enhances the field's ability to get out of a local minimum.

3.4.2 Explosive bubble nucleation

Even in the absence of the parametric resonance, the field cannot remain trapped in a false minimum forever and should eventually make a transition to the true minimum due to quantum tunneling [124, 125]. The transition from the false minimum is induced by nucleation of bubbles of the lower minimum and their subsequent expansion.

If the field in the false minimum is in a "vacuum" state, the bubbles are nucleated from quantum (vacuum) fluctuations. The phenomenon is similar to first-order phase transitions in statistical physics, which are instead controlled by thermal fluctuations. In the semi-classical approximation the probability of bubble nucleation per unit time per unit volume can be written as $\Gamma_{\text{nucl}} \sim e^{-B}$, where B represents the smallest Euclidean action of a configuration, in which the field bounces between the two vacua [124]. The potential energy, liberated inside the bubble, is stored dominantly in the walls. The bubbles grow in size and, eventually, fill the whole space, completing the transition.

An important feature of the considered scenario is that the field in the false minimum is in a nonequilibrium state, involving an oscillating background field and dynamically created "particle content". Importantly, we still observe the nucleation of bubbles in our simulations during the transition to the true minimum. Bubble-like field configurations are averaged out in the one-point function and, in order to observe them, we study the individual samples of the classical-statistical ensemble.

The nucleation and the subsequent dynamics of the bubbles is illustrated in Fig. 3.13, where snapshots of the field $\varphi(t, \mathbf{x})/f$ on a 2D slice at several times are shown. The colors here are chosen in correspondence with those in Fig. 3.11. In an individual run of classical-statistical simulations, parametric resonance manifests itself in the form of local inhomogeneities in position space, whose amplitude grows with time. Sufficiently large inhomogeneities start to grow in size after $tm \approx 6$, with field values of the lower minimum inside. This is how bubbles are

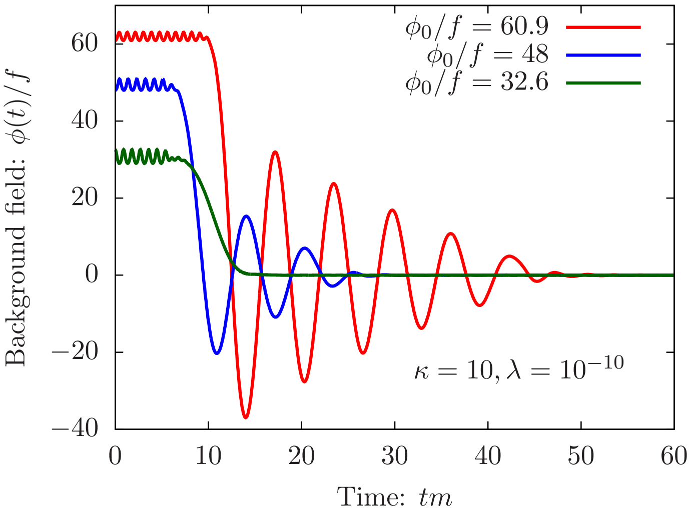

FIGURE 3.12: The evolution of the background field $\phi(t)/f$ with different initial values, corresponding to different local minima around which the initial oscillations take place. For larger values of ϕ_0/f decaying background oscillations emerge after the transition. We employ $\kappa = 10, \lambda = 10^{-10}$.

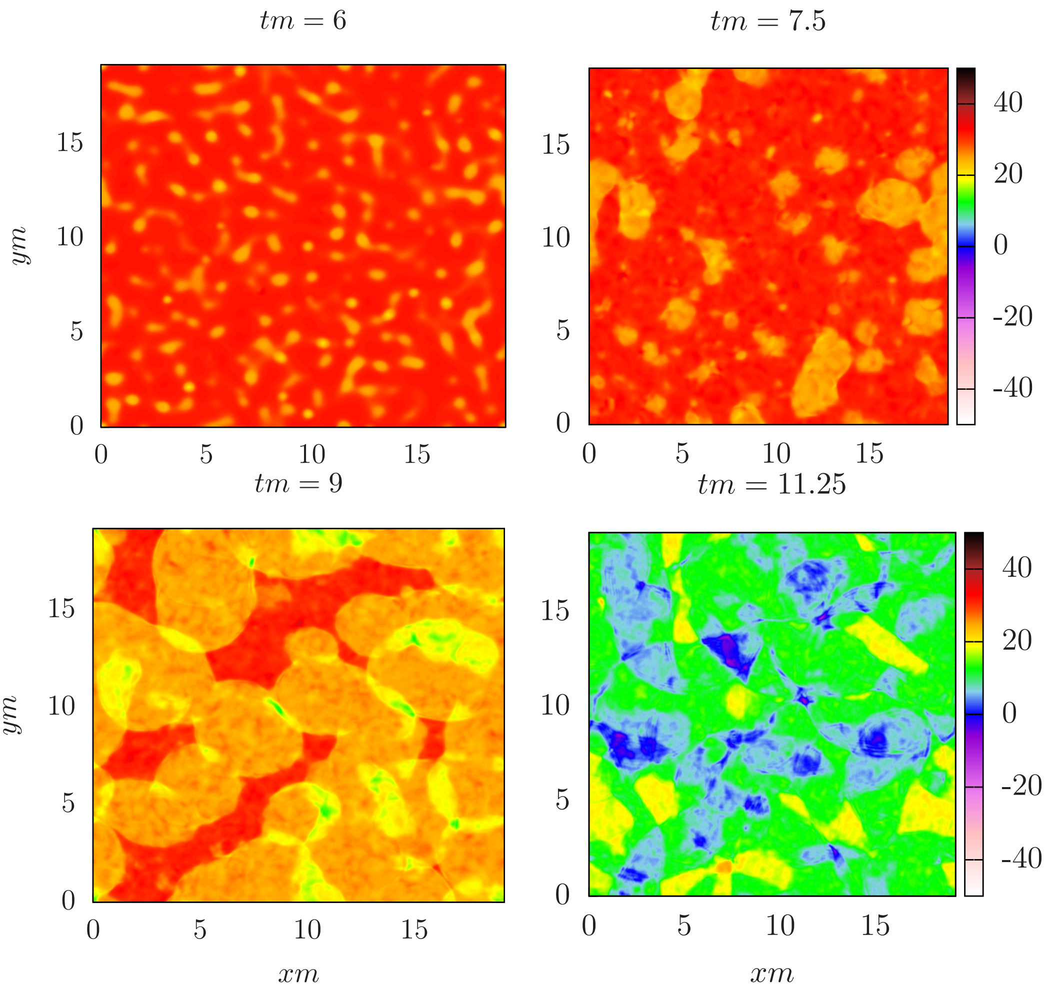

FIGURE 3.13: Several snapshots of the field $\varphi(t, \mathbf{x})$ at times $tm = 5.85$, 7.5 and 9 on a 2D slice from one simulation during the parametric resonance enhanced transition. We employ $\phi_0/f = 32.6$, $\kappa = 10$, $\lambda = 10^{-10}$. For an animation of the transition see here

nucleated in the classical-statistical regime. In the beginning the bubbles have irregular shapes, but become more spherical as they expand.

The "explosive" nucleation of bubbles in the considered regime is induced by the large fluctuations and occurs at the end of the parametric amplification, when the typical occupation numbers become $n \sim 1/\lambda$. As observed in the simulations, this mechanism of bubble nucleation can be extremely efficient and induce a fast transition from a false minimum. This is in contrast to the transitions from a vacuum state, where bubble nucleation is induced by purely quantum fluctuations and is therefore extremely suppressed. Moreover, such genuine quantum effects are neglected in the classical-statistical approximation. The latter becomes applicable in our case due to the large occupation numbers of the field in the false minimum (see also [126, 127] for the analysis of the false vacuum decay by means of classical-statistical simulations).

The rate of bubble nucleation depends on the shape of the potential as well as on the initial amplitude of the background oscillations around the false minimum. Remarkably, as a consequence of the nonequilibrium nature of the problem, this rate is also time-dependent as it is evident from the simulations. During the resonant amplification of fluctuations energy is being transferred from the coherent and homogeneous form into the inhomogeneous form of local over-densities. These over-dense regions in position space naturally allow for more efficient (local) bubble nucleation as compared to the homogeneous configuration. This explains why the probability of the transition increases on average[6] in the course of the resonant amplification of fluctuations, and reaches its maximum when the fluctuations become of the order $1/\lambda$.

One interesting feature of the considered model is that the minimum, in which the field is trapped, can be separated from the lowest one by one or more local minima and, thus, by more than one potential barrier. Nucleation of bubbles of the neighboring local minimum is the most likely, since it requires the smallest bounce action. Such bubbles are seen in Fig. 3.13, where the yellow color denotes the corresponding minimum. What can also be seen in that figure is that the overlap regions of the bubbles in some cases turn into bubbles of even lower minima. To understand this note that when two such bubbles collide, the gradient energy of the walls in this overlap region is transformed into kinetic energy. If this additional energy is sufficient, it can lead to the field jumping to an even lower minimum in the overlap region. In this case a "bubble"of that lower minimum is nucleated "classically", from the wall collisions [129]. Directly after nucleation such a bubble does not have a spherical shape, but becomes more spherical as it expands. Eventually, nucleated this way bubbles collide with each other and such nucleation events repeat. For an animation of the transition see here.

3.4.3 Getting trapped

So far we have considered the scenario of the field being trapped in a false minimum from the beginning[7]. Here we are interested in the possibility that the field gets trapped dynamically, due to the transfer of energy to the fluctuations. We thus choose the initial conditions such that the background field initially oscillates around $\phi = 0$. By getting trapped the interruption of such oscillations for at least some time is meant.

Remarkably, in most cases the amplitude of background oscillations decreases to zero without the field getting trapped in any of the false minima. This can be attributed to an efficient smearing out of the wiggles in the presence of strong fluctuations. Exceptions occur for relatively small initial amplitudes, $\phi_1/f \lesssim \kappa^2$, for which the oscillations from the beginning take place in the region with pronounced wiggles and local minima.

Finally in some cases, although very rare, the field gets trapped and performs a transition after a short time in the lattice simulation. One such situation is shown in Fig. 3.14, where the parameters $\phi_0/f = 8.17$, $\kappa = 4.5$ and $\lambda = 10^{-6}$ were used. In the left panel the time evolution of the background field is plotted, with different colors representing different minima of the classical (bare) potential. As can be seen, the field gets trapped at $tm \approx 11$.[8] In the right panel, we plot the fraction $\mathcal{N}(t)$ of the runs, in which the transition to a lower minimum did not occur yet, as a function of time. For simplicity, we have identified for a given run the transition time as the

---

[6] Quantum tunneling in the presence of an oscillating background field was studied in [128]. An important consequence is the time-dependence of the bubble nucleation rate $\Gamma_{\text{nucl}}(t)$ within the oscillation period, i.e. the nucleation rate is maximal when the field is in its extremum.

[7] Or, in an expanding universe, the field gets trapped before significant amplification of fluctuations has taken place

[8] Note that due to the presence of strong fluctuations at these times, the minima of the effective potential do not coincide with those of the classical potential.

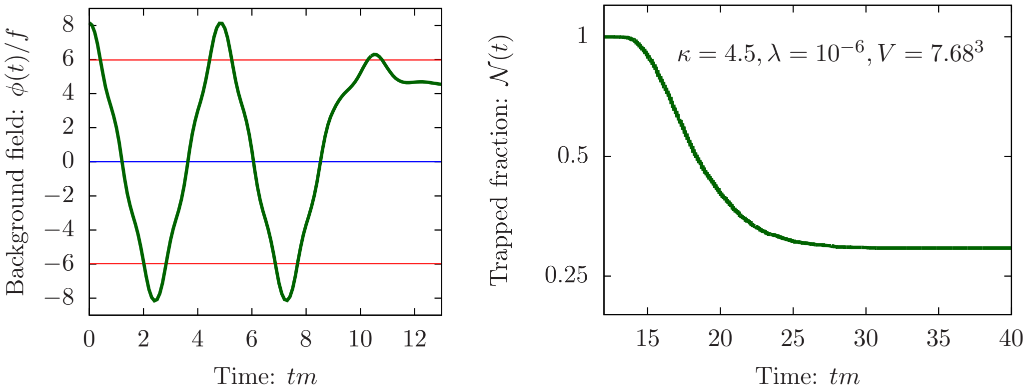

FIGURE 3.14: The time evolution and trapping of the background field ϕ_0/f (left), and the fraction of the runs, still trapped in the false minimum, as a function of time (right) , demonstrating how the transition probability decreases with time. Trapping occurs at $tm \approx 11$. Values of parameters $\phi_0/f = 8.17$, $\kappa = 4.5$ and $\lambda = 10^{-6}$ were used.

time at which the volume-averaged field in that run became smaller than $\phi' = 1.5$. In some simulations the field remains trapped. This is, however, a finite-volume effect and in the $V \to \infty$ limit the trapped fraction at late times should decrease to zero.

3.5 Summary

In this chapter we studied the amplification of quantum fluctuations in the presence of an oscillating background field, in scalar field theories with quasiperiodic potentials. Although the massive sine-Gordon model was used for our analysis, most of the results, obtained in this chapter, are applicable to more general scalar field theories with similar potentials.

The dynamics can be split into two stages. The first stage is characterized by a rapid, exponential amplification of fluctuations with certain momenta via instabilities. We have explained the main differences of this process in our system as compared to more common field theories with monomial potentials, including the amplification of fluctuations with ultrarelativistic momenta. In the second stage slower dynamics sets in, involving turbulent cascades in momentum space with universal scaling behavior. Remarkably, the main features of the dynamics, including the values of the scaling exponents of these NTFPs, are not different compared to those for more common scalar models and, in general, are insensitive to the details of the potential. We have also derived the 2PI equations of motion based on a $1/N$ expansion to NLO for our model, which can be used to study the dynamics in regimes beyond the regime of weak coupling and large occupation numbers.

Our studies demonstrate that dynamical effects play a crucial role in such systems. In particular, the growth of fluctuations should be taken into account for the transitions between local minima, when calculating the rate of bubble nucleation. Moreover, the transitions themselves should be studied in a dynamical setting, as they can involve the nucleation of bubbles of different local minima within the same transition, with colliding bubbles nucleating new bubbles of even lower minima.

We also studied how the energy transfer from the background field to the fluctuations impacts the field's ability to overcome the barriers of the potential. In recent works [130, 131] it has been argued, based on a linearized analysis, that particle production due to the wiggly shape of the potential can lead to effective "stopping" of the rolling field. This was done in the context of the relaxion mechanism. Our analysis indicates that these results should be at least revisited from the point of view of full nonlinear dynamics and that the growth of fluctuations can prevent the field from stopping at a local minimum. The question of getting trapped is important also for estimating the final abundance of the fields in the universe, as in the DM scenario, which is discussed in the next chapter.

Chapter 4

Nonperturbative production of axion-like particle dark matter

The content of this chapter is based on the work in collaboration with Jürgen Berges and Joerg Jaeckel, that has been published in [2]. In that work I did the main computations and most of the writing of the script. The figures and a significant part of the text in this chapter and in the appendix B are taken from that reference.

The previous chapter was devoted to the investigation of the rich dynamics of axion-like fields with weakly broken discrete shift symmetries i.e. in the presence of a monodromy. The potential typically features a number of "wiggles" that lead to rapid growth of fluctuations. In this chapter we investigate the role of such fields in cosmology as DM candidates and study the consequences of their nonlinear dynamics.

As it was discussed in [56], in the presence of a monodromy the couplings of ALP DM to the SM particles can be larger (see also section 2.2.2). Using classical-statistical field theory simulations on an expanding FRW spacetime, we go beyond the linear regime of [56] and treat the system in the nonlinear and, even, the fully nonperturbative regime. For a wide range of parameters the initially homogeneous field is completely converted into fluctuations, which correspond to DM particles with a nonvanishing velocity. We find three important features.

- These particles are relativistic in the beginning. However, for the most masses ($m_a \gtrsim 10^{-15}\,\mathrm{eV}$) they cool down sufficiently by matter-radiation equality and remain fully viable as CDM.
- The reduction in total energy density of ALPs due to this relativistic intermediate phase is relatively small.
- The density fluctuations are typically of order one. However, their typical length scales are much smaller than those expected for the formation of gravitationally bound objects i.e. axion miniclusters [74] (cf. also e.g. [72, 73, 132, 133]). At these small scales the localization of a small mass requires them to have a nonvanishing momentum and the resulting pressure prevents the gravitational collapse. Instead of miniclusters with huge overdensities, the density of DM therefore features large, $\mathcal{O}(1)$ fluctuations at scales $\sim (10^3 - 10^6)\,\mathrm{km}\sqrt{\mathrm{eV}/m_a}$.

The chapter is organized as follows. Section 4.1 gives an overview of the misalignment production of ALP DM and outlines the novel effects due to monodromy. In section 4.2 we study the dynamics of vacuum realignment and the growth of fluctuations in the presence of monodromy. We determine the impact of the fluctuations on the equation of state and on the energy density of DM in section 4.3, where we also consider the corresponding restrictions based on large-scale structure probes. The ALP density power spectrum and the fate of the overdensities are discussed in section 4.4. We conclude in section 4.5.

4.1 ALPs as dark matter and monodromy

Standard ALPs are known to be good candidates for DM if they are produced non-thermally in the early universe, via the so-called misalignment mechanism [26–29]. In the simplest case of this mechanism, the axion-like field is present already during inflation. After inflation it obtains some value ϕ_1, practically homogeneous throughout the observable universe. The field performs coherent oscillations around the minimum of the potential, once the Hubble parameter drops below its mass. The amplitude of oscillations decreases due to the expansion and, because of the conventional "cosine" form of the potential (2.2) for standard ALPs, very soon oscillations take place in the almost quadratic region of the potential. As a result, the field behaves exactly as ordinary matter and, in particular, dilutes according to $\rho \propto a^{-3}$. The final energy density of ALPs today can be expressed in terms of their mass m_a and the misalignment field value ϕ_1 as [26]

$$\rho_0 \approx 0.17\,\frac{\mathrm{keV}}{\mathrm{cm}^3}\sqrt{\frac{m_a}{\mathrm{eV}}}\left(\frac{\phi_1}{10^{11}\mathrm{GeV}}\right)^2. \tag{4.1}$$

Here m_a denotes the mass near the bottom of the potential, which is given by (2.3). It will be assumed in this chapter that ALPs account for the whole DM content of the universe. In that case this quantity can be compared with the observed average DM density today, $\rho_{\mathrm{CDM}} \approx 1.27\,\mathrm{keV}/\mathrm{cm}^3$ [10]. We will return to the derivation of (4.1) in section 4.3.

The periodic potential of ALPs limits their field range to $|\phi_1| < \pi f$. Therefore, assuming that ALPs make up all of DM puts, for a given ALP mass m_a, a lower bound on the decay constant f or, equivalently, an upper limit on all couplings that are proportional to $\sim 1/f$ [26]. This includes the ALP-photon coupling,

$$\mathcal{L}_{\mathrm{int}} = -\frac{1}{4} g_{a\gamma\gamma}\varphi F^{\mu\nu}\tilde{F}_{\mu\nu}, \qquad g_{a\gamma\gamma} = c_{a\gamma}\frac{\alpha}{4\pi f}, \tag{4.2}$$

where the prefactor $c_{a\gamma}$ is usually of the order of one.

As it was mentioned in section 2.2, an important effect in the presence of a monodromy is that there is no constraint $\phi_1 < \pi f$ and the potential is not bounded from above. This allows one to bypass the limitation for standard ALPs and to have ALP DM with larger couplings [56]. This is the scenario that is investigated in more detail in this chapter.

As it was already noted in [56] and discussed in greater details in the previous chapter, the evolution of the field with such a potential can lead to rapid growth of fluctuations, even if the field was initially homogeneous as expected when the field is already present during inflation. This is how this type of monodromy DM differs decisively from the ordinary ALP DM, where the field and the corresponding density remain essentially homogeneous until the structure formation sets in.

In the next sections we use classical-statistical simulations in an expanding spacetime to study the full nonlinear dynamics of such ALP DM and determine phenomenological consequences of it.

4.2 The dynamics of vacuum realignment

Our starting point is the monodromy potential (3.1) where the discrete shift symmetry of ALPs is broken by a quadratic monomial. In an expanding FRW universe the classical equations of motion in comoving coordinates read

$$\ddot{\phi} + 3H\dot{\phi} - \frac{\Delta\phi}{a^2} + \frac{\delta U}{\delta\phi} = 0, \tag{4.3}$$

where $a(t)$ is the scale factor and $H = \dot{a}/a$ is the Hubble parameter.

4.2.1 Initial conditions

In the following we consider the scenario where the axion-like field is already present during inflation [26]. The initial condition after inflation is then given by,

$$\phi(x) = \phi_1 = \text{const}, \tag{4.4}$$

that is constant throughout the entire observable universe. The subsequent evolution of $\phi(t)$ is governed approximately by (4.3), where the gradient term can be neglected due to homogeneity. The field is initially overdamped, $\partial_t\phi = 0$, and only starts to oscillate once the Hubble friction term becomes comparable to the potential term in the equations of motion. This happens, approximately, when

$$H = H_{\text{osc}} = \frac{m_a}{3},$$

although it can be delayed due to the wiggly structure of the potential depending on the value of ϕ_1. For later use, we denote the corresponding scale factor by a_{osc}. Here m_a denotes the bare mass around the global minimum of the monodromy potential (3.5), that is given by,

$$m_a^2 = \frac{\delta^2 U}{\delta\phi^2}\bigg|_{\phi=0} = m^2 + \frac{\Lambda^4}{f^2} = m^2(1+\kappa^2). \tag{4.5}$$

In addition we introduce a rescaled dimensionless comoving momentum

$$\eta = \frac{\mathrm{p}}{m_a a_{\text{osc}}}, \tag{4.6}$$

that will be frequently used in this work.

ALPs that are expected to behave as CDM should start to oscillate prior to the epoch of matter-radiation equality at $H_{\text{eq}} = 2.3 \times 10^{-28}\text{eV}$. The constraints from structure formation (for standard ALPs), including the Lyman-α forest data require $m_a \gtrsim 10^{-21}$ eV [31, 143, 144]. Moreover, $\phi_1 \gg H_I$ must hold if ALPs are present during inflation in order to avoid strong isocurvature fluctuations [26, 137, 145]. For moderate misalignment angles this therefore implies $f \gg H_I$.

So far we have discussed the initial conditions and the evolution of the homogeneous background field. However, as already mentioned, due to their growth fluctuations are highly relevant in the case of monodromy potentials. In general all fields feature unavoidable quantum fluctuations which, in Minkowski spacetime, have the form given by Eq. (2.36). For ALPs all momentum modes, that are relevant for the fragmentation dynamics, were stretched to superhorizon sizes during inflation and, as a consequence, are amplified compared to the subhorizon modes. More precisely, as $m_a \ll H_I$, the ALP can be treated as massless during inflation. Quantum fluctuations of a massless scalar field in the de-Sitter spacetime are known to have an approximately scale-independent field power spectrum (cf. e.g. [81]),

$$\Delta_\varphi = \left(\frac{H_I}{2\pi}\right)^2. \tag{4.7}$$

Here, the power spectrum can be defined from the statistical propagator,

$$\begin{aligned} \frac{1}{2}\langle\{\hat{\varphi}_{\mathbf{p}}(t), \hat{\varphi}_{\mathbf{p}'}(t')\}\rangle|_{t'=t} &= (2\pi)^3\delta^{(3)}(\mathbf{p}+\mathbf{p}')F(t,t',\mathbf{p})|_{t'=t} \\ &= (2\pi)^3\delta^{(3)}(\mathbf{p}+\mathbf{p}')\frac{2\pi^2}{\mathrm{p}^3}\Delta_\varphi(t,\mathbf{p}). \end{aligned} \tag{4.8}$$

In other words, the early universe inflation imprints Hubble sized fluctuations in the axion-like field. After inflation, all momentum modes of interest are superhorizon and remain frozen, $\partial_t F(t,t',\mathbf{p}) = 0$, until they re-enter the horizon.

The self-interactions of ALP DM are very weak i.e. $\lambda \ll 1$. Moreover, the ALP fluctuations are initially suppressed compared to the background field, $\delta\varphi \ll \phi_1$. This implies that all stages of the evolution that are of interest to us can be well described by means of the classical(-statistical) approximation, as it was explained in section 3.2.1 of the previous chapter.

4.2.2 Amplification of fluctuations: linear regime

Having set the stage we now turn to the behavior of the fluctuations which form the core of this chapter.

Treatment of fluctuations: As it was already mentioned, the inflation imprints fluctuations in the ALP field of the order $\delta\varphi \sim H_I$. Since $H_I \ll f$ holds, these initial fluctuations are much smaller compared to the scale $\delta\varphi \sim f$ at which nonlinearities set in. Therefore, initially, the dynamics can be studied by means of linearized equations of motion, as it was done in section 3.2.2. This is conveniently done in terms of conformal variables,

$$\hat{\varphi}_{\mathrm{c}} = a\hat{\varphi}, \qquad d\tau = \frac{dt}{a}. \tag{4.9}$$

The linearized equations for the momentum modes of the statistical propagator $F_{\mathrm{c}}(\tau,\tau',\mathbf{p}) = a(t)a(t')F(t,t',\mathbf{p})$ then take the form [146]

$$\left[\partial_\tau^2 + \mathbf{p}^2 + a^2m^2\left(1+\kappa^2\cos\frac{\phi}{f}\right) - \frac{1}{a}\frac{d^2a}{d\tau^2}\right]F_{\mathrm{c}}(\tau,\tau',\mathbf{p}) = 0, \tag{4.10}$$

where p is the comoving momentum, related to the physical one by $\mathrm{p}_{\mathrm{phys}} = \mathrm{p}/a$. The above expression differs from the Minkowski analogue, which was considered in the previous chapter, only by the a-dependent modification of the effective mass. To study the growth of fluctuations we have solved (4.10) numerically, for a wide range of momenta, together with the classical[1] evolution equation for the

---

[1] The backreaction of the fluctuations on the background field is negligible at this stage

background field $\phi_c(\tau) = a(t)\phi(t)$,

$$\partial_\tau^2 \phi_c + \Big(a^2 m^2 - \frac{1}{a}\frac{d^2 a}{d\tau^2}\Big)\phi_c + a^3 \frac{\Lambda^4}{f} \sin\Big(\frac{\phi_c}{af}\Big) = 0. \tag{4.11}$$

For the scale factor in a radiation-dominated universe we have taken [80]

$$a = \sqrt{1 + 2H_i(t - t_i)} = 1 + H_0(\tau - \tau_i), \tag{4.12}$$

which in addition to $a(t) \sim t^{1/2}$ fixes $a(t_i) = 1$ and $H(t_i) = H_i$. Here the i-index corresponds to the initial time of the simulation and H_0 is the value of the Hubble parameter at that time. One can check from (4.12) that the terms containing second derivatives of the scale factor in (4.10) and (4.11) vanish for a radiation-dominated expansion. To properly account for the horizon re-entry of all modes of interest, we have chosen H_i to be of the same order as the largest momentum of the modes. For ϕ and F we have employed the set of initial conditions described in the previous section.

In terms of the conformal variables the occupation numbers can be defined completely analogous to the case of Minkowski spacetime (2.28) (see also [146]),

$$n(t(\tau), \mathbf{p}) + 1/2 = \sqrt{F_{\rm c}(\tau, \tau', \mathbf{p})\partial_\tau \partial_{\tau'} F_{\rm c}(\tau, \tau', \mathbf{p})}|_{\tau'=\tau}. \tag{4.13}$$

Defined in this way, these are occupation numbers per comoving volume and, therefore, for sub-horizon modes, they do not change due to the expansion. This is different for super-horizon modes. In this case the occupation number grows with time, which is a consequence of the Hawking radiation emitted from the horizon [147]. This is the effect that accounts for the amplification of fluctuations during inflation.

When solving the evolution equations numerically, all dimensionful quantities are expressed in units of m, and the decay constant is rescaled out from the equations after the transformation $\phi \to \phi/f$. As a result the dynamics depends only on the values of three dimensionless parameters: κ, ϕ_1/f and H_I/f, with the latter determining the initial strength of the fluctuations.

Growth of fluctuations: Having set up the technique to deal with the fluctuations in the linear regime let us now return to physics. For small values of $\kappa \ll 1$ the evolution proceeds essentially as for a quadratic potential, i.e. a free field. The dynamics is dominated by the behavior of the homogeneous field. We are, however, more interested in the case where the potential has stronger "wiggles". As a benchmark case we take $\kappa = 10$. The initial condition for the field and its fluctuations can be specified by fixing the initial field value as well as the Hubble scale. Here we take $\phi_1/f = 1000$ and $H_I/f = 10^{-10}$.

The evolution of the background field in the linear regime is straightforward. It starts to oscillate around $a_{\rm osc}$ and then it is damped by the Hubble friction as can be seen in Fig. 4.1, where the linear regime extends up to $a < 19\, a_{\rm osc}$.

The behavior of fluctuations is more interesting. Once the background field starts to oscillate, fluctuations are subject to a parametric resonance instability. [2]

---

[2] We do not consider the production of SM particles arising due to their coupling to the ALP field. For sufficiently weak couplings this should be a small effect. For example, for the case of a photon coupling the relevant parameter for the growth of fluctuations is $g_{a\gamma\gamma}\phi \sim \alpha\phi/(2\pi f)$, which is $\lesssim 1$ in our case. Significant growth is expected only if it is $\gtrsim 10$ [148–151].

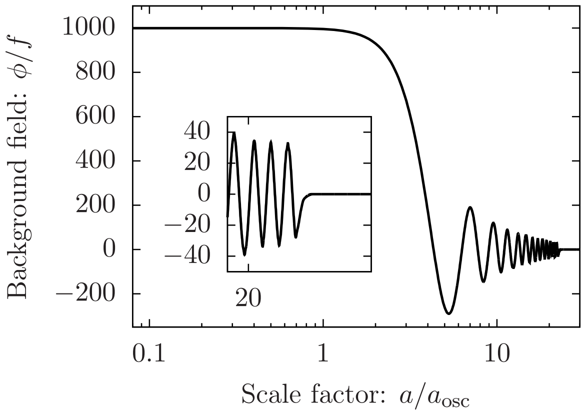

FIGURE 4.1: The evolution of the background field $\phi(t)/f$ as a function of the scale factor $a(t)/a_{\rm osc}$, demonstrating the transition from the "overdamped" to the oscillatory phase, as well as the collapse of the background field in the nonperturbative regime with strong fluctuations. The collapse, which occurs at $a \approx 22a_{\rm osc}$, is shown with a better resolution in the inset. We employ $\phi_1/f = 1000$, $\kappa = 10$ and $H_I/f = 10^{-10}$.

The resonance, in the absence of the expansion, was studied in the previous chapter, as well as in [56] and was shown to exhibit a number of instability bands. The same holds in the presence of the expansion. However, there are two essential modifications. The first is that the amplitude of the oscillations of ϕ decreases with time due to the expansion, thus the effective mass of the fluctuations in (4.10) is not strictly periodic. Second, in terms of conformal variables, the expansion causes an increase of characteristic mass scales in (4.10) proportional to the scale factor, reflecting the red-shift of physical momenta.

In Fig. 4.2 we plot the linear evolution of several momentum modes of the two-point function $F(t, t_0, \mathbf{p})$, defined in (4.8). After the horizon re-entry the modes start to oscillate with an amplitude decreasing with the expansion. As expected, modes with higher momenta re-enter the horizon earlier. Once a mode enters an

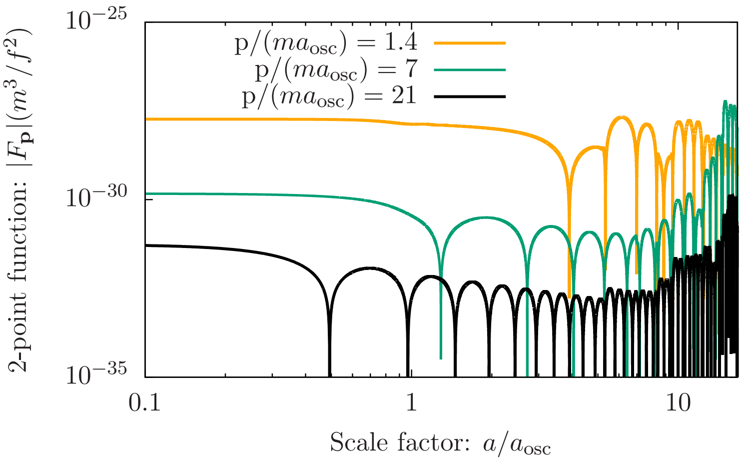

FIGURE 4.2: The linear evolution of absolute values of several momenta modes of the statistical propagator $|F(t, t_0, \mathbf{p})|(m^3/f^2)$ as a function of the scale factor $a(t)/a_{\rm osc}$, demonstrating the horizon re-entry of the modes, as well as their subsequent enhancement due to instabilities. We employ $\phi_1/f = 1000$, $\kappa = 10$ and $H_I/f = 10^{-10}$.

instability band it starts to grow until the continuing red-shifting moves it out of the instability band again. Such intermittent growth can be observed in Fig. 4.2. The intermittent nature is most apparent in the high momentum mode shown in black. The wider is the instability band the more time is spent by the mode to grow. Therefore the high-momentum narrow instability bands are less efficient compared to the lowest-momentum bands, where usually the dominant growth occurs.

4.2.3 Amplification of fluctuations: beyond the linear regime

The linear approximation becomes inaccurate once fluctuations become sufficiently large. The condition for the first nonlinear corrections becoming important can be determined in an analogous way to the case of Minkowski spacetime, that was discussed in the previous chapter, with a difference that initially $F \sim \mathcal{O}(H_I^2)$. This implies that secondary instabilities set in when parametrically $F \sim \mathcal{O}(H_I f)$ for the strongest resonant modes. This can be understood by comparing the stable modes to the one-loop correction $\sim \lambda F_{\text{res}}^2$. Secondaries result in a broader and smoother spectrum of fluctuations in the momentum space. The dynamics becomes nonperturbative if $F \sim \mathcal{O}(f^2)$. In this stage the background field transfers its energy to the fluctuations until it completely decays.

Simulating the nonlinear regime: To study the dynamics beyond the linear regime we have performed classical-statistical lattice simulations in an expanding FRW universe. We have developed a C++ program, similar to LATTICEEASY [152]. It solves the classical equations of motion, using conformal variables, in terms of which the expansion manifests itself only via the time-dependence of the mass scales. Red-shifting restricts the lattice simulations to not too late times, such that the mass scale is still within the resolution of the lattice. Our program first solves the linearized equations without taking into account their back-reaction on the background field. Before the fluctuations become nonlinear, i.e. secondary instabilities set in, we switch to the lattice simulation. The field configuration obtained from the linear evolution is used as an initial condition for the lattice simulation according to (2.52). This allows us to partially avoid running out of lattice points due to the rapid red-shifting at early times[3] and to evolve the field for longer times. We have used cubic lattices with up to 1024^3 points, periodic boundary conditions, and a fixed comoving volume.

Like in the linear regime, the dynamics in terms of rescaled dimensionless quantities depends only on the parameters κ, ϕ_1/f and H_I/f.

Evolution in the nonlinear regime: We now discuss the behavior in the nonlinear regime. The ALP field gets diluted with time due to the expansion. After some time it explores the approximately quadratic region of the potential near its minimum. Self-interactions become extremely weak at this stage and the evolution of the occupation numbers slows down. For small values of ϕ_1/f, such "freezing" of the spectrum happens already after a couple of oscillations of the background field, which allows ignoring the growth of fluctuations. This is the case for standard ALPs, for which the constraint $\phi_1/f < \pi$ holds. In the presence of a monodromy the value of ϕ_1/f can be larger and, therefore, the occupation numbers can become large before they "freeze".

---

[3] Note that the expansion happens most rapidly at early times.

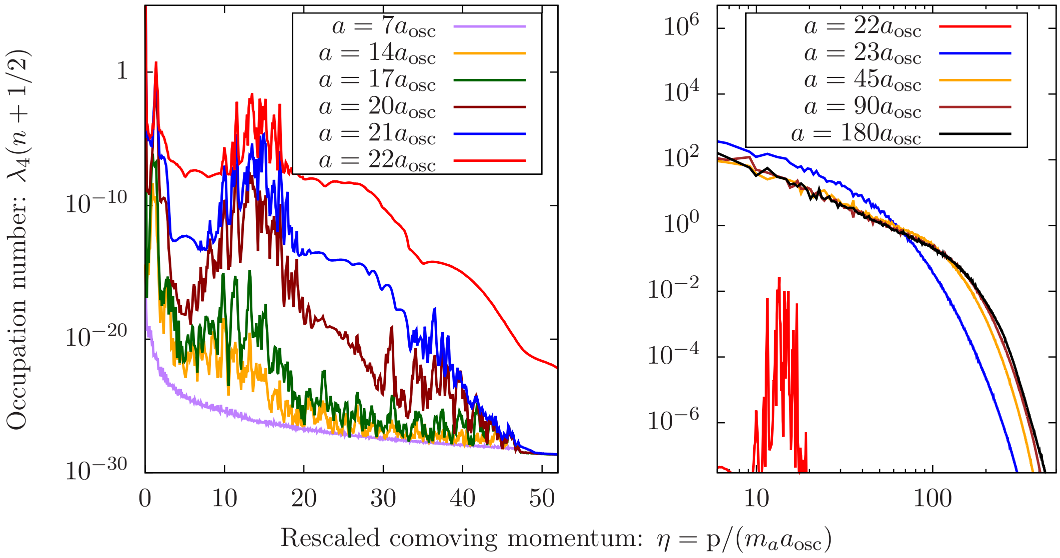

FIGURE 4.3: Several snapshots of occupation numbers at different scale factors. We employ $\phi_1/f = 1000$, $\kappa = 10$ and $H_I/f = 10^{-10}$.

Looking at the background field we observe a rapid drop of the amplitude to zero at $a/a_{\rm osc} \approx 23$. This arises when the fluctuations become sufficiently large and their growth rapidly extracts the energy from the background field.

The evolution of the fluctuations can be best understood in terms of the occupation numbers (4.13). The occupation numbers at different times are shown in Fig. 4.3. At first we see the expected growth of fluctuations. We note that the broad bands in the left plot at intermediate times, $19 < a/a_{\rm osc} < 22$, are a result of secondary instabilities, that were discussed in the previous chapter.

Once the background field has collapsed we observe a smooth direct cascade towards higher momenta, for $a/a_{\rm osc} > 23$. This is the self-similar energy cascade, that was studied in section 3.3.2 of the previous chapter. However, at later times the present cascade extremely slows down due to the dilution from the expansion. Indeed, when the density decreases interactions slow down the evolution and the occupation numbers effectively freeze out and only continue to red-shift. In terms of comoving momenta this simply means that the distribution of the occupation numbers remains constant as can be seen by comparing the late-time brown and black curves. The effect of "freezing" is investigated in great detail in the next chapter.

4.3 Structure formation, the equation of state and today's energy density

In the previous section we described how the field evolution through the wiggly regions causes a massive growth of fluctuations and, in particular, of fluctuations with rather high momenta. As can be seen from Fig. 4.3, the rescaled comoving momenta can be as high as $\eta \sim 100\, m_a$. Taking into account the expansion the physical momenta are still ultrarelativistic, $\mathrm{p}_{\rm phys} \sim 10\, m_a$. This raises two questions:

- Will the particles be sufficiently nonrelativistic to allow a successful structure formation?

- How much of the gain in the energy density from increasing ϕ_1 is lost due to the faster dilution of the energy density for relativistic species?

In this section we address these questions.

4.3.1 Viability as DM

We start with the question about the structure formation and the requirement for ALPs to be sufficiently cold at the matter-radiation equality. Below we estimate the typical velocities of ALPs at the matter-radiation equality and compare them to those of (allowed) warm DM.

The (nonrelativistic) velocity of the ALP at the matter-radiation equality,

$$\mathrm{v}_{\mathrm{eq}} = \frac{\mathrm{p}}{m_a a_{\mathrm{eq}}} = \eta \frac{a_{\mathrm{osc}}}{a_{\mathrm{eq}}},$$

is related to its co-moving momentum η via

$$\mathrm{v}_{\mathrm{eq}} = 2.63\,\eta \sqrt{\frac{10^{-28}\mathrm{eV}}{m_a}\,\frac{\mathcal{F}^{1/3}(T_{\mathrm{osc}})}{\mathcal{F}^{1/3}(T_{\mathrm{eq}})}}. \tag{4.14}$$

To derive this expression we used the conservation of comoving entropy [80],

$$\frac{a_{\mathrm{osc}}}{a_{\mathrm{eq}}} = \frac{T_{\mathrm{eq}}}{T_{\mathrm{osc}}}\left(\frac{g_{s,\mathrm{eq}}}{g_{s,\mathrm{osc}}}\right)^{1/3}, \tag{4.15}$$

for the ratio of the scale factors. Also, the temperature in the radiation-dominated universe can be expressed as

$$T = \sqrt{\frac{H M_{\mathrm{Pl}}}{1.66\sqrt{g}}}, \tag{4.16}$$

with $H_{\mathrm{eq}} = 2.3 \times 10^{-28}$eV and $H_{\mathrm{osc}} = m_a/3$. The numbers of effective degrees of freedom in the early universe $g(T)$ and $g_s(T)$, related to energy and entropy densities, can be found in [153] and are shown in Fig. 4.4. The dimensionless factor

$$\mathcal{F}(T_{\mathrm{osc}}) = \left(\frac{g_{s,0}}{g_{s,\mathrm{osc}}}\right)\left(\frac{g_{\mathrm{osc}}}{g_0}\right)^{3/4} \tag{4.17}$$

takes values between 1 and 0.3, reflecting the change of the effective numbers of degrees of freedom between a_{osc} and a_0 [26].

As can be seen in Fig. 4.3, the evolution of the ALP occupation numbers expressed in comoving momenta freezes at around $a \sim 100 a_{\mathrm{osc}}$. This is due to the drop in interaction rates resulting from the dilution by the Hubble expansion. From then on we can take the spectrum to be essentially frozen. The highest significantly occupied comoving momentum is of the order $\eta_{\mathrm{max}} \gtrsim 100$. Inserting this into (4.14) we arrive at

$$\mathrm{v}_{\mathrm{eq,max}} \sim 10^{-3}\sqrt{\frac{10^{-15}\,\mathrm{eV}}{m_a}\,\frac{\mathcal{F}^{1/3}(T_{\mathrm{osc}})}{\mathcal{F}^{1/3}(T_{\mathrm{eq}})}}. \tag{4.18}$$

The strongest constraints on the velocities of DM particles arise from the Lyman-α forest data on the matter power spectrum at small (nonlinear) scales [154]. For typical thermal relic warm DM candidates it leads to a lower bound on the mass of the particles $m_{\mathrm{warmDM}} \gtrsim$ keV (cf., e.g. [155]), and the corresponding velocities at matter-radiation equality are

$$\mathrm{v}_{\text{warm DM, eq}} \sim 10^{-3} \qquad \text{for} \qquad m_{\text{warm DM}} \times \text{keV}. \tag{4.19}$$

Requiring the same velocities for the (nonthermal) ALP DM, from (4.18) we obtain the constraint

$$m_a \gtrsim 10^{-15}\,\text{eV}, \tag{4.20}$$

in order to have a successful structure formation from monodromy ALP DM. Note that these constraints apply only in the regime when the amplification of fluctuations is significant and leads to the fragmentation of the ALP field.

4.3.2 Equation of state

Even if velocities are sufficiently small to allow for the structure formation to proceed, there is still an important effect of the growth of fluctuations and the production of relativistic particles: the equation of state is changed for some time after oscillations begin. This is what we will study in this subsection.

The equation of state parameter is defined as

$$w = \frac{p}{\rho}, \tag{4.21}$$

where p and ρ are the expectation values of the pressure and the energy density, respectively. They are given by

$$\begin{aligned} p &= \langle \frac{1}{2}\dot{\varphi}^2 - \frac{1}{6}(\nabla\varphi)^2 - U(\varphi)\rangle, \\ \rho &= \langle \frac{1}{2}\dot{\varphi}^2 + \frac{1}{2}(\nabla\varphi)^2 + U(\varphi)\rangle. \end{aligned} \tag{4.22}$$

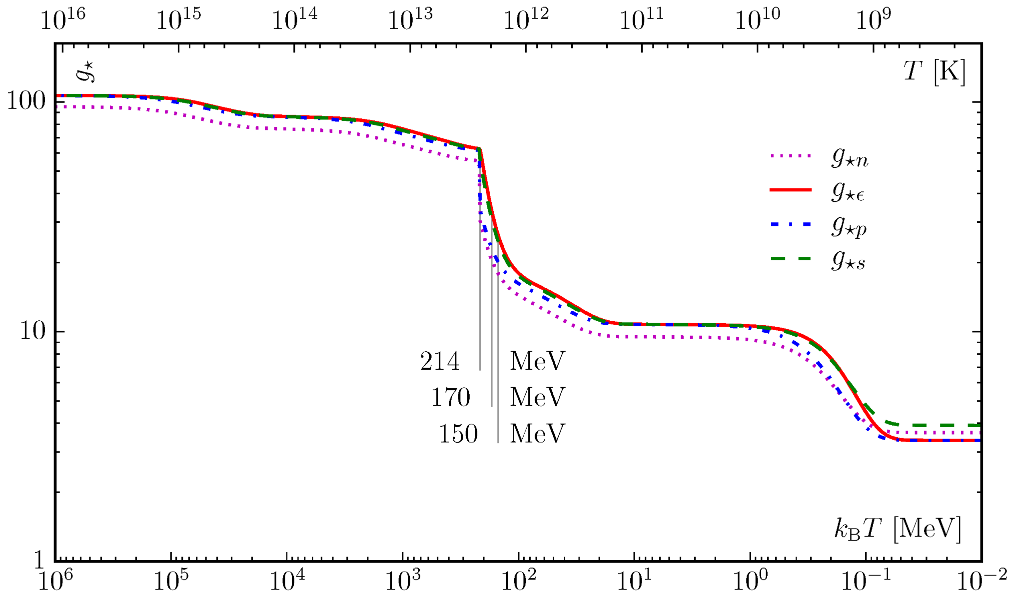

FIGURE 4.4: The temperature-dependent numbers of effective degrees of freedom for entropy g_s, pressure g_p, energy g_ϵ and number g_n densities. Figure is taken from [153].

Our baseline expectations are that a constant homogeneous background field leads to $w \approx -1$. For a homogeneous background field oscillating around $\phi = 0$, w oscillates between 1 and -1. In the case of a purely quadratic potential these oscillations are such that the average over a few oscillations is $\bar{w} = 0$, corresponding to a system dominated by nonrelativistic fluctuations (matter). If ultra-relativistic fluctuations are dominant (radiation), $w \approx 1/3$. Taking all of this into account, we expect that:

- At early times $w = -1$.
- After the background field starts to oscillate, w oscillates between -1 and 1.
- As the background oscillation amplitude decreases, the field spends more time in the concave regions of the potential. In these regions potential energy is dominant over kinetic energy, which shifts $\bar{w}$ towards negative values (see also [56]).
- The growth of fluctuations with large momenta shifts $\bar{w}$ in the opposite direction, towards $w = 1/3$.
- After the collapse of the background field, w is between 0 and $1/3$.
- Because of the redshift of momenta, $w \to 0$ at late times.
- If the field settles in a false minimum and obtains an expectation value, the corresponding vacuum energy does not dilute with time and, therefore, will dominate the energy content after some time, leading to $w \to -1$. For our purposes this dark energy contribution must be subtracted from the total energy density.

Our numerical simulations verify the behavior described above. As an illustration, in Fig. 4.5 the equation of the state parameter w is shown as a function of $\ln(a/a_{\rm osc})$ in the case of $\phi_1/f = 1000$, $\kappa = 10$ and $H_I/f = 10^{-10}$. The gray continuous line represents the numerically extracted w (linear mode evolution glued with the lattice simulation). The black dots represent the values of $\bar{w}$, averaged over short periods of time. As expected, it shifts down as the background field oscillates with a smaller amplitude and probes the tachyonic regions of the potential. The oscillatory behavior of w ends with the collapse of the background field.

As it was already mentioned, the redshift and the finite lattice size restrict numerical simulations to not too late times. To access w at late times, we performed the following extrapolation. As discussed in the previous subsection, at late times $a/a_{\rm osc} \gtrsim 100$ the Hubble expansion has sufficiently diluted the particles. The rate of self-interactions becomes small, and the occupation numbers evolve very slowly. This allows us to approximate them as constant in comoving coordinates (as we already did in the previous subsection).

At late times, when the interaction rates drop, the pressure and the energy can be expressed in terms of the occupation numbers,

$$\begin{aligned} p &\approx \frac{1}{a^4}\int_{\mathbf{p}} \frac{\mathrm{p}^2}{3\omega(t,\mathrm{p})} n(t,\mathrm{p}), \\ \rho &\approx \frac{1}{a^4}\int_{\mathbf{p}} \omega(t,\mathrm{p}) n(t,\mathrm{p}). \end{aligned} \tag{4.23}$$

Here, $\omega^2(t,\mathrm{p}) \approx \mathrm{p}^2 + a(t)^2 m_a^2$ and the factors of a^{-4} arise from the transformation from conformal variables back to the original ones. At these times the change of w

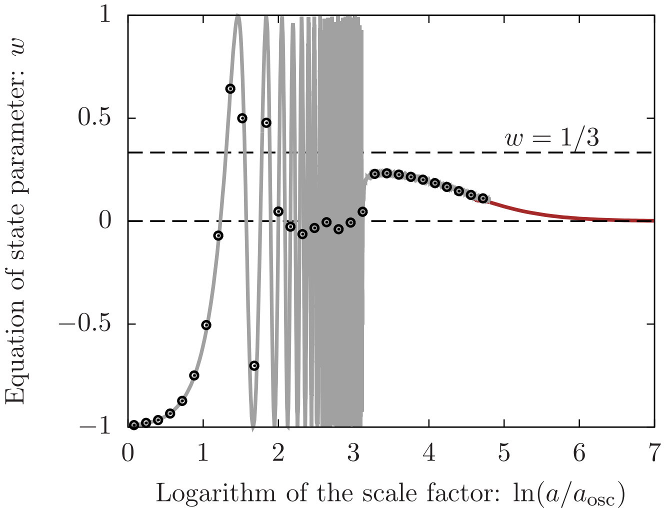

FIGURE 4.5: Equation of the state parameter w as a function of the logarithm of the scale factor $\ln(a/a_{\rm osc})$. The continuous gray line is extracted numerically, from the linear mode evolution glued with the lattice simulation. The black dots represent the values of $\bar{w}$, averaged over short periods of time. The brown line is obtained by extrapolation in the frozen regime. We employ $\phi_1/f = 1000$, $\kappa = 10$ and $H_I/f = 10^{-10}$.

in time arises mostly from the growth of the scale factor, which enters the dispersion relation. We performed an extrapolation of w to late times using (4.23) with the latest available momentum distribution function. The result is represented by the brown line in Fig. 4.5.

4.3.3 Energy density today

The deviations from $w = 0$ before the epoch of matter-radiation equality, which were discussed in the previous section, lead to an energy density today that is different from the one in the case of standard ALPs. While standard ALPs dilute as matter ($\bar{w} \approx 0$), shortly after the oscillations start [26], the monodromy ALPs have a significant phase where $w \neq 0$. We now estimate the change in the DM density resulting from this.

Using the continuity equation

$$d[a^3(\rho + p)] = a^3 dp \tag{4.24}$$

and solving it for an arbitrary time-dependent or, equivalently, a-dependent parameter w leads to

$$\rho(a) = \rho' \Big(\frac{a}{a'}\Big)^{-3} \exp\Big[- 3 \int_{a'}^{a} w(\widetilde{a}) d \ln\Big(\frac{\widetilde{a}}{a'}\Big)\Big]. \tag{4.25}$$

Here a' and ρ' are the scale factor and the energy density at some reference time. In the case of a constant w this simplifies to $\rho(a) \propto s^{-3(1+w)}$.

The ALPs energy density today can be thus written as

$$\rho_0 = \rho_{\rm osc} \Big(\frac{a_0}{a_{\rm osc}}\Big)^{-3} \mathcal{Z}_0^{\rm osc}, \tag{4.26}$$

where the dimensionless prefactor

$$\mathcal{Z}_{a_2}^{a_1} = \exp\Big[-3\int_{a_1}^{a_2} w_\phi(\widetilde{a})d\ln\widetilde{a}\Big], \tag{4.27}$$

describes how much the energy density of ALPs is suppressed on top of the $\propto a^{-3}$ dilution of nonrelativistic matter. This can be caused e.g. by an intermediate ultrarelativistic phase, which leads to $w = 1/3$.

As it was already mentioned, if the background field ends up in a false minimum, some of its energy is transformed into the form of dark energy (see also [156]). This energy has to be subtracted in the calculation of the DM density. As it was explained in the previous chapter, getting trapped in a false minimum is likely for large values of κ and small values of ϕ_1/f, such that $\phi_1/f \lesssim \kappa^2$. In this case the field often gets trapped during the first couple of oscillations, or can also be trapped from the very beginning. The subsequent dynamics is then analogous to the case of standard ALPs and, in particular, the growth of fluctuations is insignificant. In contrast, when ϕ_1/f is significantly larger compared to κ^2, the field typically completes its oscillations around the lowest minimum. This is because the fluctuations manage to become strong and have the effect of smearing out the wiggles in the effective potential, making it unlikely for the field to get trapped. In the following, we concentrate on the case of ending up in the true minimum, so that no dark energy contribution has to be subtracted. We return to the aspects of trapping in Section 4.4.1.

Calculation of the final energy density: Excluding the possibility of ending up in a false minimum, w inevitably approaches zero at sufficiently late times. This means that $\mathcal{Z}_0^{\text{osc}}$ in (4.27) can be extracted from the simulations as the late-time nearly constant value of $\mathcal{Z}_a^{\text{osc}}$ for large values of the scale factor a. For the energy density ρ_{osc} one can write

$$\rho_{\text{osc}} \approx \frac{1}{2}m^2\phi_1^2 + \Lambda^4\Big[1-\cos\Big(\frac{\phi_1}{f}\Big)\Big] = \frac{1}{2}m_a^2\phi_1^2\mathcal{R}_\kappa\Big(\frac{\phi_1}{f}\Big), \tag{4.28}$$

where

$$\mathcal{R}_\kappa(x) = \frac{1}{1+\kappa^2}\Big(1+\frac{2\kappa^2}{x^2}(1-\cos x)\Big). \tag{4.29}$$

In order to simplify the expression for ρ_{osc}, we focus on the case when ϕ_1/f significantly exceeds κ. This is usually the interesting regime of dynamics, where fragmentation takes place. This allows one to neglect the second term in $\mathcal{R}_\kappa$ and today's energy density ρ_0 from (4.26) takes the form

$$\rho_0 = \Big[\frac{1}{2}m_a^2\phi_1^2\Big(\frac{a_{\text{osc}}}{a_0}\Big)^3\Big]\Big(\frac{\mathcal{Z}_0^{\text{osc}}}{1+\kappa^2}\Big). \tag{4.30}$$

The expression in the squared brackets in the last equation is exactly what is calculated for the energy density of standard ALP DM today [26] and leads to (4.1) if one inserts the conservation of comoving entropy as in (4.15), the expression (4.16) and the value of $T_0 = 2.73\text{K}$ for today's temperature of the universe.

For monodromy ALP DM the expression for the energy density today is therefore modified to

$$\rho_0 = 0.17\,\frac{\text{keV}}{\text{cm}^3}\sqrt{\frac{m_a}{\text{eV}}}\Big(\frac{\phi_1}{10^{11}\text{GeV}}\Big)^2\Big(\frac{\mathcal{Z}_0^{\text{osc}}}{1+\kappa^2}\Big)\mathcal{F}(T_{\text{osc}}), \tag{4.31}$$

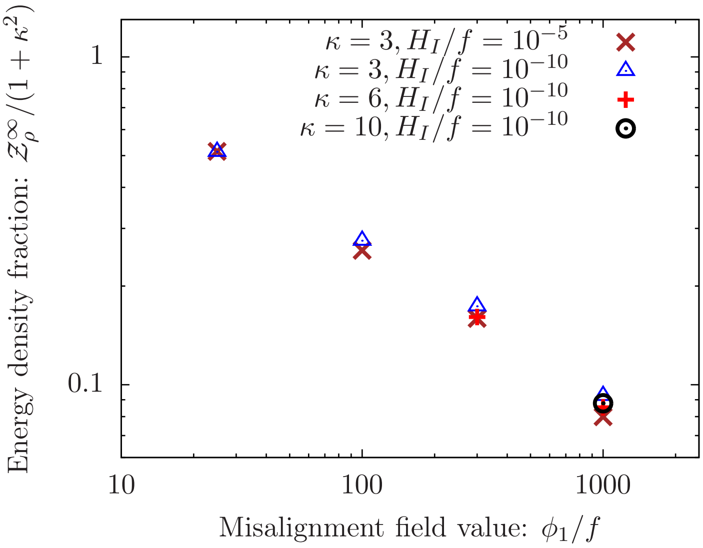

FIGURE 4.6: The numerically extracted values of the prefactor $\mathcal{Z}_\rho^\infty/(1+\kappa^2)$, as a function of the misalignment field value ϕ_1/f, for different values of κ and H_I/f.

In the expression above, ρ_0 is expressed in terms of the ALP mass m_a, the misalignment field value ϕ_1, the parameter κ and the factor $\mathcal{Z}_0^{\rm osc}$, which in turn depends on κ, ϕ_1/f and H_I/f.

The values of the additional prefactor $\mathcal{Z}_\rho^\infty/(1+\kappa^2)$, extracted from the simulations for different values of the parameters, are shown in Fig. 4.6. As can be seen in the plot, $\mathcal{Z}_\rho^\infty$ decreases with an increasing initial field value ϕ_1/f, which is expected since more fluctuations are produced in that case, shifting w more towards $1/3$. Remarkably, the dependence of the term on the values of H_I/f and κ is very weak.

Overall, Fig. 4.6 shows that the dilution due to the fluctuations is rather modest. The increased field amplitude easily compensates for this effect on today's energy density. In other words, the range of decay constants f that allow for sufficient DM production can be extended in the presence of a monodromy. For example, at a fixed mass m_a increasing the initial field value from $\phi_1 = f$ to $\phi_1 = 1000\,f$ leads to an increase in today's energy density by a factor of $\sim 10^6\, Z_\rho^\infty/(1+\kappa^2) \gtrsim 10^5$. Stated differently, we can choose a value of f that is smaller by a factor of $10^{5/2}$ and have a correspondingly larger value of the coupling, with today's energy density fixed.

4.4 Strong fluctuations on small scales and their evolution

As we have seen in section 4.2.2, for sufficiently large κ and ϕ_1/f the energy density of the initially homogeneous background field is completely converted into fluctuations. In that sense all of the DM is made from these (large) fluctuations. In order to better understand the macroscopic picture, in this section we translate these field fluctuations into energy density fluctuations and study the fate of those overdensities during the large-scale structure formation.

4.4.1 Power spectrum of density fluctuations

The density field of DM is conveniently described in terms of the so-called energy density contrast, which is defined as

$$\delta(\mathbf{x}) = \frac{\rho(\mathbf{x}) - \langle\rho\rangle}{\langle\rho\rangle}. \tag{4.32}$$

With this the dimensionless density contrast power spectrum can be defined analogously to the field power spectrum, from the Fourier transform of the density contrast,

$$\langle\delta(t,\mathbf{p})\delta(t,\mathbf{p}')\rangle = (2\pi)^3\delta^{(3)}(\mathbf{p}+\mathbf{p}')\frac{2\pi^2}{\mathrm{p}^3}\Delta_\delta(t,\mathrm{p}). \tag{4.33}$$

It is straightforward to check that the mean of the density contrast vanishes,

$$\langle\delta(\mathbf{x})\rangle = 0, \tag{4.34}$$

while its variance can be expressed as

$$\langle\delta^2(\mathbf{x})\rangle = \int d(\ln\mathrm{p})\Delta_\delta(\mathrm{p}). \tag{4.35}$$

As already indicated, at early times energy is stored dominantly in the background field and the energy density contrast is very small, $\delta \ll 1$. After the fluctuations grow and the background field collapses, the power spectrum Δ_δ becomes $\mathcal{O}(1)$[4]. At late times the field dynamics slows down and, as a consequence, the power spectrum does not change with time anymore, where the overall red-shift due to the expansion is included since comoving momenta are used. This holds until gravity becomes important, as we discuss in the next subsection.

We have extracted the power spectrum $\Delta_\delta(t,\mathrm{p})$ numerically, from classical-statistical simulations[5]. In the left panel of Fig. 4.7 the late-time (frozen) power spectra are shown versus the comoving momenta, for two different values of the parameters for which the fluctuations become nonperturbatively large before freezing (green and purple). As can be seen in the plot, the power spectra have similar shapes. Remarkably, at their maximum $\Delta_\delta \approx 0.5$ in all cases, indicating that we indeed have large fluctuations in the density at relatively small scales i.e. at $\eta \gg 1$, which is reminiscent of an inhomogeneous foam. The locations of the maxima depend strongly on the initial field amplitude and very weakly on κ and H_I/f. While increasing ϕ_1/f pushes the location of the maximum towards higher momenta, the opposite does not work for small values of ϕ_1/f. For instance, if $\phi_1/f \sim 10$ fluctuations remain small leading to a much weaker power spectrum. As an example, in the left panel of Fig. 4.7 we show in blue the power spectrum for such a smaller initial field value.

Let us now discuss in more detail the parameters for which the overdensities become $\mathcal{O}(1)$. To illustrate this, in the right panel of Fig. 4.7 we have plotted the

---

[4] While these fluctuations are isocurvature in nature, their length scale is way too small to be constrained by the CMB measurements (cf. [138, 157] for similar situations).

[5] Alternatively one could extract it from the spectrum of field fluctuations as done, e.g. in [138, 157].

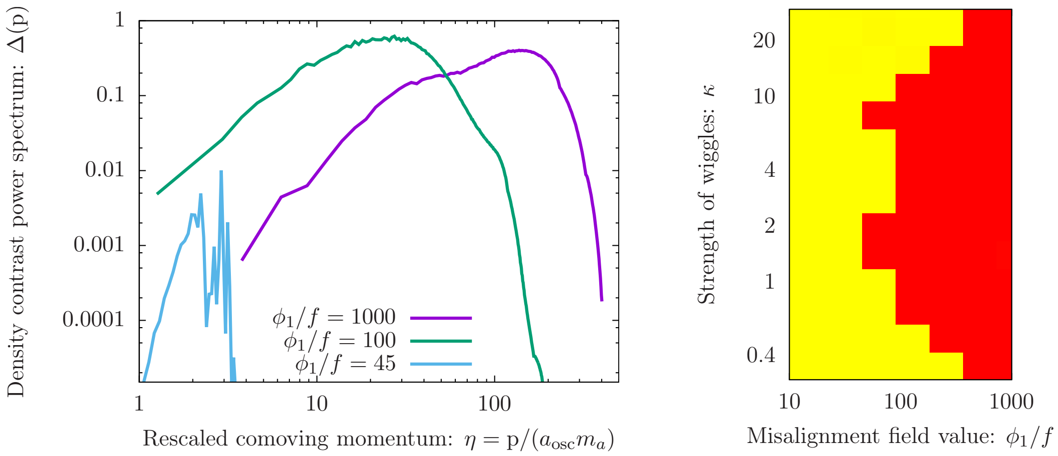

FIGURE 4.7: Left: Several snapshots of the power spectrum, $\Delta(\mathrm{p}) = \mathrm{p}^3\langle|\delta(\mathbf{p})|^2\rangle/(2\pi^2 V)$, as a function of the rescaled comoving momentum $\eta = \mathrm{p}/(m_a a_{\rm osc})$, for $\kappa = 3$. Right: Fraction r of the total energy density in the fluctuations. We have sampled 112 different combinations of ϕ_1/f and κ. Points for which $r \ll 1$ are marked in yellow, and those for which $r \approx 1$ are shown in red. We employ $H_I/f = 10^{-10}$.

fraction r of the total energy density in the fluctuations[6],

$$r = \frac{\rho_{\rm fluc}}{\langle \rho \rangle}, \tag{4.36}$$

for different values of ϕ_1/f and κ. The values of r were obtained by performing numerical simulations with 112 different combinations of ϕ_1/f and κ. We have set H_I/f to 10^{-10}, although the dependence on this parameter is rather weak. The yellow color in the plot corresponds to $r \ll 1$, i.e. most of the energy being stored in the background field even at late times. The red color corresponds to $r \approx 1$. We have stopped the simulations once the energies in the oscillating background field and in the fluctuations became equal, since this is inevitably followed by the fragmentation of the background field. In other words, the red region in the plot corresponds to having $\mathcal{O}(1)$ overdensities at late times.

As can be seen, for values of κ of order one, the overdensities become $\mathcal{O}(1)$ already for $\phi_1/f \sim 100$. For smaller values of κ this transition occurs at larger field values, which is expected since the growth of fluctuations is slower in that case. Also in the upper part of the plot the transition to $r \approx 1$ occurs at larger field values. The reason is the high probability of getting trapped when $\phi_1/f \lesssim \kappa^2$ is satisfied, as it was explained in Section 4.3.3. This prevents the fluctuations from growing significantly. Note, that even in the red region, in few cases the field ends up in a false minimum. Besides the reduction of the final DM density, this does not lead to any qualitative differences in the dynamics and, in particular, the power spectra have shapes similar to those in the left part of Fig. 4.7.

4.4.2 The fate of the overdensities

The $\mathcal{O}(1)$ density fluctuations, imprinted during the nonperturbative dynamics, are reminiscent of the post-inflationary axion scenario [31]. There the PQ symmetry breaking happens after inflation and, thus, the axion field does not undergo the

---

[6] In (4.36), as well as in (4.32) we subtract the dark energy density, if it's nonzero.

inflationary "homogenization" throughout the entire observable universe. Instead, it takes random values in causally disconnected regions. Under gravity the resulting overdensities [7] are known to form gravitationally bound objects called axion miniclusters [72, 74]. It is tempting to consider the formation of miniclusters also from the fluctuations in our case, which is done in this section.

As it was shown in [72, 73], for pressureless matter the collapse of an overdensity with a density contrast δ occurs at the scale factor

$$x \approx \frac{0.7}{\delta}, \tag{4.37}$$

where

$$a = x a_{\text{eq}} \tag{4.38}$$

and a_{eq} is the scale factor at the epoch of the matter-radiation equality. The analysis in that works was based on the Press-Schechter spherical collapse model.

This indicates that $\mathcal{O}(1)$ fluctuations should collapse around the time of the matter-radiation equality. However, in the case of monodromy DM we need to be a bit more careful. The reason is that the length scale of the $\mathcal{O}(1)$ fluctuations is significantly smaller as can be seen from the fact that the peak of the power spectrum occurs at comoving momenta of the order (cf. Fig. 4.7)

$$\eta_{\max} = \frac{\mathrm{p}_{\max}}{m_a a_{\text{osc}}} \gtrsim 10.$$

In contrast, the QCD axion field in the post-inflationary scenario typically has $\mathcal{O}(1)$ density fluctuations of the size of the horizon at the time when the field starts to oscillate, i.e. on comoving scales $\mathrm{p}_{\text{post-inf}}/a_{\text{osc}} \sim H_{\text{osc}} \sim m(T_{osc})/3$ [31]. However, at this time the axion mass typically still increases due to the temperature dependence of nonperturbative QCD effects giving rise to its potential. As a result, the characteristic momentum of the overdensities, measured in units of the final axion mass, is smaller and, in terms of the rescaled comoving momentum that we introduced,

$$\eta_{\text{post-inf}} \lesssim 1.$$

The length scale of the fluctuations from fragmentation is therefore significantly smaller. As we demonstrate below, the corresponding small but nonvanishing pressure, due to the gradient energy of the field, can have significant effects on the evolution.

The spherical collapse model: To study the fate of the overdensities we employ an adapted version of the spherical collapse model from [72, 73], which also includes the pressure effects.

By the time of interest ALPs have become nonrelativistic (this limit of QFT is described in section 6.3) and the decoupling of overdensities from the background Hubble expansion can be described by means of Newtonian gravity. In the spherical collapse model one considers a quasi-homogeneous and spherical overdense region of radius r, density ρ, pressure p, and total mass M. The Newtonian equations of motion for the radius have the form [158]

$$\frac{d^2 r}{dt^2} = -\frac{8\pi G}{3}\rho_R r - \frac{GM}{r^2} - \frac{1}{\rho}\frac{dp}{dr}, \tag{4.39}$$

---

[7] Similarly for the case of DM created from inflationary ALP fluctuations [138].

where G is Newton's constant and ρ_R is the background density of radiation. The second term on the right-hand side is the gravitational force due to the matter inside the spherical shell. The last term represents the pressure gradient force (see e.g. [159]).

Delegating the details of the calculation of the internal pressure for ALP DM to the appendix B, here we simply mention that its origin is the field gradient energy. More specifically, in the nonrelativistic regime the energy density of the field inside a spherical shell with a radius r has the form (see Eq. (6.3) from chapter 6)

$$E(r) = \frac{1}{2m_a}\int_{r'<r}\Big[\nabla\Psi^*\nabla\Psi\Big] \sim \frac{M}{m_a^2 r^2}, \tag{4.40}$$

where we neglected the self-interactions of the field and $M = m_a \int \Psi^*\Psi$.

Following [72, 73], we first introduce the dimensionless variable R, which characterizes the deviation of the overdensity from the background Hubble expansion,

$$R(t) = \frac{r(t)}{r_{\text{flow}}(t)} = \frac{r(t)}{a(t)\xi}, \tag{4.41}$$

such that $R = 1$ before the overdensity collapses and ξ is the value of the comoving radius of the overdensity at those early times. As shown in the appendix B, in terms of the variable x from (4.38) the evolution of $R(x)$ is governed by

$$x\Big(1+x\Big)\ddot{R} + \Big(1+\frac{3}{2}x\Big)\dot{R} + \frac{1}{2}\Big[\frac{1+\delta}{R^2} - R\Big] - \frac{C}{xR^3} = 0. \tag{4.42}$$

Here the dots indicate derivatives with respect to x. The last term in (4.42) is an additional term, compared to [72, 73], due to the outwards pressure. The only dependence on the comoving size ξ of the initial overdensity in the above equation is contained in this pressure term or, more precisely, in its prefactor C. The prefactor, calculated in appendix B, is given by

$$C(\eta) \approx \eta^4. \tag{4.43}$$

Here $\eta = \mathrm{p}/(m_a a_{\text{osc}})$ is the initial comoving momentum scale of the overdensity, as in Fig. 4.7.

Gravity versus pressure: Now we can find the condition under which the overdensity can overcome the pressure force and collapse. Essentially, this requires that the gravitational attraction is stronger than the pressure, i.e.

$$\frac{\delta}{2R^2} > \frac{C}{xR^3}. \tag{4.44}$$

This is equivalent to

$$x > x_C = \frac{2C}{\delta} \approx \frac{2\eta^4}{\delta}. \tag{4.45}$$

This condition is remarkably simple and, in particular, does not depend on parameters such as the mass of ALPs.

For the fluctuations with $\delta \sim 1$ and $\eta \gtrsim 10$, as expected from Fig. 4.7, we conclude that the typical fluctuations have not yet collapsed today, when $x_0 \sim 3000$. This is consistent with what one would expect from the Jeans analysis similar to the one in [133] i.e. fluctuations below the Jeans scale do not grow. In contrast, in the post-inflationary axion scenario $\eta \lesssim 1$ and the pressure is too small to prevent the collapse into miniclusters at $x \approx 0.7/\delta$. Therefore, the DM density in our case carries strong fluctuations but not the huge overdensities $\gtrsim 10^9$ as for miniclusters.

Finally let us briefly attempt the first discussion of today's size of the fluctuations and their fate during the large-scale structure formation. The physical size of an overdensity at a scale factor $a = xa_{\text{eq}}$ is given by

$$R \sim \frac{a}{\text{p}} \sim \left(\frac{H_{\text{osc}}}{H_{\text{eq}}}\right)^{1/2} \frac{1}{m_a \eta} x \sim 10^4 \text{km} \sqrt{\frac{\text{eV}}{m_a}} \frac{1}{\eta} x. \tag{4.46}$$

If gravity plays no role, one would expect, for $\eta \sim \text{few} \times 10 - 100$, typical sizes of the fluctuations today of the order

$$R_0 \sim (10^5 - 10^6) \text{km} \sqrt{\frac{\text{eV}}{m_a}}, \tag{4.47}$$

where we used $x_{\text{today}} \sim 3000$. However, such small-scale structures are part of galaxies and clusters. As they only feel their local gravitational field, we expect that their Hubble growth stops as soon as the structure they are contained in decouples from the Hubble expansion. Inside structures we, therefore, expect a somewhat smaller size of the fluctuations,

$$R_0^{\text{in structure}} \sim (10^5 - 10^6) \text{km} \sqrt{\frac{\text{eV}}{m_a}} \frac{a_{\text{structure}}}{a_0}, \tag{4.48}$$

where $a_{\text{structure}}$ is the scale factor at the time when the structure decouples and therefore depends on the type of structure the fluctuations are contained within. This can be as low as 10^3 km for early structures with $(a_{\text{structure}}/a_0) \sim 100$.

4.5 Summary

In this chapter we have investigated the role of a monodromy for ALP DM and the resulting, potentially observable, consequences. The interactions of ALPs with the SM particles can be larger. In the case when the wiggles of the potential are sufficiently strong and the initial misalignment field value is large enough (the red region in the right panel of Fig. 4.7), rapid growth of fluctuations occurs soon after the field starts to oscillate, i.e. at $H \lesssim m_a/3$. This is the interesting regime that we have focused in this chapter. Below we summarize our main findings.

Fluctuations quickly become nonlinear, dominating the energy density, whereas the homogeneous field component fragments. The dynamics of such DM is therefore dominated by these fluctuations. This occurs well inside the epoch of radiation domination and, therefore, much earlier than for standard ALP DM, where the field remains essentially homogeneous until the structure formation becomes important in the matter-dominated universe.

The growth of fluctuations corresponds to a conversion of the homogeneous background field into relativistic particles. We find that physical momenta up to a $\text{few} \times 100\, m_a$ are significantly populated. Shortly after the field starts oscillating the equation of state is thus close to $1/3$, seemingly unsuitable for DM. However, as already mentioned, this occurs deep inside the radiation-dominated area. The expansion effectively cools the gas and the equation of state returns to a value close to zero, as appropriate for cold DM. The relativistic period leads to a reduction in the total energy density compared to a situation where there is no significant growth of fluctuations and the equation of state parameter remains zero during the entire evolution. While non-negligible, this effect does not destroy the possible enhancement in the couplings, made available by the enlarged field range.

The most dramatic change from standard ALP DM lies in the structure at very small scales. The process of fragmentation imprints strong, $\mathcal{O}(1)$ density fluctuations. This is similar to the post-inflationary axion scenario, where the field takes random values in causally disconnected regions when it starts to oscillate and, thus, carries similarly $\mathcal{O}(1)$ overdensities. However, in contrast to the post-inflation axion scenario these structures do not collapse into miniclusters as their physical size is significantly smaller and the internal pressure, resulting from the field gradient energy, counteracts the gravitational force. Instead, the DM has a "foamy" structure of the density at small scales with typical fluctuations of order one. This is summarized in the table below, where the relevant comoving momenta are indicated.

Fluctuations in the post-inflation axion scenario, QCD axion.	$\eta \lesssim 1$	small pressure, miniclusters form.
Fluctuations from fragmentation, monodromy ALPs.	$\eta \gtrsim 10$	large pressure, overdensities have not collapsed.

This "foamy" structure of DM is probably hard to probe in astrophysical observations. However, if it survives inside the galaxy, it could lead to an interesting fluctuating signal in Earth bound direct detection experiments (see e.g. [160–169]).

Chapter 5

Gravitational wave signatures of nonperturbative dynamics

The content of this chapter is based on the work done in collaboration with Joerg Jaeckel, and is presented in the preprint [3]. In that work I did the main computations and most of the writing of the script. Large parts of the text and most of the figures in this chapter and in the appendix C are taken from that reference.

In the previous chapters we investigated the nonlinear dynamics of ALPs in the presence of a monodromy and described how the resonant amplification of fluctuations can trigger the fragmentation of the homogeneous field. Such ALPs can still be viable DM candidates, although the dynamics of fragmentation significantly modifies the spatial structure of such DM on small scales, compared to to the case of standard ALPs.

In this chapter we focus on a different observational signature of the nonperturbative dynamics of ALPs. The process of fragmentation of the coherent field accumulates a significant fraction of the energy into an anisotropic form, which sources a stochastic GW background. Once produced, GWs travel almost unimpeded and, thus, can deliver information about the nonequilibrium processes that took place in the early universe.

We start our discussion by a brief review of the elementary theory of GWs based on linearized Einstein equations of gravity in section 5.1. In that section we also summarize the important sources that can produce GWs and the current status of GW detection experiments.

Section 5.2 is devoted to the calculation of the stochastic GW background that is produced from the nonperturbative production of ALP DM. Our analysis combines analytical estimates for the signal strength with numerical lattice computations, and the two approaches yield consistent results. In accordance with the common expectations (see e.g. [170]), we find strong bounds on the possible strength of such a signal, imposed by the abundance of DM in the universe today.

Remarkably, an extended intermediate phase of ultrarelativistic dynamics after the fragmentation allows the production of a stronger GW signal and, at the same time, matching the correct final abundance of DM. We investigate the dynamics in this regime in section 5.3 by deriving a simplified kinetic description. As we demonstrate, the signal in some cases may be within reach of future GW detectors, allowing a complementary probe of this type of DM.

Finally, we conclude in section 5.4.

5.1 GW backgrounds

GW backgrounds can be of either astrophysical or cosmological origin. The first class includes mergers of black holes or neutron stars [171, 172], as well as the collapse of supernovae [173]. Instead, cosmological backgrounds can originate during and after inflation [174, 175], from possible phase transitions in the early universe [176], etc. While so far only GWs from astrophysical sources have been detected [177–179], future improvement of the sensitivities of these experiments will open new possibilities to explore the physics of the early universe.

The aim of this section is to provide a brief review of the linearized theory of gravity, which is commonly used for the calculation of stochastic GW backgrounds of cosmological origin. We also summarize the current status of the GW detection experiments.

5.1.1 Linearized theory of gravity

GWs correspond to transverse-traceless (TT) tensor-like perturbations of the metric tensor [180]. In the synchronous gauge, which fixes $g_{00} = 1$ and $g_{0i} = 0$, such perturbations on top of the background FRW metric have the form

$$g_{\mu\nu}(t,\mathbf{x}) = \begin{pmatrix} 1 & 0 \\ 0 & -a^2(t)\Big(\delta_{ij} + h_{ij}(t,\mathbf{x})\Big) \end{pmatrix}, \tag{5.1}$$

with $|h_{ij}| \ll 1$. The equations of motion for h_{ij} are then obtained by linearizing the Einstein field equations [180],

$$\ddot{h}_{ij} + 3H\dot{h}_{ij} - \frac{\Delta h_{ij}}{a^2} = \frac{16\pi}{M_{\rm Pl}^2}\Pi_{ij}^{TT}. \tag{5.2}$$

The TT condition, $\partial_i h_{ij} = h_{ii} = 0$, leaves the metric perturbations with two independent components, which correspond to the two polarizations of GWs. Π_{ij}^{TT} is the TT projection of the total anisotropic energy-momentum tensor which, for a scalar field, is given by [174, 175]

$$\Pi_{ij}(t,\mathbf{x}) = \frac{1}{a^2}\Big[\partial_i\varphi(t,\mathbf{x})\partial_j\varphi(t,\mathbf{x}) - \delta_{ij}\Big(\mathcal{L}(\varphi(t,\mathbf{x})) - \langle p\rangle\Big)\Big], \tag{5.3}$$

where $\mathcal{L}$ is the Lagrange density and $\langle p\rangle$ the background pressure of the universe. The components, proportional to δ_{ij} drop out after taking the TT projection.

In other words, GWs are sourced by the gradients of the field, which explains why the growth of fluctuations and the subsequent fragmentation of the field are important sources of gravitational radiation. GW backgrounds from scalar field fragmentation have been studied in e.g. [75, 174, 175, 181, 182], mostly in the context of post-inflationary preheating. GWs are also produced during the transitions between local minima, from the collisions of bubbles of the low minimum, as well as from the turbulent dynamics [106, 183]. In particular, the authors of [106] considered a dynamical phase decomposition after axion monodromy inflation. GW backgrounds from the fragmentation of ALPs were studied in [77].

The strength of such stochastic backgrounds is conveniently described in terms of the dimensionless parameter $\Omega_{\rm GW}$, which determines the fraction of energy density in GWs per logarithmic frequency to the total energy density of the universe,

$$\frac{\rho_{\rm GW}}{\rho_{\rm c}} = \int d(\ln\nu)\ \Omega_{\rm GW}(\nu), \tag{5.4}$$

where ν is the frequency, $\rho_c = (3/8\pi)M_{\rm Pl}^2 H^2$ is the critical density of the universe and $\rho_{\rm GW}$ is the energy density in GWs, which is given by[1] [174]

$$\rho_{\rm GW}(t) = \frac{M_{\rm Pl}^2}{32\pi}\langle\frac{1}{2}\dot{h}_{ij}(t,\mathbf{x})\dot{h}_{ij}(t,\mathbf{x}) + \frac{1}{2}\nabla h_{ij}(t,\mathbf{x})\nabla h_{ij}(t,\mathbf{x})\rangle = \frac{M_{\rm Pl}^2}{32\pi V}\int_{\mathbf{p}}\Big(|\dot{h}_{ij}(t,\mathbf{p})|^2\Big). \tag{5.5}$$

where, in the last term, averaging over an oscillation time was performed.

5.1.2 Detection of GWs

Experiments aimed at detecting GWs can be classified into the following three categories:

- **Ground-based laser interferometers**, such as the Laser Interferometer Gravitational wave Observatory (LIGO) [184], VIRGO [185], GEO [186] and TAMA [187]. They use wave interference to detect the propagation of GWs in the typical frequency range $10 - 10^3$Hz. By today, the LIGO and Virgo have detected several signals from mergers of black holes with masses of ~ 10 solar mass, as well as a signal from the collision of neutron stars [177–179].

- **Space-based laser interferometers**, such as the Laser Interferometer Space Antenna (LISA) [188], which is planned to launch within the next decades, the Big Bang Observer (BBO) [79] and the Deci-Hertz Interferometer GW Observatory (DECIGO) [189]. Due to the larger arm lengths these interferometers can detect gravity waves with smaller frequencies ($10^{-4} - 10^{-2}$Hz).

- **Pulsar timing arrays:** Pulsars are rapidly rotating neutron stars, which emit very regular beams of radio waves. By investigating the variations in the arrival times of such beams, emitted by a large array of well-understood pulsars, it is possible to detect the propagation of GWs [190]. The three primary PTA projects, that are currently operating, are the Parkes Pulsar Timing Array (PPTA) [191], the North American Nanohertz Observatory for GWs (NANOGrav) [192] and the European Pulsar Timing Array (EPTA) [193], collaborating under the International Pulsar Timing Array (IPTA) project [194]. They use arrays of millisecond pulsars and are designed to detect GWs with frequencies $10^{-9} - 10^{-7}$Hz. So far no detection of GWs has been made, excluding backgrounds with $\Omega_{\rm GW} \gtrsim 10^{-9}$. Longer timing as well as new telescopes such as the Square Kilometre Array (SKA) [78] will significantly improve the sensitivity of PTAs within the next years.

Fig. 5.1, taken from [195], summarizes the sensitivity curves of the above mentioned experiments on the $\Omega_{\rm GW,0}h^2$ versus ν/Hz plane, where $\Omega_{\rm GW,0}$ is the fractional energy density in GWs today and $h = 0.68$ [10]. This list is complemented with the efforts for indirect detection of primordial GWs from inflation in the form of a specific (B-mode) polarization in the CMB [196].

---

[1] In these expressions summation over the indices i and j is implied.

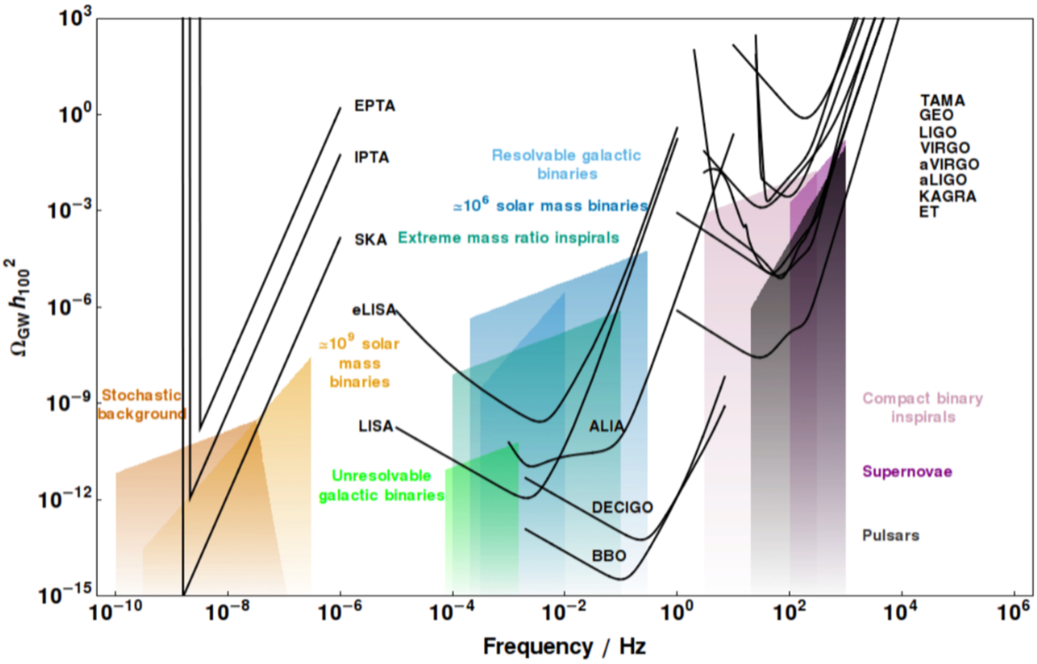

FIGURE 5.1: Sensitivity curves for different GW detectors and the predicted backgrounds from various sources. Figure is taken from [195].

5.2 GW production from ALP DM fragmentation

Having reviewed the current status of GW detection experiments we now proceed with a detailed analysis of the stochastic GW background production from the nonperturbative dynamics of ALP DM in the presence of a monodromy.

We start with a brief outline of the dynamics in section 5.2.1. Analytical estimates of the typical frequency and strength of the signal are then performed in section 5.2.2. The frequency is mostly determined by the mass of ALPs and, hence, spans a whole range of possible values. Our main result is Eq. (5.22), which determines the upper bound on the signal strength from ALP DM, depending on its typical frequency. In section 5.2.3 we present the numerical calculation of the GW signal and demonstrate the consistency with the analytical estimates. In the numerical approach the linear metric perturbations are evolved according to (5.2), using a modified version of the "HLATTICE" code [197].

5.2.1 Outline of the dynamics

In this subsection we briefly outline the main stages of the dynamics, which were discussed in great detail in the previous chapter.

We consider the scenario of the misalignment mechanism, in which the ALP field is present during inflation and denote the initial field value by ϕ_1. The field is effectively frozen and starts to perform coherent oscillations once the Hubble parameter becomes comparable to the curvature of the potential.

For sufficiently large misalignment angles ϕ_1/f the fluctuations of the ALP field are resonantly amplified, triggering the complete fragmentation of the homogeneous component. Directly after fragmentation ALPs are usually relativistic (see Fig. 4.5), such that their energy density dilutes efficiently, as $\propto a^{-4}$. ALPs also cool

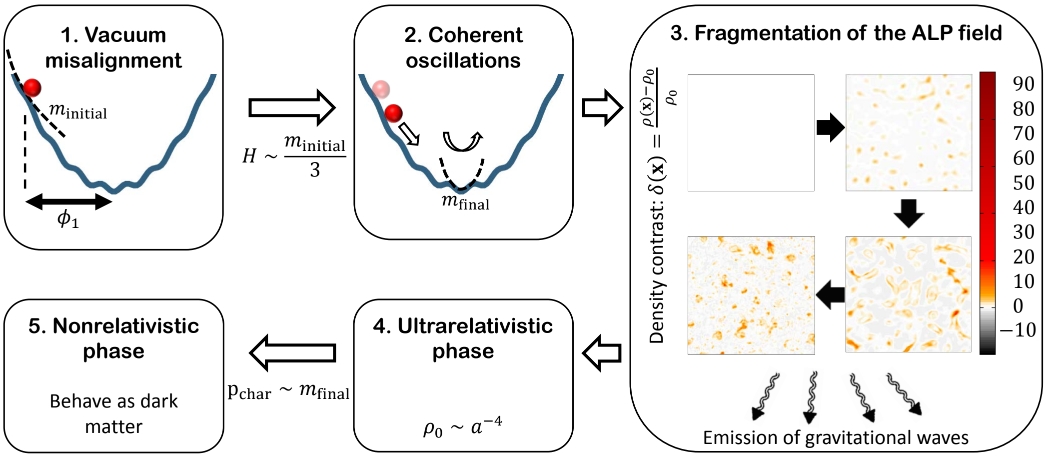

FIGURE 5.2: The main stages of the misalignment production of ALPs involving nonperturbative dynamics. Initially the field is frozen (1) and starts to oscillate (2) after the Hubble parameter H drops bellow the curvature of the potential m_{initial}. This is followed by the fragmentation of the ALP field (3), a process that produces a stochastic GW background and is illustrated by plotting several snapshots of the energy density contrast $\delta(\mathbf{x}) = (\rho(\mathbf{x})-\rho_0)/\rho_0$ along a 2D slice. After the fragmentation ALPs are ultrarelativistic (4) and become nonrelativistic (5) after their characteristic physical momenta p_{char} drop bellow the curvature at the bottom of the potential m_{final}.

down with expansion and become nonrelativistic once their characteristic physical momenta drop below their mass. After this they can successfully participate in structure formation.

This sequence of stages of the dynamics is illustrated in Fig. 5.2. In particular, in the third panel, which describes the fragmentation of the ALP field, several snapshots of the energy density contrast $\delta(\mathbf{x}) = (\rho(\mathbf{x}) - \rho_0)/\rho_0$ along a 2D slice are shown. These are obtained from a classical lattice simulation of the field dynamics.

In Fig. 5.2, the distinction between two different mass scales is made explicit. One of them, which we denote as m_{initial}, is the typical curvature of the potential near ϕ_1 and determines the onset of coherent oscillations via the condition $H \sim m_{\text{initial}}/3$. The other parameter, denoted as m_{final}, is the curvature at the bottom of the potential and the transition to the nonrelativistic regime at late times happens when the characteristic physical momenta drop below this mass, $\mathrm{p}_{\text{char}} \sim m_{\text{final}}$. For the monodromy potential in (3.1) these masses are of the same order[2] and the curvature near the bottom is equal to

$$m_a^2 = m^2 + \frac{\Lambda^4}{f^2} = m^2(1+\kappa^2), \qquad \kappa^2 = \frac{\Lambda^4}{m^2 f^2}. \tag{5.6}$$

For more general potentials however the bottom mass can be different and, in particular, sufficiently smaller. This would lead to an extended ultrarelativistic phase and will be important in the context of gravitational wave production, as we demonstrate later.

---

[2] Here we assume that κ takes moderate values, not much larger than one.

5.2.2 Analytical estimates

This subsection is devoted to the analytical estimates of the peak strength and frequency of the GW signal produced during the nonperturbative ALP dynamics. After describing the transformation of the frequency and the energy fraction of the GW signal to today's variables we estimate its strength from Eq. (5.2). We then fix the energy density of ALPs based on today's DM abundance to find the signal strength from ALP DM.

Transformation to today's observables: Today's frequency of GWs is related to the comoving momentum η by a simple red-shift,

$$\nu = \frac{1}{2\pi}\frac{\mathrm{p}}{a_0} = \frac{\eta m_a}{2\pi}\left(\frac{a_{\mathrm{osc}}}{a_0}\right). \tag{5.7}$$

For the ratio of the scale factors one can use the conservation of comoving entropy (4.15), the expression for the temperature during the epoch of radiation-domination (4.16) and the temperature today $T_0 = 2.73\mathrm{K}$, as it was done in section 4.3.1. Recalling that $H_{\mathrm{osc}} = m_a/3$, the formula (5.7) can be re-written as

$$\nu = \left(\frac{\sqrt{3}\sqrt{1.66}g_0^{1/4}T_0\sqrt{\mathrm{eV}}}{2\pi\sqrt{M_{\mathrm{Pl}}}\mathrm{Hz}}\right)\mathrm{Hz}\,\eta\sqrt{\frac{m_a}{\mathrm{eV}}}\mathcal{F}^{1/3}(T_{\mathrm{osc}}) = 1.56\times 10^{-3}\mathrm{Hz}\,\eta\sqrt{\frac{m_a}{\mathrm{eV}}}\mathcal{F}^{1/3}(T_{\mathrm{osc}}). \tag{5.8}$$

where $\mathcal{F}(T)$, defined in (4.17), reflects the change of the effective numbers of degrees of freedom. As can be seen the frequency is mostly determined by the ALP mass.

The energy density in GWs dilutes as a^{-4}, hence their fractional energy density today $\Omega_{\mathrm{GW},0}$ can be expressed as [198],

$$\Omega_{\mathrm{GW},0} = \frac{\rho_0}{\rho_{c,0}} = \Omega_{\mathrm{GW,emit}}\left(\frac{a_{\mathrm{emit}}}{a_0}\right)^4\left(\frac{H_{\mathrm{emit}}}{H_0}\right)^2 = \left(\frac{1.66^2\times g_0 T_0^4}{M_{\mathrm{Pl}}^2 H_0^2}\right)\Omega_{\mathrm{GW,emit}}\mathcal{F}^{4/3}(T_{\mathrm{emit}}), \tag{5.9}$$

where we again used the conservation of comoving entropy. Calculating the term in the brackets, the formula (5.9) can be re-written as

$$\Omega_{\mathrm{GW},0} = 9.39\times 10^{-5}\Omega_{\mathrm{GW,emit}}\mathcal{F}^{4/3}(T_{\mathrm{emit}}). \tag{5.10}$$

Equations (5.8) and (5.10) are used in our numerical simulations to transform the variables to today's observables, as well as in our analytical estimates of the GW production, described below.

Parametric estimates for the GW signal: We now perform parametric estimates for the GW production. For simplicity we assume that most of it takes place near some scale factor a_{emit}. This is naturally identified with the end of the resonant amplification of fluctuations and the fragmentation of the background field (the third stage in Fig. 5.2). We denote by $\mathrm{p}_\star = \eta_\star m_a a_{\mathrm{osc}}$ the comoving momentum at which the dominant resonant production takes place, and by $\nu_\star$ the corresponding frequency. For our parametric estimates we assume that the GW spectrum is peaked at a momentum of the same order as $\mathrm{p}_\star$ and denote the fractional energy density at the peak by $\Omega_{GW,\star}$. In what follows we estimate that fractional density.

From the wave equation (5.2) it follows that [199]

$$|(h_{\mathrm{p}_\star,\mathrm{emit}})_{ij}| \sim \frac{16\pi}{M_{Pl}^2(\mathrm{p}_\star/a_{\mathrm{emit}})^2}|(\Pi_{\mathrm{p}_\star,\mathrm{emit}})_{ij}^{TT}|. \tag{5.11}$$

For simplicity we ignore the index structure of metric perturbations, i.e. identify $h_{ij} \to h$, and associate the Π_{ij}^{TT} to the energy density of the ALP field, i.e.

$$\Pi_{ij}^{TT} = \alpha\rho_\varphi, \tag{5.12}$$

where $\alpha \lesssim 1$ quantifies the fraction of the energy stored in the fluctuations. These are of course crude approximations, but should suffice for a parametric estimate.

The energy density $\rho_{\mathrm{GW,emit}}$ in GWs at a_{emit} can be written as

$$\rho_{\mathrm{GW,emit}} = \frac{M_{Pl}^2}{32\pi V}\int|\dot{h}_{\mathrm{p}}|^2\frac{4\pi}{(2\pi)^3}\mathrm{p}^2 d\mathrm{p} \approx \frac{M_{Pl}^2}{8V(2\pi)^3}\int d(\ln\mathrm{p})\mathrm{p}^3\left(\frac{\mathrm{p}}{a_{\mathrm{emit}}}\right)^2|h_{\mathrm{p}}|^2. \tag{5.13}$$

Here V indicates the control volume for the Fourier transform which will drop out of the final expressions.

The GW energy fraction at the momentum $\mathrm{p}_\star$ is then given by

$$\begin{aligned}\Omega_{\mathrm{GW,emit}}(\nu_\star) \approx& \frac{M_{Pl}^2}{8\rho_{c,\mathrm{emit}}V(2\pi)^3}\frac{\mathrm{p}_\star^5}{a_{\mathrm{emit}}^2}|h_{\mathrm{p}_\star,\mathrm{emit}}|^2\\ \sim& \frac{16^2\pi^3}{3M_{Pl}^4H_{\mathrm{emit}}^2V(2\pi)^3}\alpha^2|\rho_{\varphi,\mathrm{p}_\star,\mathrm{emit}}|^2\mathrm{p}_\star a_{\mathrm{emit}}^2,\end{aligned} \tag{5.14}$$

where in the last step we inserted (5.11) as well as expressed the critical density at a_{emit} in terms of the Hubble parameter $H_{\mathrm{emit}}^2 = 8\pi\rho_{c,\mathrm{emit}}/(3M_{Pl}^2)$.

Noting that the spectra are typically peaked at the resonant momentum, we can employ Parseval's relation to re-express the Fourier components $\rho_{\varphi,\mathrm{p}_\star,\mathrm{emit}}$ in terms of position space ALP energy density $\rho_{\varphi,\mathrm{emit}}$,

$$V\rho_{\varphi,\mathrm{emit}}^2 = \int_{\mathbf{p}}|\rho_{\varphi,\mathrm{p,emit}}|^2 = \frac{4\pi}{(2\pi)^3}\int d(\ln\mathrm{p})|\rho_{\varphi,\mathrm{p,emit}}|^2\mathrm{p}^3 \approx \frac{4\pi}{(2\pi)^3}|\rho_{\varphi,\mathrm{p}_\star,\mathrm{emit}}|^2\mathrm{p}_\star^3\beta. \tag{5.15}$$

In this equation we used the typical logarithmic width of the spectrum of the fluctuations in momentum space,

$$\beta = \Delta\ln\mathrm{p}, \tag{5.16}$$

where usually $\beta \gtrsim 1$. Inserting this into (5.14) yields

$$\Omega_{\mathrm{GW,emit}}(\nu_\star) \sim \frac{64\pi^2}{3M_{Pl}^4H_{\mathrm{emit}}^2}\frac{\rho_{\varphi,\mathrm{emit}}^2}{(\mathrm{p}_\star/a_{\mathrm{emit}})^2}\frac{\alpha^2}{\beta}. \tag{5.17}$$

It is convenient to re-express the energy fraction in terms of quantities at a_{osc}. For this we note that

$$H_{\mathrm{emit}} = H_{\mathrm{osc}}\left(\frac{a_{\mathrm{osc}}}{a_{\mathrm{emit}}}\right)^2 = \frac{m_a}{3}\left(\frac{a_{\mathrm{osc}}}{a_{\mathrm{emit}}}\right)^2, \qquad \rho_{\varphi,\mathrm{emit}} \approx \rho_{\varphi,\mathrm{osc}}\left(\frac{a_{\mathrm{osc}}}{a_{\mathrm{emit}}}\right)^3\mathcal{Z}_{\mathrm{emit}}^{\mathrm{osc}}. \tag{5.18}$$

The factor $\mathcal{Z}_{\mathrm{emit}}^{\mathrm{osc}}$ in the second equation (and defined in Eq. (4.27)) accounts for the nontrivial evolution of the ALP energy density between a_{osc} and a_{emit} compared to the standard $\propto a^{-3}$ dilution for matter.

Inserting (5.18) into (5.17) yields

$$\Omega_{\mathrm{GW},0}(\nu_\star) \sim 0.18 \frac{\rho^2_{\varphi,\mathrm{osc}}}{M^4_{Pl} m^4_a \eta^2_\star} (\mathcal{Z}^{\mathrm{osc}}_{\mathrm{emit}})^2 \mathcal{F}^{4/3}(T_{\mathrm{emit}}) \frac{\alpha^2}{\beta}. \tag{5.19}$$

GW signal from ALP DM: We now make the assumption that DM consists solely of ALPs to obtain an upper bound on the GW signal strength. The energy density of ALPs in (5.19) can be expressed in terms of the today's value of DM density $\rho_{\varphi,0} = 1.27\,\mathrm{keV/cm}^3$ [10], using the transformation from Eq. (4.26). This leads to

$$\Omega_{\mathrm{GW},0}(\nu_\star) \sim 1.1 \times 10^{-32} \left[\frac{\mathrm{eV}}{m_a}\right] \left(\eta_\star \mathcal{Z}^{\mathrm{emit}}_0 \mathcal{F}^{1/3}(T_{\mathrm{osc}})\right)^{-2} \frac{\alpha^2}{\beta}, \tag{5.20}$$

where we again employed the conservation of comoving entropy and the relation $\mathcal{Z}^{\mathrm{osc}}_0 = \mathcal{Z}^{\mathrm{osc}}_{\mathrm{emit}} \mathcal{Z}^{\mathrm{emit}}_0$ which follows directly from the definition of $\mathcal{Z}$ in Eq. (4.27). For the sake of simplicity we also assume that $\mathcal{F}(T_{\mathrm{osc}}) \approx \mathcal{F}(T_{\mathrm{emit}})$.

Eq. (5.20) determines the peak GW signal strength for a given ALP mass. Combining this expression with Eq. (5.8) for the peak frequency,

$$\nu_\star = 1.56 \times 10^{-3} \mathrm{Hz} \eta_\star \sqrt{\frac{m_a}{\mathrm{eV}}} \mathcal{F}^{1/3}(T_{\mathrm{osc}}), \tag{5.21}$$

one arrives at a remarkably simple relation between the peak energy fraction $\Omega_{\mathrm{GW},0,\star}$ and the peak frequency $\nu_\star$,

$$\Omega_{\mathrm{GW},0}(\nu_\star) \sim 2.7 \times 10^{-38} \frac{1}{(\nu_\star/\mathrm{Hz})^2} \frac{1}{(\mathcal{Z}^{\mathrm{emit}}_0)^2} \frac{\alpha^2}{\beta}. \tag{5.22}$$

Summary: The estimates of the signal strength in this subsection were very general and did not rely much on the specification of the ALP potential $U(\phi)$. The main requirement was that the typical curvature of the potential is given by m_a. It was, however, assumed that the spectrum is centered close to the resonant momenta. Nonlinear effects tend to broaden the spectrum and, as we demonstrate in the next section, somewhat modify this picture. Nevertheless, (5.22) reveals the important features of the GW spectrum.

It follows from (5.22) that on top of the inverse-squared dependence on the peak frequency, the peak energy fraction is determined solely from the value of the suppression factor $\mathcal{Z}^{\mathrm{emit}}_0$, defined in Eq. (4.27). If $\mathcal{Z}^{\mathrm{emit}}_0 = \mathcal{O}(1)$, the signal peak is beyond the planned sensitivities of future GW detection experiments, irregardless of the value of the ALP mass. This is the case for the standard monodromy potential from (3.1), for which the values of $\mathcal{Z}^{\mathrm{emit}}_0$ can be found in Fig. 4.6. We nevertheless investigate this scenario numerically in the next subsection to test the analytical estimates. In particular, in Fig. 5.4 the analytical estimate, denoted by the blue circle, is shown together with the numerically calculated GW spectrum for $m_a = 10^{-16}$eV and a particular set of parameters. The (numerically extracted) final GW spectra for different values of parameters are shown in Fig. 5.5. The bound on the signal strength is lifted if ALPs dilute their energy more efficiently after the emission of GWs, i.e. if $\mathcal{Z}^{\mathrm{emit}}_0 \ll 1$. We focus on this scenario in section 5.3.

5.2.3 GW production from lattice simulations

Our analytical estimates are expected to become less accurate for larger misalignment angles ϕ_1/f, since it assumes more time between the end of resonant amplification and the final fragmentation. In that case the signal peak is expected to be weaker and, instead, the signal to be broader. Moreover, these estimates do not take into account the production of GWs after fragmentation, during the turbulent dynamics of ALPs. Finally, the calculation of $\mathcal{Z}_0^{\rm emit}$ and of the typical velocities at matter-radiation equality requires a better knowledge of the ALP spectrum. This motivates the more rigorous analysis based on numerical lattice simulations, which is described in this subsection.

The classical-statistical simulations of the dynamics of the scalar field were performed as in the previous chapter. Linear metric perturbations and the corresponding GW spectra were computed using the HLATTICE code [197], which evolves linear metric perturbations coupled to the scalar field according to Eq. (5.2). The code was originally designed for the simulation of post-inflationary preheating dynamics. To adjust it for the case of misalignment production of ALP DM, the following modifications were done:

- The field evolves on a radiation-dominated background, $a \sim \sqrt{t}$, without having any impact on this background expansion rate.
- The horizon entry of frozen modes is properly taken into account, by "gluing" the lattice simulation to an early linear evolution, as described in the previous chapter. In other words, we first evolve the momentum modes of the fluctuations linearly, starting with the scale-independent power spectrum (cf. e.g. [81]),
$$\Delta_\phi = \left(\frac{H_I}{2\pi}\right)^2, \tag{5.23}$$
imprinted after inflation, and then, prior to the onset of nonlinear effects, switch to the lattice simulation. In this way we also neglect the GW production during this early linear phase, which, however, is anyways exponentially suppressed.
- We always assume that ALPs constitute the total abundance of DM. For given values of the ALP masses and the misalignment angle ϕ_1/f, this fixes the absolute value of ϕ_1 via Eq. (4.31). We therefore first simulate the ALP dynamics and extract the value of $\mathcal{Z}_0^{\rm osc}$, and only afterwards calculate ϕ_1 and the corresponding GW signal strength. For the monodromy potential (3.1), considered in this section, we extract this value directly from the lattice simulations, as it was done in the previous chapter (see Fig. 4.6). In contrast, in the case of $m_{\rm final} \ll m_a$, which is investigated in section 5.3, full numerical simulations become very expensive and, in order to determine $\mathcal{Z}_0^{\rm osc}$, we employ a simplified kinetic description for the dynamics at late times.
- The energy fraction $\Omega_{\rm GW,emit}$ is calculated by dividing the energy density in the GWs by $\rho_c = (3/8\pi)M_{\rm Pl}^2 H^2$, where H is the Hubble parameter during the simulation.
- We use (5.8) and (5.10) to transform the simulation variables to today's observables.

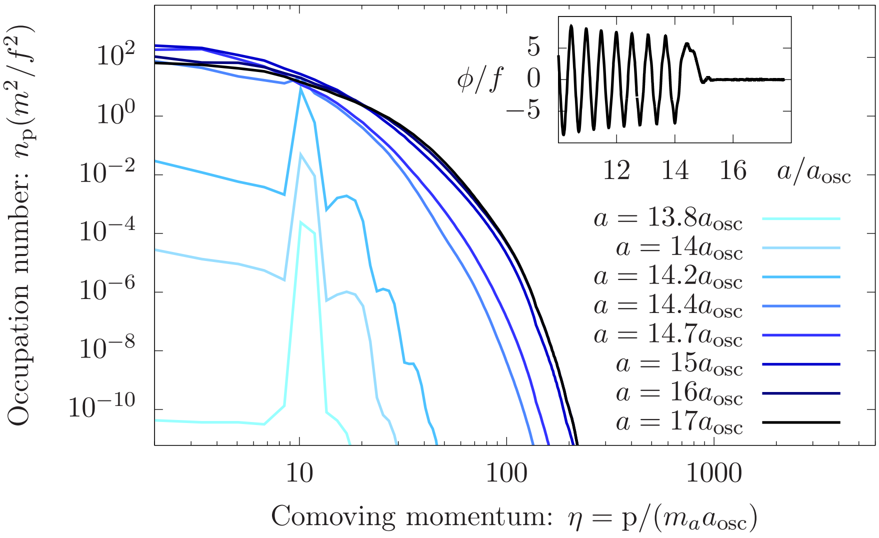

FIGURE 5.3: Several snapshots of ALP occupation numbers versus their comoving momenta during the fragmentation of the field. Different colors, changing from light to dark blue, correspond to different scale factors in the range $a/a_{\mathrm{osc}} = 13.8 - 17$. The inset shows the evolution of the background field ϕ/f at these scale factors. We employ $\phi_1/f = 200$, $\kappa = 3$ and $H_I/f = 10^{-10}$.

The simulations were performed on grids with a fixed comoving volume and up to 512^3 lattice points. We have verified that the results are insensitive to variations of the volume and the lattice spacing.

Results from the simulations: We now present the main results obtained from our numerical simulations for the monodromy potential given by (3.1).

Several snapshots of ALP occupation numbers, extracted from numerical simulations, are shown in Fig. 5.3 versus their comoving momenta, for a particular set of the parameters $\phi_1/f = 200$, $\kappa = 3$ and $H_I/f = 10^{-10}$. Different colors correspond to different scale factors in the range $a/a_{\mathrm{osc}} = 13.8 - 17$, that is when the fragmentation takes place. The inset shows the collapse of the background field ϕ/f (the one-point function) for these scale factors. Fig. 5.4 shows snapshots of the produced GW spectrum $\mathrm{Log}_{10}[h^2\Omega_{\mathrm{GW},0}]$, as a function of the logarithmic frequency, for the same scale factors as in the previous figure. Here we used $m_a = 10^{-16}\mathrm{eV}$ for the ALP mass. All quantities are transformed to today's values and we used $h = 0.68$ [10].

As one can observe in these figures, the two spectra evolve in a similar way, however the GW spectrum, being linearly sourced by the ALP field, does not decrease with time. The resonant growth of ALP fluctuations is accompanied by a GW production at momenta of the same order. The broadening of the ALP spectrum due to nonlinear effects is reflected in an analogous broadening of the GW spectrum. At later times the evolution of both spectra slows down due to the interaction rates becoming smaller compared to the expansion rate. We discuss this last aspect in more details in the next section.

We also compare the GW spectrum at its peak strength, which is acquired during the collapse of the background field, with our analytical estimates from the previous section. To this end we insert $\nu_\star \approx 1.5 \times 10^{-10}\mathrm{Hz}$, which corresponds to $\eta_\star \approx 10$, into (5.22). We use the numerically extracted value $Z_0^{\mathrm{emit}} \approx 0.6$ (for this particular set of parameters), where we identify $a_{\mathrm{emit}} \approx 15a_{\mathrm{osc}}$. We set $\alpha = \beta = 1$.

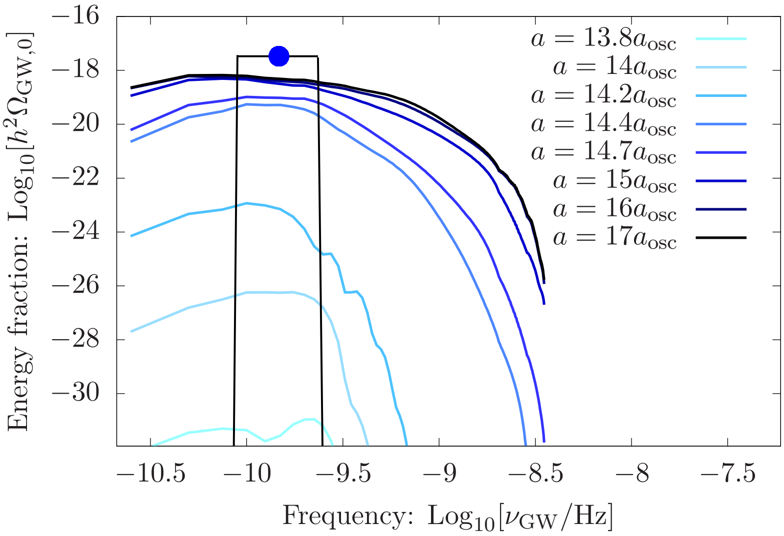

FIGURE 5.4: Several snapshots of the fractional GW spectrum, transformed to today's variables, during the fragmentation of the field. Different colors correspond to different scale factors, same as in Fig. 5.3. The blue circle corresponds to the analytical estimate based on (5.22) and the black rectangle demonstrates the logarithmic width of $\beta = 1$, used in that estimate. We employ $\phi_1/f = 200$, $\kappa = 3$ and $H_I/f = 10^{-10}$, as well as set $m_a = 10^{-16}\mathrm{eV}$.

The obtained estimate is indicated by the blue circle in Fig. 5.4. As can be seen, it matches reasonably well with the result of the numerical calculation, although it is somewhat higher compared to the numerical result. The latter can be understood from the fact that $\beta = 1$, used in that analytical estimate, would approximately correspond to the black rectangle in Fig. 5.4, and is smaller than the actual logarithmic width of the spectrum, as can be seen in that figure.

Having extracted the late-time (frozen) GW spectra, in Fig. 5.5 we plot them for different ALP masses and misalignment angles, thereby obtaining the parameter space spanned by the GW signal, indicated by the dashed slopes. As can be seen, larger misalignment angles lead to a GW production at higher frequencies, however the overall parameter space spanned by the signal is not affected by this dramatically. We have also performed simulations with a larger value of $\kappa = 6$, which led to a strength of the GW signal very similar to the one from $\kappa = 3$. In contrast, for $\kappa \lesssim 1$ the signal is suppressed due to the weakness of the resonance.

5.3 Enhanced GW signal from an extended ultrarelativistic dynamics

In the previous section we estimated the bounds on the GW signal from ALP DM fragmentation. The peak energy fraction of the signal $\Omega_{\mathrm{GW},\star,0}$ is related to its characteristic frequency via (5.22) or, equivalently,

$$\Omega_{\mathrm{GW},\star,0}(\nu_\star) \propto \frac{1}{\nu_\star^2}\frac{1}{(\mathcal{Z}_0^{\mathrm{emit}})^2}.$$

Importantly, this bound is very general and comes solely from the requirement of not overproducing the DM.

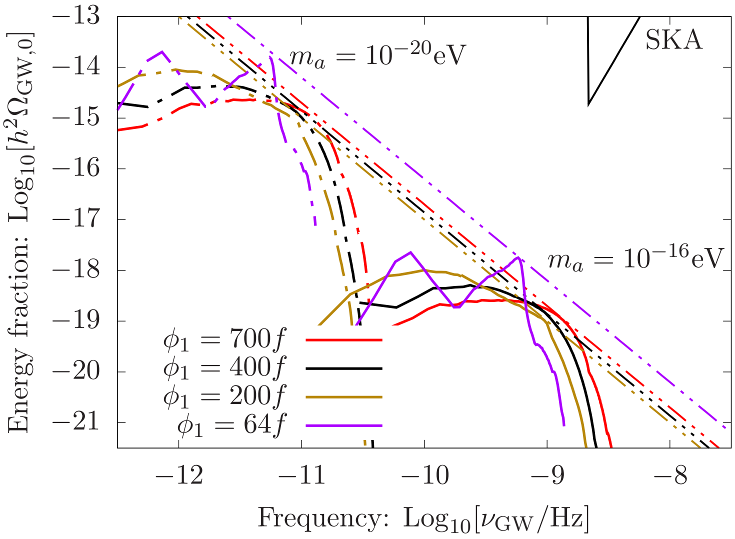

FIGURE 5.5: The parameter space for the numerically extracted GW spectra from fragmentation for the potential of (3.1) for different misalignment angles ϕ_1/f. The dashed lines indicate the numerically obtained envelopes of the signals scaling as in (5.22). We employ $\kappa = 3$ and $H_I/f = 10^{-10}$. For comparison we show the SKA sensitivity [78, 195].

It can be inferred that, on top of the inverse-squared dependence on the frequency, the overall bound on the signal strength is set by the value of $\mathcal{Z}_0^{\mathrm{emit}}$, given by (4.31). The latter determines how much the energy of ALPs has been suppressed between the emission of the signal and today on top of the $\propto a^{-3}$ dilution for non-relativistic matter. In other words, the signal is stronger for smaller $\mathcal{Z}_0^{\mathrm{emit}}$. This is expected since a smaller value of $\mathcal{Z}_0^{\mathrm{emit}}$ implies that the ALP field constituted a larger fraction of the total energy of the universe when the GWs were mostly emitted and, therefore, the signal carried an accordingly larger energy fraction.

Remarkably, an extended intermediate phase of ultrarelativistic dynamics after the fragmentation (the stage (4) in Fig. 5.2), during which the energy density of ALPs dilutes as $\propto a^{-4}$, leads to small values of $\mathcal{Z}_0^{\mathrm{emit}}$ and, therefore, allows the production of a stronger GW signal from the fragmentation and, at the same time, matching the correct final abundance of DM. For the standard monodromy potential (3.1), which was considered in the previous section, this phase is typically short and ends once the characteristic physical momenta, due to the red-shift, drop below the mass m_a. Therefore, the ultrarelativistic phase is extended in the case when the final mass near the bottom of the potential is very small. This scenario is investigated in details in this section.

A small mass near the bottom of the potential extends the ultrarelativistic phase of nonlinear dynamics and, thus, requires longer simulation times. We combine the numerical analysis based on lattice simulations, as in the previous section, with a simplified kinetic analysis at late times, in order to describe this extended far-from-equilibrium dynamics of ALPs. The second approach becomes available due to the dramatic reduction in the complexity of the dynamics, related to the approach of the system to a NTFP. This simplified description allows us to estimate the duration of the ultrarelativistic phase, as well as the typical velocities of ALPs at matter-radiation equality, without performing extensive lattice simulations of the full dynamics, which become extremely difficult in the presence of a large hierarchy of scales. In particular, we find that such an enhanced GW background can be possibly probed by future GW detection experiments.

In section 5.3.1 we discuss how large mass hierarchies can be embedded into the monodromy potential. As we explain in the next section, such hierarchies usually feature repulsive self-interactions, which is somewhat unusual for ALPs and leads to the emergence of a homogeneous condensate. The dynamics and the GW production in the presence of such hierarchies are also briefly discussed. In section 5.3.3 we describe the simplified kinetic description of the dynamics at late times, with the details being delegated to the appendix C. The final GW spectra are presented in section 5.3.4 and the constraints on such dark matter are discussed in section 5.3.5.

5.3.1 The small mass and repulsive self-interactions

For monodromy ALPs the final mass can be small if the sign in front of the periodic term is negative[3], i.e.

$$U(\varphi) = \frac{1}{2}m^2\varphi^2 - \Lambda^4\Big(1 - \cos\frac{\varphi}{f}\Big). \tag{5.24}$$

Near its minimum the potential has the form

$$U(\varphi) = \frac{1}{2}(1-\kappa^2)m^2\varphi^2 + \frac{\lambda}{4!}\varphi^4 - \frac{\lambda f^{-2}}{6!}\varphi^6 ... \tag{5.25}$$

and is convex if $\kappa < 1$. By taking $\kappa \approx 1$ the mass near the bottom of the potential can be made very small.

A similar possibility appears in the case of a "double-cosine" modulation. For example, we consider the following potential,

$$U(\varphi) = \frac{1}{2}m^2\varphi^2 + \Lambda^4\Big(1 - \cos\frac{\varphi}{f}\Big) + r\Lambda^4\Big(1 - \cos\frac{2\varphi}{f}\Big), \tag{5.26}$$

that has the following form near the minimum

$$U(\varphi) = \frac{1}{2}(1+\kappa^2+4r\kappa^2)m^2\varphi^2 - \frac{\lambda(16r+1)}{4!}\varphi^4 + \frac{\lambda f^{-2}}{6!}(1+64r)\varphi^6 - ... \tag{5.27}$$

If the value of r very slightly exceeds $-(1+\kappa^2)/4\kappa^2$ (for large values of κ this corresponds to $r \approx -1/4$), the mass near the bottom is again very small. Unlike the "single-cosine" modulation, in this case κ, which approximately determines the strength of the wiggles, can still be large. Because of this generality we focus on this second possibility. In what follows, the small bare mass near the bottom of the potential is denoted by m_{final}, whereas $m_a^2 = (1+\kappa^2)m^2$.

5.3.2 The dynamics and GW production

The tuning of the bare mass near the bottom does not affect the early dynamics, including the amplification of fluctuations and the decrease of the background field amplitude[4]. However this modification plays an important role after the collapse

---

[3] This scenario was discussed in section 3.3.1.

[4] In particular, the second cosine has a smaller amplitude than the first one.

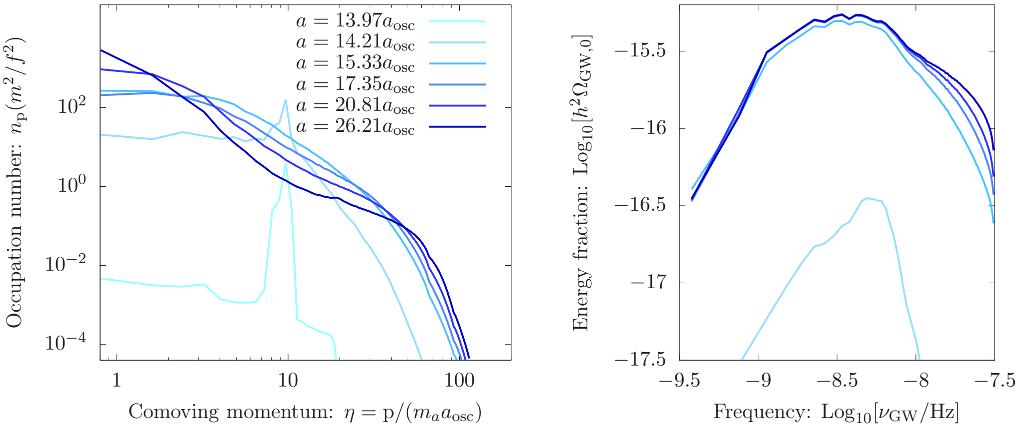

FIGURE 5.6: Snapshots of ALP occupation numbers (left) and fractional GW spectra (right) in the presence of repulsive self-interactions. Colors from light to dark blue correspond to scale factors in the range $a/a_{\rm osc} = 14 - 26$. We employ $\phi_1/f = 200$, $\kappa = 3$, $H_I/f = 10^{-10}$ and $m_{\rm final} = 10^{-3}m_a$.

of background oscillations i.e. when the field settles near $\phi = 0$. For a smaller mass it takes longer time until the self-interactions become unimportant due to dilution. In particular, the spectrum freezes much later in this case. This makes the analysis based on lattice simulations harder due to the larger hierarchy of scales and the required simulation times.

Now we briefly discuss the dynamics at relatively late times to see which interaction terms are relevant in that regime. The sextic and higher-order terms in the potential (5.27) are sub-dominant and can be neglected when $\langle\varphi^2\rangle/f^2 \lesssim 1$. Importantly, the small value of the bare mass near the bottom, however, becomes relevant only when the typical field values become sufficiently small. Indeed, from the following expression for effective mass

$$M^2 = m_{\rm final}^2 + \frac{\lambda}{2}\langle\varphi^2\rangle, \tag{5.28}$$

it follows that the transition to the "mass-dominated" regime occurs when $\lambda\langle\varphi^2\rangle \sim m_{\rm final}^2$ or, equivalently, when

$$\left(\frac{\kappa^2+1}{\kappa^2}\right)\frac{m_{\rm final}^2}{m_a^2} \sim \frac{\langle\varphi^2\rangle}{f^2} \tag{5.29}$$

is satisfied[5]. In the case that is of interest to us, we have $m_{\rm final}^2/m_a^2 \ll 1$. Therefore, for $m_{\rm final}^2/m_a^2 \lesssim \langle\varphi^2\rangle/f^2 \lesssim 1$ there is an extended intermediate stage of the dynamics, during which the potential can be well approximated as a massless conformal quartic. An important feature of this approximate conformal symmetry is that the evolution equations in the radiation-dominated FRW universe, expressed in terms of comoving coordinates and conformal field and time variables, are the same as those in a Minkowski spacetime. Thus the analysis from chapter 3 of the NTFPs can be directly applied here.

We now present the numerical studies of the ALP dynamics and the GW production in the considered model. The simulations were performed as described

---

[5] For $\kappa \gtrsim 1$ the term in the brackets (5.29) is of order one.

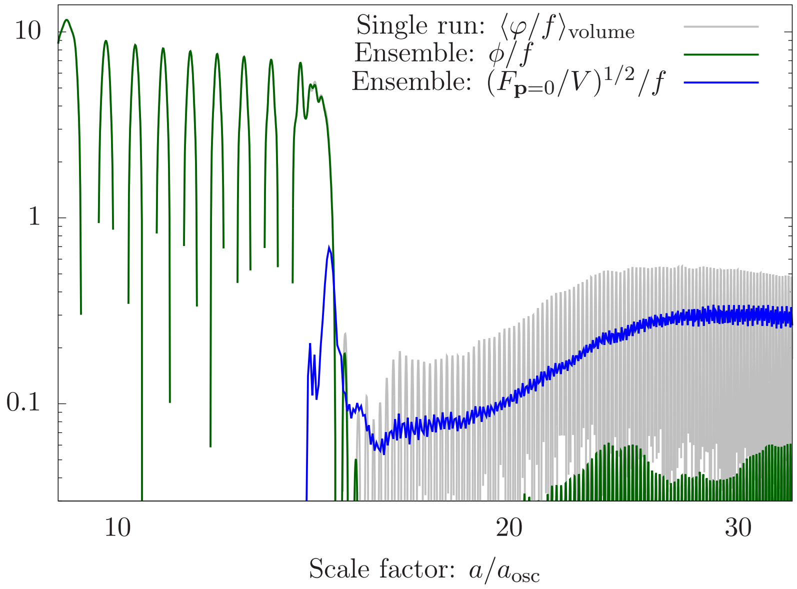

FIGURE 5.7: The collapse of the ALP field and condensation in the presence of repulsive self-interactions. The green line corresponds to the one-point function, the blue line to the zero-momentum mode of the two-point function and the gray line represents the volume average of the field within one classical simulation. We employ $m_b = 10^{-3} m_a$.

in section 5.2.3, except that the "double-cosine" potential (5.26) was used. We set $m_{\text{final}} = 10^{-3} m_a$ in this section. We use $\kappa = 3$, $\phi_1/f = 200$ and $H_I/f = 10^{-10}$ in this and the following subsections.

It is important that the modification of the potential changes the sign of the quartic coupling, making it repulsive.[6]. Such interactions induce the build-up of a homogeneous condensate after fragmentation, as it was explained in section 3.3.1 of chapter 3.

In the left panel of Fig. 5.6 several snapshots of ALP occupation numbers at different scale factors, as functions of the comoving momentum, are shown. The snapshots of the fractional GW spectrum at the same scale factors are shown in the right panel of that figure. Here the strength of the signal is obtained by estimating the value of $\mathcal{Z}_0^{\text{osc}}$, which is explained in the next subsection.

One observes two main differences in this figure, compared to Figs. 5.3 and 5.4:

- There is a more regular direct energy cascade, compared to the attractive case, which is accompanied by a GW radiation at corresponding momenta. The self-similar evolution of the cascade was studied in section 3.3.2 of chapter 3 and the scaling exponents wer found to be $\beta \approx -1/5$ and $\alpha \approx 4\beta$ (see also [22]).

- In addition to the direct cascade, an inverse cascade emerges transporting particle number to low momenta. As it was explained in section 3.3.1 of chapter 3, the evolution of the inverse cascade also becomes self-similar, with exponents $\beta \approx 1/2$ and $\alpha \approx 3\beta$ (see also [114]). As can be seen, at least in the considered model the inverse cascade does not much GWs.

Both the one-point function $\phi(t)$ and the homogeneous mode of the two-point $F(t,t,\mathrm{p})|_{\mathbf{p}=0}$, extracted from classical-statistical simulations, as well as the volume

---

[6] In the second case r is at most approximately $-1/4$

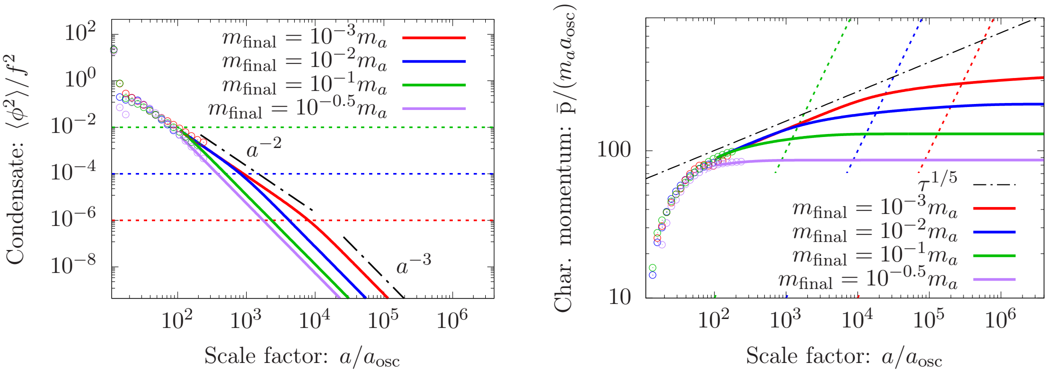

FIGURE 5.8: The amplitude of the condensate $\langle\phi^2\rangle/f^2$ (left) and the characteristic comoving momentum $\bar{\rm p}/(m_a a_{\rm osc})$ (right) as functions of the scale factor for different mass ratios $m_{\rm final}/m_a$, indicated by different colors. The points are from lattice simulations and the solid lines correspond to the extrapolation. In the left panel the dotted lines show the corresponding ratios $m^2_{\rm final}/m^2_a$ for each color. They approximately separate the relativistic ($\propto a^{-2}$) and the nonrelativistic ($\propto a^{-3}$) regimes of the condensate dynamics, as explained in the main text. In the right panel the dotted lines of different colors denote $(m_{\rm final}/m_a)(a/a_{\rm osc})$, such that their intersection with the corresponding solid line is at $\bar{\rm p}_{\rm phys} \approx m_{\rm final}$. The dashed black line indicates the $\tau^{1/5}$ growth of $\bar{\rm p}$, observed at early times in that plot. We employ $\phi_1/f = 200$, $\kappa = 3$ and $H_I/f = 10^{-10}$.

averaged field from a single classical simulation are shown in Fig. 5.7, as functions of the scale factor, for $m_{\rm final} = 10^{-3} m_a$. The difference of these two configurations was explained in section 3.3.1 of chapter 3. Remarkably, the fragmentation of the ALP field is accompanied by a gravitational signal of a similar strength as in the attractive case. In other words, even though a quasi-homogeneous field is re-created after fragmentation, this process is fast enough to produce a strong signal.

A smaller mass near the bottom of the potential requires a longer simulation of the dynamics, which becomes increasingly difficult to perform on a lattice. A rough way to calculate the prefactor Z^0_{osc} would be to use the latest available ALP spectrum from the simulation for later times of the dynamics. This approximation, however, neglects the direct cascade of the distribution which additionally extends the ultrarelativistic phase. Instead, as explained in the next subsection, we describe the dynamics of the direct cascade by assuming its self-similar evolution and solving the kinetic equation for the characteristic momentum scale.

5.3.3 Simplified kinetic description of the late-time dynamics

The fact that the momentum distribution of ALPs is governed by NTFPs at late times allows us to describe the dynamics in that regime in terms of only few variables. This is done by means of a simplified kinetic description of the dynamics. The details of our method for the simplified description are described in the appendix C. Here we summarize the main ideas and present the results.

We describe the dynamics of the direct cascade by assuming its self-similar evolution and solving the kinetic equation for the characteristic momentum scale $\bar{\rm p}(a)$. We also keep track of the occupation number at the characteristic momentum $\bar{n}(a)$, which is related to the momentum via energy conservation, and the condensate amplitude $\langle\phi^2(a)\rangle$ for which we solve approximate classical equations of motion.

In the left panel of Fig. 5.8 the extrapolated condensate amplitude $\langle\varphi^2\rangle/f^2$ is shown with solid lines as a function of the scale factor. The points at early times are from the lattice simulations. Different colors correspond to different values of $m^2_{\rm final}/m^2_a$. These values are also shown in the plot with the dotted lines in corresponding colors. One observes the transition from the quartic-dominated relativistic regime, characterized by an approximately constant $\langle\varphi^2_c\rangle$, to the mass-dominated nonrelativistic regime during which $\langle\varphi^2\rangle \propto a^{-3}$. As it was mentioned in the previous subsection, the transition between these regimes happens approximately when (5.29) is satisfied i.e. when the solid line intersects the dotted line.

In the right panel of Fig. 5.8 the extrapolated evolution of the characteristic comoving momentum $\bar{\rm p}/(m_a a_{\rm osc})$ is shown with solid lines for the same values of the mass ratios as in the left panel. The points of corresponding color at early times are from the lattice simulation. One indeed observes the $\propto \tau^{1/5}$ growth at early times. The growth slows down once the bottom mass becomes important i.e. when the transition to the nonrelativistic regime in the left panel occurs. The characteristic momenta at this point are still relativistic. This can be seen by comparing the solid lines to the dotted lines of corresponding colors, which denote $(m_{\rm final}/m_a)(a/a_{\rm osc})$. The intersection of these two lines corresponds to

$$\bar{\rm p}/a \approx m_{\rm final},$$

i.e. the characteristic high momentum modes becoming nonrelativistic.

Our extrapolation allows to keep track of the equation of state of the system. We do this by re-scaling the momentum occupation numbers according to $\bar{\rm p}(a)$ and $\bar{n}(a)$, and calculating the energy and the pressure of both components of the system. Using Eq. (4.23), the equation of state parameter can be written as

$$w = \frac{p_c}{\rho_c} = \frac{p_{\phi,c} + V^{-1}\int_{\mathbf{p}} n_{\rm p}({\rm p}^2/3\omega_{\rm p})}{\rho_{\phi,c} + V^{-1}\int_{\mathbf{p}} n_{\rm p}\omega_{\rm p}}, \tag{5.30}$$

where, for simplicity, we use conformal variables.

Calculated, in this way, $w(a)$ is shown in Fig. 5.9 for the same values of the mass ratios as in Fig. 5.8. The points of corresponding color at early times are from the lattice simulation. We average w over the oscillation period to get rid of its oscillations. The plot demonstrates the expectation that the ALPs exhibit an intermediate phase with $w = 1/3$. The transition to $w = 0$ is completed when the high momentum modes become nonrelativistic. Integration of $w(a)$ gives the values of $\mathcal{Z}_0^{\rm osc}$, used for calculation of the GW spectra.

We note that, particularly for the green and purple lines in Fig. 5.9, corresponding to $m_{\rm final} = 10^{-1}m_a$ and $m_{\rm final} = 10^{-0.5}m_a$ respectively, we have a sizeable overlap between the numerical data and the analytic extrapolation and we see a good agreement. While, in part, this is due to the involved fitting of parameters between the simulation and the analytical approximation, nevertheless, we take it as an indication of the validity of our approximation.

5.3.4 Enlarged parameter space for the GW signal

Below we present the main numerical results of this section. They are summarized in Fig. 5.10, where the GW spectra, extracted from the numerical simulations for the latest times, are shown. At these times the ALP field has already fragmented and most of the GWs were produced much earlier.

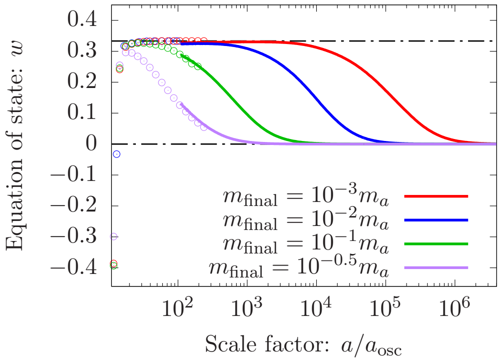

FIGURE 5.9: The equation of state parameter $w = p/\rho$ as a function of the scale factor for different mass ratios $m_{\rm final}/m_a$, indicated by different colors. The points are from lattice simulations and the solid lines correspond to the extrapolation. We employ the same parameters as in Fig. 5.8.

The gold curves correspond to the simple potential (3.1), such that $m_{\rm final} = m_a$, and the solid and the dashed lines correspond to different values of the mass. The corresponding parameter space for the gravitational signal is indicated by the envelope line of the same color.

The remaining curves in Fig. 5.10 correspond to the late-time spectra of GWs in the model of (5.26), such that $m_{\rm final} \ll m_a$. Each color corresponds to a particular value of the mass ratio $m_{\rm final}/m_a$. One indeed observes the increasing range of the signal in the parameter space as this ratio is being decreased, consistent with the expectation from our analytical estimate (5.22). Remarkably, already for $m_{\rm final} = 10^{-3} m_a$ the range of the signal overlaps with the planned sensitivity of pulsar timing arrays, i.e. the SKA [78, 195]. In particular, the solid red curve corresponds to

$$m_{\rm final} = 10^{-16} {\rm eV}, \quad r = 10^{-3} \qquad ({\rm SKA}).$$

BBO and LISA: It is possible to extend the signal range even further, up to the future sensitivities of space-based interferometers, although this requires an even stronger tuning of the mass near the bottom. In particular, BBO [79] and LISA [200]) are most sensitive to signals peaked at around $\nu \sim 10^{-1}$Hz and $\nu \sim 10^{-3}$Hz, respectively. It follows from the analytical estimate (5.21) (using $\eta_\star \sim 10$ as before) that the ALP masses m_a most relevant for these detector are

$$m_a \sim 40\,{\rm eV} \text{ for BBO}, \qquad m_a \sim 10^{-2}\,{\rm eV} \text{ for LISA}.$$

From the planned sensitivity of BBO, $\Omega_\star \sim 10^{-15}$, and that of LISA, $\Omega_\star \sim 10^{-12}$, the corresponding enhancement factor $\mathcal{Z}_0^{\rm emit}$ can be estimated using (5.22) to be $\mathcal{Z}_0^{\rm emit} \sim 2 \times 10^{-11}$ and $\mathcal{Z}_0^{\rm emit} \sim 6 \times 10^{-11}$, respectively. The final step is to determine the mass ratios $r = m_{\rm final}/m_a$ which lead to such values of the enhancement factor. Here we estimate the dependence $\mathcal{Z}_0^{\rm emit}(r)$ analytically. To this end, we note that, as it follows from the definition in Eq. (4.27), $\mathcal{Z}_0^{\rm emit}(r) \propto a_{\rm nr}^{-1}(r)$, where $a_{\rm nr}(r)$ is the scale factor at which the transition to the nonrelativistic regime takes place for given r. The latter can be estimated from the condition

$$m_{\rm final}(r) = m_a r \sim \frac{\bar{\rm p}(a_{\rm nr}(r))}{a_{\rm nr}(r)} \propto a_{\rm nr}^{-4/5}(r),$$

where we use the form of the self-similar evolution $\bar{\rm p}(a) \propto \tau^{1/5}(a) \propto a^{1/5}$. This

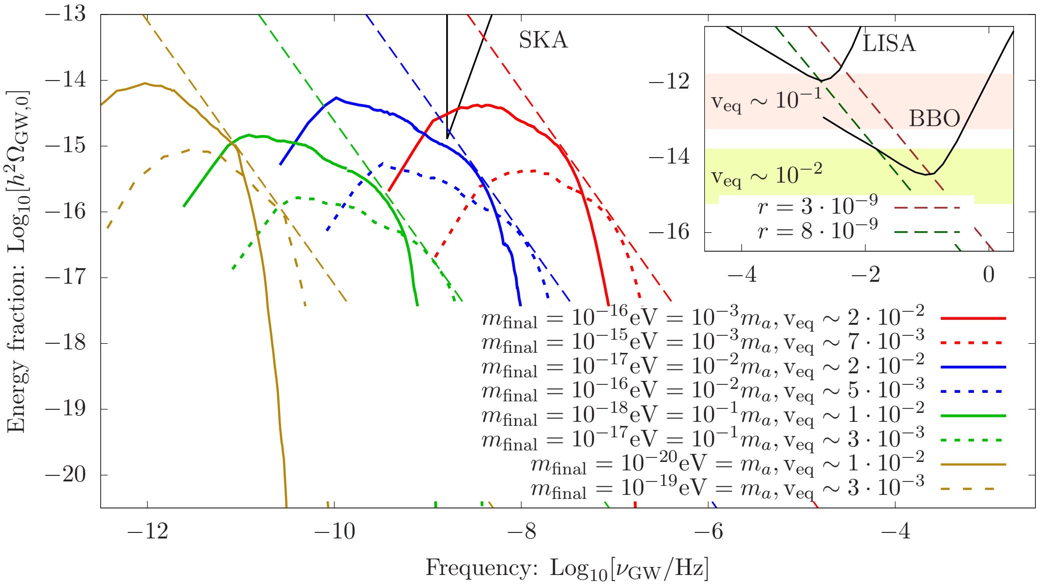

FIGURE 5.10: GW spectra in models with an extended ultrarelativistic phase. The spectra are shown for several values of the mass with different colors corresponding to different mass ratios $r = m_{\text{final}}/m_a$. The golden color corresponds to the standard monodromy potential (3.1) and attractive self-interactions, also shown in Fig. 5.5. The dashed slopes indicate the envelopes of the signal strength as in Fig. 5.5. The inset shows analytical estimates for the signal envelopes at smaller values of r, as explained in section 5.3.4. The sensitivities of relevant GW experiments are indicated with solid black lines according to [195] and the estimated typical velocities at matter-radiation equality are stated. We employ $\phi_1/f = 200, \kappa = 3$ and $H_I/f = 10^{-10}$.

implies a simple dependence $\mathcal{Z}_0^{\text{emit}}(r) \propto r^{5/4}$, and, using the already calculated values of $\mathcal{Z}_0^{\text{emit}}$ for $r \geq 10^{-3}$ we arrive at the following estimates for the relevant masses that can lead to a detectable signal,

$$m_{\text{final}} \sim 10^{-8}\text{eV},\ r \sim 3 \times 10^{-9}\ (\text{BBO}), \qquad m_{\text{final}} \sim 10^{-11}\text{eV},\ r \sim 6 \times 10^{-9}\ (\text{LISA}).$$

The signal boundaries based on these two values of r are shown in the inset of Fig. 5.10, where also the sensitivity curves of the corresponding detectors are shown with black continuous lines [195].

5.3.5 Constraints from structure formation

So far we have discussed the constraints on the GW signal strength based on the amount of DM in the universe. Obviously, there are additional constraints, mostly from large-scale structure formation probes. These require ALPs to be sufficiently cold/pressureless to participate in structure formation as discussed in this section.

After the fragmentation the ALP field splits into a quasi-homogeneous condensate and high-momentum particles. Initially the particles take most of the energy of the system, more than 90%. However, as the simulations show, at the end of nonlinear dynamics this fraction decreases significantly and becomes of the same order. The reason for this is the late phase of the dynamics, during which the condensate already dilutes as $\propto a^{-3}$, however, the high-momentum particles still need to redshift to become nonrelativistic. We discuss the constraints for successful structure formation for both types DM configurations.

Constraints on the homogeneous component: The authors of [201] derived constraints, based on the data on structure formation on linear scales $\mathrm{k} \lesssim 0.2h/\mathrm{Mpc}$, for DM in the form of a homogeneously oscillating scalar field with a potential $U(\phi) = m^2\varphi^2/2 + \lambda\varphi^4/4$. They obtained the following bound on the mass and the coupling of the field,

$$\log_{10}(\lambda) < -91.86 + 4\log_{10}\Big(\frac{m}{10^{-22}\mathrm{eV}}\Big). \tag{5.31}$$

For sufficiently small masses at the bottom, the potential (5.26) can be approximated as quartic to very good precision at late times. We can thus directly apply the above bound to the considered setup. Substituting

$$m \to m_b, \qquad\qquad \lambda \to -\frac{\lambda(16r+1)}{3!} \approx \frac{\lambda}{2} \approx \frac{m_a^2}{2f^2},$$

one arrives at

$$2\log_{10}\Big(\frac{m_a}{m_b}\Big) + 1.56 < 2\log_{10}\Big(\frac{m_b}{10^{-22}\mathrm{eV}}\Big) + 2\log_{10}\Big(\frac{f}{10^{14}\mathrm{GeV}}\Big). \tag{5.32}$$

For given values of the masses this represents a lower bound on the decay constant (and for fixed ϕ_1/f also on the misalignment field value ϕ_1). For the situations indicated by solid lines in Fig. 5.10 this bound implies $f > 6 \times 10^{11}\mathrm{GeV}$, while for the ones indicated by dashed lines $f > 6 \times 10^{10}\mathrm{GeV}$. The actual values of the decay constant are about $2 - 3 \times 10^{14}\mathrm{GeV}$ for the solid lines and about $1 - 2 \times 10^{14}\mathrm{GeV}$ for the dashed lines. The constraints are thus satisfied.

We are not aware of similar constraints from nonlinear structure formation on smaller scales, which are expected to be stronger.

Constraints on the typical velocities: The typical nonrelativistic velocities of ALPs at matter-radiation equality are related to their characteristic comoving momentum $\bar{\mathrm{p}}$ via Eq. (4.14) which, for the considered potential with a small mass at the bottom, generalizes to

$$\mathrm{v}_{\mathrm{eq}} = \frac{\mathrm{p}}{a_{\mathrm{eq}}m_{\mathrm{final}}} = 2.63\,\eta\sqrt{\frac{10^{-28}\mathrm{eV}}{m_{\mathrm{final}}}}\frac{\mathcal{F}^{1/3}(T_{\mathrm{osc}})}{\mathcal{F}^{1/3}(T_{\mathrm{eq}})}\sqrt{\frac{m_a}{m_{\mathrm{final}}}}, \tag{5.33}$$

The constraints on the velocities of ALP DM were already discussed in section 4.3.1 of the previous chapter. Surveys of structure formation on linear scales require $\mathrm{v}_{\mathrm{eq}} \lesssim 10^{-1}$. A stronger bound appears from the Lyman-α forest data on a nonlinear structure formation. Here one typically expects $\mathrm{v}_{\mathrm{eq}} \lesssim 10^{-3}$, however, complicated numerical simulations are required to make the constraints more precise.

The typical velocities at matter-radiation equality were estimated using (5.33), from the late-time asymptotic values of $\bar{\mathrm{p}}$, which are shown in the right panel of Fig. 5.8. For the solid curves ($h^2\Omega_{GW} \sim 10^{-15} - 10^{-14}$) in Fig. 5.10 these typical velocities are $\sim 10^{-2}$, whereas for the dotted lines $v_{\mathrm{eq}} \sim 10^{-3} - 10^{-2}$. The constraints from a linear structure formation are clearly satisfied in this case. The situation for a nonlinear structure formation is less clear and the particles might turn out to be somewhat warmer. It is also important to keep in mind that a significant fraction of the energy density of ALPs is the form of a homogeneous condensate, which is expected to decrease the ALP pressure and soften the constraints. An answer to this question requires further investigation.

The anticipated bands for the values of typical velocities at matter-radiation equalities $\mathrm{v}_{\mathrm{eq}} \sim 10^{-1}$ and $\mathrm{v}_{\mathrm{eq}} \sim 10^{-2}$ are indicated by the pink and yellow colors in the inset of Fig. 5.10. Note that although less fine-tuning is required for the LISA case, the typical velocities near matter-radiation equality are quite large and therefore may cause trouble with nonlinear structure formation.

5.4 Summary

In this chapter we described how GW detection experiments can detect signatures of the nonperturbative production of ALP DM. We have estimated the stochastic GW background both analytically and numerically. Despite the strong constraints on the signal, arising from the requirement of not over-producing the DM, the signal from the fragmentation can be sufficiently strong to be observed by GW experiments. This can happen if ALPs exhibit an extended relativistic phase of dynamics after the fragmentation, a scenario which we studied in detail in this work by assuming a small mass near the bottom of the potential.

The scenario with large mass hierarchies, discussed in this chapter, provides an efficient mechanism for enhancing the GW signal from ALP DM. A similar mechanism is provided if the ALPs have a significant coupling to the dark photon sector. The GW background produced from the decay of ALPs into dark photons was calculated in [198, 202]. The authors, however, relied on a linearzied analysis. In contrast, in our case the nonlinear aspects play a crucial role for the fragmentation dynamics of monodromy ALPs.

Our main findings are summarized in Fig. 5.10, which contains the relevant GW spectra. The signal can be detectable by pulsar timing arrays for ALPs with $m_{\text{final}} = 10^{-16}\text{eV}$. Here a fine-tuning of the order 10^{-3} of the mass at the bottom of the potential is required. An even more severe fine tuning of the order of 10^{-10} would bring the signal into the sensitivity range of space-based interferometers such as BBO ($m_{\text{final}} = 10^{-8}\text{eV}$) or LISA ($m_{\text{final}} = 10^{-11}\text{eV}$). We have also confirmed that the constraints from the linear structure formation are satisfied in this case. The situation with the nonlinear structure formation is less clear and requires further investigation. Particularly, it would be interesting to understand the role of a homogeneous condensate on structure formation and find possible observational signatures.

Chapter 6

Simulating cosmological dynamics with ultracold quantum gases

The material presented in this chapter is based on work in preparation [4], done in collaboration with Jürgen Berges, Kevin Geier, Philipp Hauke, Markus Oberthaler, as well as the members of the "BECK" experiment. Kevin Geier and I are the co-first authors of the upcoming publication. My contribution to that work was focused on investigating the connections of the considered system to cosmological dynamics, employing the methods of nonequilibrium QFT for the analytical description of primary and secondary instabilities in the system, and the study of the self-similar solutions from the kinetic description. The figures of section 6.5.3 are taken from that work.

As it was discussed in the previous chapters, the dynamics of scalar fields in the early universe can be very rich and is lacking a complete understanding. Over the recent years, interest has increased in simulating various aspects of the dynamics in the early universe in table-top experimental setups [203, 204]. In such systems the characteristic energy scales are much lower, which allows one to realize and test phenomena that are otherwise inaccessible.

In this chapter we argue that modern experiments with ultracold atomic Bose gases provide a powerful platform for the simulation of the nonperturbative scalar field dynamics in the post-inflationary universe. With the help of advanced cooling techniques sufficiently low temperatures can be achieved in these experiments, so that most of the atoms are brought to the ground state, leading to the formation of an atomic BEC. Such a coherent state mimics the universe right after cosmic inflation, when the energy was dominantly stored in a homogeneous "inflaton condensate", as well as the "dark matter condensate" formed via the misalignment mechanism. Remarkably, the toolbox of nonequilibrium QFT, that was described in chapter 2 for relativistic systems, can also be used to describe the dynamics of atomic Bose gases [205].

An important restriction on the dynamics of an atomic BEC arises from the conservation of the total number of atoms, which prevents the resonant decay of the condensate. We propose a temporal modulation of the interatomic interaction strength, which can be experimentally achieved with the help of magnetic fields [58], in order to incorporate effects that, in the relativistic system, lead to a resonant particle production. The modulation allows us to observe the linear, as well as the secondary amplification of the sound waves on top of the BEC, as well as the subsequent turbulent energy transport towards higher momenta. We analyze the self-similar evolution associated with this NTFP in an atomic gas by means of a kinetic description. The final stages of the dynamics after switching off the modulation, when the system expected to relax to thermal equilibrium, are not captured by semiclassical approximation schemes, which particularly motivates an experimental study of this process.

The chapter is organized as follows. In section 6.1 we provide a brief review of the quantum field theoretical description of ultracold atomic gases, including the 2PI framework and the equations of motion. In section 6.2, we propose how an expanding d-dimensional FRW geometry for a Bose gas can be encoded into the time-dependence of its interaction strength. We proceed by describing how the equations, governing the dynamics of an atomic Bose gas, can be derived as an effective nonrelativistic description of scalar field dynamics in an FRW universe in section 6.3. The modulation of the scattering length, which leads to a resonant amplification of the fluctuations on top of the BEC is discussed in section 6.4. This modulation drives the system far from equilibrium and, in section 6.5, we study the subsequent approach of the system to a NTFP and the associated universal energy transport in momentum space, both in the presence of the modulation as well as after switching it off. The interplay between expansion and thermalization for our setup is also discussed. Finally, we conclude in section 6.6. We keep $\hbar$ and c in all expressions of this chapter.

6.1 Field-theoretical methods for ultracold atoms

First atomic BECs have been realized already in 1995, in experiments with the vapors of rubidium [206], sodium [207] and lithium [208]. Since then the studies of atomic quantum gases have rapidly evolved from an exotic field of research into an important part of modern physics. Such systems are particularly well suited for the investigation of quantum many-body dynamics in its various regimes for a number of reasons, including the possibility to control and manipulate the atoms using electric and magnetic fields, the experimental accessibility of typical timescales of interest and the powerful imaging techniques available to track the dynamics. A great overview of the physics of ultracold atoms can be found in [57].

Importantly, many methods of QFT have proven to be successful in describing the physics of ultracold atomic systems [205, 209–212]. This, combined with the above-mentioned advantages, suggests the possibility to utilize such systems as experimental simulators of QFT, with potential applications to the early universe cosmology and the prospect of extending the existing studies to regimes in which analytical and numerical investigation becomes difficult.

In this section we briefly review the theoretical framework for the description of the many-body dynamics of an atomic quantum gas, extending some of the concepts from section 2.3 to the considered system.

6.1.1 Microscopic description

The many-body Hamiltonian of a dilute atomic Bose gas has the form [57, 213]

$$\begin{aligned}\hat{H}_{\mathrm{MB}} =& \int \mathrm{d}^3\mathrm{x}\Big(\hat{\Psi}^\dagger(t,\mathbf{x})\Big[-\frac{\hbar^2}{2m}\Delta + V_{\mathrm{trap}}(\mathbf{x})\Big]\hat{\Psi}(t,\mathbf{x})\Big)\\ &+\frac{1}{2}\int \mathrm{d}^3\mathrm{x}\mathrm{d}^3\mathrm{y}\hat{\Psi}^\dagger(t,\mathbf{x})\hat{\Psi}^\dagger(t,\mathbf{y})V_{(2)}(\mathbf{x}-\mathbf{y})\hat{\Psi}(t,\mathbf{x})\hat{\Psi}(t,\mathbf{y}). \qquad (6.1)\end{aligned}$$

Here m is the mass of atoms and $\hat{\Psi}$ denotes the field operator, which satisfies the commutation relations,

$$[\Psi(t,\mathbf{x}),\Psi^\dagger(t,\mathbf{y})]=\delta(\mathbf{x}-\mathbf{y}),\qquad[\Psi(t,\mathbf{x}),\Psi(t,\mathbf{y})]=[\Psi^\dagger(t,\mathbf{x}),\Psi^\dagger(t,\mathbf{y})]=0.\tag{6.2}$$

In general $\hat{\Psi}$ can be a multi-component field, if the nuclear and electronic spin degrees of freedom of the atoms are taken into account (see also [214, 215] for the description of spinor Bose gases). In this chapter we restrict ourselves to the most common type of atomic BECs [206–208] with no internal degrees of freedom. The first line in (6.1) contains the free part of the Hamiltonian, which includes the kinetic term and the trapping potential V_{trap}. In the second line the two-body interaction term is written. Due to the diluteness, the three- and higher-body interactions can be neglected. Moreover, at low energies the two-body term can be approximated by an effective contact interaction,

$$V_{(2),\text{eff}}(\mathbf{x}-\mathbf{y})=g\delta(\mathbf{x}-\mathbf{y}),$$

characterized by a single coupling $g=4\pi a_s\hbar^2/m$, proportional to the scattering length a_s of the atoms.

A very tight confinement in some direction can induce effective low dimensional (1d or 2d) geometries. At the same time, the sufficient shallowness of the trapping potential in the remaining directions allows one to ignore the effects of the trap for the dynamics that happens on smaller length scales. For simplicity, we restrict our attention to d-dimensional homogeneous systems in this chapter.

The interactions between alkali atoms can be efficiently adjusted by applying external magnetic fields. This becomes available due to the presence of so-called Feshbach resonances [216], describing a resonant scattering between the atoms [217]. Such resonances have been successfully exploited in experiments with ultracold atoms, allowing the investigation in a controlled manner of both the strongly interacting and the noninteracting regimes. In this work we allow for such a time-dependence of the coupling, $g\to g(t)$.

The microscopic description of a Bose gas can alternatively be formulated in terms of a functional path integral, as in (2.23). The classical action for a nonrelativistic Bose gas has the form [205]

$$S[\Psi]=\int\mathrm{d}^d\mathrm{x}\Big[\frac{i\hbar}{2}(\Psi^\dagger\dot{\Psi}-\dot{\Psi}^\dagger\Psi)-\frac{\hbar^2}{2m}\nabla\Psi^\dagger\nabla\Psi-\frac{g}{2}(\Psi^\dagger\Psi)^2\Big].\tag{6.3}$$

The classical equations of motion, derived from this action, are of the form of a nonlinear Schrödinger equation,

$$i\hbar\frac{\partial\Psi}{\partial t}=-\frac{\hbar^2}{2m}\Delta\Psi+g\Psi^\dagger\Psi\Psi,\tag{6.4}$$

referred to as the Gross-Pitaevskii equation (GPE).

6.1.2 Nonequilibrium dynamics

The powerful toolbox of nonequilibrium QFT, that was described in section 2.3 for relativistic scalar fields, can also be applied to ultracold atomic gases. In particular, the classical(-statistical) approximation becomes valid in the regime of weak couplings and large occupation numbers. Such a description is then governed by the classical evolution equations (6.4) and is also referred to as the truncated Wigner approximation [211, 212].

Furthermore, the 2PI effective action can be constructed for the nonrelativistic system, as it was done in [205, 209, 218], allowing one to employ systematic nonperturbative approximation schemes. As described in [205], this can be conveniently done by switching to the real and imaginary parts of the complex field operator,

$$\hat{\varphi}_1(x) = \sqrt{2}\,\mathrm{Re}\hat{\Psi}(x), \quad \hat{\varphi}_2(x) = \sqrt{2}\,\mathrm{Im}\hat{\Psi}(x),$$

treating them as the two components of an $\mathcal{O}(2)$-symmetric field theory.

The presence of a nonvanishing one-point function $\phi_i(x) = \langle\hat{\varphi}_i(x)\rangle$ generates effective cubic interactions (cf. Eq. (2.31)) in addition to the quartic one, which follows from the shift $\varphi_i \to \phi_i + \varphi_i$ in the action (6.3). The resulting interaction part of the action, in terms of the fields φ_i, reads

$$S_{\mathrm{int}}[\varphi, \phi] = \left(-\frac{g}{8}\right)\int_{x,C}\Big[\varphi_i(x)\varphi_i(x)\varphi_j(x)\varphi_j(x) + 4\phi_i(x)\varphi_i(x)\varphi_j(x)\varphi_j(x)\Big]. \tag{6.5}$$

The 2PI equations of motion can be derived by a variational principle from the 2PI effective action, in a complete analogy to the relativistic case, discussed in section 2.3. For the spectral and statistical components of the full propagator

$$G_{ij}(x,y) = \langle\mathcal{T}\hat{\varphi}_i(x)\hat{\varphi}_j(y)\rangle - \phi_i(x)\phi_j(y) = F_{ij}(x,y) - \frac{i}{2}\mathrm{sgn}_C(x^0 - y^0)\rho_{ij}(x,y),$$

the corresponding equations have the form [205]

$$\begin{aligned}
[-i\hbar\sigma_{2,ik}\partial_{x_0} - M_{ik}(x)]F_{kj}(x,y) &= \int_{t_0}^{x_0} dz\Sigma^{\rho}_{ik}(x,z)F_{kj}(z,y) - \int_{t_0}^{y_0} dz\Sigma^{F}_{ik}(x,z)\rho_{kj}(z,y),\\
[-i\hbar\sigma_{2,ik}\partial_{x_0} - M_{ik}(x)]\rho_{kj}(x,y) &= \int_{y_{t_0}}^{x_0} dz\Sigma^{\rho}_{ik}(x,z)\rho_{kj}(z,y),
\end{aligned} \tag{6.6}$$

where

$$M_{ij}(x) = \delta_{ij}\Big[-\frac{\hbar^2\Delta_{\mathbf{x}}}{2m} + \frac{g}{2}\Big(\phi_k(x)\phi_k(x) + F_{kk}(x,x)\Big)\Big] + g\Big(\phi_i(x)\phi_j(x) + F_{ij}(x,x)\Big). \tag{6.7}$$

Note that the "tadpole" diagram, which is the only local contribution to the self-energy, is explicitly included in $M_{ij}(x)$.

Similar to their relativistic counterparts, the nonrelativistic 2PI equations of motion can be recast into a form similar to the Boltzmann equation, under additional assumptions such as a relatively smooth time evolution, an effective loss of memory and "on-shell" quasiparticles. This derivation can be found in [209, 210, 219].

6.2 Expanding spacetime

An important ingredient of cosmology is the expansion of the universe, which is well described by the FRW metric, characterized by a scale factor $a(t)$. In this section we propose how such an expanding geometry can be incorporated into an ultracold atomic gas. As we demonstrate, a time-dependent rescaling of the variables allows us to map the dynamics of an expanding Bose gas into that of a static one with a time-dependent scattering length. This mapping removes the necessity to expand the trap and lifts the associated restrictions on the size of the experiment and on the atomic densities.

Recall that the (classical) equations of motion of a (minimally coupled) real scalar field $\varphi(t, \mathbf{x})$ in an FRW universe have the form

$$\frac{1}{c^2}\ddot{\varphi} + \frac{1}{c^2}dH\dot{\varphi} - \frac{\Delta\varphi}{a^2} + \frac{\delta U}{\delta\varphi} = 0. \tag{6.8}$$

Here we consider a slightly more general case of arbitrary d spatial dimensions, instead of $d = 3$. The above equation demonstrates the two modifications compared to Minkowski spacetime, that are the presence of the "Hubble" friction term, accounting for the dilution of the field due to expansion, and the a^{-2} factor in front of the gradient term, arising because comoving coordinates are used. The substitution to conformal variables $d\tau = dt/a$ and $\varphi_c = a^{(d-1)/2}\varphi$ allows to get rid of both modifications at the cost of making the mass and the coupling parameters, contained in the potential, $a(t)$-dependent (see e.g. section 4.2.2).

The dynamics of an ultracold atomic Bose gas is instead well described by nonrelativistic equations of motion (6.4). One way of incorporating expansion in such a system is to physically expand the gas by changing the trapping potential [220–222], as schematically illustrated in the left part of Fig. 6.1. This has been done in experiments with a ring-shaped condensate in [221], where the authors even observed preheating-like dynamics after rapidly expanding the trap. While this approach is the most straightforward, in practice there are usually limitations related to the size of the system, making the implementation intricate.

Alternatively one can maintain a fixed trapping potential, associating the spatial distances with the comoving ones. In that case the GPE (6.4) should be modified to the following form (see e.g. [223]),

$$i\hbar\frac{\partial\Psi}{\partial t} = -\frac{\hbar^2}{2ma^2}\Delta\Psi + g\Psi^\dagger\Psi\Psi - i\hbar\frac{d}{2}H\Psi. \tag{6.9}$$

Here one observes a a^{-2} dependence in the gradient term analogous to the relativistic case, whereas the "Hubble" friction term manifests itself as a nonhermitean term in the Hamiltonian. This approach is illustrated in the central part of Fig. 6.1. Equation (6.9) corresponds to the nonrelativistic limit of (6.8) in the presence of a quartic self-interaction, as it is demonstrated in section 6.3.

Remarkably, expansion in Bose gases can also be encoded solely into the time-dependence of the scattering length. This is achieved after performing the following time-dependent rescaling of the field and time variables in (6.9),

$$\Psi = a^{-d/2}\widetilde{\Psi}, \qquad dt = a^2 d\eta, \tag{6.10}$$

which leads to the standard form of GPE with an $a(t)$-dependent quartic coupling,

$$i\hbar\frac{\partial\widetilde{\Psi}}{\partial\eta} = -\frac{\hbar^2}{2m}\Delta\widetilde{\Psi} + \left(\frac{g}{a^{d-2}}\right)\widetilde{\Psi}^\dagger\widetilde{\Psi}\widetilde{\Psi}. \tag{6.11}$$

This approach is illustrated in the right part of Fig. 6.1. In other words, the field re-definition factors out the overall dilution of the fields, and the factor a^{-2} in front of the kinetic term is compensated by the new time η, which will be referred to as

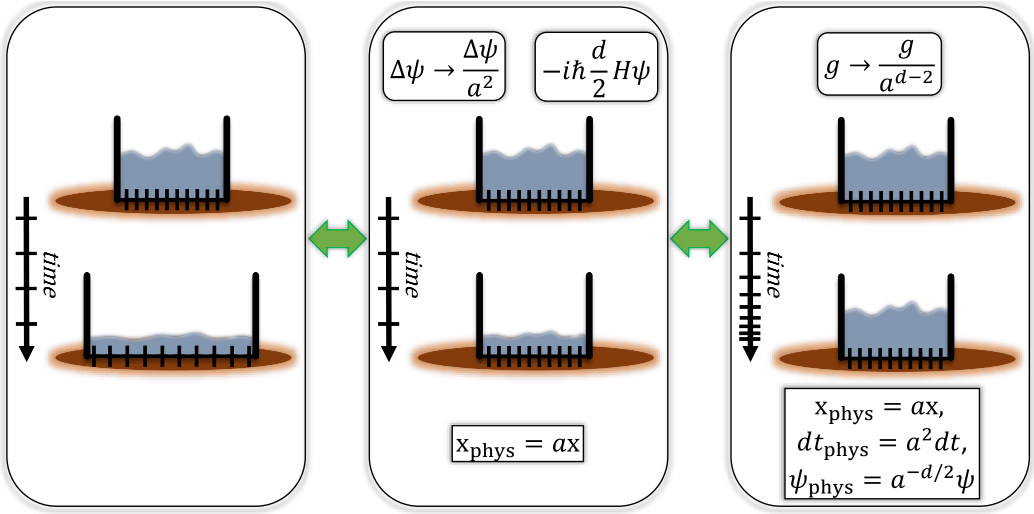

FIGURE 6.1: Schematic illustration of a trapped Bose gas and the three ways of incorporating expansion: by expanding the trapping potential (left), by adding a nonhermitean (friction) term and modifying the kinetic term (center), by modifying the scattering length (right). The last two cases require additional back-transformation to physical variables.

the lab time, ticking slower with expansion. This transformation is the analogue of the one to conformal variables for relativistic fields.

In this chapter we adopt the last approach. The time-dependence of the scattering length can be tuned experimentally with the help of Feshbach resonances. Importantly, this approach does not involve decreasing atom densities. The absence of physical expansion removes the additional limitations on the size of the experiment and allows the simulation of a wide range of expanding backgrounds.

An important feature of the above transformation is that in the case of two spatial dimensions the quartic coupling remains time-independent after the substitution (6.10). This is a consequence of the scale-invariance of the system for $d = 2$ [224, 225]. In other words, the equations of motion are the same as in the case of a static spacetime. Expansion i.e. the scale factor $a(t)$ enter only the back-transformation to original field variable, as well as to the physical temporal and spatial coordinates. This makes our approach especially efficient for $d = 2$. The scale-invariance is valid in the classical(-statistical) regime and is broken by quantum anomalies [226]. It is the analogue of conformal invariance of the (relativistic) φ^4 theory in $3 + 1$ dimensions [22].

Another interesting property of the above-described mapping is that in the case of sufficiently fast expansion the physical time t can become infinite for a finite value of the lab time η i.e. $\eta(t = \infty) < \infty$. This can be demonstrated on a typical power-law expansion of the form,

$$a(t) = \left(1 + \frac{H_0 t}{\gamma}\right)^{\gamma}, \tag{6.12}$$

which sets $a(0) = 1$ and $H(0) = H_0$. The lab time is then given by

$$\begin{aligned}\eta(t) = \int_0^t d\eta = \int_0^t \frac{dt}{a^2} &= \frac{1}{H_0}\frac{\gamma}{1-2\gamma}\left[\left(1 + \frac{H_0 t}{\gamma}\right)^{1-2\gamma} - 1\right] \\ &= \frac{1}{H_0}\frac{\gamma}{1-2\gamma}\left[a(t)^{\frac{1-2\gamma}{\gamma}} - 1\right],\end{aligned} \tag{6.13}$$

and, if $\gamma > 1/2$, the lab time at which $a = \infty$ and $t = \infty$ depends on the initial value of the Hubble parameter and is given by $\eta(t = \infty) = H_0^{-1}\gamma/(2\gamma - 1)$. This includes the case of expansion in a matter-dominated universe, $\gamma = 2/3$, for which $\tau(t = \infty) = 2/H_0$. It is worth noting that the situation is different for the conformal time τ, introduced in the context of relativistic fields. The latter is defined as $d\tau = dt/a$ and, as a result, becomes infinite with infinite physical time for the expansion both in a matter-dominated and in a radiation-dominated universe.

6.3 Connection to relativistic dynamics

So far the connection between the dynamics of the Bose gas governed by (6.11), as well as (6.9), and that of a relativistic scalar field in a FRW spacetime (6.8) has not been discussed. In the section we derive the mapping between the two descriptions for the case of a scalar potential[1]

$$U(\varphi) = \frac{m^2c^2}{\hbar^2}\frac{\varphi^2}{2} + \frac{\lambda\varphi^4}{4!}. \tag{6.14}$$

The two fields are related via

$$\varphi = \sqrt{\frac{\hbar^2}{2mc}}\Big[\Psi e^{-\frac{i}{\hbar}mc^2t} + \text{h.c.}\Big] = \sqrt{\frac{2\hbar^2}{mc}}\mathrm{Re}\Big[\Psi e^{-\frac{i}{\hbar}mc^2t}\Big], \tag{6.15}$$

whereas the quartic couplings satisfy

$$g = \frac{\lambda\hbar^4}{8m^2c}. \tag{6.16}$$

As we explain below, the mapping is valid in the nonrelativistic regime, for not too strong fields and not too rapid expansion rates. Important relativistic effects that lead to particle production are neglected in this mapping, which leads to the necessity of additional modification in our setup, as explained in the next section.

From (6.15) it follows that the time derivatives of φ can be expressed as,

$$\dot\varphi = \sqrt{\frac{2\hbar^2}{mc}}\mathrm{Re}\Big[\Big(\dot\Psi - \frac{i}{\hbar}mc^2\Psi\Big)e^{-\frac{i}{\hbar}mc^2t}\Big], \tag{6.17}$$

$$\ddot\varphi = \sqrt{\frac{2\hbar^2}{mc}}\mathrm{Re}\Big[\Big(\ddot\Psi - 2\frac{i}{\hbar}mc^2\dot\Psi - \frac{m^2c^4}{\hbar^2}\Psi\Big)e^{-\frac{i}{\hbar}mc^2t}\Big]. \tag{6.18}$$

The cubic term in (6.9) can be written as

$$\varphi^3 = \Big(\frac{2\hbar^2}{mc}\Big)^{3/2}\mathrm{Re}\Big[\Psi e^{-\frac{i}{\hbar}mc^2t}\Big]^3 = \frac{1}{4}\Big(\frac{2\hbar^2}{mc}\Big)^{3/2}\mathrm{Re}\Big[(3|\Psi|^2\Psi e^{-\frac{i}{\hbar}mc^2t} + \Psi e^{-\frac{i}{\hbar}mc^2t})^3\Big]. \tag{6.19}$$

Inserting everything into the equations of motion (6.8) with the potential of (6.14) and noting that the third term in (6.18) is canceled with the mass term, one arrives

---

[1] We reinstate the factors of $\hbar$ and c, which can be done by dimensional analysis.

at

$$\mathrm{Re}\left[\Big[\frac{1}{c^2}(\ddot{\Psi} - \frac{2i}{\hbar}mc^2\dot{\Psi}) + \frac{1}{c^2}3H(\dot{\Psi} - \frac{i}{\hbar}mc^2\Psi) - \frac{\Delta\Psi}{a^2} + \right.$$
$$\left. \frac{\lambda}{24}\left(\frac{2\hbar^2}{mc}\right)\left(3|\Psi|^2\Psi + \Psi^3 e^{-2\frac{i}{\hbar}mc^2t}\right)\Big]e^{-\frac{i}{\hbar}mc^2t}\right] = 0, \tag{6.20}$$

where we consider a more general $d+1$-dimensional spacetime, leading to the substitution $3H \to dH$ in the equations of motion.

Nonrelativistic limit: So far no approximations have been employed. We now make an assumption that the dominant fraction of the energy of the field arises from oscillation due to the mass term in (6.8). For this several conditions have to be satisfied (see also [20, 114, 115] for the case of a Minkowski spacetime):

1. Not too strong fields, such that the corrections to the mass are subleading. In particular, for the quartic model this means $\lambda\langle\varphi^2\rangle \ll m^2c^2/\hbar^2$.
2. Nonrelativistic typical momenta, $|\mathbf{p}| \ll mc$.
3. Not too rapid expansion, $H \ll mc^2/\hbar$, so that the field is in the regime of performing oscillations with a decaying amplitude rather than in the overdamped regime.

These three assumptions together imply that the function Ψ in (6.15) varies much slower compared to the exponential term,

$$|\Psi| \gg \frac{\hbar}{mc^2}|\dot{\Psi}| \gg \frac{\hbar^2}{m^2c^4}|\ddot{\Psi}|, \tag{6.21}$$

which allows one to neglect the second-order time derivative in the first bracket in (6.20), as well as the first-order time derivative in the second bracket. Moreover, the last term in (6.20) performs rapid oscillations compared to other slowly varying terms and therefore is effectively "averaged out" in the nonrelativistic limit. Note that it is this term that accounts for number-changing processes in relativistic theory, and neglecting it leads to a conserved particle number. What remains in (6.20) are slowly varying terms multiplied by the rapidly oscillating exponent and, therefore, in the above-described limit (6.20) reduces to a complex-valued equation

$$-\frac{2im}{\hbar}\dot{\Psi} - dH\frac{im}{\hbar}\Psi - \frac{\Delta\Psi}{a^2} + \frac{\lambda}{8}\frac{2\hbar^2}{mc}|\Psi|^2\Psi = 0,$$

which is exactly the GPE (6.9) with the quartic coupling g given by (6.16).

The nonrelativistic description of quantum field dynamics in terms of the slowly-varying field Ψ, which was described in this section, automatically leads to an emergent conservation of total particle number. This limit corresponds to the third red circle in Fig. 2.4, which summarizes the effective descriptions of QFT, used in this work. It can thus be concluded that an atomic BEC is a natural quantum simulator for the dynamics of ALP dark matter in the late universe, after the nonrelativistic description becomes applicable.

6.4 Preheating in an atomic BEC

In this section we describe how ultracold atomic gases can be exploited to simulate the dynamics of nonperturbative, resonant particle production in the presence of a strong background field i.e. preheating.

It is tempting to use a homogeneous[2] atomic BEC to mimic the state of the universe after inflation, filled with the homogeneous inflaton field, or the coherent ALP field produced from the vacuum misalignment mechanism. However, the parametric resonance, which is usually responsible for the rapid amplification of fluctuations in those systems, is as such a relativistic effect. The oscillations of the scalar field around the minimum of its potential are averaged out after taking the nonrelativistic limit. The conserved atom number prevents the decay of a nonrelativistic BEC. Hence, in order to observe preheating in an atomic BEC, the system requires some modification.

Several experimental setups have been already proposed to simulate the above-mentioned effect in the context of post-inflationary dynamics. In [227, 228], the authors considered tunnel-coupled 1D BECs and studied oscillations and formation of breathers in their relative phase field, which at low energies is described by the sine-Gordon model. The authors of [229] considered Josephson oscillations of a BEC in a double-well trapping potential and studied quasiparticle creation and thermalization. In [230], two-component 1D BECs were considered and primary and secondary instabilities were analyzed. In [231], the dynamics of 1D BECs after changing their trapping frequency was studied, including the nonseparability of the produced quasi-particle pairs.

Here we propose a temporal modulation of the interatomic interactions to generate a resonant amplification of the sound waves on top of the BEC [59–61], similar to the post-inflationary parametric resonance. We start with writing down the linearized 2PI equations of motion to study the spectrum of the excitations on top of the BEC. We then demonstrate how the fluctuations can be amplified via a periodic modulation of the scattering length and describe the correspondence to the oscillations of the scalar field around the minimum of its potential. The modulation leads both to linear instabilities as well as to the nonlinear, secondary amplification of the fluctuations at later times, as we demonstrate by means of the 2PI equations of motion.

6.4.1 Linearized equations of motion

The spectrum of excitations on top of a BEC and their instabilities can be studied with the help of linearized 2PI equations, obtained by neglecting all loop corrections in Eq. (6.6), where ϕ_i plays the role of the BEC. At that order the statistical propagator and the spectral functions decouple from each other. The equations of motion for the statistical propagator take the form

$$\Big[-i\hbar\sigma_{2,ik}\partial_{x_0} + \delta_{ik}\Big(\frac{\hbar^2\Delta_{\mathbf{x}}}{2m} - \frac{g}{2}\phi_l(x)\phi_l(x)\Big) - g\phi_i(x)\phi_k(x)\Big]F_{kj}(x,y) = 0. \tag{6.22}$$

---

[2] In experiments, the BEC is of course not homogeneous due to the presence of a trapping potential.

It is convenient to introduce the "normal" and the "anomalous" correlation functions, defined as [205]

$$\widetilde{n}(x,y) = \frac{1}{2}\langle\{\hat{\Psi}(x), \hat{\Psi}^\dagger(y)\}\rangle - \langle\hat{\Psi}(x)\rangle\langle\hat{\Psi}^\dagger(y)\rangle = \frac{1}{2}F_{ij}(x,y)(\delta_{ij} + \sigma_{2,ij}), \tag{6.23}$$

$$\widetilde{m}(x,y) = \frac{1}{2}\langle\{\hat{\Psi}(x), \hat{\Psi}(y)\}\rangle - \langle\hat{\Psi}(x)\rangle\langle\hat{\Psi}(y)\rangle = \frac{1}{2}F_{ij}(x,y)(\sigma_{3,ij} + i\sigma_{1,ij}), \tag{6.24}$$

which are complex-valued functions. Inserting the above definitions into Eq. (6.22) leads to the following pair of equations

$$\left[i\hbar\partial_{x_0} + \frac{\hbar^2\Delta_{\mathbf{x}}}{2m} - 2g(x^0)|\Psi(x)|^2\right]\widetilde{n}(x,y) - g(x^0)\Psi^2(x)\widetilde{m}^*(x,y) = 0, \tag{6.25}$$

$$\left[i\hbar\partial_{x_0} + \frac{\hbar^2\Delta_{\mathbf{x}}}{2m} - 2g(x^0)|\Psi(x)|^2\right]\widetilde{m}(x,y) - g(x^0)\Psi^2(x)\widetilde{n}^*(x,y) = 0, \tag{6.26}$$

for the two correlation functions. Throughout the section 6.4 we assign the notation of the field Ψ without an operator hat for the one-point function.

The form of the above equations is familiar from the Bogolyubov theory for the excitations on top of a BEC [232]. They can be diagonalized by means of yet another linear transformation. Since we consider spatially homogeneous systems, the background field depends only on time, $\Psi(x) \to \Psi(x_0)$. Neglecting the backreaction of the fluctuations in the linear regime, its evolution is governed by the GPE (6.9) (cf. Eq. (3.6)) and is given by

$$\Psi(x_0) \propto \exp\Big(-\frac{i}{\hbar}\int \mathrm{d}x_0 g(x_0) n_0\Big).$$

Here $n_0 = |\Psi(x_0)|^2$ denotes the density of the condensate, which is approximately constant in the linear regime. Performing the transformation

$$n_1(x,y) = \widetilde{n}(x,y)\Psi^*(x_0) + \widetilde{m}^*(x,y)\Psi(x_0),$$
$$\Phi_1(x,y) = \Big(-\frac{i}{2n_0}\Big)\Big(\widetilde{n}(x,y)\Psi^*(x_0) - \widetilde{m}^*(x,y)\Psi(x_0)\Big),$$

the equations of motion (6.25) and (6.26) are recast into the form

$$\partial_{x_0} n_1(x,y) = -\frac{\hbar n_0}{m}\Delta_{\mathbf{x}}\Phi_1(x,y), \tag{6.27}$$

$$-\hbar\partial_{x_0}\Phi_1(x,y) = g n_1(x,y) - \frac{\hbar^2}{4mn_0}\Delta_{\mathbf{x}} n_1(x,y). \tag{6.28}$$

Excitations on top of the condensate behave as sound waves or as quasi-particles according to the famous Bogolyubov dispersion relation [232],

$$\epsilon_{\mathrm{p}}^2 = \hbar^2\omega_{\mathrm{p}}^2 = \frac{\mathrm{p}^2}{2m}\Big(\frac{\mathrm{p}^2}{2m} + 2gn_0\Big). \tag{6.29}$$

This can be seen by taking the time derivative of the first equation in (6.27), inserting the second one, and Fourier transforming n_1 with respect to the relative spatial coordinate, which leads to

$$\Big(\partial_t^2 + \omega_{\mathrm{p}}^2(t)\Big)n_1(t,t',\mathbf{p}) = 0. \tag{6.30}$$

For small momenta the dispersion relation is linear, $\epsilon_{\mathrm{p}} = c_s \mathrm{p}$, and describes sound waves. The speed of sound is given by

$$c_s^2 = \frac{g n_0}{m}. \tag{6.31}$$

For large momenta the dispersion relation takes the quasi-particle form $\epsilon_{\mathrm{p}} = \mathrm{p}^2/2m$. The transition between the two regimes takes place near $\mathrm{p}^2/2m = g n_0$ or, equivalently, near $\mathrm{p} = \hbar/\xi$, where $\xi = \hbar/(\sqrt{2} m c_s)$ is referred to as the healing length.

In the sound wave regime the gradient term in Eq. (6.28) is much smaller compared to the $g n_1$ term. Solving that equation with respect to n_1 and inserting into (6.27) one obtains the following wave equation, valid at small momenta

$$\partial_{x_0}^2 \Phi_1(x,y) - \left(\frac{\partial_{x_0} g}{g}\right) \dot{\Phi}_1(x,y) - c_s^2 \Delta \Phi_1(x,y) = 0. \tag{6.32}$$

6.4.2 Linear amplification of fluctuations

In this subsection we discuss the instabilities for the excitations, which lead to their exponential amplification. In the simplest case when the scattering length is positive and constant, $g > 0$ and $\dot{g} = 0$, the frequency in (6.30) is constant as well and no amplification takes place. This reflects the fact that in the case of repulsive self-interactions the configuration of a homogeneous condensate has the lowest possible energy for a given particle number.

If the scattering length is switched from positive to a negative constant value i.e. $g = -|g| < 0$, sound waves will exhibit a tachyonic instability (see also [233]). The presence of an instability can be seen already from the Bogolyubov dispersion relation (6.29) and from (6.30), which lead to an imaginary frequency for momenta with $\mathrm{p}^2 < 4|g|n_0 m$. The corresponding momentum modes then grow as

$$n_1(t,t',\mathbf{p}) \propto \Phi_1(t,t',\mathbf{p}) \propto \exp\left(\sqrt{\left(2|g|n_0 - \frac{\mathrm{p}^2}{2m}\right)\frac{\mathrm{p}^2}{2m\hbar^2}}\, t\right), \quad \mathrm{p} < \sqrt{4|g|n_0 m}. \tag{6.33}$$

Here we have used that, according to the second equation in (6.27), the amplitude of $\Phi_1(t,t',\mathbf{p})$ is proportional to the one of $n_1(t,t'\mathbf{p})$. In other words, all sound wave modes exhibit an amplification. A negative coupling would lead to the collapse of the condensate after a sufficient amount of time and the formation of strong overdensities in position space due to the attractive self-interactions [234].

Periodic modulation of the scattering length: An elegant way to generate instabilities for the sound waves is by applying a periodic modulation of the scattering length around some positive value. This leads to a parametric resonance instability [235, 236], analogous to the one in relativistic scalar field theories [17, 21]. Parametric resonance leads to an exponential amplification of modes, for which resonance conditions are satisfied.

As an illustration we consider a harmonic modulation of the coupling,

$$g(t) = g_0(1 - r\sin(\omega t)). \tag{6.34}$$

The equations of motion for the momentum modes of the sound waves then take the form

$$\ddot{\Phi}_1(t,t'\mathbf{p}) + \frac{r\omega\cos\omega t}{1 - r\sin\omega t}\dot{\Phi}_1(t,t',\mathbf{p}) + \frac{(1 - r\sin\omega t)g_0 n_0}{m}\left(\frac{\mathrm{p}}{\hbar}\right)^2 \Phi_1(t,t'\mathbf{p}) = 0, \tag{6.35}$$

The resonant momentum and the growth exponent can be estimated analytically for the case of a weak modulation, $r \ll 1$. The most unstable momentum for the above harmonic modulation is approximately given by

$$\frac{\mathrm{p}_{\mathrm{res}}}{\hbar} = \frac{\omega}{2c_s} = \frac{\omega}{2}\sqrt{\frac{m}{n_0 g_0}}. \tag{6.36}$$

The corresponding mode grows as

$$n_1(t,t',\mathbf{p}) \propto \Phi_1(t,t',\mathbf{p}) \propto \exp\Big(\frac{\omega r}{8}t\Big). \tag{6.37}$$

The width and the strength of the resonance band increase when the ratio of the periodic term in (6.34) to the constant term is increased.

As a consequence of the time-dependence of the Hamiltonian the total energy of the system increases with time, in contrast to the conserved total number of atoms. After a sufficient amplification of the fluctuations, the periodic modulation can be turned off. This would correspond to the background field having decayed most of its energy.

Connection to the "relativistic" parametric resonance: We now discuss the connection between the periodic modulation of the coupling and the relativistic corrections to (6.11) enabling parametric resonance.

In contrast to relativistic field equations (6.8), which do not possess any continuous symmetry, an effective particle number conservation due to $U(1)$ symmetry emerges after taking the nonrelativistic limit. More specifically, this happens after neglecting the $U(1)$ violating interaction term in (6.20) due to its rapid oscillations, i.e. the interaction term has the form

$$\sim g\Big(\underbrace{\Psi^3 e^{-2\frac{i}{\hbar}mc^2 t}}_{\text{number-changing, rapidly oscillating}} + \underbrace{3\Psi\Psi^\dagger\Psi}_{\text{number-conserving, slowly varying}}\Big).$$

It is this term, that enables parametric resonance, since it leads to a periodic frequency for the momentum modes. This can be seen after a linearization procedure around the homogeneous condensate, $\Psi(t,\mathbf{x}) \to \Psi_0(t) + \Psi(t,\mathbf{x})$, which leads to

$$\sim g\Big(\Psi_0^2\Psi e^{-2\frac{i}{\hbar}mc^2 t} + 2|\Psi_0|^2\Psi + \Psi_0^2\Psi^\dagger\Big).$$

While it unclear how to engineer the first interaction term from the above expression in an atomic Bose gas, a very similar term arises in the presence of a modulated coupling,

$$\sim g[1 - r\sin(\omega t)]\Big(2|\Psi_0|^2\Psi + \Psi_0^2\Psi^\dagger\Big).$$

In this way, the modulation leads to a resonant production of excitations on top of the BEC, at frequencies $\sim \omega$, which can be taken much smaller than $mc^2/\hbar$.

6.4.3 Secondary instabilities

As in the case of relativistic systems, loop corrections in the 2PI equations of motion eventually become important, after the resonant modes of the fluctuations have gotten sufficiently amplified. The leading loop corrections lead to secondary instabilities, which we calculate in this section. Large parts of the calculation are very similar to those presented in section 3.2.3 of chapter 3, and we mention them briefly.

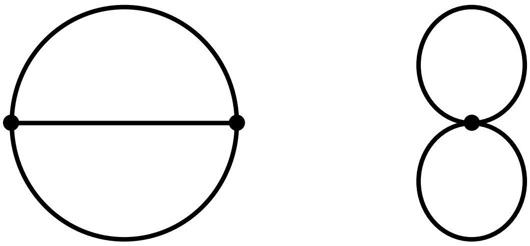

FIGURE 6.2: The diagrammatic illustration of the two-loop local (right) and nonlocal (left) contributions to the 2PI effective action, with the second one accounting for the secondary instabilities.

The LO 2PI diagrams, constructed from the interaction vertices of the action (6.5), are shown in Fig. 6.2. Using the standard techniques of Feynman diagrams, the "tadpole" diagram on the right is found to have the form [205]

$$\Gamma_2^{\mathrm{LO,local}}[G] = -\int_{x,C} \frac{g(x_0)}{8}\Big(G_{ii}(x,x)G_{jj}(x,x) + 2G_{ij}(x,x)G_{ij}(x,x)\Big) \qquad (6.38)$$

The corresponding contribution to the self-energy can be calculated using (2.35). As in the relativistic case, this contribution is local and contributes to the effective mass. It has been explicitly included in the definition (6.7). As can be seen from that definition, this correction becomes relevant when the components of F_{ij} become of the order of the condensate density n_0.

The other LO correction, depicted on the left side of Fig. 6.2, becomes important earlier and accounts for the secondary instabilities (see e.g. [21, 230]), as in the relativistic system. Using standard Feynman rules, this contribution is found to be

$$\begin{aligned}\Gamma_2^{\mathrm{LO,local}}[G] = i\int_{xy,C} \frac{g(x_0)g(y_0)}{4\hbar}\phi_b(x)\phi_d(y)\Big(&G_{ac}(x,y)G_{ac}(x,y)G_{bd}(x,y)\\ &+2G_{ac}(x,y)G_{ad}(x,y)G_{bc}(x,y)\Big), \qquad (6.39)\end{aligned}$$

and the self-energy, according to (2.35), has the form

$$\begin{aligned}\Sigma_{ij}(x,y;\phi,G) = -\frac{g(x^0)g(y^0)}{2\hbar}\Big[&\phi_i(x)\phi_j(y)G_{ac}(x,y)G_{ac}(x,y)\\ +2\phi_b(x)\phi_d(y)G_{ij}(x,y)G_{bd}(x,y) &+ 2\phi_b(x)\phi_d(y)G_{id}(x,y)G_{bj}(x,y)\\ +2\phi_b(x)\phi_j(y)G_{ic}(x,y)G_{bc}(x,y) &+ 2\phi_i(x)\phi_d(y)G_{aj}(x,y)G_{ad}(x,y)\Big]. \qquad (6.40)\end{aligned}$$

Including this contribution into the 2PI equations of motion (6.6) leads to integrals over the past evolution i.e. memory integrals on the right-hand side. Due to the exponential growth of the fluctuations these integrals are however dominated by the latest times. This allows simplifying the equations, which can be done following the same lines as in section 3.2.3, as well as in [20, 230]. Note that Σ contains terms proportional to

$$
\begin{aligned}
G_{\alpha\beta}(x,y)G_{\gamma\delta}(x,y) = {} & \underbrace{F_{\alpha\beta}(x,y)F_{\gamma\delta}(x,y) - \frac{1}{4}\rho_{\alpha\beta}(x,y)\rho_{\gamma\delta}(x,y)}_{\Sigma_F} \\
& - \frac{i}{2}\mathrm{sgn}_C(x^0 - y^0)\,\underbrace{F_{\alpha\beta}(x,y)\rho_{\gamma\delta}(x,y) + \rho_{\alpha\beta}(x,y)F_{\gamma\delta}(x,y)}_{\Sigma_\rho} \qquad (6.41)
\end{aligned}
$$

We focus on the equations of motion for the statistical propagator. The $\int \Sigma^\rho F$ term in Eq. (6.6) in the above-mentioned limit of $z^0 \to x^0$ represents a "tadpole"-like contribution, which becomes important only at later times (cf. section 3.2.3, as well as [21]) similar to the other "tadpole" diagram. For the $\int \Sigma^F \rho$ term one obtains

$$
-\int_{t_0}^{y_0} dz \Sigma^F_{ac}(x,z)\rho_{cb}(z,y) \approx -\int_{y_0-c}^{y_0} dz \Sigma^F_{ac}(x,z)\rho_{cb}(z,y) \approx i\hbar c \Sigma^F_{ac}(x,y)\sigma_{2,cb}, \qquad (6.42)
$$

where $c^{-1} = \mathcal{O}(g_0 n_0)$ is some parameter of the order of the oscillation frequency. Here we have used the fact that at $x_0 = y_0$ the spectral function is determined solely by the commutation relations (6.2),

$$
\rho_{ij}(x,y)|_{x^0=y^0} = i\langle[\hat{\varphi}_i(x), \hat{\varphi}_j(y)]\rangle|_{x^0=y^0} = -i\,\sigma_{2,ij}\,\delta(\mathbf{x}-\mathbf{y}). \qquad (6.43)
$$

In Σ^F there are terms $\propto F^2$ and $\propto \rho^2$, similar to (3.9). The $\propto \rho^2$ part in Σ^F is suppressed for $y_0 \to x_0$, as the components of ρ are of order one in that limit due to (6.43). As a result, that contribution is negligible for equal-time observables, such as the occupation numbers, compared to the exponentially growing contribution from the $\propto F^2$ part. Neglecting this part is equivalent to the classical-statistical approximation for the dynamics.

For the sake of completeness, we present the final form of the approximate one-loop equations of motion for the description of secondary instabilities. Using the transformation (6.23) and (6.24), one arrives at the following equation for the momentum modes of the normal two-point function $\widetilde{n}(t,t',\mathbf{p})$,

$$
\begin{aligned}
&\Big[i\partial_t - \frac{\mathbf{p}^2}{2m} - 2g(t)|\Psi(t)|^2\Big]\widetilde{n}(t,t',\mathbf{p}) - g(t)\Psi^2(t)\widetilde{m}^*(t,t',\mathbf{p}) = icg(t)g(t') \\
&\times \int_{\mathbf{q}} \Big[4\Psi(t)\Psi^*(t')\Big(\widetilde{n}(t,t',\mathbf{q})\widetilde{n}^*(t,t',\mathbf{p}-\mathbf{q}) + \widetilde{m}(t,t',\mathbf{q})\widetilde{m}^*(t,t',\mathbf{p}-\mathbf{q})\Big) \\
&\quad +4\Psi^*(t)\Psi^*(t')\widetilde{n}(t,t',\mathbf{q})\widetilde{m}(t,t',\mathbf{p}-\mathbf{q}) + 4\Psi(t)\Psi(t')\widetilde{n}(t,t',\mathbf{q})\widetilde{m}^*(t,t',\mathbf{p}-\mathbf{q}) \\
&\quad +2\Psi^*(t)\Psi(t')\widetilde{n}(t,t',\mathbf{q})\widetilde{n}(t,t',\mathbf{p}-\mathbf{q})\Big], \qquad (6.44)
\end{aligned}
$$

and of the anomalous correlator $\widetilde{m}(t,t',\mathbf{p})$,

$$
\begin{aligned}
&\Big[i\partial_t - \frac{\mathbf{p}^2}{2m} - 2g(t)|\Psi(t)|^2\Big]\widetilde{m}(t,t',\mathbf{p}) - g(t)\Psi^2(t)\widetilde{n}^*(t,t',\mathbf{p}) = -icg(t)g(t') \\
&\times \int_{\mathbf{q}} \Big[4\Psi(t)\Psi(t')\Big(n(t,t',\mathbf{q})n^*(t,t',\mathbf{p}-\mathbf{q}) + m(t,t',\mathbf{q})m^*(t,t',\mathbf{p}-\mathbf{q})\Big) \\
&\quad +4\Psi^*(t)\Psi(t')\widetilde{m}(t,t',\mathbf{q})\widetilde{n}(t,t',\mathbf{p}-\mathbf{q}) + 4\Psi(t)\Psi^*(t')\widetilde{m}(t,t',\mathbf{q})\widetilde{n}^*(t,t',\mathbf{p}-\mathbf{q}) \\
&\quad +2\Psi^*(t)\Psi^*(t')\widetilde{m}(t,t',\mathbf{q})\widetilde{m}(t,t',\mathbf{p}-\mathbf{q})\Big]. \qquad (6.45)
\end{aligned}
$$

The momentum integrals on the right-hand side are analogous to the ones in (3.16) and, therefore, lead to a secondary exponential amplification of the fluctuations, e.g.

$$\widetilde{n}(t,t',\mathbf{p}) \sim e^{2\gamma(t+t')}, \tag{6.46}$$

in the momentum range $\mathrm{p} \lesssim 2\mathrm{p}_{\mathrm{res}}$.

The emergence of both the primary as well as the secondary instabilities was observed in the numerical lattice simulations, based on the classical-statistical approximation.

6.5 Turbulent thermalization of Bose gases

The momentum distribution of the particles after their resonant production is highly nonthermal, featuring large occupation numbers at low momenta. In the subsequent stages of the far-from-equilibrium dynamics the system usually approaches NTFPs, which manifest themselves in the form of universal scaling behavior of the distribution function.

In the previous chapters the significance of the regime of universal dynamics was demonstrated. In particular, the direct energy transport can bring the system close to thermal equilibrium or, alternatively, it can eventually "freeze" due to cosmological expansion. In chapter 5 the knowledge of scaling exponents of the cascade allowed us to estimate analytically the characteristic momenta of the particles at much later times. This knowledge is also important in the context of post-inflationary reheating, for estimating the reheating temperature of the universe.

In this section we discuss the possibility of realizing the above-mentioned phenomena in a Bose gas. We start by describing the kinetic framework and studying its scaling solutions for the direct cascade. The dynamics both in the presence of a modulation of the scattering length as well as after switching it off is considered. A direct self-similar energy transport has not been observed so far in single-component ultracold Bose gases (see however [237] for the discussion of an analogous transport in a spinor Bose gas). Recently, an inverse particle transport [68] was simulated experimentally in one-component [238] and three-component [239] Bose gases, following a quench dynamics.

6.5.1 Kinetic description

An important tool for studying the dynamics near NTFPs is provided by the effective kinetic description of QFT. The large occupation numbers usually require going beyond perturbative kinetic theory. This is the case for the description of the inverse cascade [25], which can be adequately described with the help of vertex-resummed kinetic theory based on the nonperturbative $1/N$ expansion [205]. For the energy transport at high momenta, however, the characteristic occupation numbers are not so large and, as a consequence, only the leading diagrams of the resummation are important i.e. a "perturbative" analysis is applicable (see also [22], as well as section 3.3.2).

As in the relativistic case, the contributions to the self-energy that are relevant for the dynamics of the direct cascade are the one- and two-loop diagrams depicted in the central left part of Fig. 3.2. The Boltzmann equation, with the corresponding two collision terms taken into account, has been derived from the 2PI equations in [209] and has the form [209, 240]

$$\frac{\partial n(t,\mathbf{p})}{\partial t} = C_{2\leftrightarrow 2}[n](t,\mathbf{p}) + C_{1\leftrightarrow 2}[n](t,\mathbf{p}), \tag{6.47}$$

where

$$\begin{aligned} C_{2\leftrightarrow 2}[n] = \frac{2g^2}{(2\pi)^5\hbar^7} \int d\mathbf{p}_2 d\mathbf{p}_3 d\mathbf{p}_4 \delta(\mathbf{p}+\mathbf{p}_2-\mathbf{p}_3-\mathbf{p}_4)\delta(\epsilon_{\mathbf{p}}+\epsilon_{\mathbf{p}_2}-\epsilon_{\mathbf{p}_3}-\epsilon_{\mathbf{p}_4}) \\ \times \Big[(n_{\mathbf{p}}+1)(n_{\mathbf{p}_2}+1)n_{\mathbf{p}_3}n_{\mathbf{p}_4} - n_{\mathbf{p}}n_{\mathbf{p}_2}(n_{\mathbf{p}_3}+1)(n_{\mathbf{p}_4}+1)\Big] \end{aligned} \tag{6.48}$$

describes $2 \leftrightarrow 2$ collisions between the noncondensate atoms and

$$\begin{aligned} C_{1\leftrightarrow 2}[n] = \frac{2g^2 n_0}{(2\pi)^2\hbar^4} \int d\mathbf{p}_1 d\mathbf{p}_2 d\mathbf{p}_3 \delta(\mathbf{p}_1-\mathbf{p}_2-\mathbf{p}_3) \\ \times\delta(\epsilon_0+\epsilon_{\mathbf{p}_1}-\epsilon_{\mathbf{p}_2}-\epsilon_{\mathbf{p}_3})(\delta(\mathbf{p}-\mathbf{p}_1)-\delta(\mathbf{p}-\mathbf{p}_2)-\delta(\mathbf{p}-\mathbf{p}_3)) \\ \Big[(n_{\mathbf{p}_1}+1)n_{\mathbf{p}_2}n_{\mathbf{p}_3} - n_{\mathbf{p}_1}(n_{\mathbf{p}_2}+1)(n_{\mathbf{p}_3}+1)\Big] \end{aligned} \tag{6.49}$$

arises in the presence of the condensate and describes the effective $2 \leftrightarrow 1$ collisions[3]. ϵ_0 and $\epsilon_{\mathbf{p}}$ are the energies of condensate and noncondensate atoms, respectively.

6.5.2 Scaling exponents from kinetic theory

We now investigate the universal scaling dynamics near a NTFP. The self-similar evolution of the distribution function has the form

$$n(t,\mathrm{p}) = s^{\alpha} n(t_S, s^{\beta}\mathrm{p}) = s^{\alpha} n_S(s^{\beta}\mathrm{p}), \qquad s = t/t_S, \tag{6.50}$$

where $n_S(\mathrm{p})$ is the distribution function at some reference time t_S and α and β are the scaling exponents.

Self-similar scaling regions usually represent a transport of some conserved quantity in momentum space, such as the energy or the particle number for repulsive self-interactions. These two conserved quantities are can be represented as,

$$\frac{N}{V} = \int_{\mathbf{p}} n(t,\mathrm{p}), \qquad \frac{E}{V} = \int_{\mathbf{p}} n(t,\mathrm{p})\epsilon(t,\mathrm{p}). \tag{6.51}$$

In the regime of modulation of the coupling the total energy grows linearly with time. We, therefore, allow for a more general form of the scaling of the total energy with time,

$$E(t) \propto t^{\gamma}, \tag{6.52}$$

where $\gamma \approx 1$ in the driven regime and $\gamma = 0$ in the absence of driving.

In the discussion of NTFPs the occupation is usually much larger than one, so that only the leading contribution to the collision terms in powers of $n_{\mathbf{p}}$ can be kept. This approximation corresponds to wave kinetic theory [219] and is represented by the black region in Fig. 2.4. Moreover, the condensate energy ϵ_0 is much smaller

---

[3] It is known that such processes are kinematically forbidden, since one can always switch to the reference frame where the 1 particle is at rest, and then the process violates energy conservation. However, this does not apply to our case, since the last expression is valid only in a specific frame, the one in which the condensate atoms are at rest.

compared to the typical values of $\epsilon_{\mathbf{p}}$ for the direct cascade and, thus, can be safely neglected.

Energy conservation: The number of the spatial dimensions d and the quantity, which is being transported, determine the ratio of the two exponents α and β. In addition to (6.52) we also assume an approximate scaling form $\epsilon_{\mathbf{p}} \propto \mathrm{p}^z$ for the quasi-particle energy. It follows from (6.29) that for a Bose gas $z \approx 2$ in the particle regime and $z \approx 1$ in the sound wave regime. Since the direct cascade takes place at high momenta, the first regime is expected to be the relevant one. In contrast, the relativistic dispersion relation is linear at high momenta, whereas at low momenta $z = 0$ if a nonvanishing mass is present.

Inserting the above scaling relations into the expression for the total energy leads to

$$\frac{E(t)}{V} \approx \int_{\mathbf{p}} n(t,\mathrm{p})\epsilon_{\mathbf{p}} \propto \int d\mathrm{p}\, n(t,\mathrm{p})\mathrm{p}^{d-1+z} \propto t^{\alpha-(d+z)\beta} \quad \leftrightarrow \quad \alpha = \gamma + (d+z)\beta, \tag{6.53}$$

The collision term: The second relation between the exponents arises from the scaling properties of the kinetic equation itself. Here we assume that the right-hand side of (6.47) is dominated by one term, and denote the corresponding sum of the numbers of incoming and outgoing particles by l ($l = 4$ for $2 \leftrightarrow 2$ and $l = 3$ for $1 \leftrightarrow 2$). It is also assumed that $n_{\mathbf{p}} \gg 1$. In particular, the $2 \leftrightarrow 2$ term, given by (6.48), in this case takes the form

$$\begin{aligned} C[n] \sim g^2 \int_{\mathbf{lqr}} & \delta(\mathbf{p}+\mathbf{l}-\mathbf{q}-\mathbf{r})\delta(\omega_{\mathbf{p}}+\omega_{\mathbf{l}}-\omega_{\mathbf{q}}-\omega_{\mathbf{r}}) \\ & \times (n_{\mathbf{p}}n_{\mathbf{q}}n_{\mathbf{r}} + n_{\mathbf{l}}n_{\mathbf{q}}n_{\mathbf{r}} - n_{\mathbf{p}}n_{\mathbf{l}}n_{\mathbf{q}} - n_{\mathbf{p}}n_{\mathbf{l}}n_{\mathbf{r}}). \end{aligned} \tag{6.54}$$

Inserting the scaling ansatz (6.50) into the above equation and comparing the scaling of the left- and right-hand sides in time one arrives at [25]

$$(l-2)\alpha = [(l-2)d - 2]\beta - 1. \tag{6.55}$$

Combining (6.53) and (6.55) leads to

$$\beta = -\frac{-1-(l-2)\gamma}{(l-2)z+2}, \qquad \alpha = \gamma + (d+z)\beta. \tag{6.56}$$

Finally, let us calculate the values of exponents explicitly:

- In the driven regime, $\gamma = 1$, for $z = 2$ both collision terms lead to the values $\beta = -1/2$, whereas $\alpha = 1 - (2+d)/2$. For two spatial dimensions $\alpha = -1$.
- In the absence of driving, $\gamma = 0$, for $z = 2$ one arrives at $\beta = -1/(2(l-1))$ and $\alpha = (2+d)\beta$. The value of β is $-1/6$ for $2 \leftrightarrow 2$ scatterings and $-1/4$ for $2 \leftrightarrow 1$ scatterings.

Note that for $d = 3$ the coupling g, within our mapping, would depend on the scale factor, which would induce an additional time-dependence into the collision integrals.

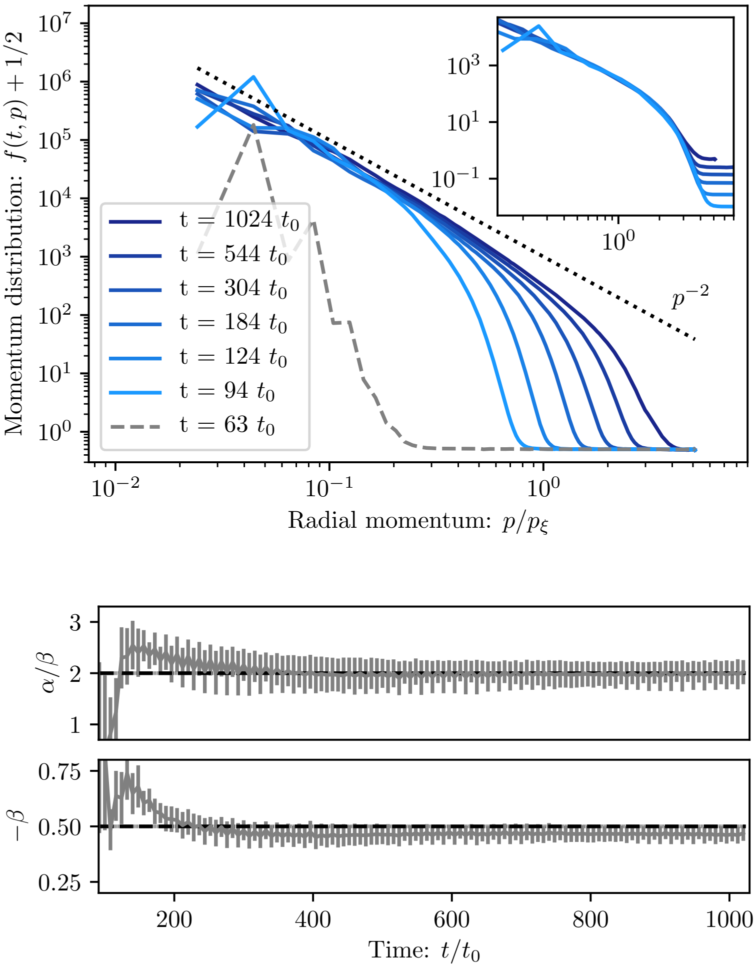

FIGURE 6.3: The self-similar energy transport in classical-statistical simulations, in the presence of a modulation of the scattering length. The figure contains several snapshots of the momentum distribution function before (main plot) and after (inset) rescaling according to (6.50). The rescaling is performed using the numerically extracted values of the scaling exponents α and β, shown in the bottom part of the figure, which are consistent with the analytical predictions from section 6.5.2.

6.5.3 Comparison with classical-statistical simulations

For the sake of completeness, in this section we present the comparison of our analytical predictions for the scaling exponents from kinetic theory with the numerical results from classical-statistical simulations in two spatial dimensions, that were performed by Kevin Geier as part of our work [4] in preparation. The scaling exponents, presented in the two plots of this section, were extracted from those simulations using the maximum likelihood method that was developed in chapter 3 of this work and described in section 3.3.2.

In the numerical simulations, which were performed on a 512^2 spatial grid and with an averaging over 100 runs, the number of atoms is $N = 10^8$ and the quartic coupling is $g = 2.5 \times 10^{-5}\hbar^2/m$. The time unit, used in this section, is given by the characteristic interaction time $t_0 = \hbar/(n_0 g)$. The coupling is modulated according to (6.34) with $r = 1$ and the frequency was chosen such that energy is injected at significantly low momenta, $\mathrm{p}_{\mathrm{res}} = 3 \times 2\pi\hbar/L$, where L is the box length with periodic boundary conditions. The emergence of self-similar energy transport in the simulations is shown in Fig. 6.3 where, in the upper part, several snapshots of the momentum distribution function are plotted, with the inset showing the rescaled distribution function (cf. figure 3.8) according to (6.50). The distribution function is rescaled using the numerically extracted time-dependent values of the scaling exponents which, as can be seen in the bottom part of the figure, indeed approach the values $\alpha = -1$ and $\beta = -1/2$ predicted by kinetic theory.

In contrast to Fig. 6.3, the modulation is switched off at $t = 80t_0$ in Fig. 6.4. Note that in both cases a characteristic power-law close to p^{-2} develops in the distribution function, which is indicated by the dotted line. The power-law p^{-d} is characteristic for weak wave turbulence [111, 219, 241] and has been even observed experimentally in [242]. As can be seen, the value of the exponent β now approaches $-1/4$, which is the prediction from the kinetic description, taking into account effective $2 \leftrightarrow 1$ scatterings. This term in the collision integral was found to be the dominant one also in the relativistic systems [22], as it was discussed in chapter 5.

6.5.4 Thermalization versus expansion

The self-similar evolution of the direct cascade continues until the occupation numbers at the characteristic momentum scale are no longer much larger than one. This is a particularly interesting regime of the dynamics, since semiclassical approximation methods are inapplicable as the quantum fluctuations become comparable to the statistical ones. In a true quantum system a relaxation to a Bose-Einstein distribution is expected to take place at this stage.

Below we describe how the thermalization time and the time, when the spectrum is expected to freeze, can be estimated in our system. To be specific we return to the original notation of the time variables with t denoting the physical time and η the lab time.

Reheating time: Neglecting the last stage of quantum relaxation to the equilibrium distribution, the self-similar evolution allows one to estimate the time for thermalization as well as the final temperature [22]. In the context of post-inflationary dynamics, this is important for determining the reheating temperature of the universe after inflation.

The condition for thermalization can be formulated as the occupation numbers at the characteristic momentum scale becoming of order one. Denoting this comoving momentum scale by $\mathrm{p_f}$, this implies that $n(\eta_{\mathrm{th}}, \mathrm{p_f}) = \mathcal{O}(1)$. The momentum scale $\mathrm{p_f}$ can be expressed in terms of the total energy density ρ during the free turbulence, via

$$k_f^d\, n(\eta_{\mathrm{th}}, \mathrm{p_f})\, \epsilon_f \sim k_f^d \times \frac{\mathrm{p}_f^2}{2m} \sim \rho,$$

where we have assumed a quasiparticle form for the dispersion relation. On the other hand, the initial characteristic scale for free turbulence can be identified with the resonant momentum, which we denote by $\mathrm{p_i}$. The thermalization time can be then written as

$$\eta_{\mathrm{th}} \sim \eta_i \left(\frac{\mathrm{p_i}}{\mathrm{p_f}}\right)^{1/\beta}. \tag{6.57}$$

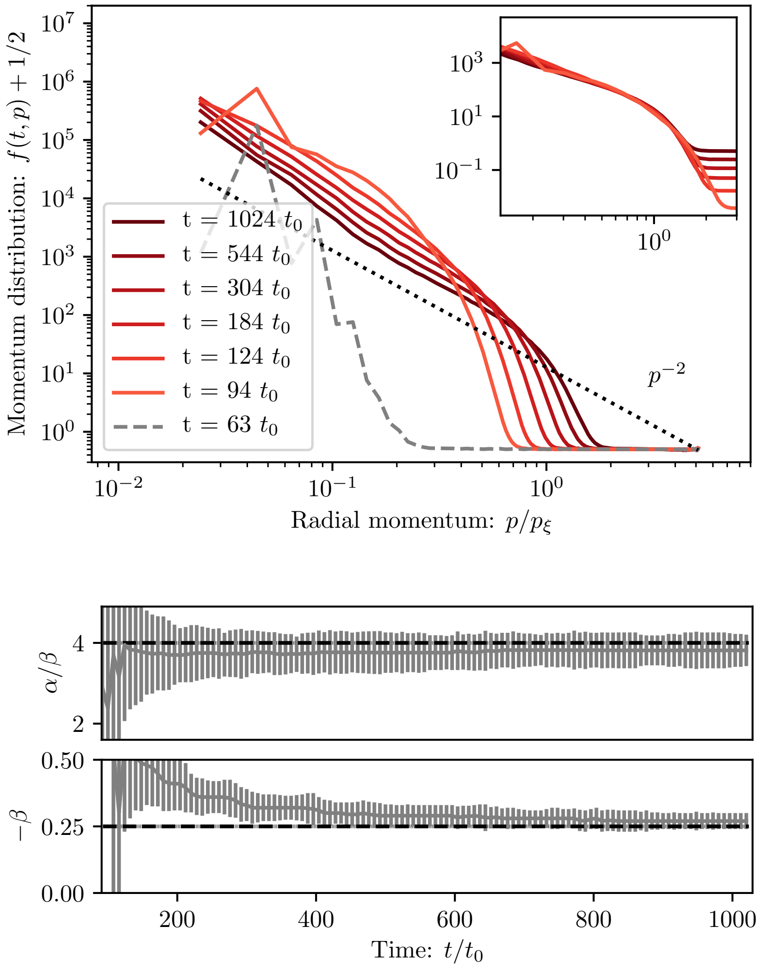

FIGURE 6.4: The self-similar energy transport in classical-statistical simulations, after switching off the modulation of the scattering length at $t = 80t_0$. Snapshots of both rescaled and original distribution functions, as well as the numerically extracted scaling exponents α and β, shown in figure as in Fig. 6.3. The exponent β takes a different value from the driven case of Fig. 6.3, consistent with the analytical predictions from section 6.5.2.

Freezing time: In an expanding spacetime the interaction rates decrease with expansion. It is thus possible that the gas is unable to achieve thermal equilibrium, if expansion is too rapid. To check this one usually compares the typical interaction rate Γ with the Hubble parameter H. If $\Gamma \gg H$, thermalization is possible, whereas for $\Gamma \ll H$ the spectrum is expected to freeze without thermalizing.

In the framework of kinetic description the distribution function should freeze after the Hubble friction dominates over the collision term. This phenomenon was observed for ALP dark matter in chapters 4 and 5. The friction term is absent in the Boltzmann equation (6.47) due to the performed transformation. In terms of the original field and time variables (6.47) takes the form

$$\frac{\partial n(t,\mathbf{p})}{\partial t} + dHn(t,\mathbf{p}) = C[n](t,\mathbf{p}). \tag{6.58}$$

The spectra can thus freeze ($n_{\mathrm{p}} \propto a^{-d/2}$) in an expanding universe, even when the occupation numbers are still large.

As one would expect, the above-described effects are still present in our setup after the transformation. According to our mapping, for $d = 2$ the dynamics of the Bose gas in an expanding spacetime is mapped into that in a static spacetime with $g = \mathrm{const}$. This means that the system always thermalizes in the simulation. To make sure whether this is also true in the physical time, one has to check that the simulation time at which the physical time becomes infinite is larger than the thermalization time,

$$\eta_{\mathrm{th}} < \eta_{\mathrm{freeze}} = \eta(t = \infty). \tag{6.59}$$

In particular, in the case of a matter-dominated universe the maximal simulation time is given by $\eta_{freeze} = 2/H_0$ (see section 6.2). This implies that larger values of the Hubble parameter correspond to a larger rate of expansion and, therefore, the system has less time to thermalize before it freezes.

The situation is different for $d = 3$, where, after the mapping, the coupling becomes time-dependent, $g \propto a^{-1}$. In the presence of a decreasing coupling the freeze-out can happen during the simulation, preventing thermalization.

6.6 Summary

In this chapter we demonstrated how single-component atomic Bose gases with tunable self-interactions can be employed for simulating various aspects of scalar field dynamics in the early universe. The modulation of the scattering length, mimicking the oscillations of the background field around the minimum of its potential, enables the resonant amplification of low-momentum fluctuations on top of the BEC. This can be followed by the approach to a NTFP, associated with a self-similar turbulent energy transport towards higher momenta, both in the presence of the modulation as well as after switching it off. Despite the nonrelativistic dispersion relation and the conservation of total particle number in a Bose gas, the similarity of the dynamics to that of reheating after cosmic inflation is remarkable.

Our analytical studies were complemented with numerical simulations based on the classical-statistical approximation and an overall agreement between the different approaches was found. The characteristic stages of the dynamics, that were described in this chapter, were all observed in the simulations, including the self-similar energy cascade with the scaling exponents consistent with the predictions from section 6.5.2. From the experimental point of view the main restriction arises is the finite number of available atoms in such experiments $N \lesssim 10^6$, which, at least in the numerical simulations, restricts the duration of the universal dynamics to moderate times.

More generally, our setup provides a unique platform for studying the thermalization dynamics of quantum many-body systems driven far-from-equilibrium and, in particular, the gradual loss in the complexity of their dynamics. The regimes of strong couplings or small occupation numbers, which are difficult to access theoretically, are particularly interesting targets for future studies.

Chapter 7

Conclusion and outlook

Nonequilibrium phenomena are common in the early universe and a better understanding of such processes is crucial for solving the open problems of cosmology and particle physics, such as the origin of inflation, DM, or the baryon asymmetry. In the present work we have explored the nonperturbative regime of the dynamics of scalar fields in the early universe, exploiting the powerful toolbox of nonequilibrium QFT.

We have investigated the phenomenological consequences of such dynamics. Our studies were focused on ALPs, which are among the best-motivated candidates for DM. We have studied the nonperturbative production of ALP DM via the misalignment mechanism and computed its equation of state, the power spectrum, and the strength of the GW signal that is produced in the course of the dynamics.

We have analyzed the nonperturbative dynamics in nonrelativistic systems, such as atomic Bose gases in tabletop experiments. Remarkably, the very same theoretical approaches are applicable for the QFT description of such systems and, despite the vastly different scales, they can exhibit a very similar behavior.

Below we present a summary of the main results of this thesis and discuss possible future research.

In chapter 3 we study the fragmentation dynamics of coherently oscillating "axion-like" fields, whose discrete shift symmetry is broken by a quadratic monomial. Our analysis is based on classical-statistical simulations, combined with perturbative (loop) and nonperturbative ($1/N$) expansions of the 2PI effective action.

The perturbative approach allows us to describe the early stages of the dynamics, when the fluctuations are exponentially amplified due to parametric instabilities. Our analysis is similar to the one in [21], where a scalar theory with quartic self-interactions was considered. We characterize the spectrum of primary and secondary instabilities and point out the main differences compared to the φ^4 model. The stage of resonant amplification is followed by the decay of coherent oscillations. The $1/N$ expansion to NLO, together with the transport equations that we derive from it, complement our numerical studies of the late-time dynamics near NTFPs after the decay. Such fixed points are characterized by a self-similar scaling behavior of the momentum distribution function [23, 25, 118, 119]. The form of the transport equations that we derive is such that the contribution from the higher-order self-interactions of the "cosine" potential at NLO is encoded as a shift in a modified quartic coupling $\widetilde{\lambda}(t)$. This is consistent with the observation of the same scaling exponents for the NTFPs in classical-statistical simulations as in φ^4 theory. Remarkably, the resummed kinetic equations contain a dependence on the sign of the modified coupling, which is a manifestation of the qualitatively different dynamics in the case of attractive self-interactions where, in particular, the inverse cascade is absent, as observed in the simulations.

We have explored the regime in which the potential contains several local minima and the field can get trapped in one of them. It is found, by means of classical-statistical simulations, that an amplification of fluctuations strongly impacts the transition of the field from a false minimum. Particularly, we observe an efficient nucleation of bubbles at the end of the parametric resonance.

This effect of time-dependent bubble nucleation may be essential for generic first-order phase transitions in cosmology, where the field in the false minimum can be in an out-of-equilibrium state, and deserves further investigation. Importantly, the usual static picture of bubble nucleation from vacuum or thermal states [124, 243] does not capture such effects. The classical-statistical description, that was employed in this work, provides a powerful framework for the studies of dynamical aspects of nonequilibrium phase transitions. In the future, it would be interesting to find analytical estimates for the nucleation rate for a given spectrum of fluctuations, in the absence or even in the presence of an oscillating background field. This could be achieved within the classical-statistical framework, which is a valid approximation due to the large occupation numbers and small couplings involved, and can shed more light on the above mentioned dynamical effects.

The analysis in chapter 3 sets the stage for the investigation of specific cosmological scenarios. In chapter 4 we study the properties of ALP DM that is produced via the vacuum misalignment mechanism, in the presence of a (quadratic) monodromy. Our studies are based on classical-statistical lattice simulations of the dynamics on an expanding FRW background spacetime. We have found that for sufficiently strong wiggles and large oscillation amplitudes the resonant amplification of fluctuations triggers a fragmentation of the initially homogeneous ALP field. The process of the fragmentation happens soon after the onset of coherent oscillations of the ALP field, when the universe is still dominated by radiation. Our numerical analysis allows us to keep track of the momentum distribution and the equation of state of ALPs after the fragmentation. We have found that, despite the intermediate ultrarelativistic phase of dynamics after fragmentation, the typical physical momenta of ALPs sufficiently decrease due to the expansion, and the ALPs remain viable as DM for a wide range of masses. We have estimated the constraint $m_a \gtrsim 10^{-15}$eV on the mass range of ALP DM based on the Lyman-α forest data.

Investigation of the properties of ALP DM has become especially important because of increasing experimental efforts to detect them. Not only does the presence of a monodromy lift the bounds on ALP couplings e.g. to photons, as it was noted in [56], but it also affects the spatial distribution of DM, which is studied in chapter 4. As it is found in our numerical simulations, the process of the fragmentation imprints strong, $\mathcal{O}(1)$ overdensities in the field. We numerically extract the power spectrum of these overdensities at late times, after the self-interactions of ALPs become unimportant. The power spectrum is found to be peaked at relatively small length scales.

The presence of strong inhomogeneities on small scales is unusual for ALP DM. To analyze the evolution of these overdensities, we use a spherical collapse model [72], which we adapt to take into account the internal gradient pressure of the overdensity. This pressure, which is a manifestation of "wave-like" nature of light ALPs, is found to dominate over the gravitational attraction, preventing the overdense regions from collapsing into gravitationally bound objects. While such fluctuations in the distribution of DM may be difficult to detect in astrophysical and cosmological observations due to their small size, they are potentially detectable in direct detection experiments looking for ALP DM [160–169].

The evolution of the overdensities, imprinted from the process of fragmentation, is qualitatively different from those in the post-inflationary axion scenario, which are present already at the onset of oscillations and have a larger typical size. In the second case the pressure is weaker, allowing the collapse into axion miniclusters. Our adapted model of spherical collapse allows us to relate the size of an overdensity to its pressure and formulate the conditions necessary for the collapse. We verify that these conditions are indeed satisfied in the post-inflationary axion scenario.

An interesting question for future research is whether nonlinear effects due to gravity could significantly damp [244] the fluctuations that do not collapse. Answering this question would require going beyond the spherical collapse model and to apply techniques such as the lattice simulation of nonrelativistic field dynamics with Newtonian gravity taken into account i.e. the Schrödinger-Newton system [245]. The latter has been used in the studies of axion miniclusters [246, 247]. The possibility of NTFPs in this regime would be an especially interesting aspect of such studies.

The process of fragmentation of the ALP field leads to yet another important observational signature, in addition to the ones identified in chapter 4. It produces a stochastic GW background, calculated in chapter 5. The progress in GW detection [177, 178] will open significant opportunities for exploring the early universe and, in particular, for the search of such signatures of nonperturbative dynamics.

For our analysis we combine analytical estimates for the signal strength with numerical computations, by evolving linear metric perturbations. The requirement of not overproducing DM imposes strong bounds on the GW signal from ALP DM, making its detection difficult. As we have found, this bound can be lifted if the curvature of the ALP potential near its minimum is very small, leading to an extended phase of dynamics governed by NTFPs. In the presence of such large mass hierarchies, a straightforward analysis, based on numerical lattice computations, becomes extremely complicated due to the long periods of far-from-equilibriuum evolution and the different scales involved in the dynamics. To overcome this problem, we make use of our studies of the scaling exponents near NTFPs in chapter 3. We derive a simplified kinetic description of the self-similar dynamics on an expanding background spacetime. This allows us to estimate the duration of the ultrarelativistic phase and the characteristic velocities of ALPs. Such a GW background could be explored in future experiments, including pulsar timing arrays, i.e. “SKA” [78], as well as high-sensitivity space-based detectors like “BBO” [79].

In the scenario where the ALP field plays the role of the inflaton, the GW signal from the fragmentation in the preheating stage is stronger compared to the case of ALP DM, however, its frequency is usually rather high. The signal can potentially be extended to the experimentally interesting lower-frequency region if the dynamics involves getting trapped in a false minimum and a subsequent transition from that minimum induced by bubble nucleation [106]. In the future it will be important to study the GW production from such transitions, taking into account the dynamical nature of this process, which is described in chapter 3. In particular, the time dependence of the bubble nucleation rate and the large amount of bubble collisions in the presence of many local minima will modify standard estimates [183, 248] for GW production from cosmological phase transitions.

It should be kept in mind that the classical-statistical framework has a finite range of validity and cannot describe genuine quantum effects. For phase transitions after inflation with a low-frequency GW production one expects bubble nucleation to have a rather small rate (see e.g. [106]) and, thus, possibly be governed by quantum fluctuations. Moreover, quantum effects are necessarily involved in the thermalization towards Bose-Einstein or Fermi-Dirac distributions, which are never reached in a classical statistical description. A common approach to include such effects is the 2PI effective action (see e.g. [108]). A radically different alternative is based on quantum simulators, which is discussed in the final chapter of this work.

In chapter 6 the nonequilibrium dynamics in nonrelativistic scalar field theories, which can describe experiments with trapped ultracold atomic gases, is studied. The characteristic stages of the dynamics, that were discussed in the previous chapters for relativistic fields, are also observed in the nonrelativistic system. Here the conservation of total particle number prevents the resonant decay of a homogeneous background field. This restriction is compensated in our studies by a temporal modulation of the strength of the quartic self-interaction, which in cold atom experiments can be induced by means of external magnetic fields. A time-dependence of the interaction strength can encode also the expanding background FRW geometry in such systems, after an appropriate transformation of the time and field variables.

Thus ultracold atomic experiments can be used to test and simulate a variety of nonequilibrium many-body phenomena relevant but not restricted to the early universe cosmology. Such experiments have the potential of extending the existing theoretical studies beyond the range of validity of conventional approximations e.g. to the regimes of strong couplings or small occupation numbers. An especially interesting direction for future research would be the possibility of simulating the process of a false vacuum decay in QFT using ultracold atomic gases, with some efforts already having been made [249–251]. Moreover, exploring other tabletop experimental platforms such as spinor atomic gases [214, 215], nonlinear optical systems [252] and quantum computers [253], may further indicate the importance of the quantum simulation of nonequilibrium many-body dynamics in a laboratory.

Our studies demonstrate how simplicity can emerge in the dynamics far from equilibrium. The approach of the system to a NTFP represents a dramatic reduction in complexity of the dynamics, that is determined by a few universal scaling exponents only. This may be preceded by a stage of "prescaling", established recently in the studies of quark-gluon plasma dynamics related to heavy-ion collisions [254]. In this stage the system exhibits a "hydrodynamic" behavior, fully described in terms of a few slowly varying degrees of freedom, i.e. the time-dependent scaling exponents. Such behavior is also observed in our numerical simulations of relativistic field dynamics (see Fig. 3.8), and that of a nonrelativistic Bose gas, during the transition from driven to free turbulence. The reduction of complexity, which comes with such prescaling behaviour, was at the core of our simplified description of the extended stage of ultrarelativistic dynamics in terms of only a few variables in chapter 5. We have thus demonstrated that making use of the emergence of effective descriptions from QFT can be very important for the studies of early universe cosmology.

Acknowledgements

I am very thankful to everyone who supported me during my Ph.D. studies.

First of all, I would like to express my deepest gratitude to my supervisors Jürgen Berges and Joerg Jaeckel for giving me the opportunity to work on this project and for providing me with permanent guidance and support. I am very thankful for their patience, for the ideas that they generously shared with me during my studies, as well as for valuable advising. I am very lucky to have such amazing supervisors.

I would like to sincerely thank Philipp Hauke for always being so supportive to me, for his encouragement and for the incent to widen my research interests towards the field of quantum simulation.

My sincere gratitude to Kevin Geier for our fruitful collaboration and for sharing with me his expertise in the field of ultracold atoms. Many thanks to all members of the "BECK" experiment in the Oberthaler group for their collaboration and sharing with us their experience. Last but not least, I am very grateful to Kirill Boguslavski for his help and attention to my research.

I am very thankful to Björn Malte Schäfer for kindly agreeing to be a referee of my thesis, and to Jörg Evers and Markus Oberthaler for being part of my examination committee.

Throughout the years spent at the Institute for Theoretical Physics (ITP) in Heidelberg I was surrounded by many great people. I express my sincere gratitude to all my colleagues. Special thanks to Gregor Fauth, Robert Ott, Daniel Spitz and Lennert Thormählen, for proofreading parts of my thesis, as well as to Gonzalo Alonso-Álvarez, Erekle Arshilava, Oscar Garcia, Michael Heinrich, Daniel Kirchhof, Alexander Lehmann, Aleksas Mazeliauskas, Dustin Peschke, Frederic del Pozo, Linda Shen, Malo Tarpin, Pablo Soler, Torsten Zache and my former colleagues, for creating an inspiring and enjoyable environment.

Many thanks to all secretaries at the ITP and, especially, to Tina Kuka and Lijana Diestel, for always helping me.

I would like to thank my family members for their endless love and support.

Appendix A

The calculation of the source term for secondary instabilities

Some parts of the material presented in this appendix were also discussed in the context of the reference [21] by Berges and Serreau.

In this appendix to chapter 3 we evaluate the integral $I(t,t',\mathrm{p})$ of the source term leading to secondary instabilities, given by (3.18), and study the evolution of the fluctuations in its presence. Although in the second case we stick to the massive sine-Gordon model, the results can be easily generalized to other models.

Parametric resonance leads to a fluctuation spectrum consisting of several exponentially growing peaks i.e. $F(t,t',\mathbf{p}) = \sum_i F_i(t,t',\mathbf{p})$, with F_i characterizing the i-th peak. We denote the absolute values of the momenta of the peak centers by p_i and the corresponding growth exponent as $\mu_i = \mu(\mathrm{p}_i)$, such that $F_i(t,t',\mathbf{p}_i) \sim e^{\mu_i(t+t')}$. The integral I can be then written as

$$I(t,t',\mathrm{p}) = \sum_{i,j} I_{ij}(t,t',\mathrm{p}), \qquad I_{ij}(t,t',\mathrm{p}) = \int \frac{d^3\mathbf{q}}{(2\pi)^3} F_i(t,t',\mathbf{p}-\mathbf{q}) F_j(t,t',\mathbf{q}). \quad \text{(A.1)}$$

We make a Gaussian ansatz for the peaks, $\mu(\mathrm{p}) \approx \mu_i - (\mu_i''/2)(\mathrm{p}-\mathrm{p_i})^2$, with $\mu_i'' > 0$ characterizing the width of the i-th peak. The two-point function can be then written as

$$F_i(t,t',\mathbf{p}) = F(t,t',\mathrm{p}_i) e^{-(\mu_i''/2)(\mathrm{p}-\mathrm{p_i})^2(t+t')}. \quad \text{(A.2)}$$

For most values of momentum p in (A.1) the width of the peaks can be neglected i.e. the gaussian peaks can be replaced by δ-peaks,

$$F_i(t,t',\mathbf{p}) \to F(t,t',\mathrm{p}_i)\sqrt{2\pi}[\mu_i''(t+t')]^{-1/2}\delta(\mathrm{p}-\mathrm{p_i}).$$

Inserting this form into (A.1) gives

$$I_{ij}(t,t',\mathrm{p}) = \frac{F(t,t',\mathrm{p}_i)F(t,t',\mathrm{p}_j)\mathrm{p_i p_j}}{2\pi} \frac{1}{\sqrt{\mu_i''\mu_j''}(t+t')\mathrm{p}} \quad \text{(A.3)}$$

for $|\mathrm{p_i} - \mathrm{p_j}| \leq \mathrm{p} \leq \mathrm{p_i} + \mathrm{p_j}$ and zero otherwise.

Only terms with $i = j$ contribute to $I(t,t',\mathrm{p})$ at $\mathrm{p} = 0$. The divergence of (A.3) for $\mathrm{p} \to 0$ is due to the δ-peak approximation. To evaluate the integral near $\mathrm{p} = 0$ the form of (A.2) should be used. For small momenta p the integrand in (A.1) is then Taylor-expanded up to the quadratic order in p. The resulting integrals over q are evaluated using standard saddle point approximation around $\mathrm{q} \approx \mathrm{p_i}$, which leads to

$$I(t,t',\mathrm{p}) = \sum_i I_{ii}(t,t',\mathrm{p}) = \sum_i I_{ii}(t,t',0)(1 - \mathrm{p}^2 \mu_i''(t+t')/6), \tag{A.4}$$

where

$$I_{ii}(t,t',0) = \frac{F^2(t,t',\mathrm{p}_i)\mathrm{p}_i^2}{2\pi}\sqrt{\frac{1}{\pi\mu_i''(t+t')}}. \tag{A.5}$$

The sharp momentum cut-offs in (A.3) are also due to the δ-peak approximation and are replaced by an exponential decay in the case of finite width of the peaks.

Due to the exponential growth, in many cases the strongest peak gives the dominant contribution to the source term, $I(t,t',\mathrm{p}) \approx I_{00}(t,t',\mathrm{p})$. In this case the spectrum, generated from secondary instabilities, decreases on average with p, extending from $\mathrm{p} = 0$ up to approximately twice the momentum of the strongest peak, $\mathrm{p} = 2\mathrm{p}_0$.

Having found the expression for the integral in the source term we now discuss its impact on the evolution of the fluctuations. Combining the above expressions with (3.16), the equations of motion for the momentum modes of the statistical propagator have the form

$$\begin{aligned}&\Big[\partial_t^2 + \mathbf{p}^2 + m^2\Big(1 + \kappa^2 \cos\frac{\phi(t)}{f}\Big)\Big]F(t,t',\mathbf{p}) \\ &= \sin\frac{\phi(t)}{f}\sum_{i,j} F(t,t',\mathrm{p}_i)F(t,t',\mathrm{p}_j)\alpha_{ij}(t,t',\mathrm{p}),\end{aligned} \tag{A.6}$$

where $F(t,t',\mathrm{p}_i)F(t,t',\mathrm{p}_j)\alpha_{ij}(t,t',\mathrm{p}) = \lambda\kappa^2(\alpha^2/4)\sin(\phi(t')/f)I_{ij}(t,t',\mathrm{p})$. To study the secondary instabilities we consider modes that are stable on the linear level or much less enhanced compared to the most unstable fluctuations. For these modes (A.6) is a linear inhomogenous differential equation. The solution can be written as $F = F^{(0)} + \sum_{i,j} F^{(i,j)}$, where $F^{(0)}$ describes the mode evolution in the absence of the source and $F^{(i,j)}$ solves (A.6) in the presence of the corresponding source term. Since the statistical propagators on the right-hand side exhibit an exponential growth, $F(t,t',\mathrm{p}_k) = e^{\mu_k(t+t')}\widetilde{F}(t,t',\mathrm{p}_k)$, it is convenient to factor out the corresponding growth of the solution $F^{(i,j)}$. The latter will have the form $F^{(i,j)}(t,t',\mathbf{p}) = e^{(\mu_i+\mu_j)(t+t')}\widetilde{F}^{(i,j)}(t,t',\mathbf{p})$, with the function $\widetilde{F}^{(i,j)}(t,t',\mathbf{p})$ satisfying

$$\begin{aligned}&\Big[\partial_t^2 + 2(\mu_i+\mu_j)\partial_t + (\mu_i+\mu_j)^2 + \omega_{\mathbf{p}}^2\Big]\widetilde{F}^{(i,j)}(t,t',\mathbf{p}) \\ &= \sin\frac{\phi(t)}{f}\widetilde{F}(t,t',\mathrm{p}_i)\widetilde{F}(t,t',\mathrm{p}_j)\alpha_{ij}(t,t',\mathrm{p}).\end{aligned} \tag{A.7}$$

In the last equation the time-dependent frequency was replaced by its average frequency $\omega_{\mathbf{p}}$ due to the absence of strong parametric resonance for that mode. Ignoring the time-dependence of α_{ij}, this equation describes a damped and periodically driven harmonic oscillator and, therefore, $\widetilde{F}^{(i,j)}(t,t',\mathbf{p}) \propto \alpha_{ij}(t,t',\mathrm{p})$. It is well known, that the strongest amplification occurs for modes with resonant frequencies. As can be seen from (A.3) and (A.4), the functions α_{ij} do not contain a periodic component. Hence only the remaining three terms on the right-hand side of (A.7) account for the resonant amplification. We have confirmed the emergence of resonant peaks by including the source term, calculated using the approximation of narrow δ-peaks from (A.3), in the linear equations of motion for the fluctuations and solving them numerically.

Appendix B

The modified spherical collapse model

The content of this appendix is based on the work in collaboration with Jürgen Berges and Joerg Jaeckel, that has been published in [2]. In that work I did the main computations and most of the writing of the script. The large part of the text in this appendix is taken from that reference.

In this appendix to chapter 4 we describe the spherical collapse model [72, 73], adapted to take into account the nonvanishing pressure of the overdensities of monodromy ALP dark matter.

We consider an over-density of radius r, density ρ, pressure p and total mass M. The Newtonian equation of motion for the radius has the form [158]

$$\frac{d^2r}{dt^2} = -\frac{8\pi G}{3}\rho_R r - \frac{GM}{r^2} - \frac{1}{\rho}\frac{dp}{dr}, \tag{B.1}$$

where G is Newton's constant and ρ_R is the background density of radiation. The second term on the right-hand side is the gravitational force due to the matter insider the spherical shell and the last term is the pressure gradient force [159]. The total mass is conserved and related to the initial[1] density contrast δ of the overdensity by

$$M = \frac{4\pi}{3}\rho r^3 = \frac{4\pi}{3}\bar{\rho}(1+\delta)r^3. \tag{B.2}$$

The pressure term can be estimated by noting that ALPs have already become non-relativistic by the time of interest, such that $\epsilon_{\mathbf{p}} \approx m_a$. Therefore,

$$\rho \approx m_a \frac{N}{V} = \frac{M}{V} \propto r^{-3}, \qquad p \approx \frac{\langle \mathrm{p}^2 \rangle}{3m_a}\frac{N}{V} \approx \frac{\langle \mathrm{p}^2 \rangle}{3m_a^2}\rho = \frac{\alpha^2}{3m_a^2 r^2}\rho \propto r^{-5}. \tag{B.3}$$

where N is the number of ALPs in the over-density and $\alpha \sim 2\pi$ relates the radius to the characteristic momentum. The acceleration due to the pressure is then given by

$$-\frac{1}{\rho}\frac{dp}{dr} = \frac{1}{\rho}\frac{5p}{r} = \frac{5\alpha^2}{3m_a^2 r^3}. \tag{B.4}$$

The radius of the over-density can be expressed as $r(t) = \xi a(t)R(t)$, where ξ is the comoving radius before decoupling and $R(t)$ describes the deviation of the radius from the background Hubble flow (such that $R = 1$ at early times, before decoupling). Transforming from time to the variable $x = a/a_{\mathrm{eq}}$, as explained in [72].

---

[1] The density contrast starts to grow after the over-density collapses.

in our case leads to

$$x\Big(1+x\Big)\ddot{R}+\Big(1+\frac{3}{2}x\Big)\dot{R}+\frac{1}{2}\Big[\frac{1+\delta}{R^2}-R\Big]-\frac{C}{xR^3}=0. \tag{B.5}$$

The last term in (B.5) is the extra-term due to the non-vanishing pressure. The prefactor C is given by

$$C=\frac{5\alpha^2}{8\pi G\bar{\rho}_{\rm eq}a_{\rm eq}^4\xi^4m_a^2}, \tag{B.6}$$

where $\bar{\rho}_{\rm eq}$ is the average density of ALP dark matter at the epoch of matter-radiation equality.

The expression for C can be found by relating the comoving radius of the over-density to its characteristic comoving momentum, $\xi=\alpha/{\rm p}$. Using the relation

$$\frac{H_{\rm eq}}{H_{\rm osc}}=\frac{a_{\rm osc}^2}{a_{\rm eq}^2} \tag{B.7}$$

for the Hubble parameter in a radiation-dominated universe, this leads to

$$C=\frac{5\alpha^2}{8\pi G\bar{\rho}_{\rm eq}}\frac{{\rm p}^4}{m_a^2a_{\rm eq}^4\alpha^4}=\frac{5\alpha^2}{8\pi G\bar{\rho}_{\rm eq}}\frac{9H_{\rm eq}^2\eta^4}{\alpha^4}, \tag{B.8}$$

where $\eta={\rm p}/(m_a a_{\rm osc})$. Finally, noting that at the epoch of matter-radiation equality $H_{\rm eq}^2=(8\pi G/3)2\bar{\rho}_{\rm eq}$, we arrive at

$$C(\eta)=\frac{30}{\alpha^2}\eta^4\approx 0.76\,\eta^4, \tag{B.9}$$

where in the last step we set $\alpha\approx 2\pi$. As can be seen, the parameter C is proportional to the fourth power of the typical dimensionless rescaled comoving momentum η of the over-density.

Appendix C

Simplified kinetic description

The content of this appendix is based on the work done in collaboration with Joerg Jaeckel, and is presented in the preprint [3]. In that work I did the main computations and most of the writing of the script. Large parts of the text in this appendix are taken from that reference.

In this appendix to chapter 5 we describe the analysis of the dynamics near NTFPs in an expanding FRW spacetime, based on a simplified kinetic description. Such a description allows us to obtain estimates for the duration of the extended ultrarelativistic phase after fragmentation of ALPs which have a very small mass near the bottom of the potential. It also allows us to estimate the typical velocities after the freezing of the ALP spectrum.

After the fragmentation of the ALP field, the momentum distribution function, in the presence of repulsive self-interactions, is split into two cascades (see Fig. 5.6). This allows us to characterize the field dynamics in terms of a few quantities describing both momentum regions, as we describe below.

The dynamics at small momenta: The final result of the inverse cascade at low momenta is the emergence of a homogeneous condensate, which carries most of the particle number. In lattice simulations condensation is completed after a finite time, which increases with the volume of the simulation. In other words, the condensate would not become homogeneous across the entire universe within a finite amount of time. Nevertheless, the typical scale of inhomogeneities in the low momentum region is from the beginning larger than the inverse mass, and increases as long as the inverse cascade continues. For simplicity, the entire infrared region can be thus approximated as homogeneous, starting at times when its formation is completed in simulations with moderate volumes.

The dynamics of such a homogeneous component in our description is extrapolated by solving the classical field equations:

$$\ddot{\phi}(t) + 3H\dot{\phi}(t) + m^2\phi(t) + \frac{\Lambda^4}{f}\sin\left(\frac{\phi(t)}{f}\right) + 2r\frac{\Lambda^4}{f}\sin\left(2\frac{\phi(t)}{f}\right) = 0. \tag{C.1}$$

The dynamics at large momenta: At high momenta a direct cascade develops after the collapse. As it is demonstrated in the following sections, deviations from the scaling behavior appear when the mass near the bottom of the potential becomes important. At this point the cascade slows down and eventually freezes. To study this effect we evolve the characteristic momentum mode $\bar{\mathrm{p}}(a)$ and the occupation number at that momentum $\bar{n}(a)$ according to a simplified Boltzmann equation, which is derived below.

C.1 Deviations from the self-similar evolution

As it was explained in section 5.3.1, for the most of the extended ultrarelativistic phase of the dynamics after fragmentation, the potential can be well approximated as massless (conformal) quartic. An important feature of this approximate conformal symmetry is that the evolution equations in the radiation-dominated FRW universe, expressed in terms of comoving coordinates and conformal field and time variables, are the same as those in a Minkowski spacetime.

The self-similar behavior of the direct cascade at high momenta, where $\omega_{\rm p} \approx {\rm p}$ is satisfied, for the conformal φ^4 theory has been studied in [22] (see also section 6.5.2 chapter 6). The scaling exponents of the self-similar evolution,

$$n(\tau, {\rm p}) = \Big(\frac{\tau}{\tau_S}\Big)^{\alpha} n_S\Big(\Big(\frac{\tau}{\tau_S}\Big)^{\beta} {\rm p}\Big),$$

are found to be $\beta \approx -1/5$ and $\alpha \approx 4\beta$, where n_S denotes the spectrum at time τ_S. These values can be obtained by solving the Boltzmann equation for a collision term of three-body scattering processes (see also Eq. (C.6)).

The self-similar evolution of the energy cascade takes place in the regime of high occupations, $1 \ll \bar{n} \ll \lambda^{-1}$, and terminates when $\bar{n}$ becomes of order one. At this stage genuine quantum effects become important and the system is expected to thermalize. This regime of the dynamics is not captured by the classical-statistical approximation, which is instead valid when the spectrum has large occupations at low momenta.

In order to estimate the time when the characteristic occupation numbers would become of order unity, we note that from the above scaling relations it follows that $\bar{n}(\bar{\rm p}) \propto \bar{\rm p}^{-\alpha/\beta} \propto \bar{\rm p}^{-4}$. Estimating the proportionality constant from the left panel in Fig. 5.6 we arrive at

$$\bar{n} \sim \frac{1}{\lambda}\Big(\frac{30}{\bar{\eta}}\Big)^4 = \frac{1}{\lambda}\Big(\frac{30 m_a a_{\rm osc}}{\bar{\rm p}}\Big)^4 \sim \frac{1}{\lambda}\Big(\frac{a}{15 a_{\rm osc}}\Big)^{4\beta}, \tag{C.2}$$

where we also used an estimation $\bar{\rm p}(a) \sim (30 m_a a_{\rm osc})(a/(15 a_{\rm osc}))^{-\beta}$ from that figure.

On the other hand, the scaling behavior described above is valid only in the ultrarelativistic regime. The small mass near the bottom of the potential eventually leads to deviations from such behavior. These deviations are expected to become important when

$$\bar{\rm p} \sim m_{\rm final} a, \tag{C.3}$$

and, using the above estimate for the characteristic momentum $\bar{\rm p}$, one arrives at

$$30\Big(\frac{a}{15 a_{\rm osc}}\Big)^{-\beta} = r\Big(\frac{a}{a_{\rm osc}}\Big). \tag{C.4}$$

Inserting the numerical values for the exponents into the above expressions we obtain parametric estimates for the scale factor for thermalization as well as for the onset of nonrelativistic dynamics,

$$\frac{a}{a_{\rm osc}} \sim \frac{15}{\lambda} \text{ for thermalization, } \frac{a}{a_{\rm osc}} \sim \Big(\frac{30}{r}\Big)^{\frac{5}{4}} \text{ for the onset of the nonrelativistic regime.} \tag{C.5}$$

The cascade freezes soon after the onset of the nonrelativistic behavior. The freeze-out can be understood not from thermalization but because the interaction rate is suppressed compared to the Hubble expansion.

For all values of λ and r that are relevant for our ALP models, thermalization happens at much larger scale factors than the transition to the nonrelativistic regime of the dynamics. This implies that the ALPs do not achieve thermal equilibrium when they become nonrelativistic and that the description of this transition can be based on the classical-statistical approximation.

C.2 Kinetic description and the freeze-out

In this subsection we demonstrate how the onset of nonrelativistic dynamics, which happens when (C.3) is satisfied, leads to the freeze-out of the cascade. To do this we first write down the kinetic equation describing the cascade, without assuming ultrarelativistic dynamics. We then derive from it a simplified evolution equation for the occupation numbers at the characteristic momentum. We then verify its power-law behavior in the ultrarelativistic regime as well its slow down when the nonrelativistic corrections set in.

The kinetic equation that describes the dynamics of the direct cascade has been derived in [22]. It can be written as

$$\partial_\tau n_{\mathrm{p}} = n'_{\mathrm{p}} H_0 = I_{(3)} + I_{(4)} + ...,$$

where $I_{(l)}$ is the collision term corresponding to l-body scatterings. As it is shown in [22], the dynamics is dominated by three-body scatterings that arise from the quartic vertex in the presence of a condensate. The corresponding collision term in the regime of large occupation numbers, $n_{\mathbf{p}} \gg 1$, has the form [22]

$$\begin{aligned} I_{(3)} = & \int \frac{\lambda^2 \langle \phi_c^2 \rangle}{2} \frac{d^3\mathrm{k} d^3\mathrm{q} \delta^{(3)}(\mathbf{p} - \mathbf{k} - \mathbf{q})}{(2\pi)^2 2\omega_{\mathbf{p}} 2\omega_{\mathbf{k}} 2\omega_{\mathbf{q}}} \delta(\omega_{\mathbf{0}} + \omega_{\mathbf{p}} - \omega_{\mathbf{k}} - \omega_{\mathbf{q}}) \Big[n_{\mathbf{k}} n_{\mathbf{q}} - n_{\mathbf{p}}(n_{\mathbf{k}} + n_{\mathbf{q}}) \Big] \\ & -2 \int \frac{\lambda^2 \langle \phi_c^2 \rangle}{2} \frac{d^3\mathrm{k} d^3\mathrm{q} \delta^{(3)}(\mathbf{p} + \mathbf{k} - \mathbf{q})}{(2\pi)^2 2\omega_{\mathbf{p}} 2\omega_{\mathbf{k}} 2\omega_{\mathbf{q}}} \delta(\omega_{\mathbf{p}} + \omega_{\mathbf{k}} - \omega_{\mathbf{0}} - \omega_{\mathbf{q}}) \Big[n_{\mathbf{p}} n_{\mathbf{k}} - n_{\mathbf{q}}(n_{\mathbf{p}} + n_{\mathbf{k}}) \Big] \end{aligned} \quad \text{(C.6)}$$

where $\omega_{\mathbf{p}}^2 = \mathrm{p}^2 + M^2$ is the particle energy and $\langle \phi_c^2 \rangle(\tau) = F_c(\tau, \tau, \mathbf{p} = 0)$ describes the condensate in terms of conformal variables.

One can see already from the (C.6) why the onset of nonrelativistic regime leads to the slow-down of the dynamics. The particle energies, present in the denominator of the collision integral, grow as

$$\omega_{\mathrm{p}} = \sqrt{\mathrm{p}^2 + M^2} \approx M \approx m_{\mathrm{final}} a$$

when they become dominated by the rest mass. This leads to the suppression in the right-hand side of (C.6). [1] Also the $\langle \phi_c^2 \rangle$ term is approximately in the quartic-dominated regime and decreases in the mass-dominated regime.

We now derive the simplified evolution equation for the characteristic modes. Assuming that the shape of the distribution function does not change much throughout the entire dynamics and that the collision term is dominated by momenta close

---

[1] In the language of the physical time and the occupation numbers per physical volume the kinetic equation has the form

$$\partial_t n_{\mathrm{p}} + 3 H n_{\mathrm{p}} = C[n],$$

and the freeze-out happens as a result of the Hubble friction term dominating over the collision term.

to the characteristic momentum, we can replace the occupation numbers in the squared brackets of (C.6) by the characteristic occupation $\bar{n}(\tau)$ and the energies in the denominator by the characteristic energy $\bar{\omega}(\tau) = \omega(\tau, \bar{\mathrm{p}})$. The momentum integrals over the delta-functions give

$$\int d^3\mathrm{k} d^3\mathrm{q} \delta^{(3)}(\mathbf{p} - \mathbf{k} - \mathbf{q})\delta(\omega_\mathbf{0} + \omega_\mathbf{p} - \omega_\mathbf{k} - \omega_\mathbf{q}) = \int d^3\mathrm{k}\delta(\omega_\mathbf{0} + \omega_\mathbf{p} - \omega_\mathbf{k} - \omega_{\mathbf{p}-\mathbf{k}})$$

$$\propto \int d\mathrm{k}\mathrm{k}^2\delta(\omega_\mathbf{0} + \omega_\mathbf{p} - \omega_\mathbf{k} - \omega_{\mathbf{p}-\mathbf{k}}) \sim \bar{\mathrm{p}}^2(\tau)\left[\frac{\bar{\mathrm{p}}(\tau)}{\bar{\omega}(\tau)}\right]^{-1}.$$

Combining everything leads to the following form of the simplified kinetic equation for the characteristic momentum mode,

$$\bar{n}' \approx C_{(3)}\frac{\langle\phi_c^2\rangle\bar{n}^2\bar{\mathrm{p}}}{\bar{\omega}^2}, \tag{C.7}$$

where $C_{(3)}$ is an unknown constant, which encodes the details of the kinetic equation, but should not change much with time. Instead of calculating it we simply find the constant by matching the extrapolation with the lattice simulation.

Of course, the derivation of the above equation is not rigorous. Nevertheless, (C.7) provides an insight into the dynamics. Importantly, the $\bar{\mathrm{p}} \propto \tau^{1/5}$ solution is recovered in the ultrarelativistic regime, $\bar{\omega} \approx \bar{\mathrm{p}}$, under the assumption that $\langle\phi_c^2\rangle$ stays approximately constant. Moreover, it also describes the slow-down of the cascade once the nonrelativistic behavior sets in, as illustrated in Fig. 5.8.

C.3 Energy conservation for the direct cascade

In a static spacetime the direct cascade transports conserved energy. However, in an expanding spacetime energy is not conserved. In the language of conformal variables, this is due to the time-dependence of the Hamiltonian, induced by the scale factor. The ultrarelativistic regime in φ^4 theory is a special case, since the time-dependence drops and a conserved quantity $\rho_c = a^4\rho$ emerges.

To be able to extend the discussion about the energy cascades beyond the ultrarelativistic regime we note that in an expanding universe the energy dilutes according to

$$\frac{\rho'}{\rho} = \frac{-3 - 3w(a)}{a}, \tag{C.8}$$

where the primes denote derivatives with respect to the scale factor. This equation will be used as the generalization of the energy conservation condition in a static spacetime and will allow us to relate the exponents α and β.

The parameter w can be determined from the energy and the pressure of the field, given by

$$\rho \approx \frac{1}{a^4}\int_\mathbf{p} \omega(t, \mathrm{p})n(t, \mathrm{p}), \quad p \approx \frac{1}{a^4}\int_\mathbf{p} \frac{\mathrm{p}^2}{3\omega(t, \mathrm{p})}n(t, \mathrm{p}).$$

The energy during the direct cascade is centered around the characteristic momentum, which allows us to express the energy and the pressure in terms of $\bar{\mathrm{p}}(a)$ and

$\bar{n}(a)$, as well as the corresponding particle energy $\bar{\omega} = \omega(\bar{\mathrm{p}})$, according to

$$\rho \propto \frac{1}{a^4}\bar{\mathrm{p}}^3\bar{n}\bar{\omega}, \quad p \propto \frac{1}{a^4}\bar{\mathrm{p}}^3\bar{n}\frac{\mathrm{p}^2}{3\bar{\omega}}. \tag{C.9}$$

The corresponding equation of state parameter w can be estimated from (C.9) as

$$w = \frac{p}{\rho} = \frac{\bar{\mathrm{p}}^2}{3\bar{\omega}^2}. \tag{C.10}$$

Now, from the first equation in (4.23) it follows that

$$\frac{\rho'}{\rho} = 3\frac{\bar{\mathrm{p}}'}{\bar{\mathrm{p}}} + \frac{\bar{n}'}{\bar{n}} + \frac{\bar{\omega}'}{\bar{\omega}} - \frac{4}{a}.$$

Therefore, using (C.8), the energy conservation for the direct cascade can be expressed as

$$3\frac{\bar{\mathrm{p}}'}{\bar{\mathrm{p}}} + \frac{\bar{n}'}{\bar{n}} + \frac{\bar{\omega}'}{\bar{\omega}} = \frac{1-3w}{a}. \tag{C.11}$$

Let us consider some particular cases. In the ultrarelativistic regime $\bar{\omega} \approx \bar{\mathrm{p}}$ and $w \approx 1/3$, which leads to the standard energy conservation in φ^4 theory,

$$4\frac{p'}{p} + \frac{\bar{n}'}{\bar{n}} = 0.$$

In contrast, in the nonrelativistic regime, where $\bar{\omega} \approx Ma$ and $w \approx 0$. As a result, for a constant mass M, the third term is approximately $1/a$ and the conservation reads

$$3\frac{p'}{p} + \frac{\bar{n}'}{\bar{n}} = 0.$$

To summarize the appendix, we solve a set of coupled equations for the homogeneous component (C.1), for the characteristic momentum scale (C.7) and the one reflecting energy conservation (C.11). These equations are supplemented by the approximate equation for the particle energy at the characteristic momentum $\bar{\omega}(a)$,

$$\bar{\omega}^2 = \bar{\mathrm{p}}^2 + m_{\mathrm{final}}^2 a^2 + \frac{\lambda\langle\phi_c^2\rangle}{2}. \tag{C.12}$$

We initialize the variables ϕ_c, $\bar{n}$ and $\bar{\mathrm{p}}$ as well as the prefactor $C_{(3)}$ using the data from lattice simulations. The results from this analysis are summarized in Sec. 5.3.3 and, in particular, in figures 5.8 and 5.9.

Bibliography

[1]J. Berges, K. Boguslavski, A. Chatrchyan, and J. Jaeckel, "Attractive versus repulsive interactions in the Bose-Einstein condensation dynamics of relativistic field theories", Phys. Rev. **D96**, 076020 (2017).

[2]J. Berges, A. Chatrchyan, and J. Jaeckel, "Foamy Dark Matter from Monodromies", JCAP **1908**, 020 (2019).

[3]A. Chatrchyan and J. Jaeckel, "Gravitational waves from the fragmentation of axion-like particle dark matter", arXiv preprint hep-ph:2004.07844 (2020).

[4]J. Berges, A. Chatrchyan, K. Geier, P. Hauke, and M. K. Oberthaler, "Analog reheating of the universe in the laboratory", in preparation (2020).

[5]G. Aad et al., "Observation of a new particle in the search for the Standard Model Higgs boson with the ATLAS detector at the LHC", Phys. Lett. B **716**, 1–29 (2012).

[6]S. Chatrchyan et al., "Observation of a New Boson at a Mass of 125 GeV with the CMS Experiment at the LHC", Phys. Lett. B **716**, 30–61 (2012).

[7]F. Zwicky, "Die Rotverschiebung von extragalaktischen Nebeln", Helv. Phys. Acta **6**, 110–127 (1933).

[8]S. W. Allen, A. E. Evrard, and A. B. Mantz, "Cosmological parameters from observations of galaxy clusters", Annual Review of Astronomy and Astrophysics **49**, 409–470 (2011).

[9]D. Clowe, M. Bradac, A. H. Gonzalez, M. Markevitch, S. W. Randall, C. Jones, and D. Zaritsky, "A direct empirical proof of the existence of dark matter", Astrophys. J. **648**, L109–L113 (2006).

[10]N. Aghanim et al., "Planck 2018 results. VI. Cosmological parameters", (2018).

[11]A. H. Guth, "The Inflationary Universe: A Possible Solution to the Horizon and Flatness Problems", Phys. Rev. **D23**, [Adv. Ser. Astrophys. Cosmol.3,139(1987)], 347–356 (1981).

[12]A. A. Starobinsky, "A New Type of Isotropic Cosmological Models Without Singularity", Phys. Lett. **B91**, [,771(1980)], 99–102 (1980).

[13]A. R. Liddle and D. H. Lyth, *Cosmological inflation and large scale structure* (2000).

[14]A. A. Starobinsky, "Dynamics of Phase Transition in the New Inflationary Universe Scenario and Generation of Perturbations", Phys. Lett. **117B**, 175–178 (1982).

[15]L. Kofman, A. D. Linde, and A. A. Starobinsky, "Reheating after inflation", Phys. Rev. Lett. **73**, 3195–3198 (1994).

[16]J. Rubio, "Higgs inflation", Front. Astron. Space Sci. **5**, 50 (2019).

[17]L. Kofman, A. D. Linde, and A. A. Starobinsky, "Towards the theory of reheating after inflation", Phys. Rev. **D56**, 3258–3295 (1997).

[18]J. M. Cornwall, R. Jackiw, and E. Tomboulis, "Effective Action for Composite Operators", Phys. Rev. **D10**, 2428–2445 (1974).

[19] L. V. Keldysh, “Diagram technique for nonequilibrium processes”, Zh. Eksp. Teor. Fiz. **47**, [Sov. Phys. JETP20,1018(1965)], 1515–1527 (1964).

[20] J. Berges, “Nonequilibrium Quantum Fields: From Cold Atoms to Cosmology”, arXiv preprint hep-ph:1503.02907 (2015).

[21] J. Berges and J. Serreau, “Parametric resonance in quantum field theory”, Phys. Rev. Lett. **91**, 111601 (2003).

[22] R. Micha and I. I. Tkachev, “Turbulent thermalization”, Phys. Rev. **D70**, 043538 (2004).

[23] J. Berges, A. Rothkopf, and J. Schmidt, “Non-thermal fixed points: Effective weak-coupling for strongly correlated systems far from equilibrium”, Phys. Rev. Lett. **101**, 041603 (2008).

[24] J. Berges and D. Sexty, “Strong versus weak wave-turbulence in relativistic field theory”, Phys. Rev. **D83**, 085004 (2011).

[25] A. Piñeiro Orioli, K. Boguslavski, and J. Berges, “Universal self-similar dynamics of relativistic and nonrelativistic field theories near nonthermal fixed points”, Phys. Rev. **D92**, 025041 (2015).

[26] P. Arias, D. Cadamuro, M. Goodsell, J. Jaeckel, J. Redondo, and A. Ringwald, “WISPy Cold Dark Matter”, JCAP **1206**, 013 (2012).

[27] J. Preskill, M. B. Wise, and F. Wilczek, “Cosmology of the Invisible Axion”, Phys. Lett. **120B**, 127–132 (1983).

[28] L. F. Abbott and P. Sikivie, “A Cosmological Bound on the Invisible Axion”, Phys. Lett. **120B**, 133–136 (1983).

[29] M. Dine and W. Fischler, “The Not So Harmless Axion”, Phys. Lett. **120B**, 137–141 (1983).

[30] W. Hu, R. Barkana, and A. Gruzinov, “Cold and fuzzy dark matter”, Phys. Rev. Lett. **85**, 1158–1161 (2000).

[31] D. J. E. Marsh, “Axion Cosmology”, Phys. Rept. **643**, 1–79 (2016).

[32] D. H. Weinberg, J. S. Bullock, F. Governato, R. Kuzio de Naray, and A. H. G. Peter, “Cold dark matter: controversies on small scales”, Proc. Nat. Acad. Sci. **112**, 12249–12255 (2015).

[33] R. D. Peccei and H. R. Quinn, “CP Conservation in the Presence of Instantons”, Phys. Rev. Lett. **38**, [,328(1977)], 1440–1443 (1977).

[34] S. Weinberg, “A New Light Boson?”, Phys. Rev. Lett. **40**, 223–226 (1978).

[35] F. Wilczek, “Problem of Strong P and T Invariance in the Presence of Instantons”, Phys. Rev. Lett. **40**, 279–282 (1978).

[36] C. T. Hill and A. K. Leibovich, “Deconstructing 5-D QED”, Phys. Rev. **D66**, 016006 (2002).

[37] N. Arkani-Hamed, H.-C. Cheng, P. Creminelli, and L. Randall, “Extra natural inflation”, Phys. Rev. Lett. **90**, 221302 (2003).

[38] P. Svrcek and E. Witten, “Axions In String Theory”, JHEP **06**, 051 (2006).

[39] A. Arvanitaki, S. Dimopoulos, S. Dubovsky, N. Kaloper, and J. March-Russell, “String Axiverse”, Phys. Rev. **D81**, 123530 (2010).

[40] B. S. Acharya, K. Bobkov, and P. Kumar, “An M Theory Solution to the Strong CP Problem and Constraints on the Axiverse”, JHEP **11**, 105 (2010).

[41] M. Cicoli, M. Goodsell, and A. Ringwald, “The type IIB string axiverse and its low-energy phenomenology”, JHEP **10**, 146 (2012).

[42] J. Callan Curtis G., R. F. Dashen, and D. J. Gross, “Toward a Theory of the Strong Interactions”, Phys. Rev. D **17**, 2717 (1978).

[43] P. B. Greene, L. Kofman, and A. A. Starobinsky, “Sine-Gordon parametric resonance”, Nucl. Phys. **B543**, 423–443 (1999).

[44] A. Arvanitaki, S. Dimopoulos, M. Galanis, L. Lehner, J. O. Thompson, and K. Van Tilburg, “The Large-Misalignment Mechanism for the Formation of Compact Axion Structures: Signatures from the QCD Axion to Fuzzy Dark Matter”, arXiv preprint astro-ph.CO:1909.11665 (2019).

[45] J. E. Kim, H. P. Nilles, and M. Peloso, “Completing natural inflation”, JCAP **0501**, 005 (2005).

[46] I. Ben-Dayan, F. G. Pedro, and A. Westphal, “Hierarchical Axion Inflation”, Phys. Rev. Lett. **113**, 261301 (2014).

[47] K. Choi, H. Kim, and S. Yun, “Natural inflation with multiple sub-Planckian axions”, Phys. Rev. **D90**, 023545 (2014).

[48] T. Higaki and F. Takahashi, “Natural and Multi-Natural Inflation in Axion Landscape”, JHEP **07**, 074 (2014).

[49] N. Kaloper and L. Sorbo, “A Natural Framework for Chaotic Inflation”, Phys. Rev. Lett. **102**, 121301 (2009).

[50] L. McAllister, E. Silverstein, and A. Westphal, “Gravity Waves and Linear Inflation from Axion Monodromy”, Phys. Rev. **D82**, 046003 (2010).

[51] E. Silverstein and A. Westphal, “Monodromy in the CMB: Gravity Waves and String Inflation”, Phys. Rev. **D78**, 106003 (2008).

[52] F. Marchesano, G. Shiu, and A. M. Uranga, “F-term Axion Monodromy Inflation”, JHEP **09**, 184 (2014).

[53] P. W. Graham, D. E. Kaplan, and S. Rajendran, “Cosmological Relaxation of the Electroweak Scale”, Phys. Rev. Lett. **115**, 221801 (2015).

[54] L. Abbott, “A Mechanism for Reducing the Value of the Cosmological Constant”, Phys. Lett. B **150**, 427–430 (1985).

[55] J. D. Brown and C. Teitelboim, “Dynamical Neutralization of the Cosmological Constant”, Phys. Lett. **B195**, 177–182 (1987).

[56] J. Jaeckel, V. M. Mehta, and L. T. Witkowski, “Monodromy Dark Matter”, JCAP **1701**, 036 (2017).

[57] C. J. Pethick and H. Smith, *Bose–einstein condensation in dilute gases*, 2nd ed. (Cambridge University Press, 2008).

[58] C. Chin, R. Grimm, P. Julienne, and E. Tiesinga, “Feshbach resonances in ultracold gases”, Rev. Mod. Phys. **82**, 1225–1286 (2010).

[59] S. E. Pollack, D. Dries, R. G. Hulet, K. M. F. Magalhães, E. A. L. Henn, E. R. F. Ramos, M. A. Caracanhas, and V. S. Bagnato, “Collective excitation of a bose-einstein condensate by modulation of the atomic scattering length”, Phys. Rev. A **81**, 053627 (2010).

[60] I. Vidanovich, A. Balaz1, H. Al-Jibbouri, and A. Pelster, “Nonlinear bose-einstein-condensate dynamics induced by a harmonic modulation of the s-wave scattering length”, Phys. Rev. A **84**, 013618 (2011).

[61] J. H. V. Nguyen, M. C. Tsatsos, D. Luo, A. U. J. Lode, G. D. Telles, V. S. Bagnato, and R. G. Hulet, “Parametric excitation of a bose-einstein condensate: from faraday waves to granulation”, Phys. Rev. X **9**, 011052 (2019).

[62] A. D. Linde, “Chaotic Inflation”, Phys. Lett. B **129**, 177–181 (1983).

[63] N. Okada, V. N. ¸Seno˘ guz, and Q. Shafi, “The Observational Status of Simple Inflationary Models: an Update”, Turk. J. Phys. **40**, 150–162 (2016).

[64] P. Gorenstein and W. Tucker, “Astronomical signatures of dark matter”, Advances in High Energy Physics **2014** (2014).

[65] S. Yu. Khlebnikov and I. I. Tkachev, “Classical decay of inflaton”, Phys. Rev. Lett. **77**, 219–222 (1996).

[66] G. Aarts, G. F. Bonini, and C. Wetterich, “On Thermalization in classical scalar field theory”, Nucl. Phys. **B587**, 403–418 (2000).

[67] J. Berges and S. Borsanyi, “Range of validity of transport equations”, Phys. Rev. **D74**, 045022 (2006).

[68] J. Berges and D. Sexty, “Bose condensation far from equilibrium”, Phys. Rev. Lett. **108**, 161601 (2012).

[69] M. A. Amin, M. P. Hertzberg, D. I. Kaiser, and J. Karouby, “Nonperturbative Dynamics Of Reheating After Inflation: A Review”, Int. J. Mod. Phys. **D24**, 1530003 (2014).

[70] J. Berges, “Controlled nonperturbative dynamics of quantum fields out of equilibrium”, Nucl. Phys. **A699**, 847–886 (2002).

[71] G. Aarts, D. Ahrensmeier, R. Baier, J. Berges, and J. Serreau, “Far from equilibrium dynamics with broken symmetries from the 2PI - 1/N expansion”, Phys. Rev. **D66**, 045008 (2002).

[72] E. W. Kolb and I. I. Tkachev, “Large amplitude isothermal fluctuations and high density dark matter clumps”, Phys. Rev. **D50**, 769–773 (1994).

[73] J. Enander, A. Pargner, and T. Schwetz, “Axion minicluster power spectrum and mass function”, JCAP **1712**, 038 (2017).

[74] C. J. Hogan and M. J. Rees, “AXION MINICLUSTERS”, Phys. Lett. **B205**, 228–230 (1988).

[75] A. Kusenko and A. Mazumdar, “Gravitational waves from fragmentation of a primordial scalar condensate into Q-balls”, Phys. Rev. Lett. **101**, 211301 (2008).

[76] M. A. Amin, R. Easther, and H. Finkel, “Inflaton Fragmentation and Oscillon Formation in Three Dimensions”, JCAP **1012**, 001 (2010).

[77] N. Kitajima, J. Soda, and Y. Urakawa, “Gravitational wave forest from string axiverse”, JCAP **1810**, 008 (2018).

[78] R. Smits, M. Kramer, B. Stappers, D. Lorimer, J. Cordes, and A. Faulkner, “Pulsar searches and timing with the square kilometre array”, Astron. Astrophys. **493**, 1161–1170 (2009).

[79] J. Crowder and N. J. Cornish, “Beyond LISA: Exploring future gravitational wave missions”, Phys. Rev. **D72**, 083005 (2005).

[80] E. W. Kolb and M. S. Turner, “The Early Universe”, Front. Phys. **69**, 1–547 (1990).

[81] D. Baumann, “Inflation”, in Physics of the large and the small, TASI 09, proceedings of the Theoretical Advanced Study Institute in Elementary Particle Physics, Boulder, Colorado, USA, 1-26 June 2009 (2011), pp. 523–686.

[82] M. E. Peskin and D. V. Schroeder, *An Introduction to quantum field theory* (Addison-Wesley, Reading, USA, 1995).

[83] A. A. Belavin, A. M. Polyakov, A. S. Schwartz, and Yu. S. Tyupkin, “Pseudoparticle Solutions of the Yang-Mills Equations”, Phys. Lett. **59B**, [,350(1975); ,350(1975); ,350(1975)], 85–87 (1975).

[84] S. Coleman, *Aspects of Symmetry: Selected Erice Lectures* (Cambridge University Press, Cambridge, U.K., 1985).

[85] “Baryons”, Physics Letters B **667**, Review of Particle Physics, 1061 –1206 (2008).

[86] R. J. Crewther, P. Di Vecchia, G. Veneziano, and E. Witten, “Chiral Estimate of the Electric Dipole Moment of the Neutron in Quantum Chromodynamics”, Phys. Lett. **88B**, [Erratum: Phys. Lett.91B,487(1980)], 123 (1979).

[87] C. Vafa and E. Witten, “Parity Conservation in QCD”, Phys. Rev. Lett. **53**, 535 (1984).

[88] O. Klein, “Quantum Theory and Five-Dimensional Theory of Relativity. (In German and English)”, Z. Phys. **37**, [,76(1926)], 895–906 (1926).

[89] T. Kaluza, “Zum Unitätsproblem der Physik”, Sitzungsber. Preuss. Akad. Wiss. Berlin (Math. Phys.) **1921**, [Int. J. Mod. Phys.D27,no.14,1870001(2018)], 966–972 (1921).

[90] R. Amorim and J. Barcelos-Neto, “Compactification of gauge theories and the gauge invariance of massive modes”, Braz. J. Phys. **32**, 227–231 (2002).

[91] R. Sundrum, “Tasi 2004 lectures: To the fifth dimension and back”, in Theoretical Advanced Study Institute in Elementary Particle Physics: Many Dimensions of String Theory (TASI 2005) Boulder, Colorado, June 5-July 1, 2005 (2005), pp. 585–630.

[92] I. Antoniadis, K. Benakli, and M. Quiros, “Finite Higgs mass without supersymmetry”, New J. Phys. **3**, 20 (2001).

[93] M. Dhuria, G. Goswami, and J. Prasad, “Extranatural Inflation Redux”, Phys. Rev. D **96**, 083529 (2017).

[94] A. Hebecker, T. Mikhail, and P. Soler, “Euclidean wormholes, baby universes, and their impact on particle physics and cosmology”, Front. Astron. Space Sci. **5**, 35 (2018).

[95] K. Furuuchi, “Excursions through KK modes”, JCAP **1607**, 008 (2016).

[96] L. McAllister, P. Schwaller, G. Servant, J. Stout, and A. Westphal, “Runaway Relaxion Monodromy”, JHEP **02**, 124 (2018).

[97] R. Blumenhagen and E. Plauschinn, “Towards Universal Axion Inflation and Reheating in String Theory”, Phys. Lett. B **736**, 482–487 (2014).

[98] A. Hebecker, S. C. Kraus, and L. T. Witkowski, “D7-Brane Chaotic Inflation”, Phys. Lett. B **737**, 16–22 (2014).

[99] L. McAllister, E. Silverstein, A. Westphal, and T. Wrase, “The Powers of Monodromy”, JHEP **09**, 123 (2014).

[100] S. Dimopoulos, S. Kachru, J. McGreevy, and J. G. Wacker, “N-flation”, JCAP **08**, 003 (2008).

[101] C. D. Carone, J. Erlich, A. Sensharma, and Z. Wang, “Two-field axion-monodromy hybrid inflation model: Dante’s Waterfall”, Phys. Rev. D **91**, 043512 (2015).

[102] A. R. Liddle and D. H. Lyth, “COBE, gravitational waves, inflation and extended inflation”, Phys. Lett. B **291**, 391–398 (1992).

[103] K. Freese, J. A. Frieman, and A. V. Olinto, “Natural inflation with pseudo - Nambu-Goldstone bosons”, Phys. Rev. Lett. **65**, 3233–3236 (1990).

[104] T. Banks, M. Dine, P. J. Fox, and E. Gorbatov, “On the possibility of large axion decay constants”, JCAP **06**, 001 (2003).

[105] G. Steigman, “Primordial Nucleosynthesis in the Precision Cosmology Era”, Ann. Rev. Nucl. Part. Sci. **57**, 463–491 (2007).

[106] A. Hebecker, J. Jaeckel, F. Rompineve, and L. T. Witkowski, “Gravitational Waves from Axion Monodromy”, JCAP **1611**, 003 (2016).

[107] G. Aarts and J. Berges, “Nonequilibrium time evolution of the spectral function in quantum field theory”, Phys. Rev. **D64**, 105010 (2001).

[108] J. Berges and J. Cox, “Thermalization of quantum fields from time reversal invariant evolution equations”, Phys. Lett. B **517**, 369–374 (2001).

[109] J. Berges and B. Wallisch, “Nonthermal Fixed Points in Quantum Field Theory Beyond the Weak-Coupling Limit”, Phys. Rev. **D95**, 036016 (2017).

[110] L. Shen and J. Berges, “Spectral, statistical and vertex functions in scalar quantum field theory far from equilibrium”, Phys. Rev. D **101**, 056009 (2020).

[111] L. V. S. Zakharov V. E. and F. G., “Kolmogorov Spectra of Turbulence I : Wave Turbulence”, Springer-Verlag, Berlin (1992).

[112] J. Berges, K. Boguslavski, S. Schlichting, and R. Venugopalan, “Basin of attraction for turbulent thermalization and the range of validity of classical-statistical simulations”, JHEP **05**, 054 (2014).

[113] J. Berges and T. Gasenzer, “Quantum versus classical statistical dynamics of an ultracold Bose gas”, Phys. Rev. **A76**, 033604 (2007).

[114] J. Berges and J. Jaeckel, “Far from equilibrium dynamics of Bose-Einstein condensation for Axion Dark Matter”, Phys. Rev. **D91**, 025020 (2015).

[115] J. Deng, S. Schlichting, R. Venugopalan, and Q. Wang, “Off-equilibrium infrared structure of self-interacting scalar fields: Universal scaling, Vortex-antivortex superfluid dynamics and Bose-Einstein condensation”, Phys. Rev. **A97**, 053606 (2018).

[116] J. Berges, K. Boguslavski, S. Schlichting, and R. Venugopalan, “Universal attractor in a highly occupied non-Abelian plasma”, Phys. Rev. **D89**, 114007 (2014).

[117] G. N. Felder, J. Garcia-Bellido, P. B. Greene, L. Kofman, A. D. Linde, and I. Tkachev, “Dynamics of symmetry breaking and tachyonic preheating”, Phys. Rev. Lett. **87**, 011601 (2001).

[118] J. Berges and G. Hoffmeister, “Nonthermal fixed points and the functional renormalization group”, Nucl. Phys. **B813**, 383–407 (2009).

[119] J. Berges, K. Boguslavski, S. Schlichting, and R. Venugopalan, “Universality far from equilibrium: From superfluid Bose gases to heavy-ion collisions”, Phys. Rev. Lett. **114**, 061601 (2015).

[120] J. Berges, K. Boguslavski, S. Schlichting, and R. Venugopalan, “Nonequilibrium fixed points in longitudinally expanding scalar theories: infrared cascade, Bose condensation and a challenge for kinetic theory”, Phys. Rev. **D92**, 096006 (2015).

[121] A. H. Guth, M. P. Hertzberg, and C. Prescod-Weinstein, “Do Dark Matter Axions Form a Condensate with Long-Range Correlation?”, Phys. Rev. **D92**, 103513 (2015).

[122] P. K. Townsend, “Spontaneous Symmetry Breaking in O(n) Symmetric phi**6 Theory in the 1/n Expansion”, Phys. Rev. **D12**, [Erratum: Phys. Rev.D16,533(1977)], 2269 (1975).

[123] P. K. Townsend, “Consistency of the 1/n Expansion for Three-Dimensional phi**6 Theory”, Nucl. Phys. **B118**, 199–217 (1977).

[124] S. R. Coleman, “The Fate of the False Vacuum. 1. Semiclassical Theory”, Phys. Rev. **D15**, [Erratum: Phys. Rev.D16,1248(1977)], 2929–2936 (1977).

[125] J. Callan Curtis G. and S. R. Coleman, “The Fate of the False Vacuum. 2. First Quantum Corrections”, Phys. Rev. D **16**, 1762–1768 (1977).

[126] J. Braden, M. C. Johnson, H. V. Peiris, A. Pontzen, and S. Weinfurtner, “A New Semiclassical Picture of Vacuum Decay”, arXiv preprint hep-th:1806.06069 (2018).

[127] M. P. Hertzberg and M. Yamada, “Vacuum Decay in Real Time and Imaginary Time Formalisms”, Phys. Rev. D **100**, 016011 (2019).

[128] L. Darmé, J. Jaeckel, and M. Lewicki, “Towards the fate of the oscillating false vacuum”, Phys. Rev. **D96**, 056001 (2017).

[129] R. Easther, J. T. Giblin Jr, L. Hui, and E. A. Lim, “A New Mechanism for Bubble Nucleation: Classical Transitions”, Phys. Rev. **D80**, 123519 (2009).

[130] N. Fonseca, E. Morgante, R. Sato, and G. Servant, “Relaxion Fluctuations (Self-stopping Relaxion) and Overview of Relaxion Stopping Mechanisms”, arXiv preprint hep-ph:1911.08473; DESY 19-203, DESY-19-203 (2019).

[131] N. Fonseca, E. Morgante, R. Sato, and G. Servant, “Axion fragmentation”, JHEP **04**, 010 (2020).

[132] E. W. Kolb and I. I. Tkachev, “Axion miniclusters and Bose stars”, Phys. Rev. Lett. **71**, 3051–3054 (1993).

[133] M. Fairbairn, D. J. E. Marsh, J. Quevillon, and S. Rozier, “Structure formation and microlensing with axion miniclusters”, Phys. Rev. **D97**, 083502 (2018).

[134] J. Redondo, “Bounds on Very Weakly Interacting Sub-eV Particles (WISPs) from Cosmology and Astrophysics”, in Proceedings, 4th Patras Workshop on Axions, WIMPs and WISPs (AXION-WIMP 2008): Hamburg, Germany, June 18-21, 2008 (2008), pp. 23–26.

[135] J. Jaeckel and A. Ringwald, “The Low-Energy Frontier of Particle Physics”, Ann. Rev. Nucl. Part. Sci. **60**, 405–437 (2010).

[136] I. G. Irastorza and J. Redondo, “New experimental approaches in the search for axion-like particles”, Prog. Part. Nucl. Phys. **102**, 89–159 (2018).

[137] G. Alonso-Álvarez and J. Jaeckel, “Exploring axionlike particles beyond the canonical setup”, Phys. Rev. **D98**, 023539 (2018).

[138] G. Alonso-Álvarez and J. Jaeckel, “Lightish but clumpy: scalar dark matter from inflationary fluctuations”, JCAP **1810**, 022 (2018).

[139] S.-Y. Ho, K. Saikawa, and F. Takahashi, “Enhanced photon coupling of ALP dark matter adiabatically converted from the QCD axion”, JCAP **1810**, 042 (2018).

[140] R. Daido, F. Takahashi, and W. Yin, “The ALP miracle: unified inflaton and dark matter”, JCAP **1705**, 044 (2017).

[141] R. Daido, F. Takahashi, and W. Yin, “The ALP miracle revisited”, JHEP **02**, 104 (2018).

[142] R. Daido, F. Takahashi, and N. Yokozaki, “Enhanced axion–photon coupling in GUT with hidden photon”, Phys. Lett. **B780**, 538–542 (2018).

[143] V. Irsic, M. Viel, M. G. Haehnelt, J. S. Bolton, and G. D. Becker, “First constraints on fuzzy dark matter from Lyman-α forest data and hydrodynamical simulations”, Phys. Rev. Lett. **119**, 031302 (2017).

[144] T. Kobayashi, R. Murgia, A. De Simone, V. Irsic, and M. Viel, “Lyman-α constraints on ultralight scalar dark matter: Implications for the early and late universe”, Phys. Rev. D **96**, 123514 (2017).

[145] L. Visinelli and P. Gondolo, “Dark Matter Axions Revisited”, Phys. Rev. D **80**, 035024 (2009).

[146] A. Tranberg, “2PI simulations in expanding backgrounds: Doing it anyway!”, Nucl. Phys. **A820**, 195C–198C (2009).

[147] G. W. Gibbons and S. W. Hawking, “Cosmological Event Horizons, Thermodynamics, and Particle Creation”, Phys. Rev. **D15**, 2738–2751 (1977).

[148] P. Agrawal, G. Marques-Tavares, and W. Xue, “Opening up the QCD axion window”, JHEP **03**, 049 (2018).

[149] P. Agrawal, N. Kitajima, M. Reece, T. Sekiguchi, and F. Takahashi, “Relic Abundance of Dark Photon Dark Matter”, Phys. Lett. **B801**, 135136 (2020).

[150] R. T. Co, A. Pierce, Z. Zhang, and Y. Zhao, “Dark Photon Dark Matter Produced by Axion Oscillations”, Phys. Rev. D **99**, 075002 (2019).

[151] M. Bastero-Gil, J. Santiago, L. Ubaldi, and R. Vega-Morales, “Vector dark matter production at the end of inflation”, JCAP **1904**, 015 (2019).

[152] G. N. Felder and I. Tkachev, “LATTICEEASY: A Program for lattice simulations of scalar fields in an expanding universe”, Comput. Phys. Commun. **178**, 929–932 (2008).

[153] L. Husdal, “On Effective Degrees of Freedom in the Early Universe”, Galaxies **4**, 78 (2016).

[154] V. K. Narayanan, D. N. Spergel, R. Dave, and C.-P. Ma, “Constraints on the mass of warm dark matter particles and the shape of the linear power spectrum from the Lyα forest”, Astrophys. J. **543**, L103–L106 (2000).

[155] M. Viel, J. Lesgourgues, M. G. Haehnelt, S. Matarrese, and A. Riotto, “Constraining warm dark matter candidates including sterile neutrinos and light gravitinos with WMAP and the Lyman-alpha forest”, Phys. Rev. **D71**, 063534 (2005).

[156] T. Kobayashi and P. G. Ferreira, “Emergent Dark Energy from Dark Matter”, Phys. Rev. **D97**, 121301 (2018).

[157] P. W. Graham, J. Mardon, and S. Rajendran, “Vector Dark Matter from Inflationary Fluctuations”, Phys. Rev. D **93**, 103520 (2016).

[158] J. E. Gunn and I. Gott J. Richard, “On the Infall of Matter into Clusters of Galaxies and Some Effects on Their Evolution”, Astrophys. J. **176**, 1–19 (1972).

[159] P. J. Armitage, “Lecture notes on the formation and early evolution of planetary systems”, arXiv preprint astro-ph:0701485.

[160] Y. Kahn, B. R. Safdi, and J. Thaler, “Broadband and Resonant Approaches to Axion Dark Matter Detection”, Phys. Rev. Lett. **117**, 141801 (2016).

[161] Y. V. Stadnik and V. V. Flambaum, “Searching for dark matter and variation of fundamental constants with laser and maser interferometry”, Phys. Rev. Lett. **114**, 161301 (2015).

[162] T. M. Shokair et al., "Future Directions in the Microwave Cavity Search for Dark Matter Axions", Int. J. Mod. Phys. **A29**, 1443004 (2014).

[163] E. Petrakou, "Haloscope searches for dark matter axions at the Center for Axion and Precision Physics Research", EPJ Web Conf. **164**, 01012 (2017).

[164] A. Droster and K. van Bibber, "HAYSTAC Status, Results, and Plans", in 13th Conference on the Intersections of Particle and Nuclear Physics (CIPANP 2018) Palm Springs, California, USA, May 29-June 3, 2018 (2019).

[165] C. Gatti et al., "The Klash Proposal: Status and Perspectives", in 14th Patras Workshop on Axions, WIMPs and WISPs (AXION-WIMP 2018) (PATRAS 2018) Hamburg, Germany, June 18-22, 2018 (2018).

[166] B. Majorovits et al., "MADMAX: A new road to axion dark matter detection", J. Phys. Conf. Ser. **1342**, 012098 (2020).

[167] B. T. McAllister, G. Flower, E. N. Ivanov, M. Goryachev, J. Bourhill, and M. E. Tobar, "The ORGAN Experiment: An axion haloscope above 15 GHz", Phys. Dark Univ. **18**, 67–72 (2017).

[168] D. Alesini et al., "Galactic axions search with a superconducting resonant cavity", Phys. Rev. **D99**, 101101 (2019).

[169] A. A. Melcon et al., "Axion Searches with Microwave Filters: the RADES project", JCAP **1805**, 040 (2018).

[170] G. Bertone et al., "Gravitational wave probes of dark matter: challenges and opportunities", arXiv preprint astro-ph.CO:1907.10610 (2019).

[171] C. Cutler and E. E. Flanagan, "Gravitational waves from merging compact binaries: How accurately can one extract the binary's parameters from the inspiral wave form?", Phys. Rev. D **49**, 2658–2697 (1994).

[172] J. Abadie et al., "Search for Gravitational Waves from Low Mass Compact Binary Coalescence in LIGO's Sixth Science Run and Virgo's Science Runs 2 and 3", Phys. Rev. D **85**, 082002 (2012).

[173] K. Kotake, K. Sato, and K. Takahashi, "Explosion mechanism, neutrino burst, and gravitational wave in core-collapse supernovae", Rept. Prog. Phys. **69**, 971–1144 (2006).

[174] J. Garcia-Bellido, D. G. Figueroa, and A. Sastre, "A Gravitational Wave Background from Reheating after Hybrid Inflation", Phys. Rev. **D77**, 043517 (2008).

[175] J. F. Dufaux, A. Bergman, G. N. Felder, L. Kofman, and J.-P. Uzan, "Theory and Numerics of Gravitational Waves from Preheating after Inflation", Phys. Rev. **D76**, 123517 (2007).

[176] C. Caprini et al., "Science with the space-based interferometer eLISA. II: Gravitational waves from cosmological phase transitions", JCAP **1604**, 001 (2016).

[177] B. P. Abbott et al., "Observation of Gravitational Waves from a Binary Black Hole Merger", Phys. Rev. Lett. **116**, 061102 (2016).

[178] B. P. Abbott et al., "GW151226: Observation of Gravitational Waves from a 22-Solar-Mass Binary Black Hole Coalescence", Phys. Rev. Lett. **116**, 241103 (2016).

[179] B. Abbott et al., "GW170817: Observation of Gravitational Waves from a Binary Neutron Star Inspiral", Phys. Rev. Lett. **119**, 161101 (2017).

[180] S. M. Carroll, *Spacetime and geometry* (Cambridge University Press, 2019).

[181] K. D. Lozanov and M. A. Amin, “Gravitational perturbations from oscillons and transients after inflation”, Phys. Rev. D **99**, 123504 (2019).

[182] Y. Sang and Q.-G. Huang, “Stochastic Gravitational-Wave Background from Axion-Monodromy Oscillons in String Theory During Preheating”, Phys. Rev. D **100**, 063516 (2019).

[183] A. Kosowsky, M. S. Turner, and R. Watkins, “Gravitational radiation from colliding vacuum bubbles”, Phys. Rev. D **45**, 4514–4535 (1992).

[184] G. M. H. and, “Advanced LIGO: the next generation of gravitational wave detectors”, Classical and Quantum Gravity **27**, 084006 (2010).

[185] F. Acernese et al., “Advanced Virgo: a second-generation interferometric gravitational wave detector”, Class. Quant. Grav. **32**, 024001 (2015).

[186] H. Luck, “The GEO-600 project”, Class. Quant. Grav. **14**, 1471–1476 (1997).

[187] M. Ando and K. Tsubono, “TAMA project: Design and current status”, AIP Conf. Proc. **523**, 128 (2000).

[188] P Amaro-Seoane, H Audley, S Babak, J Baker, E Barausse, P Bender, E Berti, P Binetruy, M Born, D Bortoluzzi, et al., “Laser interferometer space antenna. arxiv 2017”, arXiv preprint arXiv:1702.00786 (2017).

[189] S. Kawamura et al., “The Japanese space gravitational wave antenna DECIGO”, Class. Quant. Grav. **23**, S125–S132 (2006).

[190] G. Hobbs and S. Dai, “Gravitational wave research using pulsar timing arrays”, Natl. Sci. Rev. **4**, 707–717 (2017).

[191] R. N. Manchester et al., “The Parkes Pulsar Timing Array Project”, Publ. Astron. Soc. Austral. **30**, 17 (2013).

[192] F. Jenet et al., “The North American Nanohertz Observatory for Gravitational Waves”, arXiv preprint astro-ph.IM:0909.1058 (2009).

[193] M. Kramer and D. J. Champion, “The European Pulsar Timing Array and the Large European Array for Pulsars”, Class. Quant. Grav. **30**, 224009 (2013).

[194] J. P. W. Verbiest et al., “The International Pulsar Timing Array: First Data Release”, Mon. Not. Roy. Astron. Soc. **458**, 1267–1288 (2016).

[195] C. J. Moore, R. H. Cole, and C. P. L. Berry, “Gravitational-wave sensitivity curves”, Class. Quant. Grav. **32**, 015014 (2015).

[196] P. A. R. Ade et al., “Joint Analysis of BICEP2/$Keck Array$ and $Planck$ Data”, Phys. Rev. Lett. **114**, 101301 (2015).

[197] Z. Huang, “The Art of Lattice and Gravity Waves from Preheating”, Phys. Rev. **D83**, 123509 (2011).

[198] C. S. Machado, W. Ratzinger, P. Schwaller, and B. A. Stefanek, “Audible Axions”, JHEP **01**, 053 (2019).

[199] J. T. Giblin and E. Thrane, “Estimates of maximum energy density of cosmological gravitational-wave backgrounds”, Phys. Rev. **D90**, 107502 (2014).

[200] P. Amaro-Seoane et al., “Laser Interferometer Space Antenna”, (2017).

[201] J. A. R. Cembranos, A. L. Maroto, S. J. Núñez Jareño, and H. Villarrubia-Rojo, “Constraints on anharmonic corrections of Fuzzy Dark Matter”, JHEP **08**, 073 (2018).

[202] C. S. Machado, W. Ratzinger, P. Schwaller, and B. A. Stefanek, “Gravitational wave probes of axion-like particles”, arXiv preprint hep-ph:1912.01007 (2019).

[203] J. Schmiedmayer and J. Berges, “Cold Atom Cosmology”, Science **341**, 1188–1189 (2013).

[204] C.-L. Hung, V. Gurarie, and C. Chin, “From cosmology to cold atoms: observation of sakharov oscillations in a quenched atomic superfluid”, Science **341**, 1213–1215 (2013).

[205] T. Gasenzer, J. Berges, M. G. Schmidt, and M. Seco, “Non-perturbative dynamical many-body theory of a Bose-Einstein condensate”, Phys. Rev. A **72**, 063604 (2005).

[206] M. H. Anderson, J. R. Ensher, M. R. Matthews, C. E. Wieman, and E. A. Cornell, “Observation of bose-einstein condensation in a dilute atomic vapor”, Science **269**, 198–201 (1995).

[207] K. Davis, M.-O. Mewes, M. Andrews, N. van Druten, D. Durfee, D. Kurn, and W. Ketterle, “Bose-Einstein condensation in a gas of sodium atoms”, Phys. Rev. Lett. **75**, 3969–3973 (1995).

[208] C. Bradley, C. Sackett, and R. Hulet, “Bose-Einstein Condensation of Lithium: Observation of Limited Condensate Number”, Phys. Rev. Lett. **78**, 985–989 (1997).

[209] R. Baier and T. Stockamp, “Kinetic equations for Bose-Einstein condensates from the 2PI effective action”, arXiv preprint hep-ph:0412310 (2004).

[210] A. Branschadel and T. Gasenzer, “2PI nonequilibrium versus transport equations for an ultracold Bose gas”, J. Phys. B **41**, 135302 (2008).

[211] P. Blakie, A. Bradley, M. Davis, R. Ballagh, and C. Gardiner, “Dynamics and statistical mechanics of ultra-cold Bose gases using c-field techniques”, Adv. Phys. **57**, 363 (2008).

[212] A. Polkovnikov, “Phase space representation of quantum dynamics”, Annals of Physics **325**, 1790–1852 (2010).

[213] L. Landau and E. Lifshitz, “Quantum mechanics: non-relativistic theory, volume 3 of”, Course of theoretical physics (1977).

[214] Y. Kawaguchi and M. Ueda, “Spinor Bose-Einstein condensates”, Phys. Rept. **520**, 253–381 (2012).

[215] D. M. Stamper-Kurn and M. Ueda, *Spinor bose gases: explorations of symmetries, magnetism and quantum dynamics*, 2012.

[216] C. Chin, R. Grimm, P. Julienne, and E. Tiesinga, “Feshbach resonances in ultracold gases”, Reviews of Modern Physics **82**, 1225 (2010).

[217] H. Feshbach, “Unified theory of nuclear reactions”, Annals of Physics **5**, 357–390 (1958).

[218] A. M. Rey, B. Hu, E. Calzetta, and C. W. Clark, “Quantum kinetic theory of bec lattice gas: boltzmann equations from 2pi-ctp effective action”, arXiv preprint cond-mat/0412066 (2004).

[219] S Dyachenko, A. Newell, A Pushkarev, and V. Zakharov, “Optical turbulence: weak turbulence, condensates and collapsing filaments in the nonlinear schrödinger equation”, Physica D: Nonlinear Phenomena **57**, 96–160 (1992).

[220] M. Uhlmann, Y. Xu, and R. Schutzhold, “Aspects of cosmic inflation in expanding Bose-Einstein condensates”, New J. Phys. **7**, 248 (2005).

[221] S. Eckel, A. Kumar, T. Jacobson, I. B. Spielman, and G. K. Campbell, “A rapidly expanding Bose-Einstein condensate: an expanding universe in the lab”, Phys. Rev. **X8**, 021021 (2018).

[222] S.-Y. Chä and U. R. Fischer, "Probing the scale invariance of the inflationary power spectrum in expanding quasi-two-dimensional dipolar condensates", Phys. Rev. Lett. **118**, [Addendum: Phys. Rev. Lett.118,no.17,179901(2017)], 130404 (2017).

[223] A. Suárez and P.-H. Chavanis, "Hydrodynamic representation of the Klein-Gordon-Einstein equations in the weak field limit: General formalism and perturbations analysis", Phys. Rev. **D92**, 023510 (2015).

[224] R. Saint-Jalm, P. C. Castilho, É. Le Cerf, B. Bakkali-Hassani, J.-L. Ville, S. Nascimbene, J. Beugnon, and J. Dalibard, "Dynamical symmetry and breathers in a two-dimensional bose gas", Physical Review X **9**, 021035 (2019).

[225] V. Gritsev, P. Barmettler, and E. Demler, "Scaling approach to quantum non-equilibrium dynamics of many-body systems", New J. Phys. **12**, 113005 (2010).

[226] M. Olshanii, H. Perrin, and V. Lorent, "Example of a quantum anomaly in the physics of ultracold gases", Phys. Rev. Lett. **105**, 095302 (2010).

[227] C. Neuenhahn, A. Polkovnikov, and F. Marquardt, "Localized phase structures growing out of quantum fluctuations in a quench of tunnel-coupled atomic condensates", Physical review letters **109**, 085304 (2012).

[228] C. Neuenhahn and F. Marquardt, "Quantum simulation of expanding space–time with tunnel-coupled condensates", New J. Phys. **17**, 125007 (2015).

[229] A. Posazhennikova, M. Trujillo-Martinez, and J. Kroha, "Inflationary quasiparticle creation and thermalization dynamics in coupled Bose-Einstein condensates", Phys. Rev. Lett. **116**, 225304 (2016).

[230] T. V. Zache, V. Kasper, and J. Berges, "Inflationary preheating dynamics with two-species condensates", Phys. Rev. **A95**, 063629 (2017).

[231] S. Robertson, F. Michel, and R. Parentani, "Nonlinearities induced by parametric resonance in effectively 1D atomic Bose condensates", Phys. Rev. **D98**, 056003 (2018).

[232] N. N. Bogolyubov, "On the theory of superfluidity", J. Phys.(USSR) **11**, [Izv. Akad. Nauk Ser. Fiz.11,77(1947)], 23–32 (1947).

[233] U. R. Fischer and R. Schutzhold, "Quantum simulation of cosmic inflation in two-component Bose-Einstein condensates", Phys. Rev. **A70**, 063615 (2004).

[234] E. A. Donley, N. R. Claussen, S. L. Cornish, J. L. Roberts, E. A. Cornell, and C. E. Wieman, "Dynamics of collapsing and exploding bose–einstein condensates", Nature **412**, 295 (2001).

[235] P. Jain, S. Weinfurtner, M. Visser, and C. W. Gardiner, "Analogue model of a FRW universe in Bose-Einstein condensates: Application of the classical field method", Phys. Rev. **A76**, 033616 (2007).

[236] J. C. Jaskula, G. B. Partridge, M. Bonneau, R. Lopes, J. Ruaudel, D. Boiron, and C. I. Westbrook, "An acoustic analog to the dynamical Casimir effect in a Bose-Einstein condensate", Phys. Rev. Lett. **109**, 220401 (2012).

[237] C.-M. Schmied, M. Prüfer, M. K. Oberthaler, and T. Gasenzer, "Bidirectional universal dynamics in a spinor Bose gas close to a nonthermal fixed point", Phys. Rev. **A99**, 033611 (2019).

[238] S. Erne, R. Bücker, T. Gasenzer, J. Berges, and J. Schmiedmayer, "Universal dynamics in an isolated one-dimensional Bose gas far from equilibrium", Nature **563**, 225–229 (2018).

[239] M. Prüfer, P. Kunkel, H. Strobel, S. Lannig, D. Linnemann, C.-M. Schmied, J. Berges, T. Gasenzer, and M. K. Oberthaler, "Observation of universal quantum dynamics far from equilibrium", arXiv preprint cond-mat.quant-gas:1805.11881 (2018).

[240] E. Zaremba, T. Nikuni, and A. Griffin, "Dynamics of trapped bose gases at finite temperatures", Journal of Low Temperature Physics **116**, 277–345 (1999).

[241] B. Nowak, J. Schole, D. Sexty, and T. Gasenzer, "Nonthermal fixed points, vortex statistics, and superfluid turbulence in an ultracold Bose gas", Phys. Rev. **A85**, 043627 (2012).

[242] N. Navon, A. L. Gaunt, R. P. Smith, and Z. Hadzibabic, "Emergence of a turbulent cascade in a quantum gas", Nature **539**, 72 (2016).

[243] A. D. Linde, "Decay of the False Vacuum at Finite Temperature", Nucl. Phys. B **216**, [Erratum: Nucl.Phys.B 223, 544 (1983)], 421 (1983).

[244] J. Dawson, "On landau damping", The physics of fluids **4**, 869–874 (1961).

[245] R. Harrison, I. Moroz, and K. Tod, "A numerical study of the schrödinger–newton equations", Nonlinearity **16**, 101 (2002).

[246] E. D. Schiappacasse and M. P. Hertzberg, "Analysis of Dark Matter Axion Clumps with Spherical Symmetry", JCAP **01**, [Erratum: JCAP 03, E01 (2018)], 037 (2018).

[247] D. Levkov, A. Panin, and I. Tkachev, "Gravitational Bose-Einstein condensation in the kinetic regime", Phys. Rev. Lett. **121**, 151301 (2018).

[248] J. Ellis, M. Lewicki, and J. M. No, "Gravitational waves from first-order cosmological phase transitions: lifetime of the sound wave source", arXiv preprint hep-ph:2003.07360; KCL-PH-TH/2020-04, CERN-TH-2020-016, IFT-UAM/CSIC-20-35 (2020).

[249] O. Fialko, B. Opanchuk, A. Sidorov, P. Drummond, and J. Brand, "Fate of the false vacuum: towards realization with ultra-cold atoms", EPL **110**, 56001 (2015).

[250] J. Braden, M. C. Johnson, H. V. Peiris, and S. Weinfurtner, "Towards the cold atom analog false vacuum", JHEP **07**, 014 (2018).

[251] J. Braden, M. C. Johnson, H. V. Peiris, A. Pontzen, and S. Weinfurtner, "Nonlinear Dynamics of the Cold Atom Analog False Vacuum", JHEP **10**, 174 (2019).

[252] I. Carusotto and C. Ciuti, "Quantum fluids of light", Reviews of Modern Physics **85**, 299 (2013).

[253] R. P. Feynman, "Simulating physics with computers", Int. J. Theor. Phys. **21**, edited by L. Brown, 467–488 (1982).

[254] A. Mazeliauskas and J. Berges, "Prescaling and far-from-equilibrium hydrodynamics in the quark-gluon plasma", Phys. Rev. Lett. **122**, 122301 (2019).